

EFFECT OF A SUPERSOLVUS HEAT TREATMENT ON THE MICROSTRUCTURE  
AND MECHANICAL PROPERTIES OF A POWDER METALLURGY PROCESSED  
NICKEL-BASE SUPERALLOY

By

DARRYL SLADE STOLZ

A DISSERTATION PRESENTED TO THE GRADUATE SCHOOL  
OF THE UNIVERSITY OF FLORIDA IN PARTIAL FULFILLMENT  
OF THE REQUIREMENTS FOR THE DEGREE OF  
DOCTOR OF PHILOSOPHY

UNIVERSITY OF FLORIDA

2004

Copyright 2004

by

Darryl Slade Stolz

This dissertation is dedicated to the loving memory of Earl A. Stolz, Jr. and Bradford F. Gifford, Jr.

## ACKNOWLEDGMENTS

I would like to thank Dr. Gerhard E. Fuchs for all of his support and guidance over the years. His knowledge of materials science in general, and superalloys specifically has helped me grow tremendously as a researcher in the pursuit of my Ph.D. degree. I would also like to thank all of my committee members for their guidance during this project: Dr. Robert T. DeHoff, Dr. Michael J. Kaufman, Dr. John J. Mecholsky, Jr., Dr. Luisa A. Dempere, and Dr. Nagaraj K. Arakere. I would like to especially thank Sean Conway and Crucible Compaction Metals (Oakdale, PA) for all of the materials provided for this study. In addition, I would like to acknowledge the help of Gerald R. Bourne and the Major Analytical Instrumentation Center (MAIC) at the University of Florida for assistance with my research. I thank all of the members of the High Temperature Alloys Laboratory for their technical assistance, and perhaps more importantly for all of the good memories that I will keep with me after I leave Gainesville. Finally, I would like to thank my family for their love, support, and patience throughout my educational career. Without all of this help, I truly could not have completed this project.

## TABLE OF CONTENTS

	<u>page</u>
ACKNOWLEDGMENTS .....	iv
LIST OF TABLES .....	viii
LIST OF FIGURES .....	x
ABSTRACT .....	xvi
CHAPTER	
1 BACKGROUND .....	1
Composition and Microstructure .....	2
Chemistry .....	3
Gamma Matrix .....	4
Gamma Prime Phase .....	4
Carbides and Borides .....	6
Strengthening Mechanisms .....	8
Powder Metallurgy Superalloys .....	10
Powder Processing .....	13
Powder production .....	13
Powder consolidation .....	16
Challenges .....	18
Alloy 720 .....	27
Chemistry and processing .....	27
Microstructure .....	31
Objectives .....	35
2 EXPERIMENTAL PROCEDURES .....	37
Materials .....	37
Development of Heat Treatment .....	37
Heat Treatment Trials .....	39
Heat Treatment .....	41
Characterization .....	43
Determination of $\gamma'$ Solvus .....	43
Differential thermal analysis .....	44
Metallographic examination .....	44

Microstructural Analysis .....	46
Mechanical Testing.....	47
Low Cycle Fatigue Testing .....	48
High Cycle Fatigue Testing.....	54
Tensile Testing .....	55
Creep Testing.....	56
Fracture Analysis.....	59
3 RESULTS .....	60
Microstructure.....	60
Development of Heat Treatment .....	60
Heat treatment trials .....	61
Heat treatment .....	67
Characterization.....	68
Determination of $\gamma'$ Solvus.....	68
Microstructural characterization .....	72
Mechanical Testing and Fracture Analysis.....	75
Low Cycle Fatigue .....	75
High Cycle Fatigue.....	81
HCF results.....	82
HCF fractography.....	84
Tensile Testing .....	99
Tensile results.....	99
Tensile fractography.....	101
Creep Testing.....	105
Creep results .....	105
Creep fractography .....	107
4 DISCUSSION .....	114
Microstructure.....	114
Heat Treatment .....	114
Characterization.....	116
Temperature of $\gamma'$ solvus.....	117
Microstructure .....	118
Mechanical Testing.....	124
Hardness Testing .....	125
Fatigue Testing .....	126
Tensile Testing .....	139
Creep Testing.....	143
Conclusions.....	146
Future Work.....	148

APPENDIX

A DIFFERENTIAL THERMAL ANALYSIS GRAPHS.....	150
B STATISTICAL DATA .....	153
Hardness Testing .....	153
The Volume Fraction of the Gamma Prime Phase .....	155
Gamma Prime Size Distributions .....	158
Grain Size .....	162
Stress Intensity Factors .....	163
C TENSILE FRACTURE MECHANICS .....	164
LIST OF REFERENCES.....	166
BIOGRAPHICAL SKETCH .....	173

## LIST OF TABLES

<u>Table</u>	<u>page</u>
1-1: Engine systems using forged P/M superalloys.....	12
1-2: Engines and airframe systems using as-HIP P/M superalloys. ....	12
1-3: Nominal chemistry of Alloy 720 and Alloy 720LI. ....	27
2-1: Sieve analysis of the master powder blends (MPBs) in weight percent.....	38
2-2: Chemistry analysis of the master powder blends in weight percent. ....	38
2-3: Heat treatment trial matrix.....	39
2-4: The LCF test matrix.....	54
2-5: The HCF test matrix. ....	55
2-6: The Tensile test matrix. ....	56
2-7: The Creep test matrix. ....	58
3-1: The DTA results from M&P Laboratories. ....	69
3-2: The DTA results from Dirats Laboratories. ....	70
3-3: The total $\gamma'$ volume fraction, and ASTM grain size. ....	74
3-4: Results from Rockwell C hardness tests for both heat treatments. ....	74
3-5: The HCF test results and crack initiation types.....	87
3-6: Area of crack growth regions on the HCF fracture surfaces.....	94
3-7: Tensile test results. ....	99
3-8: The creep results.....	106
4-1: Stress intensity factors and plastic zone sizes for the initial crack in HCF tests.....	132
4-2: Stress intensity factors and plastic zone sizes for the final crack in HCF tests.....	134

B-1: The hardness testing statistical data.....	153
B-2: The t-test data for the hardness testing. ....	154
B-3: The primary $\gamma'$ volume fraction data for the standard heat treatment.....	156
B-4: The secondary $\gamma'$ volume fraction data for the standard heat treatment. ....	156
B-5: The tertiary $\gamma'$ volume fraction data for the standard heat treatment.....	157
B-6: The primary $\gamma'$ volume fraction data for the alternate heat treatment. ....	157
B-7: The secondary $\gamma'$ volume fraction data for the alternate heat treatment.....	158
B-8: The primary $\gamma'$ size data for the standard heat treatment. ....	159
B-9: The secondary $\gamma'$ size data for the standard heat treatment. ....	159
B-10: The tertiary $\gamma'$ size data for the standard heat treatment.....	160
B-11: The primary $\gamma'$ size data for the alternate heat treatment.....	161
B-12: The secondary $\gamma'$ size data for the alternate heat treatment. ....	161
B-13: The grain size data for the standard heat treatment. ....	163
B-14: The grain size data for the alternate heat treatment. ....	163
B-15: The t-test data for the initial crack stress intensity factors. ....	163
C-1: Area of crack in fractured tensile specimens. ....	164
C-2: Stress intensity factor for tensile tests.....	165

## LIST OF FIGURES

<u>Figure</u>	<u>page</u>
1-1. Nickel-aluminum phase diagram.....	5
1-2: The Ni <sub>3</sub> Al solid solution field at approximately 1150°C for various ternary alloys. .6	6
1-3: Flow stress as a function of temperature for Ni <sub>3</sub> Al. ....	7
1-4: Effect of valency difference on hardening of nickel alloys. N <sub>v</sub> is electron vacancy number of the solute. ....	9
1-5: Vertical gas atomizer.....	14
1-6: Formation of spherical metal powder by gas atomization.....	15
1-7: Material and fabrication savings with P/M processing of superalloys.....	18
1-8: Plastic strain suffered by smaller and larger particles during HIPing of a bimodal particle size distribution of powders. ....	20
1-9: PPB initiation site in doped René 95.....	21
1-10: Type 1 ceramic inclusion fatigue initiation site. ....	22
1-11: Comparison of average LCF lives of HIP vs. HIP + Forge and Extrude + Forge René 95.....	24
1-12: Fatigue initiation at a crystallographic defect. ....	25
1-13: Average low cycle fatigue life for a P/M superalloy during 1980 through 1996....	25
1-14: Effect of thermal exposure on microstructures of subsolvus heat treated Alloy 720 and Alloy 720LI. ....	29
1-15: Experimental TTT diagram for the formation of 0.5 and 1.0 wt% of sigma in Alloy 720LI.....	30
1-16: Mean diameter of the cooling $\gamma'$ as a function of the interrupt temperature in Alloy 720LI. ....	32
1-17: P/M Alloy 720 microstructure.....	34

1-18: Optical micrographs of Astroloy.....	35
2-1: JEOL JSM 6400 SEM.....	42
2-2: Carbolite box furnace.....	45
2-3: Tensile sample design.....	49
2-4: Creep sample design.....	50
2-5: Low cycle fatigue sample design.....	51
2-6: Instron-Satec servo-hydraulic test frame.....	52
2-7: Instron-Satec Creep frame.....	57
3-1: Heat treatment trial samples with various soak temperatures.....	62
3-2: Heat treatment trial samples with different cooling rates.....	63
3-3: Heat treatment trial samples with different soak times and final temperature before fan-air-cool.....	64
3-4: Heat treatment schedules.....	65
3-5: The standard and alternate heat treatment microstructures.....	66
3-6: MPB 96SW865 after solution heat treating at 1175°C (2147°F).....	66
3-7: MPB 96SW865 after solution heat treating at 1165°C (2129°F).....	67
3-8: The $\gamma'$ solvus trials quenched in iced brine after an hour at the solutioning temperature.....	71
3-9: The solvus trials that were fully solutioned and then control-cooled.....	72
3-10: The $\gamma/\gamma'$ microstructure in heat treated Alloy 720LI.....	73
3-11: Grain boundary microstructure of heat treated Alloy 720LI.....	74
3-12: Low cycle fatigue sample that was misaligned and tested in compression.....	76
3-13: Push/pull rods.....	76
3-14: Low cycle fatigue sample with notches machined just after the threaded region and before the shoulder of the sample.....	77
3-15: Ceramic inclusion type defect in standard heat treatment sample tested at 538°C (1000°F) and a strain range of 1.1%.....	79

3-16: Standard heat treatment sample tested at 538°C (1000°F) and a strain range of 1.0%.....	79
3-17: Alternate heat treatment sample tested at 538°F (1000°C) and a strain range of 1.0%.....	80
3-18: Relatively flat featureless region just after crack initiation in low cycle fatigue ....	81
3-19: Representative micrographs of the fast fracture region of LCF samples. ....	82
3-20: High cycle fatigue S-N curves for specimens tested at 538°C (1000°F). ....	83
3-21: High cycle fatigue S-N curves for specimens tested at 649°C (1000°F). ....	84
3-22: High cycle fatigue S-N curves for tests of the standard heat treatment at both 538°C (1000°F) and 649°C (1200°F).....	85
3-23: High cycle fatigue S-N curves for tests of the alternate heat treatment at 538°C (1000°F) and 649°C (1200°F).....	86
3-24: Optical micrographs of HCF fracture surfaces of samples tested at 649°C and 1086 MPa. ....	86
3-25: Ceramic agglomerate as initiation point in standard heat treatment sample tested at 538°C (1000°F) and a stress range of 1034 MPa (150 Ksi).....	87
3-26: EDS spectra of crack initiation for standard heat treatment sample tested at 538°C and 1034 MPa.....	88
3-27: Ceramic agglomerate as initiation point for standard heat treatment sample tested at 538°C (1000°F) and a stress range of 1086 MPa (157.5 Ksi).....	88
3-28: Slip band cracking as initiation point an alternate heat treatment sample tested at 538°C (1000°F) and 993 MPa (144 Ksi).....	89
3-29: Primary carbide as the initiation type for the standard heat treatment sample tested at 649°C (1200°F) and 1086 MPa (157.5 Ksi).....	89
3-30: EDS spectra of Ti-rich particle as initiation point of standard heat treatment sample tested at 649°C and 1086 MPa.....	90
3-31: Unknown initiation type for alternate heat treatment sample tested at 649°C (1200°F) and 1034 MPa (150 Ksi).....	91
3-32: Crack origin for alternate heat treatment sample tested at 538°C (1000°F) and 1086 MPa (157.5 Ksi). ....	91
3-33: Initial crack region of fatigue samples. ....	92

3-34: Fracture surface near initiation in standard heat treatment sample tested at 538°C (1000°F) and a stress range of 1034 MPa (150 Ksi).	93
3-35: Fracture surface of standard heat treatment tested at 538°C (1000°F) and a stress range of 1086 MPa (157.5 Ksi) outside of discolored region.	93
3-36: Fracture surfaces far from origin of samples tested at 538°C (1000°F) and 993 MPa (144 Ksi).	94
3-37: Initial crack area versus stress range for the high cycle fatigue specimens.	95
3-38: Final crack area versus stress range for the high cycle fatigue specimens.	96
3-39: Secondary cracks at primary and secondary $\gamma'$ precipitates in samples tested at 538°C and 993 MPa.	97
3-40: Secondary cracks in fatigue samples tested at 1034 MPa	97
3-41: Fatigue samples tested at 538°C and 1086 MPa showing secondary cracks.	98
3-42: Yield strength vs. temperature for both heat treatments.	100
3-43: Elongation at failure vs. temperature for both heat treatments.	101
3-44: Tensile stress-strain curve for standard heat treatment sample tested at 1400°F.	102
3-45: Tensile stress-strain curve for alternate heat treatment sample tested at 1400°F.	102
3-46: Crack initiation region in standard heat treatment tensile samples.	103
3-47: Crack initiation region in alternate heat treatment tensile samples treatment.	104
3-48: Larson-Miller plot for creep rupture in Alloy 720LI.	107
3-49: Fast fracture propagation path for standard heat treatment sample tested at 677°C (1250°F) and 1034 MPa (150 Ksi).	108
3-50: Fast fracture propagation path for alternate heat treatment at 704°C (1300°F) and 689MPa (100Ksi).	109
3-51: Standard heat treatment sample tested at 760°C (1400°F) and 483 MPa (70 Ksi) showing fast fracture propagation path.	109
3-52: Standard heat treatment sample tested at 677°C and 1034 MPa with crack initiation at a grain boundary triple point.	110
3-53: Transgranular cracking during fatigue testing in samples tested at 677°C and 1034 MPa.	111

3-54: Large secondary crack in alternate heat treatment sample tested at 677°C and 1034 MPa. ....	111
3-55: Secondary cracks in high temperature creep tests.....	111
3-56: Grain boundary crack initiation in alternate heat treatment creep samples.....	112
3-57: Secondary cracks in creep samples tested at 677°C (1250°F) and 793 MPa (115 Ksi). ....	113
4-1: The tertiary and “quaternary” $\gamma'$ precipitates in the standard heat treatment. ....	119
4-2: Serrated grain boundary structure present in the alternate heat treatment microstructure.....	120
4-3: Histogram of $\gamma'$ volume fraction for the two heat treatments.....	121
4-4: Secondary and tertiary $\gamma'$ precipitates. ....	122
4-5: Comparison of fast fracture features during HCF fatigue and grain size.....	131
4-6: Secondary cracking in standard heat treatment fatigue samples. ....	135
4-7: Secondary cracks propagating transgranularly in alternate heat treatment fatigue samples. ....	136
4-8: Large pore at a grain boundary triple point in alternate heat treatment sample tested at 538°C and 1086 MPa. ....	136
4-9: Long secondary cracks in alternate heat treatment fatigue sample tested at 538°C and 1086 MPa.....	137
4-10: Yield strength vs. test temperature for both heat treatments. ....	140
4-11: Optical pictures showing the fracture surfaces of tensile samples.....	141
4-12: Alternate heat treatment creep sample tested at 732°C and 483 MPa showing secondary cracks initiating at and propagating along grain boundaries.....	144
4-13: Alternate heat treatment creep sample tested at 677°C and 1034 MPa showing void nucleation at a grain boundary triple point and at the interface between secondary $\gamma'$ precipitates and the matrix. ....	145
A-1: The DTA Graph of sample UMBCa.....	150
A-2: The DTA graph of sample UMBCb. ....	150
A-3: The DTA graph of sample UMBEa.....	151

A-4: The DTA graph of sample UMBEb. ....	151
A-5: The DTA graph of sample UMBCc. ....	152
A-6: The DTA graph of sample UMBEc.....	150

Abstract of Dissertation Presented to the Graduate School  
of the University of Florida in Partial Fulfillment of the  
Requirements for the Degree of Doctor of Philosophy

EFFECT OF A SUPERSOLVUS HEAT TREATMENT ON THE MICROSTRUCTURE  
AND MECHANICAL PROPERTIES OF A POWDER METALLURGY PROCESSED  
NICKEL-BASE SUPERALLOY

By

Darryl Slade Stolz

August 2004

Chair: Gerhard E Fuchs

Major Department: Materials Science and Engineering

Powder Metallurgy (P/M) processed nickel-base superalloys are used as turbine disk materials in jet engines. The P/M processing results in a homogenous microstructure. Large amounts of strengthening elements can be incorporated into the chemistry of these P/M alloys. In addition, the ability to produce near net-shaped parts with powder consolidation may offer the potential for large cost savings. However, the fatigue properties of P/M superalloys in the as-consolidated form have suffered because of the defect sensitivity of the as-consolidated microstructure. Expensive, thermomechanical steps are necessary to break down defects, so that the P/M parts can be considered defect-tolerant. As a result, the true potential cost savings for using P/M superalloys in turbines have never been realized.

This program was undertaken to examine the potential for utilizing an alternate heat treatment with P/M Alloy 720LI to generate a potentially defect-tolerant

microstructure. This heat treatment had a soak above the  $\gamma'$  solvus temperature followed by a controlled cool through the solvus. This produced  $\gamma$  grains with a regular array of large dendritic-shaped secondary  $\gamma'$  within the grains.

Mechanical testing was carried out to fully evaluate the effect of this alternate heat treatment on the mechanical properties of Alloy 720LI. The standard heat treatment had longer lifetimes at the lower stress range conditions during high cycle fatigue; however, the alternate heat treatment was superior at the highest stress range. Fracture analysis suggests that this is due to the grain size difference. During tensile testing, the standard heat treatment had higher yield and ultimate strengths but lower ductility than the alternate heat treatment. This is thought to be due to the larger amounts of tertiary  $\gamma'$  present in the microstructure produced by the standard heat treatment. Finally, the standard heat treatment had longer creep lifetimes at the lowest test temperature. The alternate heat treatment performed better at the higher test temperatures. While the microstructure did not improve the fatigue properties across the board, the improved understanding of the microstructural evolution during heat treatment will help in developing new heat treatments that may provide the defect-tolerance that is necessary.

## CHAPTER 1 BACKGROUND

Superalloys have been used extensively as high temperature materials in turbine engines since the 1950s [1]. In addition to jet engines and industrial gas turbines, they have seen service in space vehicles, rocket engines, nuclear reactors, submarines, steam power plants, petrochemical equipment, heating elements, and furnace parts [2, 3]. Superalloys are generally defined by their unique ability to retain high strength at temperatures approaching 90% of their melting point and for times up to 100,000 hours at slightly lower temperatures [4]. This unique feature for a structural material coupled with the high oxidation resistance, makes superalloys the best choice for very demanding environments like jet engines and industrial gas turbines.

There are three main classes of superalloys: nickel-base, cobalt-base, and nickel-iron-base. However, Ni-base alloys generally are considered the most important, and are the most widely used of these classes, owing to their excellent blend of mechanical and chemical properties. As turbine engine materials, they are required to have high strength as well as good creep, fatigue, and corrosion resistance [3]. The first jet engine developed by Sir Frank Whittle operated with a thrust-to-weight ratio of 1.5:1 [1]. Modern commercial engines operate at a ratio of 6-8:1 with advanced engines approaching 10:1. The increases in propulsion output in jet engines have been made possible by improvements in materials as well as engine design. The demand for more efficient and powerful turbines has steadily increased the operating temperature and mechanical stress demands for superalloys. Ni-base superalloys have met these demands

through improvements in alloy processing and chemistry. Turbine blades have the highest operational temperatures of the superalloys used in jet engines, making creep resistance vital. Single crystal alloys with excellent creep resistance have been developed as blade alloys in current jet engines. On the other hand, turbine disks operate at higher loads but somewhat lower temperatures. They require good fracture toughness, low crack growth rate, and ease of inspectability [5]. Turbine disk designers have examined powder processing as a means of producing disks with higher strength and better fatigue resistance. These alloys have an excellent blend of properties; however, their high costs have limited their usage in turbine engines.

### **Composition and Microstructure**

The alloy chemistry of Ni-base superalloys has evolved tremendously over the years. The initial alloys used in gas turbine engines were modifications of oxidation-resistant stainless steels [6]. The addition of aluminum and titanium to the Nimonic (80% Ni, 20% Cr) alloy series led to the precipitation of the intermetallic phase,  $\text{Ni}_3\text{Al}$ . These were the first precipitation-hardenable superalloys. These alloys have higher strength than alloys strengthened solely by solid-solution hardening, and than those strengthened by oxide dispersion strengthening [3]. Precipitation-hardenable superalloys are preferred for the most demanding environmental conditions. The first superalloys had relatively simple compositions; however current generations can be a confusing blend of varied elements that are added to improve processing, mechanical properties, oxidation resistance, and even density. Even though there has been a tremendous amount of research into the effect of chemistry changes on the properties of these alloys, much still remains to be learned about the complex interactions between

various elements and the effects that slight changes in composition will have on the phase stability and mechanical properties of the various alloys.

### **Chemistry**

Precipitation hardenable Ni-base superalloy phase systems consist of a nickel matrix, gamma ( $\gamma$ ), which is strengthened both by solid-solution alloying elements and by the intermetallic precipitate, gamma prime ( $\gamma'$ ). Aluminum and titanium are the primary elements added to increase the amount of  $\gamma'$  in the alloy [4]. Niobium and tantalum can also be added as substitutional elements for Al and Ti. These  $\gamma'$  forming elements are added in amounts up to 8%. The most common solid-solution strengthening elements for the  $\gamma$  matrix are cobalt, iron, chromium, molybdenum, tungsten, titanium, and aluminum. While titanium and aluminum are added mostly as precipitation hardeners, they do help strengthen the  $\gamma$  matrix by solid-solution substitution. Ni-base superalloys generally contain 10-20% chromium, as it forms a protective oxide scale in addition to the solid-solution strengthening benefits. Aluminum also forms a protective  $\text{Al}_2\text{O}_3$  scale for oxidation and hot corrosion resistance. Between 5 and 15% Co is added because of its effect on the precipitation behavior of  $\gamma'$ . The addition of Co effectively alters the slope of the  $\gamma'$  solvus curve, which changes the  $\gamma'$  solvus temperature, depending on the  $\gamma'$  volume fraction in the alloy. Additionally, it increases the amount of  $\gamma'$  that will precipitate out of solution during heat treatment. Small amounts of carbon, boron, zirconium, and hafnium are added to improve grain boundary strength. Finally, it is important that the amounts of so called “tramp” elements (like silicon, phosphorus, sulfur, oxygen, and nitrogen) as well as other minor elements are carefully controlled to very small levels.

### **Gamma Matrix**

The continuous matrix phase,  $\gamma$ , is a face centered cubic (FCC) Ni-base phase that is austenitic in structure [4]. Pure nickel has neither a high elastic modulus nor a low diffusivity, which are necessary to promote creep rupture resistance. Its ability to be used at elevated temperatures for long times is attributed to the following three reasons:

- Nickel has a nearly filled third electron shell, which allows for high alloying content.
- It has the tendency to form the protective  $\text{Cr}_2\text{O}_3$  oxide scale with additions of chromium.
- It has an added inclination to form the oxidation-resistant  $\text{Al}_2\text{O}_3$  scale.

The  $\gamma$  matrix is strengthened primarily by alloying with solid-solution elements.

### **Gamma Prime Phase**

The precipitate phase,  $\gamma'$ , is an ordered  $\text{L1}_2$  intermetallic phase that is stable over a fairly narrow compositional window (Figure 1-1) [7]. Its nominal composition is  $\text{Ni}_3\text{Al}$ ; however, both the nickel and the aluminum can be substituted for, by various alloying elements [4]. Figure 1-2 [8] shows how various elements substitute in  $\text{Ni}_3\text{Al}$ . As can be seen, cobalt and copper will substitute for nickel. However, titanium, silicon, vanadium, and manganese all partition to the aluminum sites. Molybdenum, chromium, and iron are equally likely to substitute for nickel as they are for aluminum. Nickel atoms occupy the face-centered sites and aluminum atoms the corner sites [8]. More recent studies have found that niobium and hafnium also partition to the aluminum sites [4].  $\text{Ni}_3\text{Al}$  exhibits long-range order up to its melting point, and precipitates coherently with the austenitic matrix [3, 7]. In early superalloys, this precipitate was spherical; however as alloying

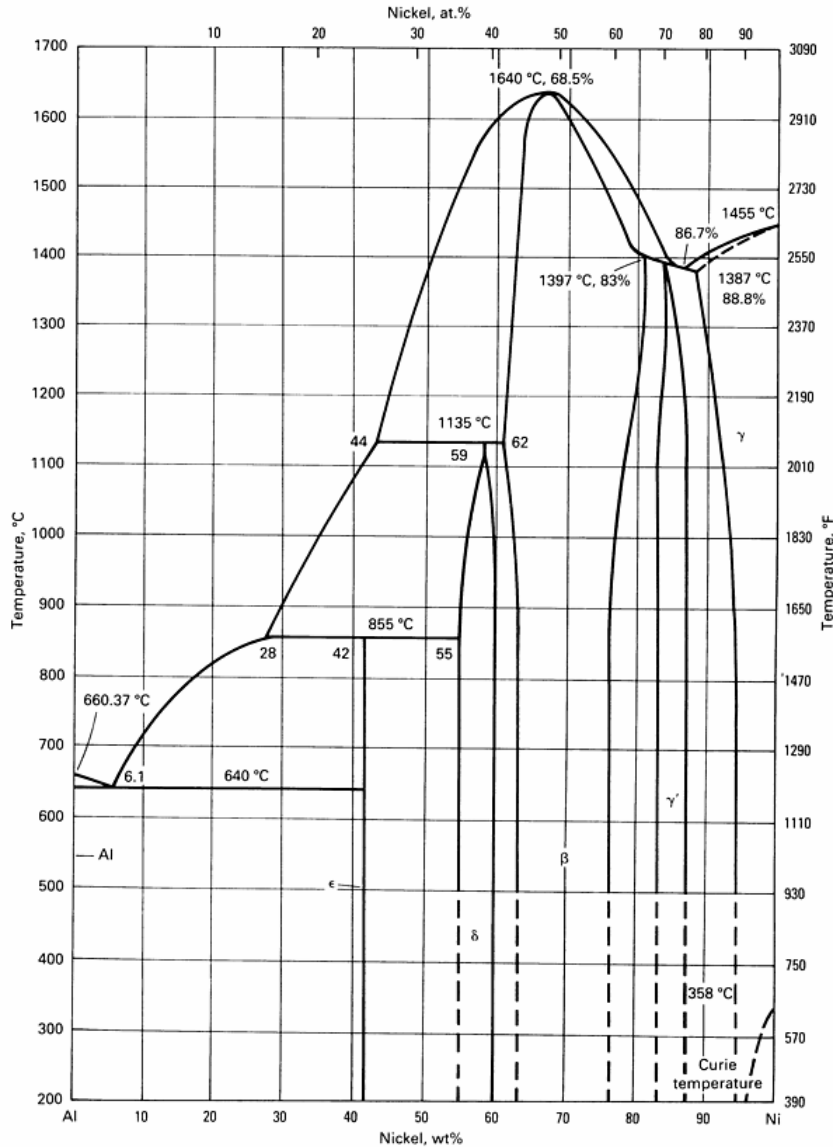


Figure 1-1. Nickel-aluminum phase diagram. Reprinted with permission from N. S. Stoloff, "Wrought and P/M Superalloys," *ASM Handbook*, **1**, ASM-International, 2003, Figure 1, p. 952.

content was increased, cuboidal precipitates were observed [3]. It was determined that the change in  $\gamma'$  morphology was related to the lattice mismatch between  $\gamma$  and  $\gamma'$ .

Spherical precipitates were noticed when the mismatch was between 0.0 and 0.2%. As the mismatch increased to between 0.5 and 1.0%, cuboidal precipitates were observed.

Finally, plate-like  $\gamma'$  were present when the mismatch reached 1.25% and above. Perhaps

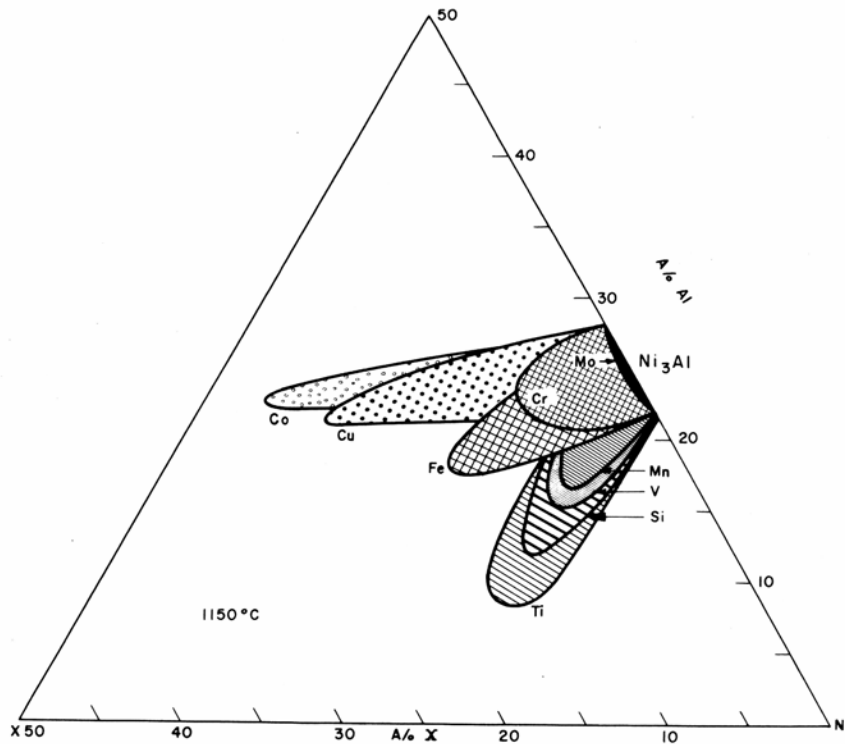


Figure 1-2: The  $\text{Ni}_3\text{Al}$  solid solution field at approximately  $1150^\circ\text{C}$  for various ternary alloys. Reprinted with permission from R. W. Guard and J. H. Westbrook, "Alloying Behavior of  $\text{Ni}_3\text{Al}$  ( $\gamma'$  phase)," *Transactions of the Metallurgical Society of AIME*, **215**, 1959, AIME, Figure 4, p. 810.

the most important property of  $\gamma'$  is that its yield strength increases with increasing temperature, making it ideal for high-temperature applications (Figure 1-3) [9]. Additionally,  $\gamma'$  is generally not considered a fracture-initiation site, because of its inherent ductility [4].

### Carbides and Borides

Carbides and borides precipitate in Ni-base superalloys in various forms including MC (metal carbide),  $\text{M}_{23}\text{C}_6$ ,  $\text{M}_6\text{C}$ , and  $\text{M}_3\text{B}_2$ . The role that they play in the microstructure and mechanical properties of superalloys is fairly complex. In some cases, their presence can be detrimental; however, other forms are beneficial to the mechanical properties. While they can lower the ductility, their presence can also

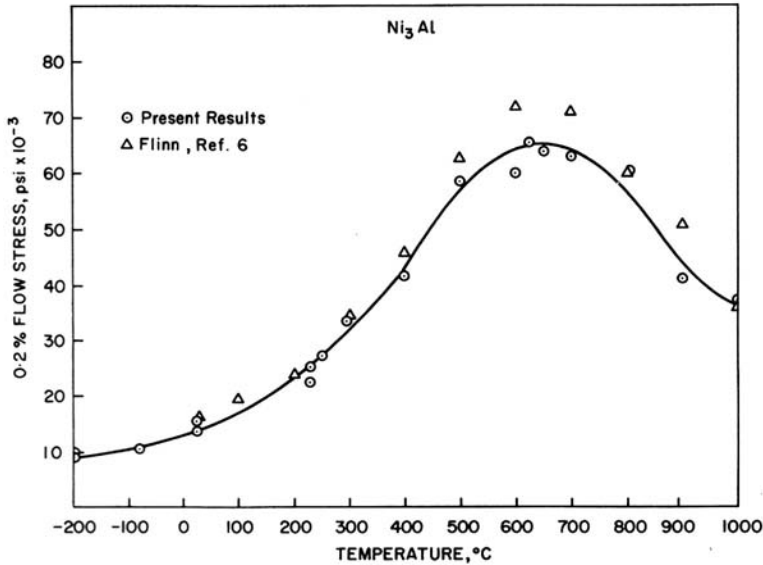


Figure 1-3: Flow stress as a function of temperature for Ni<sub>3</sub>Al. Reprinted with permission from R. G. Davies and N. S. Stoloff, "On the Yield Stress of Aged Ni-Al Alloys," *Transactions of the Metallurgical Society of AIME*, **233**, 1965, AIME, Figure 4, p. 717.

increase the creep rupture life and the chemical stability of the matrix [4]. Davis et al. [3] and Ross and Sims [4] describe different types of carbides. MC carbides generally precipitate as discrete random cubic or script particles, along grain boundaries and within the grains. They are FCC and have little or no orientation relationship to the matrix. In superalloys, their preferred order of stability is HfC, TaC, NbC, and TiC (with HfC being the most stable). The M<sub>23</sub>C<sub>6</sub> carbides form primarily as discontinuous, blocky particles with a complex cubic structure, during heat treatment or service between 760 and 980°C from the degeneration of MC carbides and carbon left in the matrix. They are generally found along grain boundaries, but can also form on twin bands, stacking faults, and twin ends. The formation reaction is



These carbides form mostly in alloys with at least moderately high chromium contents. With the presence of tungsten and molybdenum, they form with the

composition  $\text{Cr}_{21}(\text{Mo}, \text{W})_2\text{C}_6$ . Finally,  $\text{M}_6\text{C}$  carbides precipitate in blocky form along grain boundaries, or sometimes as Widmanstätten plates within the grains [3]. These carbides also have a complex cubic structure. They form between 815 and 980°C when the molybdenum and tungsten contents are higher than 6-8 atomic percent. They are stable at high temperatures, and their composition can range widely. The  $\text{M}_3\text{B}_2$  borides precipitate as hard particles, with a wide variety of shapes from blocky to half-moon. They have a tetragonal unit cell, and act to improve grain boundary strength.

### **Strengthening Mechanisms**

As stated earlier, the two main modes of strengthening in Ni-base superalloys are solid-solution strengthening and precipitation hardening. Many mechanisms contribute to strengthening from the substitution of solid-solution elements: size misfit, modulus misfit, stacking-fault energy, and short-range order. The size of the substitutional atom was shown to be an important factor in solid-solution strengthening [10]. The solute atoms have small elastic stress fields that can impede dislocation motion [11]. However, the model by Mott and Nabarro [12] to account for size misfit overestimates the strengthening effect of solute atoms. The valence state of the solute atom also affects the amount of solid-solution strengthening for a particular solute element [13, 14]. Pelloux and Grant [15] confirmed these findings for superalloys (Figure 1-4). These valency effects have been explained as being due to the modulus differences among different alloys [16]. Local variations in the modulus can attract and pin dislocations [11]. Stacking-fault interactions are an additional solid-solution strengthening mechanism that was first discovered by Suzuki [10, 11]. Solute atoms can preferentially segregate to stacking faults. In turn, the stacking-fault energy is lowered, and the separation between

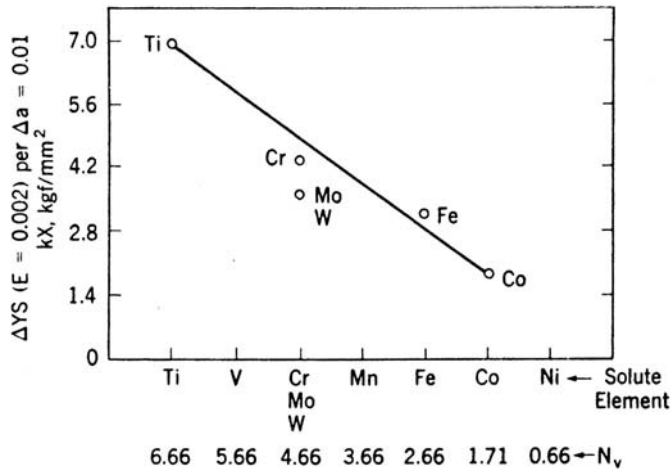


Figure 1-4: Effect of valency difference on hardening of nickel alloys.  $N_v$  is electron vacancy number of the solute. Reprinted with permission from R. M. Pelloux and N. J. Grant, "Solid Solution and Second Phase Strengthening of Nickel Alloys at High and Low Temperatures," *Transactions of the Metallurgical Society of AIME*, **218**, 1960, AIME, Figure 5, p. 234.

partial dislocations is increased. The motion of these partials is much more difficult, as a result. Finally, short-range ordering can occur in some nickel solid-solutions [12]. A dislocation moving through a region with short-range order will require more work for propagation, as it locally disrupts the energetically favorable ordered state [11].

Strengthening from precipitates can be considered as additive to solid-solution strengthening. Precipitation of  $\gamma'$  in superalloys causes strengthening due to coherency strains between the matrix and precipitate, and the presence of order in the particles [12]. The strain field locally around each precipitate provides a repelling force for dislocation motion. The mechanisms of order strengthening are controlled by the type of interaction between the dislocations and the precipitates. Below a critical precipitate size, dislocations will shear the  $\gamma'$  particles. The ordered precipitate is left out of phase, creating an antiphase boundary (APB) in the precipitate. This extra force needed to create APB's in the alloy results in order strengthening. The size and spacing of the  $\gamma'$

precipitates has a large impact on the amount of strengthening from ordered particles [11]. However, if the precipitates are incoherent and larger than a critical size, dislocations will bypass them. For superalloys, this generally happens according to the Orowan bowing model. As a dislocation approaches the large precipitates, it begins to bow around them. The dislocation eventually bypasses the particles, leaving a dislocation loop that exerts a stress on approaching dislocations. This stress field from the dislocation loops results in an increase in the strength of the alloy.

### **Powder Metallurgy Superalloys**

Powder metallurgy (P/M) superalloys were first examined as a novel way of cooling turbine blades through transpiration cooling [17]. A mixture of elemental and master-alloy powders were cold-compacted and sintered. However, it was only possible to achieve approximately 90% of the theoretical density. As a result, these alloys had inadequate strength for use as turbine blades. In the early 1960s, pre-alloyed powders were developed through the use of water atomization [18]. However, these alloys suffered from poor fatigue strengths in comparison to the conventional wrought alloys. Eventually, with the use of vacuum melting and improved powder cleanliness in the mid 1960s, it was possible to produce P/M superalloys with sufficient mechanical properties, that were a potential alternative to conventional cast and wrought alloys [17].

As turbine manufacturers sought more efficient jet engines in the early 1970s, the property requirements for turbine disk materials increased beyond the capabilities of the existing alloys [19]. The new alloys were required to have a high strength-to-weight ratio, good hot workability, and higher operational temperatures. To meet these needs, alloy designers began developing cast and wrought alloys with higher concentrations of solid-solution strengthening elements, as well as  $\gamma'$  forming elements (aluminum and

titanium) [20, 21]. However, these alloys experienced major difficulties with segregation, hot workability, and ductility deficiencies as the alloying contents and ingot size necessary for larger turbine disks increased [19, 22]. These newer cast and wrought alloys were practically unforgeable [21]. With pre-alloyed powder processing, more rapid solidification rates were easily possible. These faster solidification rates resulted in much smaller dendrite-arm spacing within the powder particles, as opposed to those seen in conventionally cast ingots [23]. The increase in homogeneity for these alloys by powder processing makes them easy to forge isothermally through superplastic deformation [19, 22].

Powder-processed disk alloys provide many advantages over disk alloys processed by conventional ingot metallurgy [17, 20, 24].

- Reduced segregation in structure that allows for more heavily alloyed compositions.
- Improved hot workability after compaction.
- Near net-shape production of parts that has potential for cost-savings and conservation of rare and expensive elements.
- Finer grain size.
- Reduced carbon segregation.
- Ability to produce unique structures like oxide dispersion-strengthened (ODS) alloys.

With all of these advantages, P/M superalloys were first put into operational service in 1974 in the Pratt & Whitney F100 engine on the F-15 Eagle fighter jet [22]. A survey of engines in use in 1996 shows that powder superalloys have become widely used in both commercial and military jets since their inception. Engines that use P/M alloys

after extrusion and isothermal forging are shown in Table 1-1; while Table 1-2 shows engines that incorporate as-hot isostatically pressed (as-HIP) alloys.

Table 1-1: Engine systems using forged P/M superalloys.\*

Engine	Number produced through 1996
GE T-700	9674
GE F-404/414	3077
GE-F110	2259
GE 90	38
PW F100	6496
PW 2000	951
PW 4000	1819

\*Reprinted with permission from J. H. Moll and B. McTiernan, "Powder Metallurgy Superalloys," ASM Handbook, 7, ASM-International, 2003, Table 1.

Table 1-2: Engines and airframe systems using as-HIP P/M superalloys. \*

GE Aircraft Engines		CFM International		AlliedSignal	
Turbine	Airframe	Turbine	Airframe	Turbine	Airframe
CF6-80C2/E1	B747-400, 767 AWACS	CFM56-3B1/B2	B 737-300	GTC-131-3[A]	B2
F108-CF-100	KC-135-R	CFM56-3B2/3C	B 737-400	GTC-131-9[D]	MD-90
F110-GE-100	F-16 C/D/G	CFM56-3B4	B 737-500	GTC-131-9[B]	B737-X
F110-GE-129	F-16 D/G	CFM56-5A1	A-320-100/-200	GTC-131-9[A]	Airbus A319, A320, A321
F110-GE-400	F-14B	CFM56-5A/5B	A-319	GTCP-331-200	B757/B767 B747-200B
F118-GE-100	B2	CFM56-5B1/B2	A-321-100	GTCP-331-250	A300, A310, C17A
F404-GE-400/402	F/A-18 C/D, F-117A	CFM56-5C2/C4	A-340-200/300	GTCP-331-350	Airbus A330, A340
T-700-GE-401	Bell AH 1W, Sikorsky SH-60B/F	CFM56-7	B737-700	GTCP-331-500	B777
T-700-GE-700	Sikorsky UH-60A/L	CFM56-8	B 737-600/800	RE-220	Gulfstream V Global Express CRJ-700

\*Reprinted with permission from J. H. Moll and B. McTiernan, "Powder Metallurgy Superalloys," ASM Handbook, 7, ASM-International, 2003, Table 2.

The initial P/M processed superalloys were derived through slight modifications to the chemistries of existing alloys like IN-100, Astroloy, and René 95 [22]. Eventually,

alloys like AF115 and AF2-1DA were designed specifically for P/M processing, to take advantage of the high level of alloying that can be accommodated by this route.

However, these alloys had low resistance to crack growth from defects in the microstructure. With defect tolerance in mind, current research has centered on more defect-tolerant alloys like N18, René 88DT, and Udimet 720.

### **Powder Processing**

A wide range of powder processing methods is available to a turbine disk manufacturer. These include powder production, consolidation, post-consolidation thermo-mechanical processing (TMP), and heat treatment. All of these different processing routes give the manufacturer the flexibility to alter the microstructure and, therefore, the mechanical properties to fit the requirements for almost any particular application.

#### **Powder production**

Many different powder fabrication techniques are used for the production of metal powders. These include mechanical fabrication like machining or milling, electrolytic fabrication, chemical fabrication, and atomization [25]. Of all these different techniques, gas atomization to produce pre-alloyed powder is the most important for the production of P/M superalloys [17]. Within the category of atomization, there are a few subcategories of powder fabrication processes including inert-gas atomization, soluble gas atomization (vacuum atomization), centrifugal atomization including rotating-electrode process (REP) and electron-beam rotating process (EBRP), and rapid solidification techniques [17, 20, 22].

The REP process has received some attention from turbine disk manufacturers [26]; however, the most research into powder fabrication of superalloys has examined inert-gas

atomization. Typical cooling rates for inert-gas atomization of superalloys are in the range of  $10^4$  to  $10^6$  °C/sec [27]. A typical gas atomization rig is shown in Figure 1-5 [25]. In this process, vacuum induction melting (VIM) is used to melt high-purity raw

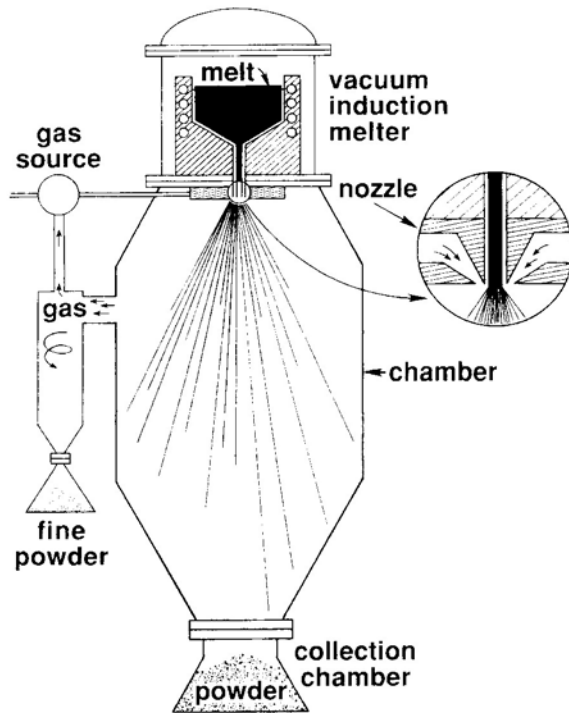


Figure 1-5: Vertical gas atomizer. Reprinted with permission from *Powder Metallurgy Science*, 1994, Metal Powder Industries Federation, 105 College Road East, Princeton, New Jersey, USA. Figure 3.14, p. 101.

materials in a crucible at the top of the atomization rig [22]. The melted alloy passes through the nozzle in a thin stream. High-pressure argon gas is then impinged the stream, to break up the melt stock into fine spherical droplets. Alternatively, nitrogen gas can be used; however, it is necessary to alter the alloy composition to account for any increase in nitrogen and the effects that will have on the final alloy. These droplets solidify as they descend through the cooling tower to the bottom of the atomization rig, where they are collected for consolidation. The fine particles are collected in a side unit, using a cyclone separator.

The particle size and size distribution can be affected by many variables during the atomization process. Generally, the more energy that is imparted onto the molten metal by the gas, the finer the powder yield produced [25]. Depending on the nozzle design, the gas can impinge the metal stream either at an angle or tangentially. In addition to the geometric parameters of the nozzle, other factors influencing the powder characteristics are gas pressure, type of gas, diameter ( $d'$ ) of the melt stream, flow characteristics of the molten material, and the ratio of mass transport of the melt and atomizing gas [17]. An expanded view of the metal stream during atomization illustrates the development of spherical particles from the initial melt stream (Figure 1-6) [25].

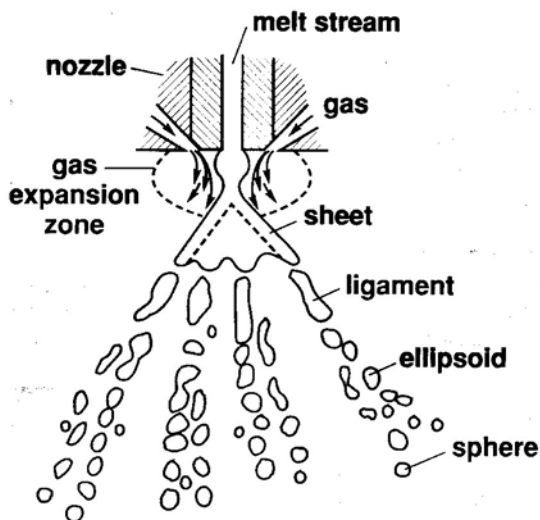


Figure 1-6: Formation of spherical metal powder by gas atomization. Reprinted with permission from *Powder Metallurgy Science*, 1994, Metal Powder Industries Federation, 105 College Road East, Princeton, New Jersey, USA. Figure 3.16, p. 103.

The gas around the molten stream expands, causing a depressurization of the liquid metal [25]. The stream, in turn, expands into a hollow cone. The high surface-area-to-volume ratio of this cone leads to instability in the geometry that, in conjunction with the inert gas stream, leads to breakup of the cone into long ligaments.

Eventually, these ligaments break up into ellipsoids, and finally into small spherical droplets. The amount of superheat in the metal before atomization plays a key role in determining the final shape and size of the powder. The level of superheat must be sufficient so that the particles do not solidify before becoming spheres. It is also crucial to eliminate any agglomerations of particles or satellite particles by proper design of the atomization process. Either of these can potentially result in poor packing of the powder before consolidation.

### **Powder consolidation**

Conventional powder-compaction techniques, like cold pressing and sintering, are insufficient in achieving a fully dense P/M superalloy billet, because of the incompressibility of superalloy powder, and the susceptibility to forming oxide scales at sintering temperature [17]. Therefore, compaction techniques that involve high pressure at elevated temperatures are necessary. Early work on P/M superalloy compaction techniques examined forge compaction [28] and extrusion [28, 29] as means of achieving fully dense P/M billets. Another novel compaction process that has received some attention is consolidation by atmospheric pressure (CAP<sup>R</sup>) [30]. However, the advancements in HIP processing of powders along with potential cost savings make this the preferred route for consolidation of superalloy powders into billet form.

The basic principle behind HIPing is the application of high pressure gas to consolidate the powder within an autoclave at elevated temperatures. The heater is generally located inside of the pressure vessel. Atomized powder, loaded into a container, is placed in the autoclave for compaction. These containers can be fabricated out of sheet metal, glass, or ceramic. While the glass and ceramic molds provide for better flexibility in both size and final part complexity, the metal cans are not as brittle

[17, 31]. They can handle higher autoclave loading. It is ideal for the powder to be spherical and have a wide size distribution, to facilitate higher packing densities before compaction [32]. The containers are loaded under vibration, to achieve packing densities approaching 80% of the theoretical density before consolidation. The cans are then evacuated and sealed before being placed in the HIP chamber. During HIPing, densification is thought to take place in a similar manner to sintering [32]. The mechanisms describing the initial bonding of powder particles during a HIP cycle [32, 33] are as follows:

- Initial elastic deformation.
- Plastic deformation of the particles by dislocation.
- Power-law creep or dislocation creep.
- Nabarro-Herring creep or volume diffusional creep.
- Coble creep or grain boundary diffusional creep.

The final stages of densification occur through the same mechanisms that govern neck growth during sintering [32].

It is possible to produce a wide range of sizes and shapes of final parts in the as-HIP condition with proper container selection and design. Through production of net-shape and near net-shape HIPed parts, there is a great potential for reduction in starting material for P/M superalloy parts (Figure 1-7) [20]. This production of net-shaped parts, in addition to the intrinsic homogeneity of atomized powders, translates directly into a cost savings for turbine disk manufacturers, as they could possibly eliminate forging operations, excess material, and costs associated with machining the final part [34, 35]. In 1976, the development of as-HIP turbine disks was viewed as “one of the most exciting and technologically important metallurgical developments in recent

years” and one that could “revolutionize the aircraft engine rotating parts industry” [34, p.502].

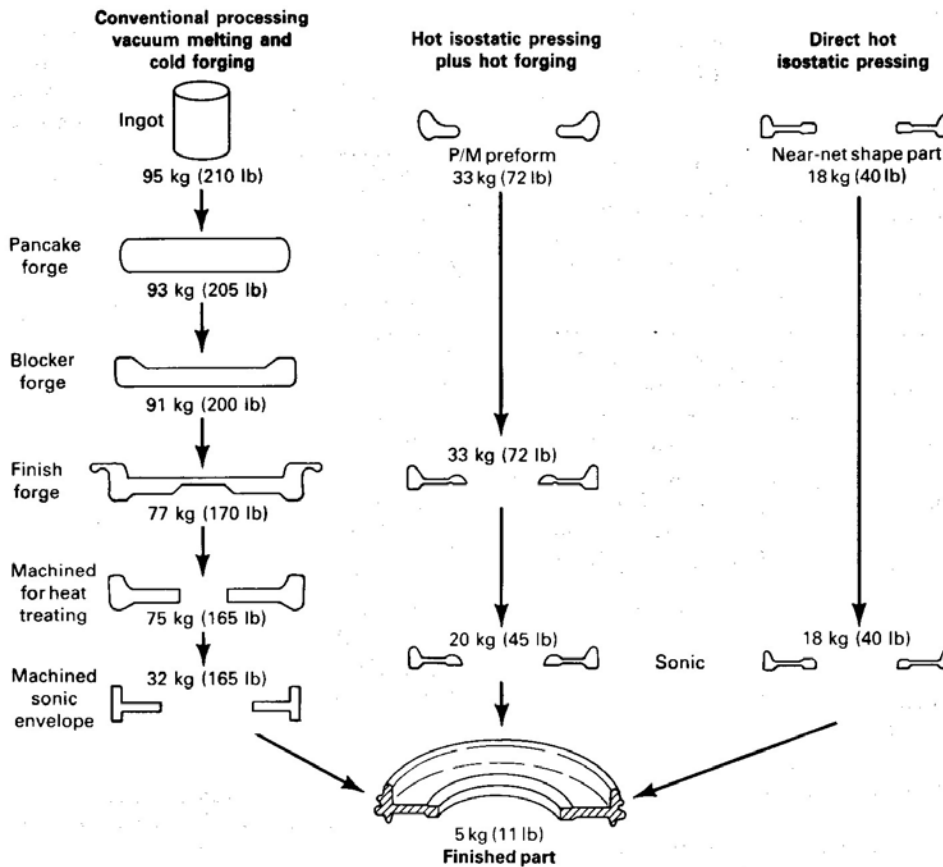


Figure 1-7: Material and fabrication savings with P/M processing of superalloys. Reprinted with permission from Eds. J. R. Davis and Davis & Associates, “Powder Metallurgy Superalloys,” *Heat Resistant Materials*, ASM-International, 1997, Figure 1, p. 272.

## Challenges

Unfortunately, these potential cost savings have never been fully realized by the turbine disk manufacturers. Powder-processed superalloys in the as-HIPed + heat treated condition do not contain enough inherent damage-tolerance for use as disk alloys in jet engines. “A damage tolerant design assumes that a component has a flaw (i.e. crack) of a size just below the non-destructive inspection detectable limit. The times to inspection and/or retirement are based on the crack growth rate of the flaw.” [36, p. 388] This

approach enables disk manufacturers to design around potential failures through knowledge of, and confidence in, tensile strength and creep and fatigue lifetimes. While as-HIPed P/M superalloys had sufficient tensile and creep capabilities through heat treatment alone [34, 37], it was soon evident that the low cycle fatigue (LCF) lifetimes contained large amounts of scatter and were highly dependant on the cleanliness of the powder and the consolidated billets freedom from defects [35]. The three main defect types found in P/M superalloys are prior particle boundaries, ceramic inclusions, and thermally induced porosity [38].

Prior particle boundaries (PPBs) have been the most extensively studied of these defect types for P/M superalloys. A HIPed billet that suffers from PPB defects will exhibit this network through the whole microstructure causing this defect type to be the most detrimental to the fatigue lifetime of the alloy. Powder particles that are left undeformed from the HIP processing can become decorated with detrimental secondary phases during the HIP cycle. Larger particles are strained to a much smaller degree than small particles during a typical HIP cycle (Figure 1-8) [38]. PPB networks tend to form on these larger undeformed powder particles [39]. Through careful analysis, it has been determined that the PPB defects consist of a semi-continuous network of carbides, oxides, oxy-carbides, and perhaps oxy-carbonitrides [23, 40, and 41]. It is thought that during the initial stages of densification during HIPing that titanium and carbon within the powder migrate to the particle surfaces as a result of oxides on the outside of the particles [40]. This results in a film of stable titanium oxy-carbides on the prior particle boundaries. These carbides are mostly MC in nature. However, there is some debate as

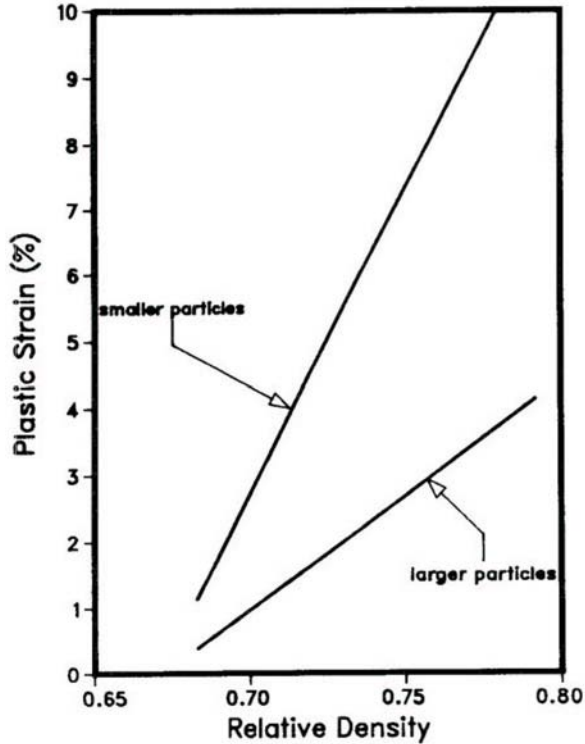


Figure 1-8: Plastic strain suffered by smaller and larger particles during HIPing of a bimodal particle size distribution of powders. Reprinted with permission from R. D. Kissinger, S. V. Nair, and J. K. Tien, "The Influence of Powder Particle Size Distribution and Pressure on the Kinetics of Hot Isostatic Pressing (HIP) Consolidation of P/M Superalloy René 95," *Superalloys 1984*, Eds. M. Gell, C. S. Kortovich, R. H. Bricknell, W. B. Kent, and J. F. Radavich, The Metallurgical Society of AIME, 1984, Figure 6, p. 291.

to the mechanisms for precipitation of these deleterious carbide and oxide precipitates. Some theorize that oxides on the powder particle surfaces serve as nucleation sites for carbides and borides [41]. However, others claim that these surfaces are not preferential sites for carbide nucleation [42]. Only extremely fine carbides were found on the surface of these powder particles. Instead, the metal-metal interfaces between powder particles that have stuck together as the result of collisions during atomization are the preferential sites for carbide precipitation. A detailed study by D. R. Chang et al. [39] examined the effects of various processing defects on mechanical properties of P/M René 95. PPBs were discovered to have an average size of approximately  $9,700 \mu\text{m}^2$  with a max size up

to  $161,300 \mu\text{m}^2$  when samples were made from -150 ( $< 106 \mu\text{m}$ ) mesh powder. In this study, -150 mesh René 95 was seeded with various dopants to induce fatigue failures at PPBs and ceramic inclusions. The dopants chosen to lead to PPB networks were Buna N (an organic carbide former) and mill scale (an inorganic oxide former). The average lifetime of as-HIPed René 95 was reduced from 37,000 cycles in the baseline (no dopant) condition to 8,675 cycles in the seeded conditions. Additionally, the frequency of failure at PPB sites was increased from 5% to 95%. A typical PPB fracture initiation site from this study is shown in Figure 1-9 [39].

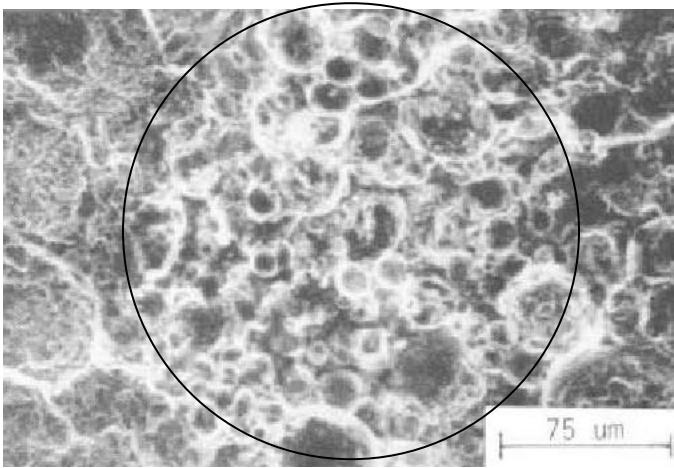


Figure 1-9: PPB initiation site in doped René 95. Reprinted with permission from D. R. Chang, D. D. Krueger, and R. A. Sprague, “Superalloy Powder Processing, Properties and Turbine Disk Applications,” *Superalloys 1984*, Eds. M. Gell, C. S. Kortovich, R. H. Bricknell, W. B. Kent, and J. F. Radavich, The Metallurgical Society of AIME, 1984, Figure 8A, p. 258.

Ceramic inclusions have also been detrimental to the fatigue properties of as-HIPed powder superalloys. A typical failure origin associated with ceramic defects is displayed in Figure 1-10 [39]. These inclusions originate from the melting crucible, the pouring tundish, and the atomizing nozzle with aluminum, zirconium, magnesium, and calcium being the major metallic elements [39]. The composition of the inclusions depends entirely on the ceramic materials used during production of the powder. In -150

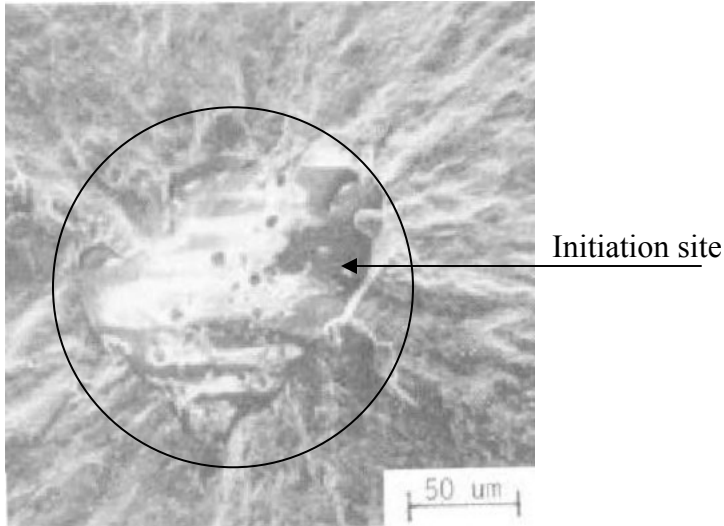


Figure 1-10: Type 1 ceramic inclusion fatigue initiation site. Reprinted with permission from D. R. Chang, D. D. Krueger, and R. A. Sprague, “Superalloy Powder Processing, Properties and Turbine Disk Applications,” *Superalloys 1984*, Eds. M. Gell, C. S. Kortovich, R. H. Bricknell, W. B. Kent, and J. F. Radavich, The Metallurgical Society of AIME, 1984, Figure 3A, p. 250.

mesh René 95, these inclusions were found to have an average size of approximately  $6500 \mu\text{m}^2$  and on some occasions up to  $64,500 \mu\text{m}^2$ . A study by W. H. Chang et al. [43] seeded -150 mesh René 95 with  $\text{Al}_2\text{O}_3$  to facilitate fatigue initiation at ceramic inclusions. LCF specimens were tested at  $1000^\circ\text{F}$  and 0.66% strain range. The average lifetime was decreased from 36,840 cycles for unseeded material to 3,411 cycles for René 95 seeded with  $\text{Al}_2\text{O}_3$ .

The third type of defect associated with premature failure of P/M superalloy specimens tested in fatigue is thermally induced porosity (TIP). During argon atomization, some of the larger particles can form voids that contain entrapped argon. The entrapped gas can then expand at high temperatures during HIP cycles or heat treatment, forming much larger voids that have a deleterious effect on the fatigue lifetimes of P/M alloys. These voids are generally less than  $1300 \mu\text{m}^2$ . Due to their

smaller size, TIP defects are not as detrimental to fatigue life as PPB's and ceramic inclusions.

To overcome the detriment in properties that these defects have caused in as-HIP P/M superalloys, turbine disk manufacturers have turned to thermomechanical processing (TMP) of the alloys. René 95 was HIPed and isothermally forged to an 80% reduction [43]. This hot working resulted in a large increase in LCF lifetime. The extrusion step broke up and reduced the size of the PPB networks; however only had a small effect on the ceramic inclusions. A second study examined the effect of consolidation by extrusion followed by isothermal forging [39]. The extrusion was carried out with a 6.5 to 1 reduction ratio. The forging resulted in a 60% reduction of the consolidated material. As a result, the tensile strength and the LCF lifetime were improved dramatically (Figure 1-11) [39]. The extrusion and isothermal forging steps served to break up both the ceramic inclusions and PPB networks. As a result, the maximum size of these defects in the TMP material is much smaller, reducing their tendency to be crack initiation sites. More samples failed at voids and crystallographic origins than in the non-TMP material. Figure 1-12 [39] is a fractograph of a typical crystallographic crack initiation site. Longer lifetimes are generally seen from samples that fail at these defects. Unfortunately, the TMP steps needed to produce a defect-tolerant microstructure are costly and limit the usage of as-HIP powder superalloys in the turbine industry.

Research into process improvements in recent years has improved the fatigue lifetime of as-HIP material to the point that the original hope for cost reduction for turbine disks is becoming more achievable. The average LCF lifetime of as-HIP alloys has increased dramatically as can be seen in Figure 1-13 [22]. Improvements in the gas

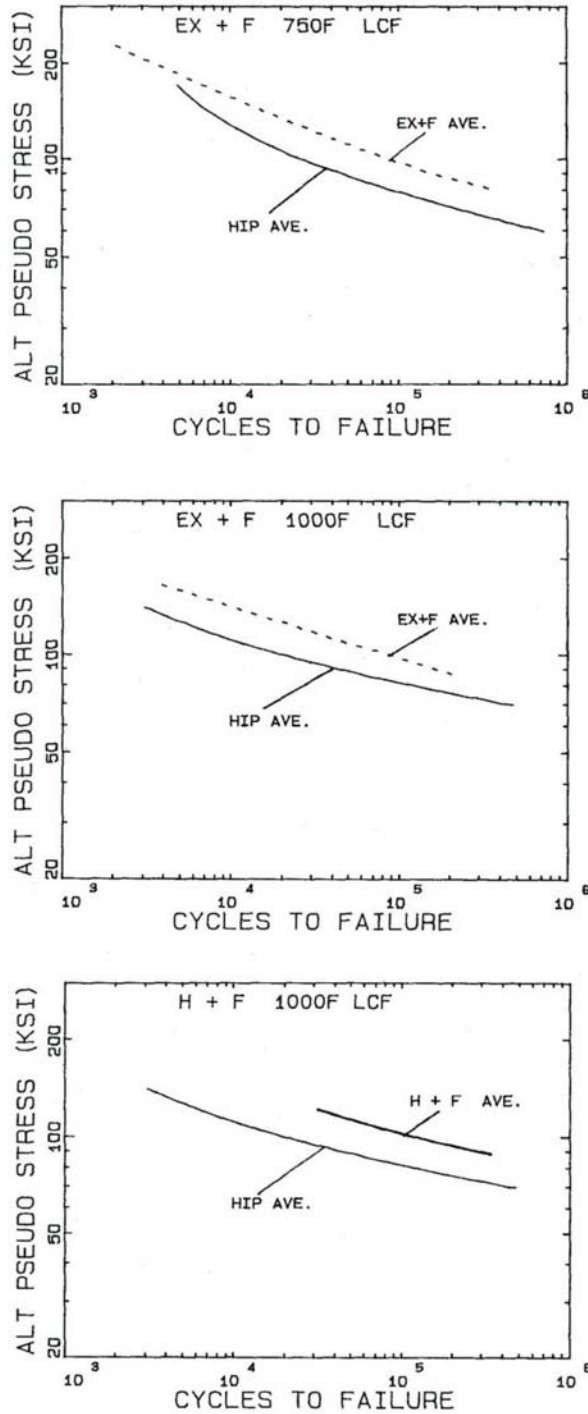


Figure 1-11: Comparison of average LCF lives of HIP vs. HIP + Forge and Extrude + Forge René 95. Reprinted with permission from D. R. Chang, D. D. Krueger, and R. A. Sprague, "Superalloy Powder Processing, Properties and Turbine Disk Applications," *Superalloys 1984*, Eds. M. Gell, C. S. Kortovich, R. H. Bricknell, W. B. Kent, and J. F. Radavich, The Metallurgical Society of AIME, 1984, Figure 11, p. 262.

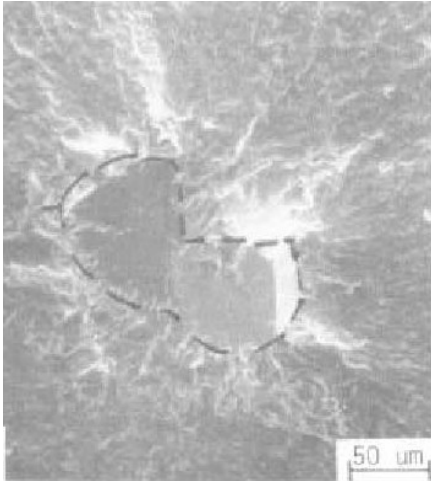


Figure 1-12: Fatigue initiation at a crystallographic defect. Reprinted with permission from D. R. Chang, D. D. Krueger, and R. A. Sprague, "Superalloy Powder Processing, Properties and Turbine Disk Applications," *Superalloys 1984*, Eds. M. Gell, C. S. Kortovich, R. H. Bricknell, W. B. Kent, and J. F. Radavich, The Metallurgical Society of AIME, 1984, Figure 10B, p. 260.

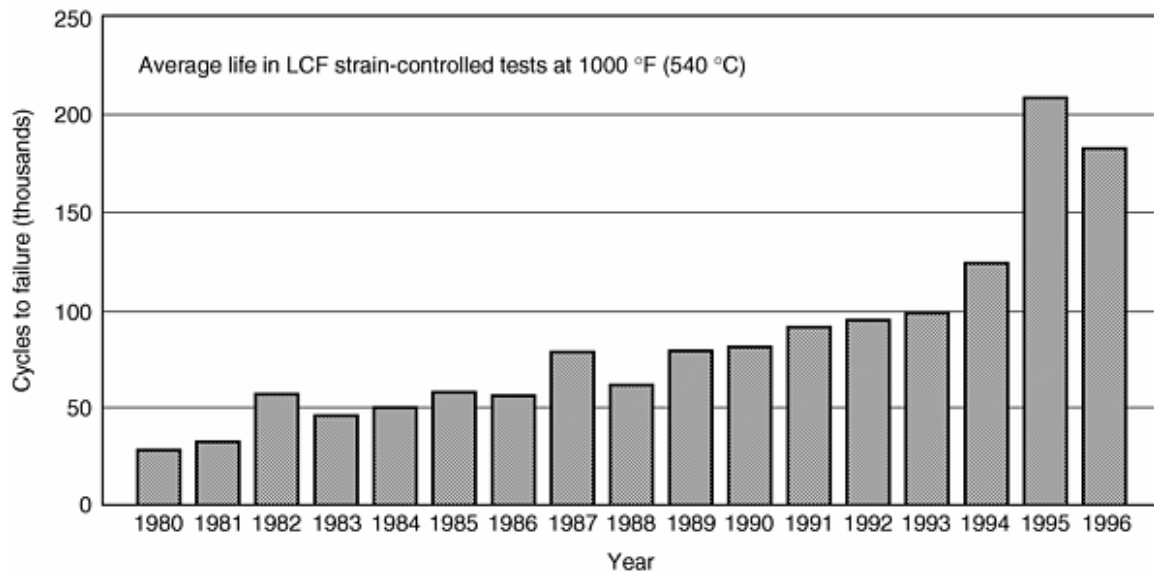


Figure 1-13: Average low cycle fatigue life for a P/M superalloy during 1980 through 1996. Reprinted with permission from J. H. Moll and B. McTiernan, "Powder Metallurgy Superalloys," *ASM Handbook*, 7, ASM-International, 2003, Figure 30, p. 900.

atomization process have resulted in fewer ceramic inclusions. Switching from commercial purity argon to high purity argon limited the number of particulates contained in the argon gas itself [38]. Studies on the melting practices have shown that

magnesia-based crucibles and electroslag remelting can reduce the oxide concentrations compared to other crucibles or melting methods [17]. Additionally, the size of potential inclusions has been reduced simply by sieving the atomized powder to finer particle sizes. The average particle size has been reduced from approximately 250  $\mu\text{m}$  to smaller than 105  $\mu\text{m}$  [22]. This has been made possible in part by the ability to produce finer powder yields from atomization. Reducing the levels of boron and carbon in the chemistry of P/M superalloys also helps minimize the PPBs. More care has also been taken when handling the powder before consolidation, to limit the amount of contaminants. Improvements in modeling the particle deformation and resulting densities of HIP cycles have allowed powder manufacturers to better understand HIP processing and to optimize the HIP cycle parameters to minimize the effect of defects on the LCF lifetimes. Original studies on deformation during HIPing concentrated on monosized particles [33]. To more closely approximate real world multimodal particle distributions, models were developed to study the densification of a bimodal distribution through HIP [44, 45]. Using these models, HIP cycles that provide more uniform deformation to all particles can be developed, resulting in an improved as-HIP material. Some have even suggested performing the HIP cycles at higher sub-solidus temperatures to facilitate grain growth past the PPB's. Finally, improvements in non-destructive evaluation (NDE) techniques have been used to help insure that defects are of sufficiently small size before any parts are put into service. It is with these improvements in superalloy powder processing in mind that a recent study examined the mechanical properties of as-HIP Alloy 720 [27]. With cleaner production methods and a supersolvus heat treatment, the properties compared favorably with extruded + isothermally forged Alloy 720.

## Alloy 720

Alloy 720 LI (low inclusion chemistry) is a powder processed nickel-base superalloy that has begun to be widely used in both the aircraft and land-based gas turbine industries over the last ten years [46]. It is a derivation from Alloy 720, which was originally developed as a cast and wrought turbine blade alloy for use in land-based gas turbines [47, 48]. To limit segregation from casting, Alloy 720 LI can be processed through powder metallurgy as an alternative to the traditional cast and wrought processing route.

### Chemistry and processing

Alloy 720 was initially designed to be chemically resistant to environmental attack through both oxidation and sulfidization. The composition of Alloy 720 and Alloy 720LI are given in Table 1-3 [46]. Titanium and aluminum were added as precipitation

Table 1-3: Nominal chemistry of Alloy 720 and Alloy 720LI.

	Ni	Cr	Co	Mo	W	Ti	Al	C	B	Zr
Alloy 720	Bal	18.0	14.8	3.0	1.25	5.0	2.5	0.035	0.033	0.03
Alloy 720LI	Bal	16.0	15.0	3.0	1.25	5.0	2.5	0.010-0.025	0.010-0.020	0.03

strengtheners because of their tendency to form  $\gamma'$ . Molybdenum, tungsten, chromium, and cobalt are all used for solid-solution strengthening of the  $\gamma$  matrix. Alloy 720 contains a high amount of chromium for oxidation and sulfidization resistance. The formation of  $\text{TiC}$ ,  $\text{Mo}_2\text{B}_3$ , and  $\text{Cr}_{23}(\text{C},\text{B})_6$  along the grain boundaries effectively limits the diffusion of oxygen and sulfur along the grain boundaries [47, 49]. This helps to retard the crack growth rate at elevated temperatures compared to other cast and wrought blade materials.

As a blade material, Alloy 720 was engineered to be used for up to 10,000 hours at 900°C. A coarse grained microstructure was optimal for turbine blade applications where creep rupture lifetime was vitally important. However, because of Alloy 720's combination of exceptional strength and hot workability, turbine manufacturers became interested in using the alloy in a fine grained condition as a potential turbine disk material [47].

It was soon discovered that the fine grain Alloy 720 is fairly susceptible to the formation of the deleterious sigma ( $\sigma$ ) phase [50]. The formation of the topologically closed-packed (TCP)  $\sigma$  phase led to a rapid deterioration in the tensile ductility, creep resistance, and toughness of the alloy. The most common nucleation sites for  $\sigma$  phase in superalloys are at large grain boundary  $\gamma'$  and at carbides [51]. The  $\sigma$  phase forms along the grain boundaries, as globular precipitates similar to chromium carbides. Alternatively, it can form as platelet or needle-like precipitates.  $\sigma$  phase has an approximate composition of  $(Cr_{0.5}, Mo_{0.1}), (Ni_{0.2}, Co_{0.2})$  in Alloy 720 [52]. Not only can these precipitates act as crack initiation sites, but they also can deplete the matrix of chromium [52]. The loss of chromium will lower the strength of the matrix, thereby causing a deficit in the mechanical properties of the alloy as a whole.

The chemistry was then refined to the current Alloy 720 LI composition to improve phase stability and reduce casting defects such as carbide and boride stringers [46]. The amount of chromium was reduced by two weight percent to decrease the stability of  $\sigma$  [53]. Additionally, the carbon and boron levels were reduced to decrease the number of nucleation sites available for the formation of  $\sigma$ . The change in chemistry

has a noticeable impact on the microstructure of exposed samples as can clearly be seen in Figure 1-14 [50]. These precipitates were found to be  $M_{23}(C,B)_6$  and  $\sigma$  phase. Reed et

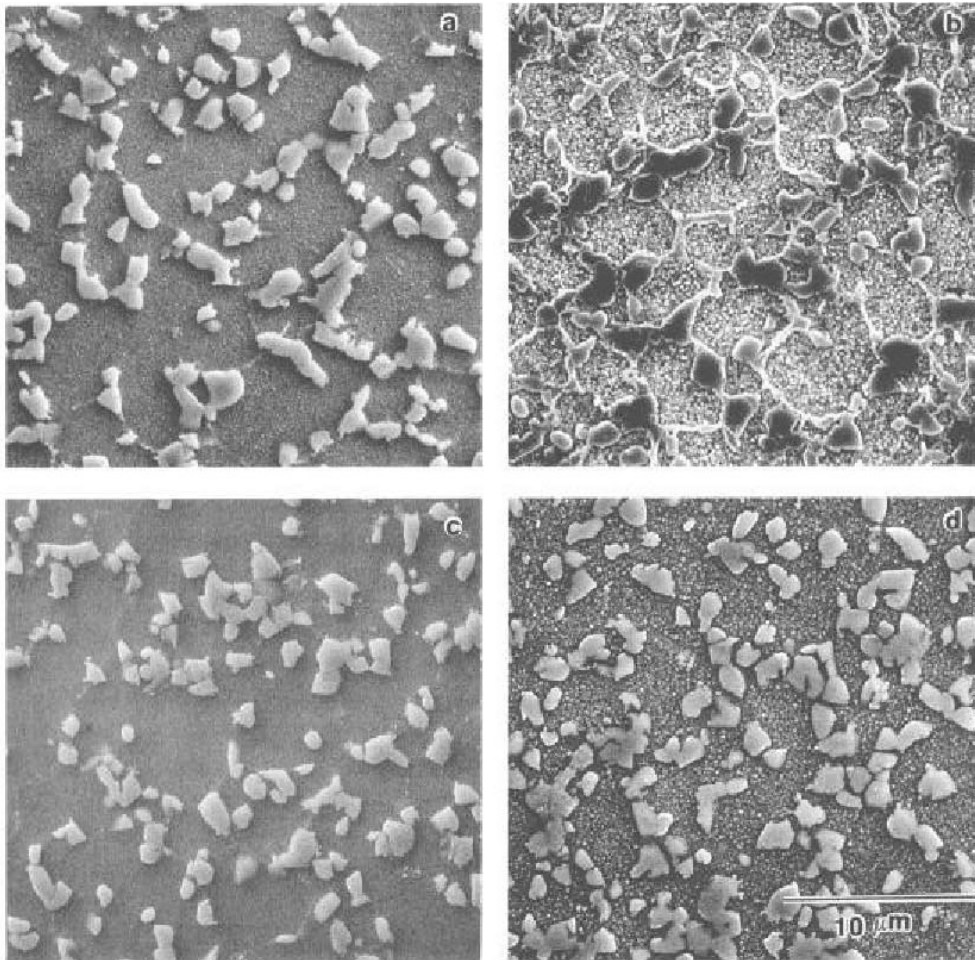


Figure 1-14: Effect of thermal exposure on microstructures of subsolvus heat treated Alloy 720 and Alloy 720LI. A) Alloy 720 as-heat treated. B) Alloy 720 after 750°C for 1000 hours. C) Alloy 720LI as-heat treated. D) Alloy 720LI after 750°C for 1000 hours. Reprinted with permission from P. W. Keefe, S. O. Mancuso, and G. E. Maurer, “Effects of Heat Treatment and Chemistry on the Long-Term Stability of a High Strength Nickel-Based Superalloy,” Superalloys 1992, Eds. S. D. Antolovich, R. W. Stusrud, R. A. MacKay, D. L. Anton, T. Khan, R. D. Kissinger, D. L. Klarston, TMS, 1992, Figure 4, p. 493.

al. [52] constructed an experimental time-temperature-transition (TTT) diagram for Alloy 720 and Alloy 720LI that shows that the chemistry change effectively delayed the onset of  $\sigma$  formation for Alloy 720LI. (Figure 1-15) [52]. The time for 1.0%  $\sigma$  formation has

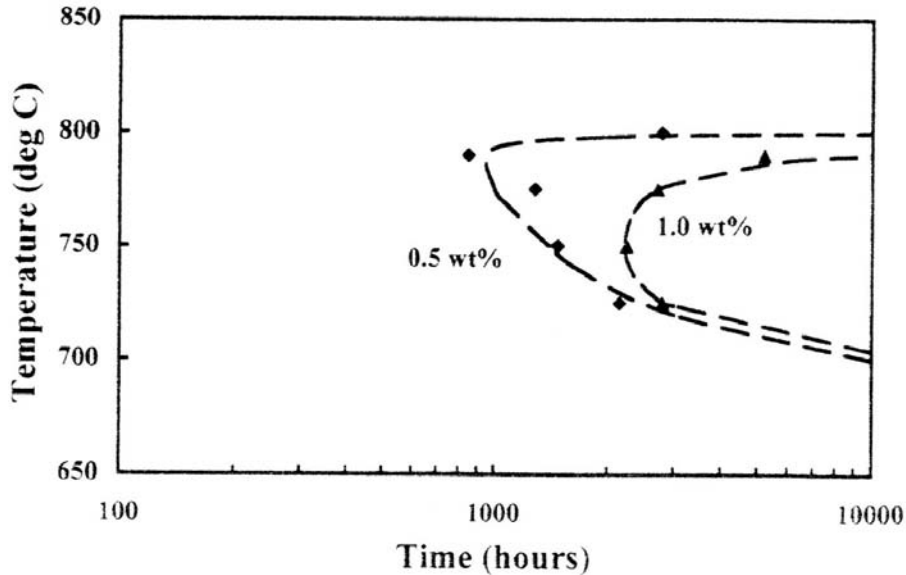


Figure 1-15: Experimental TTT diagram for the formation of 0.5 and 1.0 wt% of sigma in Alloy 720LI. Reprinted with permission from R. C. Reed, M. P. Jackson, and Y. S. Na, "Characterization and Modeling of the Precipitation of the Sigma Phase in UDIMET 720 and UDIMET 720LI," *Metallurgical and Materials Transactions A*, **30A**, 1999, Figure 9, p. 529.

been increased from 10 hours for Alloy 720 to over 1000 hours for Alloy 720LI.

Additionally, the nose of the TTT diagram has been decreased to about 750°C for the new composition, as opposed to 800°C for the original Alloy 720. It is important to note that Alloy 720 LI exhibits excellent microstructural stability below 700°C, which is above the temperatures that a high pressure turbine disk rim will see in service.

While Alloy 720LI is able to be produced by traditional cast and wrought processing, it is difficult to produce a billet of the alloy that is homogenous in grain size and chemistry. It is being processed in up to 250 mm diameter billets for Rolls-Royce engines [54]. However, even with the most current melting and ingot conversion techniques, Alloy 720LI suffers from  $\gamma'$  banding and from inhomogeneous grain sizes. Unrecrystallized grains up to ASTM 0 grain size can be found near the center of the billet

and can be difficult to fully eliminate. As a result, many turbine manufacturers have preferred the powder metallurgy processing route.

### **Microstructure**

Alloy 720LI has been reported in literature to contain approximately 55 volume percent  $\gamma'$  [46]. Both its microstructure and the resultant mechanical properties can be easily manipulated through heat treatment and forging [55]. Like many Ni-base superalloys, Alloy 720LI has a multi-modal distribution of  $\gamma'$  precipitates. It is important to note that the nomenclature for the different  $\gamma'$  sizes in P/M superalloys is different than that used for single crystal superalloys. In P/M superalloys, primary  $\gamma'$  consists of large blocky precipitates that nucleate discretely along the  $\gamma$  grain boundaries. These particles decorate and pin the  $\gamma$  grain boundaries, impeding grain growth during solution heat treatment. The secondary and tertiary  $\gamma'$  precipitates are formed by nucleation and growth during cooling from a supersolvus heat treatment. It has been proposed that the secondary  $\gamma'$  particles nucleate during quenching from the heat treatment temperature [56]. As the temperature continues to decrease, the secondary  $\gamma'$  precipitates grow in size, rejecting solute into the matrix. This continues until the diffusion rate of the solute is too slow for the precipitates to grow any further. The alloy eventually cools to a point where the driving force for nucleation of the tertiary  $\gamma'$  is large enough to occur. These particles grow in size up to 90 nm during the aging heat treatment. It is thought that the nucleation and growth process for the secondary  $\gamma'$  is in competition with that of the tertiary  $\gamma'$  [57]. At slower cooling rates, the secondary  $\gamma'$  can grow larger, leaving less supersaturation in the matrix for nucleation of the tertiary  $\gamma'$ . However, at faster cooling rates, the supersaturation in the matrix is greater when the necessary undercooling for

nucleation of the tertiary  $\gamma'$  is reached, resulting in a larger volume fraction of ultrafine  $\gamma'$ .

It is readily possible to tailor the size and morphology of the secondary (cooling)  $\gamma'$  through heat treatment alone. With a constant cooling rate of 55°C/min, the temperature at which an Alloy 720LI sample was removed and quenched had a great impact on the size of the secondary  $\gamma'$  (Figure 1-16) [57]. The size of the secondary  $\gamma'$

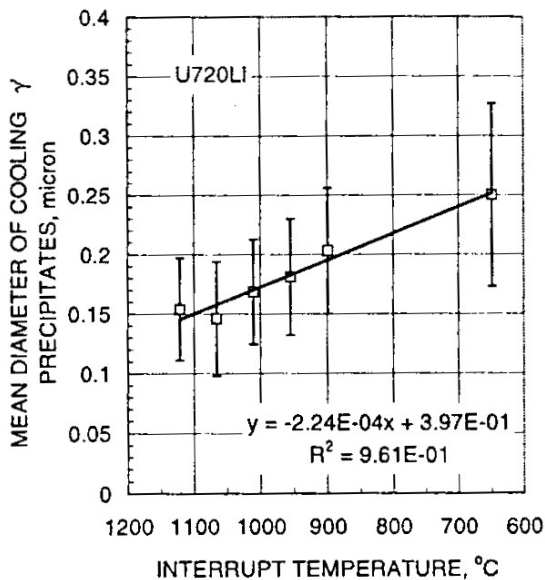


Figure 1-16: Mean diameter of the cooling  $\gamma'$  as a function of the interrupt temperature in Alloy 720LI. Reprinted with permission from J. Mao and K. Chang, "Growth Kinetics of  $\gamma'$  precipitates in P/M Superalloys," *Materials Design Approaches and Experiences*, Eds. J.-C. Zhao, M. Fahrman, and T. M. Pollock, TMS, 2001, Figure 5, p. 314.

was increased from 0.15mm to 0.25mm by changing the test interrupt temperature from 1121°C to 650°C. Additionally, the cooling rate used during a supersolvus solution heat treatment greatly effects on the size and morphology of the cooling  $\gamma'$  [58]. A wide range of varying morphologies were produced by controlling the cooling rates with different quenching media and by wrapping the samples in insulation to mimic the cooling rates seen by large turbine disks. As the cooling rate fell below 1.0°C/sec, the  $\gamma'$  size rose

dramatically from approximately 0.2  $\mu\text{m}$  to 1.0  $\mu\text{m}$ . Using all of this data, a TTT curve was constructed for the precipitation of different  $\gamma'$  morphologies in supersolvus heat treated Alloy 720LI [58]. The shape of secondary  $\gamma'$  progresses from spherical to dendritic to fan-type precipitates as the cooling rate is slowed down.

Although the carbon and boron levels in Alloy 720LI are low, carbides and borides are still present and impact the mechanical properties. The P/M material contains small uniform carbide precipitates, while the cast and wrought material has large primary carbides [59]. The most common type of carbide found in this alloy is the MC carbide. The  $\text{M}_{23}\text{C}_6$  carbides and  $\text{M}_3\text{B}_2$  borides are also present in smaller amounts. As the cooling rate is decreased, the amount of these two phases increased to the point where they can exceed the amount of primary carbides at the slowest cooling rates. It was also discovered that aging time increased the amount of  $\text{M}_{23}\text{C}_6$  and  $\text{M}_3\text{B}_2$  present in the alloy. These carbides and borides precipitate mostly along the grain boundaries. They appear as the fine white precipitates in the micrograph below (Figure 1-17) [60]. For this alloy, the MC carbide composition is predicted to be  $(\text{Cr}_{0.80}\text{Mo}_{0.19}\text{Ni}_{0.01})_{23}\text{C}_6$  [61]. The borides on the other hand are expected to be of the composition  $(\text{Mo}_{0.76}\text{Cr}_{0.24})_3\text{B}_2$ . After electrolytic extraction and x-ray diffraction analysis, it was discovered that the weight fraction of  $\sigma$ ,  $\text{M}_{23}\text{C}_6$ , and  $\text{M}_3\text{B}_2$  for subsolvus heat treated cast and wrought Alloy 720LI were all below 0.5% even after 3000 hour exposures at 800°C [61]. The MC-type carbides were found in micrographs of Alloy 720LI but not in Alloy 720 in this study. However, the amount in Alloy 720LI was not able to be measured by x-ray due to the overlap of their peaks with the peaks of  $\text{M}_{23}\text{C}_6$  carbides and  $\text{M}_3\text{B}_2$  borides, in addition to the low amount of MC carbides present in this study. These grain boundary carbides have been shown to reduce

grain boundary sliding at elevated temperatures which improves the creep resistance of the alloy [17]. The knowledge and ability to control these two additional strengthening mechanisms in P/M superalloys is important in improving the mechanical properties of these alloys.

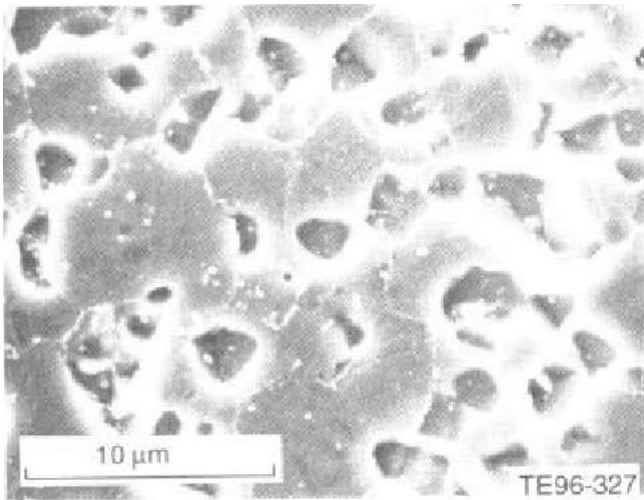


Figure 1-17: P/M Alloy 720 microstructure. Reprinted with permission from K. A. Green, J. A. Lemsky, and R. M. Gasior, "Development of Isothermally Forged P/M Udimet 720 for Turbine Disk Applications," *Superalloys 1996*, Eds. R. D. Kissinger, D. J. Deye, D. L. Anton, A. D. Cetel, M. V. Nathal, T. M. Pollock, and D. A. Woodford, TMS, 1996, Figure 5, p. 701.

In addition, the grain boundary microstructure itself plays an important role in the mechanical properties of Alloy 720LI. Through control of heat treatment, it is possible to form serrations in the grain boundaries. They form during controlled cooling through the  $\gamma'$  solvus [62]. Their amplitude and period are determined by the homogenization temperature, the cooling rate, and the final temperature for the controlled cooling. Their presence has been noted in Alloy 720 LI by Furer and Fecht [63]. It is generally thought that these serrations develop as a result of coarsening of the  $\gamma'$  precipitates close to the grain boundaries. These grain boundary serrations (Figure 1-18)

[64] have been demonstrated to have a positive effect on creep fatigue crack growth rate by impeding grain boundary sliding [64, 65].

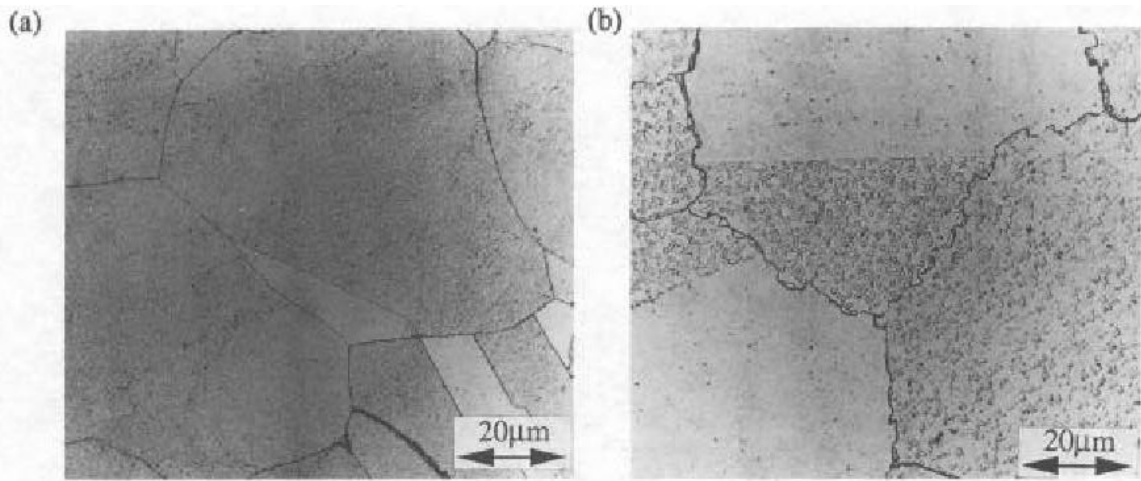


Figure 1-18: Optical micrographs of Astroloy. A) “Smooth” grain boundaries. B) Serrated grain boundaries. Reprinted with permission from H. L. Danflou, M. Marty, and A. Walder, “Formation of Serrated Grain Boundaries and Their Effect on the Mechanical Properties in a P/M Nickel Base Superalloy,” *Superalloys 1992*, Eds. S. D. Antolovich, R. W. Stusrud, R. A. MacKay, D. L. Anton, T. Khan, R. D. Kissinger, and D. L. Klarstrom, TMS, 1992, Figure 1, p. 65.

### Objectives

The increased homogeneity of powder processed Ni-base superalloys has led to dramatic improvements in the mechanical properties compared to traditional cast and wrought processing. However, the as-consolidated and heat treated P/M superalloys do not contain enough inherent defect tolerance to warrant usage in applications like jet engines, where unexpected failure can lead to tragic consequences. These alloys need expensive thermomechanical processing steps to reduce the size of defects so that they are below the critical crack initiation length for fatigue failure. Elimination of these processing steps would result in a tremendous reduction in the cost of finished and flight-ready turbine disks.

The purpose of this study was to try to improve and limit the scatter in mechanical properties of as-HIPed Alloy 720LI through heat treatment alone. In unpublished research by Pratt & Whitney, a supersolvus heat treatment improved the fatigue lifetime and fracture toughness of single crystal superalloys. A modification of this heat treatment was given to Alloy 720LI to determine the effect of a supersolvus heat treatment with a slow, controlled cooling rate on the microstructure, mechanical properties, and fracture mechanics of P/M Alloy 720LI. The creep lifetime, tensile strength, and fatigue lifetimes of specimens with a supersolvus heat treatment and a standard subsolvus heat treatment were compared. Detailed fracture analysis of the tested specimens was also performed to determine the mechanisms of failure for the two heat treatments.

## CHAPTER 2 EXPERIMENTAL PROCEDURES

### **Materials**

All materials used in this study were processed by Crucible Compaction Co. in Oakdale, PA. The alloys were gas atomized in the 2268 Kg (5000 lb) production gas atomization unit, using high-purity argon as the atomizing gas. The powder was collected and then sieved to -230 mesh (63  $\mu\text{m}$ ) size, with the majority of the powder below 400 mesh (38  $\mu\text{m}$ ). All powder particles coarser than the 230 mesh size were removed from the powder lot and returned as revert to be used in further atomization runs. The powder was then loaded into stainless or mild steel HIP cans and compacted. The HIP cycle used for all material in this study was below the gamma prime ( $\gamma'$ ) solvus (1129°C/100.0 MPa/4 h or 2065°F/14.5 Ksi/4 h). The test material came from eleven different master powder blends atomized at Crucible. There were only small differences in particle size and overall composition from one master powder blend to another. The sieve analysis for the various master powder blends is listed in Table 2-1. The compositions of all of the master powder blends, along with the nominal composition of the Alloy 720 LI, are listed in Table 2-2. All samples were provided in the as-HIPed condition.

### **Development of Heat Treatment**

Previous research by Pratt & Whitney has indicated that a supersolvus heat treatment followed by a slow cool through the  $\gamma'$  solvus temperature would produce the desired microstructure and mechanical properties in their single crystal alloys. In this

Table 2-1: Sieve analysis of the master powder blends (MPBs) in weight percent

MPB	+230	-230/+270	-270/+325	-325/+400	-400
95SW860	0	0.7	8.4	13.2	77.7
95SW861	0	0.6	8.1	13.7	77.6
96SW863	0	0.5	8.2	14.5	76.8
96SW864	0	0.5	6.4	12.7	80.4
96SW865	0	0.4	5.6	13.1	80.9
96SW887	0	0.9	8.9	14.2	76.0
96SW888	0	0.9	6.4	14.9	77.8
97SW984	0	0.4	7.5	11.1	81.0
97SW985	0	0.2	6.2	10.8	82.8
98SW035	0	0.5	5.7	13.4	80.4
98SW036	0	0.2	6.0	11.4	82.4

Table 2-2: Chemistry analysis of the master powder blends in weight percent

MPB	Ni	Cr	Co	Mo	W	Ti	Al	C	B	Zr
Nominal	Bal	16.57	14.71	3.00	1.28	5.02	2.49	0.010	0.012	0.038
95SW860	Bal	16.64	14.78	3.00	1.27	4.95	2.48	0.008	0.013	0.037
95SW861	Bal	16.67	14.88	3.01	1.28	4.91	2.55	0.010	0.013	0.040
96SW863	Bal	16.85	14.87	2.81	1.26	5.00	2.52	0.011	0.012	0.038
96SW864	Bal	16.53	14.70	3.00	1.25	4.98	2.58	0.011	0.013	0.038
96SW865	Bal	16.60	14.77	2.99	1.26	5.00	2.52	0.009	0.012	0.040
96SW887	Bal	16.64	14.74	3.00	1.27	4.98	2.47	0.012	0.014	0.037
96SW888	Bal	16.57	14.71	3.00	1.28	5.02	2.49	0.010	0.012	0.038
97SW984	Bal	16.73	14.72	3.00	1.26	4.92	2.43	0.007	0.014	0.037
97SW985	Bal	16.73	14.72	3.01	1.26	4.91	2.45	0.006	0.011	0.037
98SW035	Bal	16.6	14.63	3.01	1.29	5.03	2.47	0.011	0.011	0.040
98SW036	Bal	16.7	14.65	2.99	1.27	4.93	2.49	0.010	0.012	0.040

microstructure, there is a regular array of dendritic-shaped secondary  $\gamma'$  in the  $\gamma$  matrix.

However, specific details of the Pratt & Whitney heat treatment were not available. To

determine the alternate supersolvus heat treatment schedule needed to produce this

microstructure in Alloy 720, various heat treatment parameters were studied including soak temperature, soak time, cooling rate, and final temperature before fan air cooling.

The final heat treatment was verified through microstructural analysis.

### Heat Treatment Trials

Two solution heat treatments of Alloy 720LI were compared in this study. The control samples were given a standard subsolvus heat treatment from the literature. This heat treatment schedule is 1100°C (2012°F)/2 h. After two hours, the samples were fan-air-cooled (FAC). The alternate heat treatment was developed to match the microstructure that Pratt & Whitney’s study obtained after a supersolvus heat treatment for their single crystal superalloys. Since these P/M alloys are very different compositionally than the single crystal alloys utilized by Pratt & Whitney, the exact heat treatment temperature and the cooling rate necessary to obtain the desired microstructure in the Alloy 720LI were not known. As a result, it was necessary to perform several heat treatment trials to determine the temperature and cooling rate needed to produce the alternate microstructure. The test matrix for determining the alternate heat treatment schedule is shown in Table 2-3. The samples were heat treated in a Lindberg model

Table 2-3: Heat treatment trial matrix

Sample ID	Soak Temp.(°C)	Hold Time(h)	Cooling Rate(°C/min)	Final Temp.
A2	1175	2	3.3	1020
A3	1200	2	7.4	1020
A4	1225	2	7.2	1020
C1	1175	2	2.75	1075
C2	1175	2	0.82	1020
D2	1175	2	2.03	1020
A1	1175	4	2.75	1020
UMB1	1175	2	3.0	1020
D1	1200	2	2.75	1020

54233-V tube furnace with a Eurotherm model 818S temperature controller with a 50.8 mm (2 in) diameter mullite tube. The control thermocouple was a type R thermocouple with alumina sheathing positioned radially to the hot zone, but outside the mullite tube. A type K thermocouple, with 304 stainless steel sheathing, was inserted through the front end of the tube furnace into the hot zone to monitor the actual temperature of the samples throughout the heat treatment cycle. All samples were heated from room temperature to their hold temperature, held for two hours, and then cooled slowly in the furnace at various cooling rates to a final temperature of 1020°C (1868°F). This final temperature was selected in order to insure that the samples were cooled at least 100°C (180°F) below the solvus temperature so that all precipitation from cooling was accomplished before the more rapid cooling in air.

Upon completion of the heat treatments, the samples were removed from the furnace and allowed to fan-air-cool to room temperature. They were metallographically prepared by first mounting in diallyl phthalate using a Leco model PR-10 mounting press. The metallographic samples were then coarsely ground on a Leco model BG 20 belt grinder with a 60 grit SiC belt to remove the oxidation layer and to polish far enough into the sample to offset any temperature loss that may have occurred during transfer from the furnace to the quench bucket. The metallographic samples were then polished by hand using successive SiC papers of 120, 240, 320, 400, 600, and 800 grit. At each grit size, the samples were polished in the same direction until all of the scratches from the previous step had been removed. The sample was then rotated 90° and polished on the next highest grit paper. Once they were polished to 800 grit paper, fine polishing was performed using a Buehler Billiard cloth on a Leco model VP-50 polishing wheel, with

alumina suspensions of 15  $\mu\text{m}$  ( $5.9 \times 10^{-4}$  in) and 5  $\mu\text{m}$  ( $2.0 \times 10^{-4}$  in). The final polishing was performed on the same metallographic polishing wheel, with alumina suspensions of 1.0  $\mu\text{m}$  ( $3.9 \times 10^{-5}$  in) and 0.3  $\mu\text{m}$  ( $1.2 \times 10^{-5}$  in) on a Buehler Microcloth. Great care was taken between polishing steps to clean the samples in water using a Leco ultrasonic bath and to clean the polishing wheels, so there would be no contamination of larger sized alumina particles during the fine polishing. The surfaces were examined for scratches with an Olympus light optical microscope before moving on to the next polishing step. After polishing, the specimen surfaces were cleaned with methanol. Pratt & Whitney etchant #17 (25 mL HCl, 25 mL HNO<sub>3</sub>, 25 mL H<sub>2</sub>O, and 0.75 g molybdic acid) was then swabbed on the samples with cotton swabs for 5-20 s to etch the microstructure. This etchant selectively attacks the  $\gamma'$  precipitates to the  $\gamma$  matrix. These samples were then examined using a JEOL JSM 6400 (Figure 2-1) scanning electron microscope (SEM) at 15 KV accelerating voltage and a 15 mm (0.59 in) working distance.

### **Heat Treatment**

After the alternate heat treatment schedule was determined through these heat treatment trials and microstructural analysis, the heat treatment was carried out on the provided Alloy 720 LI mechanical testing bars at the University of Florida in an Applied Test Systems box furnace. When the samples were removed from the furnace they were given a fan-air-cool to room temperature. A type K thermocouple was used as the control thermocouple, with a second type K thermocouple with Nextel sheathing positioned directly on the sample bars for accurate monitoring of the temperature of the bars. This second thermocouple was placed under the test bars so that the bead of the thermocouple was in contact with the test bars at all times. Half of the bars received the standard



Figure 2-1: JEOL JSM 6400 SEM

solution heat treatment. The alternate heat treatment was 1175°C (2147°F) for 2 h with a 3.0°C/min (5.4°F/min) cooling rate in the furnace to 1020°C (1868°F). The samples were then removed and given a fan-air-cool to room temperature. While this heat treatment worked for the majority of the master powder blends, the soak temperature had to be reduced to 1165°C (2129°F) to produce the desired microstructure for three of the MPBs as will be discussed in the results section. The same aging heat treatment was given to all sample bars regardless of the solution heat treatment. The aging heat treatment used in this study was the standard Alloy 720 aging heat treatment found in literature. The schedule was 760°C (1400°F) for 24 h with a fan air cool and then 650°C (1200°F) for 16 h followed by a fan air cool. This heat treatment was performed in the same box furnace with the same thermocouple set-up as during the solution heat treatments.

Thirty-six bars were provided in the as-HIP condition for creep or tensile testing. These bars were approximately 19.1 mm (0.75 in) on a side and 101.6 mm (4.0 in) long.

Eighteen creep/tensile bars were heat treated using the standard heat treatment, while the other eighteen were solution heat treated according to the alternate heat treatment schedule. In addition, thirty-five bars were provided in the as-HIP condition for low cycle fatigue testing. These bars were approximately 19.1mm (0.75 in) by 25.4 mm (1.0 in) on edge and 152.4 mm (6.0 in) in length. Seventeen of the LCF bars were given the standard heat treatment, while the other eighteen test bars were given the alternate heat treatment. To verify the heat treatment, small microstructural analysis samples of each master powder blend were included along with the mechanical testing bars in each of the heat treatment runs. These samples were cubes with dimensions of approximately 19.1 mm (0.75 in) on edge.

### **Characterization**

After the heat treatments were complete, both the  $\gamma'$  solvus temperature and the microstructures of the two heat treatments were fully characterized. It was important to determine the solvus temperature in order to understand the microstructural evolution of Alloy 720LI during the heat treatments. The microstructural characterization of the two heat treatments served not only to help understand the precipitation behavior during the heat treatments, but also to help determine the effect of the two microstructures on the mechanical properties.

### **Determination of $\gamma'$ Solvus**

The  $\gamma'$  solvus temperature was determined in two complimentary ways. The two methods were differential thermal analysis and metallographic examination of the microstructure at various temperatures. These results were then compared to accurately

determine the  $\gamma'$  solvus temperature, the solidus temperature, and the liquidus temperature of Alloy 720LI.

### **Differential thermal analysis**

Differential thermal analysis (DTA) was performed at two independent laboratories. Samples for DTA were sectioned using a Leco diamond saw to produce specimens approximately 6.4 mm (0.25 in) by 9.5 mm (0.375 in) by 15.9 mm (0.625 in) in size. All DTA samples were in the as-HIPed condition with no heat treatment. Two samples from each of two different master powder blends were sent to M&P Laboratories in Schenectady, NY. These samples were heated at a constant rate of 10°C/min (18°F/min) to 1600°C (2912°F). The temperature difference between the sample and a reference sample of pure nickel was measured. These results were plotted versus temperature. One more sample of each of the two MPBs was sent to Dirats Laboratories in Westfield, MA. These samples were heated at 20°C/min (36°F/min). Once again, the temperature difference between the sample and a reference sample was measured. Two curves were plotted for these results. The first is of the temperature difference versus temperature. The second curve is of the derivative temperature difference versus temperature. All reaction temperatures were then identified by the inflection points present on the plots.

### **Metallographic examination**

In addition to DTA, solvus temperatures were determined by metallographic examination of quenched microstructures. For this portion of the study, a bar of Alloy 720 LI in the as-HIP condition was sectioned into smaller samples using a LECO cut-off saw. The metallographic examination samples were cut to approximately 6.4 mm (0.25 in) by 19.1 mm (0.75 in) by 19.1 mm (0.75 in). A Nextel-sheathed type K thermocouple

was attached to each sample with 80Ni-20Cr wire to measure the temperature of the sample accurately while in the furnace. These samples were then heated in a Carbolite model CWF 13/23 box furnace with PM 2000 elements (Figure 2-2) to various temperatures above and below the expected solvus temperature. One set of samples was



Figure 2-2: Carbolite box furnace

heated to temperatures at 5°C (9°F) intervals between 1100°C (2012°F) and 1200°C (2192°F). These samples were allowed to soak at temperature for one hour before being removed with tongs and quickly dropped into an iced-brine quench to “freeze in” the microstructure at the elevated temperature and prevent the formation of  $\gamma'$  during cooling. This quenching medium was prepared by filling a stainless steel bucket with tap water. Salt was then added to the water and stirred until the water was supersaturated with salt. Then ice was added and the water stirred until the ice no longer melted immediately. A second set of samples were solution heat treated at 1175°C (2147°F) for 1 h. They were

then slow cooled at 3°C/min (5.4°F/min) down to temperatures at 5°C (9°F) intervals between 1120°C (2048°F) and 1140°C (2084°F). These samples were allowed to soak at that temperature for an hour to allow precipitation to occur. All of these samples were then removed with tongs at their final temperature and quickly dropped into the iced-brine quench.

Once the samples were cooled, they were also metallographically prepared by first mounting in diallyl phthalate and then polishing as previously described. They were etched with Pratt & Whitney etchant #17 to reveal the  $\gamma/\gamma'$  microstructure. The SEM was used to examine the microstructures, so that the temperatures at which all phases go into solution for this alloy could be determined. These results were then compared with the DTA data to better understand the microstructural evolution of Alloy 720 during supersolvus heat treatment.

### **Microstructural Analysis**

When the heat treatment of all of the sample bars was completed, the small microstructural analysis samples were analyzed to fully characterize the microstructures of both the alternate and standard heat treatments. Each metallographic sample was mounted and polished to 0.3  $\mu\text{m}$  ( $1.2 \times 10^{-5}$  in) following the procedure listed above. In order to reveal the  $\gamma/\gamma'$  microstructure, these samples were swabbed with etchant #17. They were then examined on the SEM so the  $\gamma'$  morphology could be fully characterized after both heat treatments. An as-HIP sample and samples that had been heat treated but not aged were also examined with the SEM and with secondary electron imaging using the field emission gun (FEG) of an FEI Strata DB235 focused ion beam (FIB).

In addition, an analysis of the  $\gamma'$  volume fraction was performed according to the American Society for Testing and Materials (ASTM) standard E562-95 [66]. At least ten fields of view from the SEM were used for each sample for this analysis. A circular grid with 24 intersection points was then overlaid on the printed micrographs. Every intersection between a grid intersection and a  $\gamma'$  particle was counted. The total number of intersections was divided by the total number of grid points for that sample, giving an approximate  $\gamma'$  volume fraction.

The microstructural analysis samples for grain size determination were polished down to  $0.3\ \mu\text{m}$  ( $1.2 \times 10^{-5}$  in) to remove all etching effects. The samples were then etched with waterless Kallings etchant (5 g  $\text{CuCl}_2$ , 100 mL HCl, and 100 mL  $\text{CH}_3\text{CH}_2\text{OH}$ ) reveal the grain boundaries. The average ASTM grain size was measured according to ASTM standard E112-96 [67]. For this analysis, five fields of view were analyzed for each heat treatment. The Abrams three-circle procedure was used to count the number of times the circles intercept grains in the micrograph.

The final characterization technique that was utilized was Rockwell C hardness. The hardness of samples in the as-compacted condition, the as-solutioned condition for each heat treatment, and in the as-aged condition for each heat treatment were measured using a Rockwell hardness indenter with the Rockwell C tip. Twelve hardness values were determined for each sample to determine an average Rockwell C hardness value for each condition.

### **Mechanical Testing**

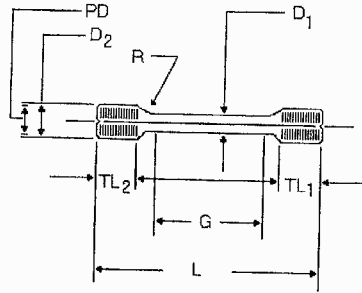
Upon completion of the heat treatment, all of the mechanical test bars were shipped to Crucible Compaction to be machined into test specimens. Crucible

outsourced the machine jobs to three different machine shops. Twelve of the creep/tensile bars (six from each heat treatment) were sent to Westmoreland Mechanical Testing & Research Inc. in Youngstown, PA to be machined into tensile samples according to the schematic in Figure 2-3. The gauge section for the tensile samples was 6.4 mm (0.25 in) in diameter and 31.8 mm (1.25 in) in length. The other twenty-four samples (twelve from each heat treatment) were sent to Joliet Metallurgical Laboratories, Inc. in Joliet, IL to be machined into creep samples according to Figure 2-4. The gauge section on the creep samples was 4.5 mm (0.177 in) in diameter and 26.0 mm (1.025 in) in length. Pin holes were machined into the shoulder of the creep specimens for attaching the extensometer frame with screws. The LCF test bars were then machined at Metcut Research Associates, Inc. in Cincinnati, OH according to Figure 2-5. The LCF test specimens had a gauge section that was 6.4 mm (0.25 in) in diameter and 19.1 mm (0.75 in) in length. These samples were later sent to Low Stress Grind in Cincinnati, OH to machine a 0.25 mm (0.01 in) notch was machined onto both shoulders of all LCF samples for attaching the knife edges of the extensometer frame. All gage surfaces were low stress ground to reduce or eliminate machining effects. Furthermore, the LCF samples were polished by hand to eliminate possible crack initiation sites.

### **Low Cycle Fatigue Testing**

The low cycle fatigue testing (LCF) was performed at the University of Florida in Gainesville, Florida in the High Temperature Alloys Laboratory using an Instron servo-hydraulic frame (Model TC 25). (Figure 2-6). This frame has an actuator with six inches of travel and is capable of loads up to 9500 Kg (21000 lbs). The LCF testing was computer controlled through the Instron Fast Track 8800 computer. The Fast Track

WESTMORELAND MECHANICAL TESTING & RESEARCH INC.  
 Youngstown, Pa. 724-537-3131  
 Inspection Sheet



TestLog	Lot No.	Sample ID	D-1	L	G	TL/2	R	Conc
533992	KT55	UCA1   137789	0.2506	3.2535	1.2337	0.6949	0.2500	0.0001
533993	KT56	UCA4   143569	0.2502	3.2460	1.2464	0.6938	0.2500	0.0002
533994	KT57	UCA5   142274	0.2500	3.2455	1.2374	0.6921	0.2500	0.0001
533995	KT58	UCA7   137789	0.2500	3.2525	1.2396	0.6992	0.2500	0.0002
533996	KT59	UCA8   137816	0.2508	3.2510	1.2424	0.6916	0.2500	0.0001
533997	KT61	UCA10   142184	0.2507	3.2515	1.2427	0.6959	0.2500	0.0001
533998	KT90	UCB1   138142	0.2494	3.2455	1.2536	0.6974	0.2500	0.0002
533999	KT91	UCB4   137762	0.2506	3.2505	1.2309	0.6992	0.2500	0.0001
534000	KT92	UCB2   138142	0.2505	3.2410	1.2446	0.7000	0.2500	0.0001
534001	KT93	UCB5   143596	0.2501	3.2450	1.2512	0.6935	0.2500	0.0001
534002	KT94	UCB3   138160	0.2507	3.2420	1.2391	0.6940	0.2500	0.0001
534003	KT95	UCB8   137816	0.2503	3.2470	1.2383	0.6926	0.2500	0.0001

Attn: Mr. Sean Conway  
 Company: Crucible Compaction Metals  
 Total Samples: 12  
 WMT&R #: 0-14345

Comment: Threads and finish are acceptable.

Inspector DCW 11-28-2000 09:47:09

KNOWINGLY OR WILLFULLY FALSIFYING OR CONCEALING  
 A MATERIAL FACT ON THIS FORM, OR MAKING FALSE,  
 FICTITIOUS OR FRAUDULENT STATEMENTS OR  
 REPRESENTATIONS HEREIN COULD CONSTITUTE  
 A FELONY PUNISHABLE UNDER FEDERAL STATUTES

Measuring Device  
 Optical Comparator X  
 Optical Comparator Y  
 0-6 Inch Caliper

Columns  
 D-1 G TL/2 R.  
 Conc  
 L

Figure 2-3: Tensile sample design. All dimensions are in inches.

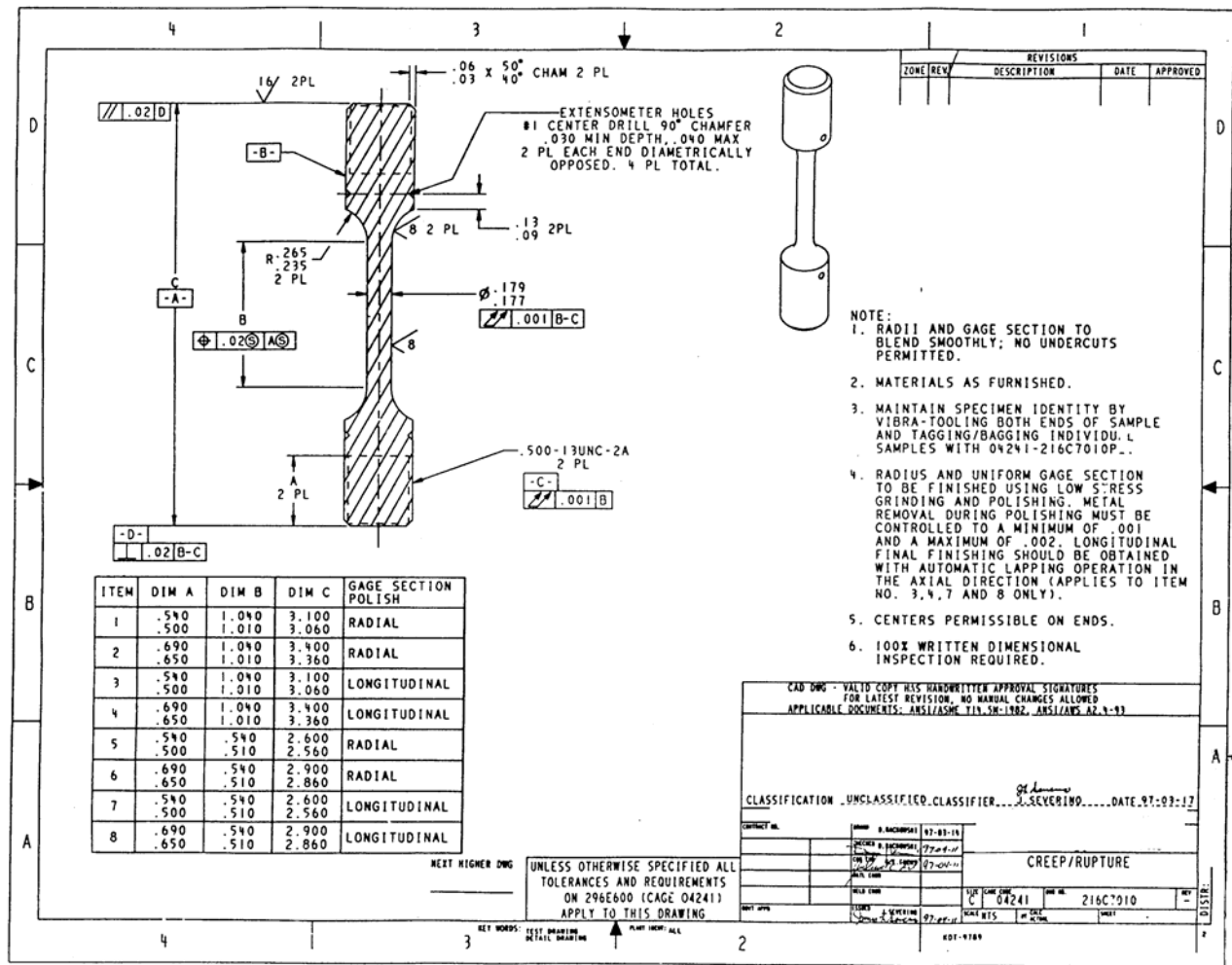


Figure 2-4: Creep sample design. All dimensions are in inches.

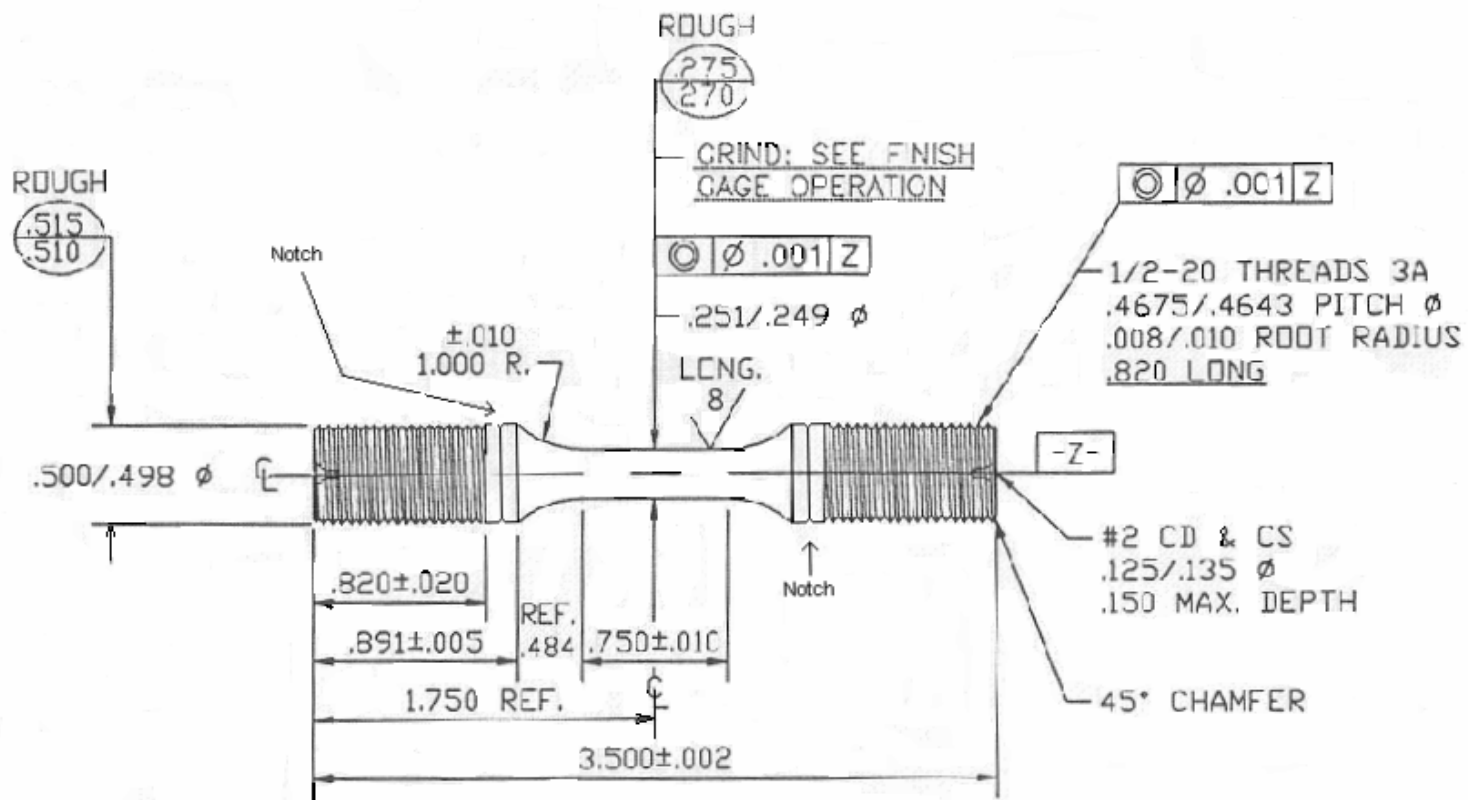


Figure 2-5: Low cycle fatigue sample design. All dimensions are in inches.



Figure 2-6: Instron-Satec servo-hydraulic test frame

computer was connected to a traditional PC on which the individual tests were setup and controlled using the LCF module of Instron's Fast Track Console software package. Loads/strains were applied to the test specimens through pull/push-rods and threaded grips. The pull/push-rods were machined by Low Stress Grind in Cincinnati, OH from material (Udimet 720) cast and wrought by PCC Airfoils in Minerva, OH. The grips were obtained from Satec and made from Mar-M 247 alloy. The specimens were heated to the test temperature by a Satec (Model SF-12 2230) clam-shell Power Positioning Furnace with Kanthal elements. Temperature was controlled by a Eurotherm model 2416 controller using a type K thermocouple. A second thermocouple was used to verify the test temperature. The two type K thermocouples, with Nextel fiber sheathing, were tied on to the gauge section of each sample using 26 AWG 80Ni-20Cr bare thermocouple

wire. A high temperature Instron extensometer frame was attached to the sample using replaceable round knife edge inserts with a 12.7 mm (0.5 in) diameter to allow the extensometer to measure strain outside of the hot zone of the furnace. The extensometer frame and the inserts were made out of Haynes 214. An Instron model 2620-826 dynamic extensometer with 12.7 mm (0.5 in) gauge length and  $\pm 2.54$  mm (0.1 in) travel length was attached to the extensometer frame using straight knife edge attachments and size 014 neoprene O-rings. Once loaded in the test frame, the specimens were heated to the test temperature by the furnace and allowed to soak at the test temperature for thirty minutes before beginning the tests.

The low cycle fatigue test matrix is listed below in Table 2-4. For all test specimens in this study, the third letter of the sample ID refers to the heat treatment. “A” is the standard heat treatment, while “B” refers to the alternate heat treatment. All tests were run with an  $R$  ( $\epsilon_{\min}/\epsilon_{\max}$ ) ratio of 0.0. Therefore, the minimum strain value for every cycle of every fatigue test was 0.0%. The maximum strain value for each cycle is equivalent to the value for the entire strain range. Two samples of each heat treatment were tested at three different temperatures and three different strain ranges. The LCF testing was performed in strain control through the first 25000 cycles at 0.333 Hz. If the specimens did not fracture before 25000 cycles, the test was switched to load control at the maximum and minimum loads during the strain controlled portion of the test. The load control portion of the test was performed at 10 Hz until fracture or until 1,000,000 cycles when the test was stopped and the sample was considered a run-out.

Table 2-4: The LCF test matrix

Heat Treatment	MPB	Serial Number	Sample ID	Temp.(°C)	Strain Range
Standard	96SW865	137789	ULA7	538	1.0%
	96SW864	135211T	ULA9b	538	1.0%
	95SW861	133978B	ULA1	538	1.1%
	95SW860	133870T	ULA2	538	1.1%
	96SW863	135276B	ULA13	538	1.2%
	96SW864	135195B	ULA14	538	1.2%
	95SW861	133468T	ULA3	649	1.0%
	95SW860	133870B	ULA5	649	1.0%
	96SW865	134340B	ULA10	649	1.1%
	96SW864	135203B	ULA11	649	1.1%
	96SW865	134277B	ULA15	649	1.2%
	96SW865	134367T	ULA16	649	1.2%
Aternate	96SW863	135294B	ULB2b	538	1.0%
	96SW865	134367B	ULB11	538	1.0%
	95SW860	133825B	ULB3	538	1.1%
	96SW864	135227B	ULB4	538	1.1%
	96SW864	135211B	ULB9	538	1.2%
	96SW863	135285B	ULB10	538	1.2%
	95SW861	133468B	ULB5	649	1.0%
	96SW864	135227T	ULB6	649	1.0%
	95SW861	133978	ULB7	649	1.1%
	96SW863	135276T	ULB8	649	1.1%
	96SW864	135195T	ULB13	649	1.2%
	96SW864	135203T	ULB15	649	1.2%

### High Cycle Fatigue Testing

All high cycle fatigue testing (HCF) was performed in the High Temperature Alloys laboratory at the University of Florida using the same servo-hydraulic frame as for the LCF testing. The HCF tests were controlled using Instorm's Fast Track Console software. The samples were loaded using the same push/pull rods and grips as in the LCF testing. The clam-shell furnace was enclosed around the test specimen and heated to the test temperature. Two type K thermocouples were attached to the gauge section of the specimens for temperature control. After a fifteen minute soak at test temperature, the HCF tests were started. These tests were run in load control at 10 Hz with an R ( $\sigma_{\min}/\sigma_{\max}$ ) ratio of 0.1. A test run with a stress range of 993 MPa (144 Ksi) was cycled

between a minimum load of 110.3 MPa (16 Ksi) and a maximum load of 1103 MPa (160 Ksi). Samples were tested until failure or until run-out, which was designated as 1,000,000 cycles. The test matrix for the HCF samples is shown in Table 2-5.

Table 2-5: The HCF test matrix

Heat Treatment	MPB	Serial Number	Sample ID	Temp.(°C)	Stress Range (MPa)
Standard	95SW860	133870B	ULA5	538	993
	96SW864	135203B	ULA11	538	1034
	96SW865	134367T	ULA16	538	1086
	95SW861	133468T	ULA3	649	993
	96SW863	135276B	ULA13	649	1034
	96SW865	134340B	ULA10	649	1086
Alternate	95SW861	133978	ULB7	538	993
	96SW863	135285B	ULB10	538	1034
	96SW865	134358B	ULB17	538	1086
	96SW864	135227T	ULB6	649	993
	96SW864	135195T	ULB13	649	1034
	96SW864	135211B	ULB9	649	1086

### Tensile Testing

The tensile testing was also carried out on the Instron servo-hydraulic test frame in the High Temperature Materials laboratory of the University of Florida. The Merlin module of the Fast Track software was used for set up and control of the tensile tests. The pull-rods and grips for the tensile testing were machined out of IN-713 superalloy by Satec. Two type K thermocouples, with Nextel sheathing, were attached to the gauge section of each elevated temperature tensile test as in the LCF testing. The same clam-shell furnace heated the samples to their test temperature. The samples were given at least a fifteen minute hold at temperature to allow the temperature inside the furnace to equilibrate before testing was commenced. The same extensometer frame from the LCF testing was used with 6.4 mm (0.25 in) diameter knife edge inserts for the elevated temperature tensile tests. The room temperature tensile tests did not require an extensometer frame, as the extensometer could be attached directly to the gauge section

of the specimens. An Instron model 2630-110 static extensometer with a 25.4 mm (1.0 in) gauge length and 25.4 mm (1.0 in) of travel was used for measuring the strain for the tensile tests. This extensometer was attached to the sample with 6.4 mm (0.25 in) steel clips. The test matrix for the tensile testing is shown below in Table 2-6. All tensile tests were conducted at a strain rate of 2.5 mm/min (0.1 in/min). The Merlin software recorded the data and then was used to produce stress/strain curves for each of the tensile tests. The software also calculated the yield strength, ultimate tensile strength, ultimate strain, and fracture strength.

Table 2-6: The Tensile test matrix

Heat Treatment	MPB	Serial Number	Sample ID	Temp.(°C)
Standard	96SW888	137789	UCA1	25
	98SW036	143569	UCA4	25
	97SW984	142274	UCA5	649
	96SW888	137789	UCA7	649
	96SW888	137816	UCA8	760
	97SW984	142184	UCA10	760
Alterante	96SW887	138142	UCB1	25
	96SW888	137762	UCB4	25
	96SW887	138142	UCB2	649
	98SW036	143596	UCB5	649
	96SW887	138160	UCB3	760
	96SW888	137816	UCB8	760

### Creep Testing

The creep specimens in this study were tested on a Satec model M3 creep frame as pictured in Figure 2-7. The High Temperature Alloys Laboratory at the University of Florida has four of these creep frames for high temperature creep testing. These frames have a sixteen-to-one ratio on the lever arm between the load pan and the sample. Two of the frames are outfitted with a Satec (model SF-16 2230) Power Positioning Furnace. These furnaces have three zones (top, middle, and bottom) that can be controlled independently to achieve the correct temperature along the entire gauge length of the test



Figure 2-7: Instron-Satec Creep frame

specimen. These furnaces have Kanthal elements. The other two creep frames have a Satec (model KSF 2-8-18) Power Positioning Furnace. These furnaces have a single hot zone with  $\text{MoSi}_2$  elements that are capable of testing up to temperatures of up to  $1500^\circ\text{C}$  ( $2732^\circ\text{F}$ ). All of these furnaces are controlled by a standard PC using the NuVision Mentor software supplied by Satec. The pull-rods and couplings used for the creep testing are the same as those described in the tensile testing section above. Three type K thermocouples were attached directly to the gauge section of each sample with 80Ni-20Cr wire. These three thermocouples allowed the computer to independently control each furnace zone on each frame so that the power output of each zone needed to maintain the correct temperature along the whole sample could be obtained. A high-temperature Instron extensometer frame was attached to each sample with screws into the pin holes on the sample shoulder. This frame and the screws were machined

from Haynes 214. A Satec model 9234K linear variable differential transformer (LVDT) displacement transducer was attached to the extensometer frame outside of the hot zone of the furnace for measuring strain on the sample during testing.

In total, twenty creep tests were performed according to the test matrix in Table 2-7. Two samples from each heat treatment were tested at every condition. Each specimen was given a one hour soak at the test temperature before beginning the test. The weight was step loaded in order to measure an approximate value for the elastic modulus for the samples. Time to 0.1%, 0.2%, 0.5%, 1.0%, 2.0%, 5.0% creep and time to creep rupture were recorded by the Mentor software. In addition, the minimum creep rate of each creep test was measured.

Table 2-7: The Creep test matrix

Heat Treatment	MPB	Serial Number	Sample ID	Temp.(°C)	Stress (MPa)
Standard	96SW888	137789	UCA12	677	1034
	97SW984	142274	UCA16	677	1034
	96SW888	137762	UCA9	677	793
	97SW984	142184	UCA11	677	793
	96SW888	137825	UCA13	704	689
	96SW887	138160	UCA18	704	689
	95SW860	133834T	UCA20	732	483
	95SW861	133807T	UCA21	732	483
	95SW860	133816B	UCA19	760	483
	95SW861	133807B	UCA22	760	483
Alternate	96SW888	137825	UCB11	677	1034
	97SW985	139888	UCB18	677	1034
	96SW888	137762	UCB7	677	793
	98SW036	143569	UCB10	677	793
	98SW036	143596	UCB6	704	689
	96SW888	137825	UCB12	704	689
	95SW861	133861T	UCB19	732	483
	95SW861	133798B	UCB20	732	483
	96SW888	137816	UCB14	760	483
	95SW861	133789T	UCB23	760	483

### Fracture Analysis

After failure, samples from each condition from the fatigue, creep, and tensile testing were evaluated to examine the fracture features and determine crack initiation site, type, and propagation path. Before analysis, all samples were cleaned in a Leco ultrasonic bath in acetone followed by methanol to clean any dirt or dust from the fracture surface. The samples were first viewed with a simple light optical microscope to get an overall view of the propagation path. Next the samples were examined on the SEM to reveal further details of the fracture surface. If the crack initiation site could be located for the sample, EDS was performed to determine the type of initiation site, e.g. inclusion, pore, machined crack, etc. Additionally, the microstructure of the crack path was investigated along the length of the fracture surface to determine what paths of failure were active during the various stages of fracture, i.e. intergranular, transgranular, ductile, or brittle. When SEM and optical examination of the fracture surface was complete, about 6.4 mm (0.25 in) of the specimen tip at fracture was sectioned off using a Leco (model VC-50) diamond saw. These samples were mounted in diallyl phthalate and polished and etched to reveal any interactions between secondary cracks and the alloy's microstructure. The samples were polished down to  $0.3\ \mu\text{m}$  ( $1.2 \times 10^{-5}$  in) as in the previous section on metallographic sample preparation. These samples were then etched with Pratt & Whitney etchant #17 to reveal the microstructure and examined on the SEM.

## CHAPTER 3 RESULTS

### Microstructure

#### Development of Heat Treatment

The first step of this study was developing the heat treatment that would result in the desired  $\gamma$ - $\gamma'$  microstructure. This microstructure was to have a regular array of large dendritic-shaped  $\gamma'$ , surrounded by tertiary  $\gamma'$ . Additionally, the grain size was to be slightly larger than both the as-HIPed and the standard heat treated microstructures. The only known variables for producing this microstructure were that the solution temperature was to be above the  $\gamma'$  solvus temperature and that there was to be a controlled-cool through this solvus temperature.

The  $\gamma'$  solvus temperature is reported in literature to be approximately 1150-1155°C (2102-2111°F) [46]. With this approximate value for the  $\gamma'$  solvus temperature, a set of heat treatment trials were run to develop the alternate, super-solvus, heat treatment for use in this study. Once the proper heat treatment was developed, the heat treatments were carried out on machined test bars. As a control variable, the standard heat treatment consisted of a two hour soak below the  $\gamma'$  solvus temperature at 1100°C (2012°F) followed by a fan-air-cool. Small, microstructural analysis samples were included for each Master Powder Blend (MPB) with all of the heat treatments. These samples were then examined to check the heat treatments and to fully characterize the microstructure.

### Heat treatment trials

Small, as-HIPed specimens were given various heat treatments according to the test matrix in Table 2-3. During these trials, the soak temperature, soak time, cooling rate, and final temperature before the fan-air-cool were varied to determine the proper heat treatment specifications. After the alternate heat treatment was developed, samples from each master powder blend were given both the alternate heat treatment as well as the standard heat treatment.

The starting point for the alternate heat treatment was a soak at 1175°C (2147°F). This temperature was chosen since it is above the reported  $\gamma'$  solvus temperature. A soak time of two hours was originally selected to allow enough time for all of the  $\gamma'$  to go fully into solution. The baseline sample for this study was A2 and had an 1175°C (2147°F) soak with a 3.3°C/minute (5.9°F/min) cooling rate to 1020°C (1868°F). The first heat treatment parameter that was examined was the solution temperature. Soak temperatures of 1200°C (2192°F) and 1225°C (2237°F) were examined, in addition to 1175°C (2147°F). Micrographs of these heat treatments can be found in Figure 3-1. Samples A3 and D1 were solution heat treated at 1200°C (2192°F), with A3 cooled at a rate of 7.4°C/min (13.3°F/min) and D1 at a rate of 2.8°C/minute (5.0°F/min). Finally, sample A4 was soaked at 1225°C (2237°F) and cooled at a rate of 7.2°C/min (13.0°F/min). All four of these samples were held at their soak temperature for two hours and cooled to 1020°C (1868°F) before they were removed from the furnace for the fan air cool. The higher heat treat temperatures did not result in the desired microstructure regardless of the cooling rate. From this set of trial samples it was determined that 1175°C (2147°F) would be used as the solution heat treatment temperature for the alternate heat treatment.

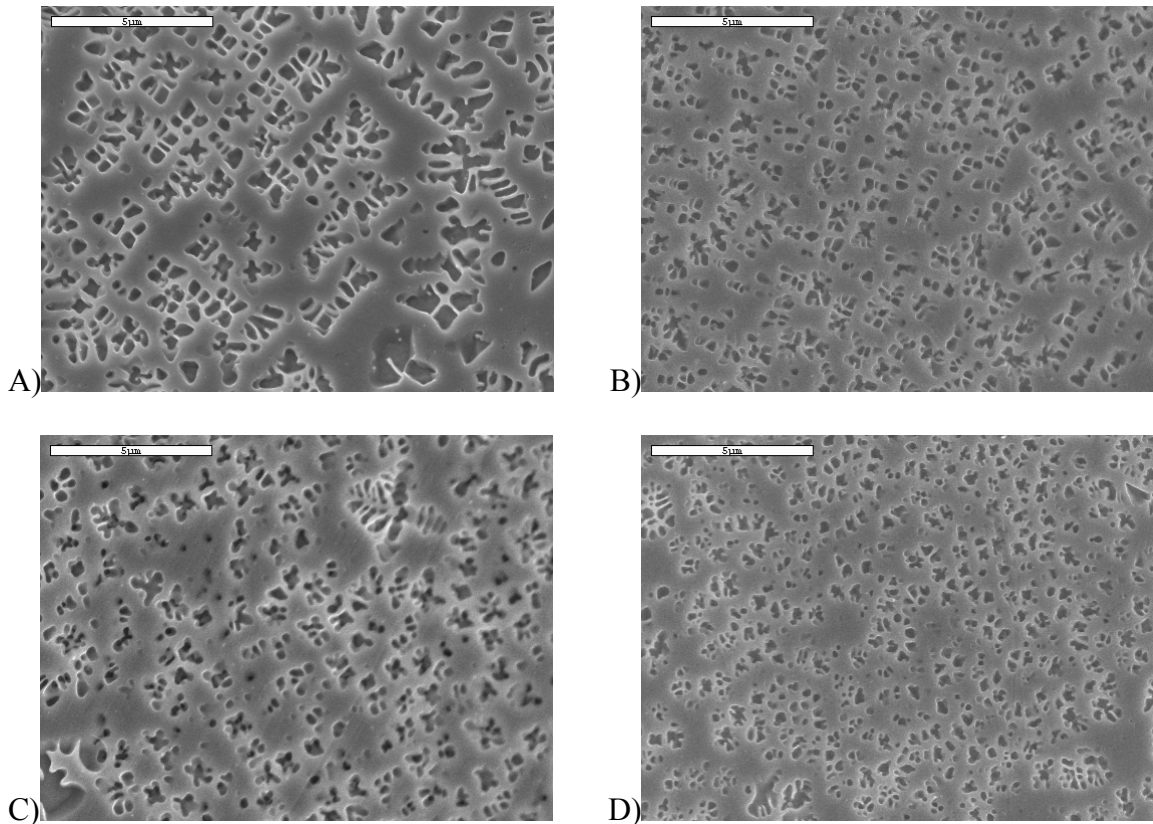


Figure 3-1: Heat treatment trial samples with various soak temperatures. A) A2 (1175°C). B) A3 (1200°C). C) D1 (1200°C). D) A4 (1225°C).

The next heat treatment parameter that was studied was the cooling rate from the solution temperature through the  $\gamma'$  solvus. When examining the previous samples, it was determined that a cooling rate of approximately 7°C/min (12.6°F/min) was too fast. Sample D1 was closer to the desired microstructure than A3. Slower cooling rates were examined to determine the optimal cooling rate. These ranged from 0.82°C/min (1.5°F/min) to 3.3°C/min (5.9°F/min). These samples are shown in Figure 3-2. Sample C2 was given a slow cooling rate of 0.82°C/min (1.5°F/min) down to 1020°C (1868°F) and then fan air cooled to room temperature. Sample D2 was cooled at a rate of 2.0°C/min (3.7°F/min). Finally, A2, as discussed above, was cooled at 3.3°C/min (5.9°F/min). All of these samples were soaked at 1175°C (2147°F) for two

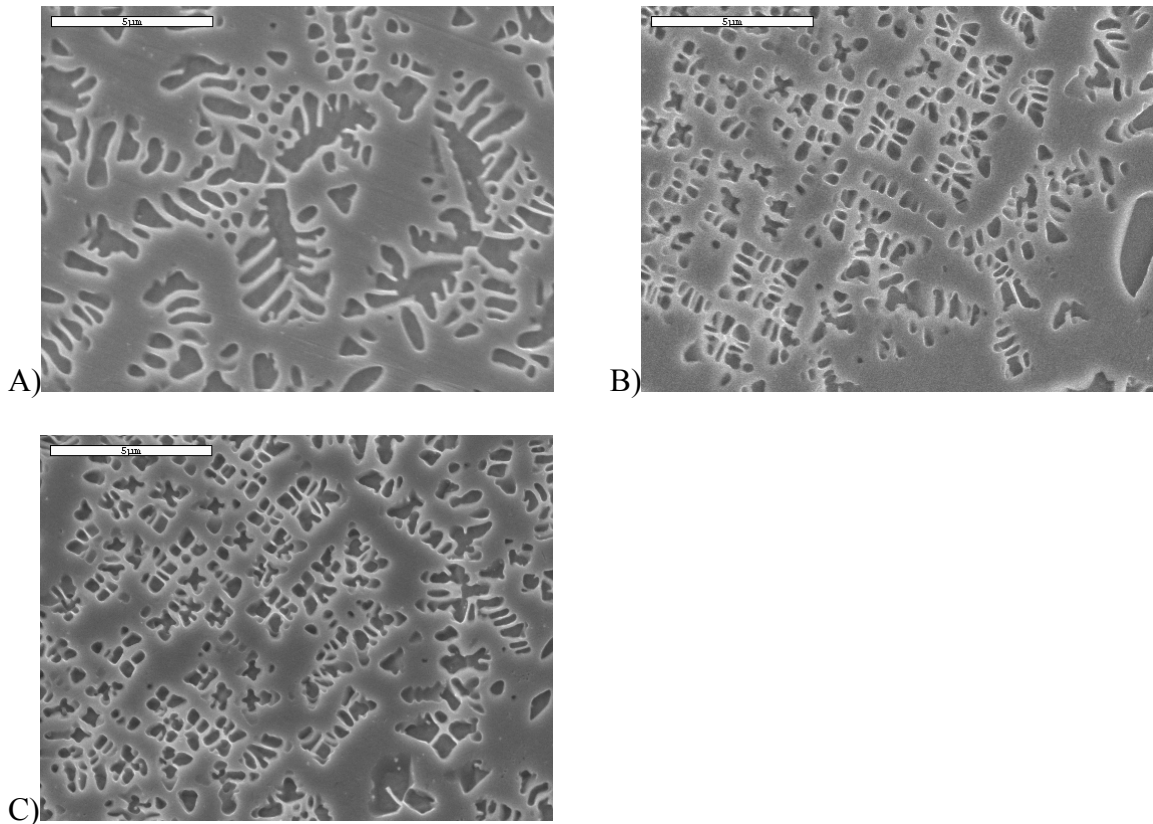


Figure 3-2: Heat treatment trial samples with different cooling rates. A) C2 (0.82°C/min). B) D2 (2.0°C/min). C) A2 (3.3°C/min).

hours before the controlled cooling. They were also all removed from the furnace when their temperature reached 1020°C (1868°F). As can be seen from the micrographs, both D2 and A2 produced the desired microstructure. The cooling rate for the final heat treatment was chosen as 3.0°C/min (5.4°F/min) as a compromise between the cooling rates of these two samples.

The final two parameters examined were the soak time and the temperature at which the sample was removed from the furnace for the fan air cool. A longer hold at the solution temperature was examined as well as a higher final temperature. Micrographs for these heat treatment trials can be found below in Figure 3-3. A2 was given a 2 h hold and a 3.3°C/min (5.9°F/min) cooling rate to 1020°C (1868°F). A1, on the other hand,

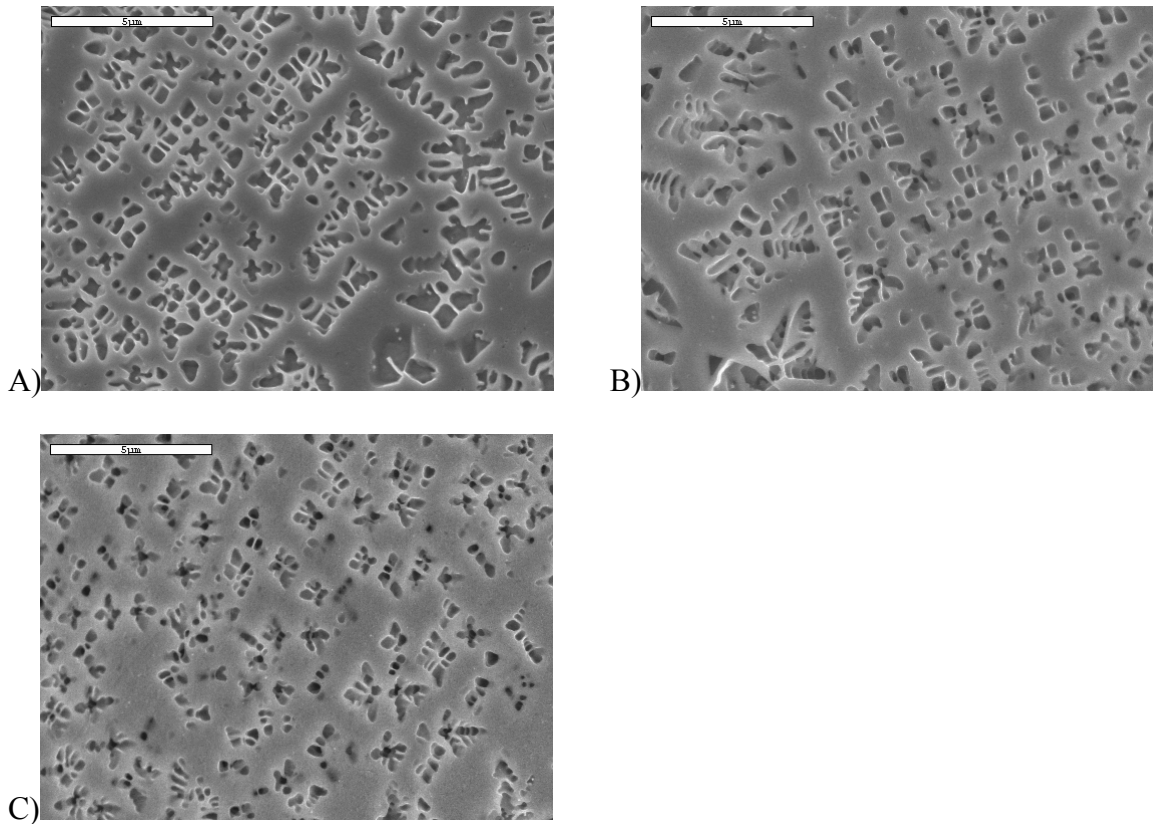


Figure 3-3: Heat treatment trial samples with different soak times and final temperature before fan-air-cool. A) A2 (2 h soak, 3.3°C/min, and 1020°C final temp.). B) A1 (4 h soak, 2.8°C/min, and 1020°C). C) C1 (2 h soak, 2.8°C/min, and 1075°C).

was held at temperature for 4 h and cooled at a rate of 2.8°C/min (5.0°F/min) until 1020°C (1868°F). Sample C1 was soaked for 2 h and slow cooled at 2.8°C/min (5.0°F/min) until a final temperature of 1075°C (1967°F). The longer hold time had an adverse affect on the microstructure, producing irregular shaped  $\gamma'$  precipitates. Additionally, the higher final temperature showed signs of dendritic shaped  $\gamma'$ , but ultimately did not allow enough time for the larger precipitates to grow. From these results, it was decided that the final heat treatment would have a 2 h hold and a final temperature of 1020°C (1868°F).

The final heat treatment schedules for both the standard and alternate heat treatments are shown below in Figure 3-4. Once the final alternate heat treatment was

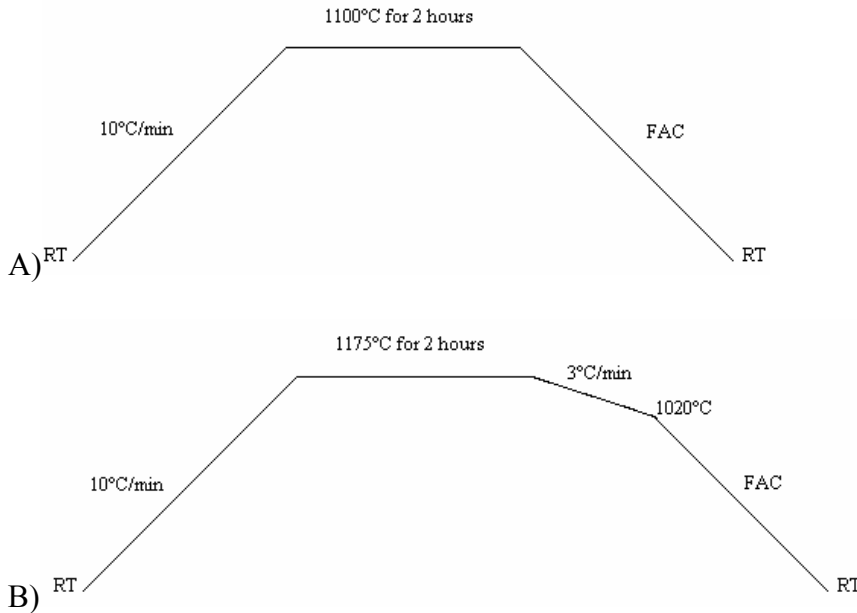


Figure 3-4: Heat treatment schedules. A) Standard heat treatment. B) Alternate heat treatment.

determined, samples of each Master Powder Blend (MPB) for the mechanical testing were given both the standard and alternate heat treatment as a check that these heat treatments work for all of them. Representative micrographs of the two heat treatments for these samples are contained in Figure 3-5. The standard heat treatment produced a similar microstructure to Figure 3-5a and Figure 3-5b in all of the MPBs. However, the alternate heat treatment produced the desired, dendritic  $\gamma'$  microstructure in only eight of the eleven MPBs. The other three (96SW865, 97SW984, and 98SW035) had microstructures similar to those found in Figure 3-6. The secondary  $\gamma'$  was irregular in shape. To counter this problem, the solution heat treatment schedule was lowered to 1165°C (2129°F). This lower solution temperature worked well and produced the desired microstructure in these three MPB's (Figure 3-7).

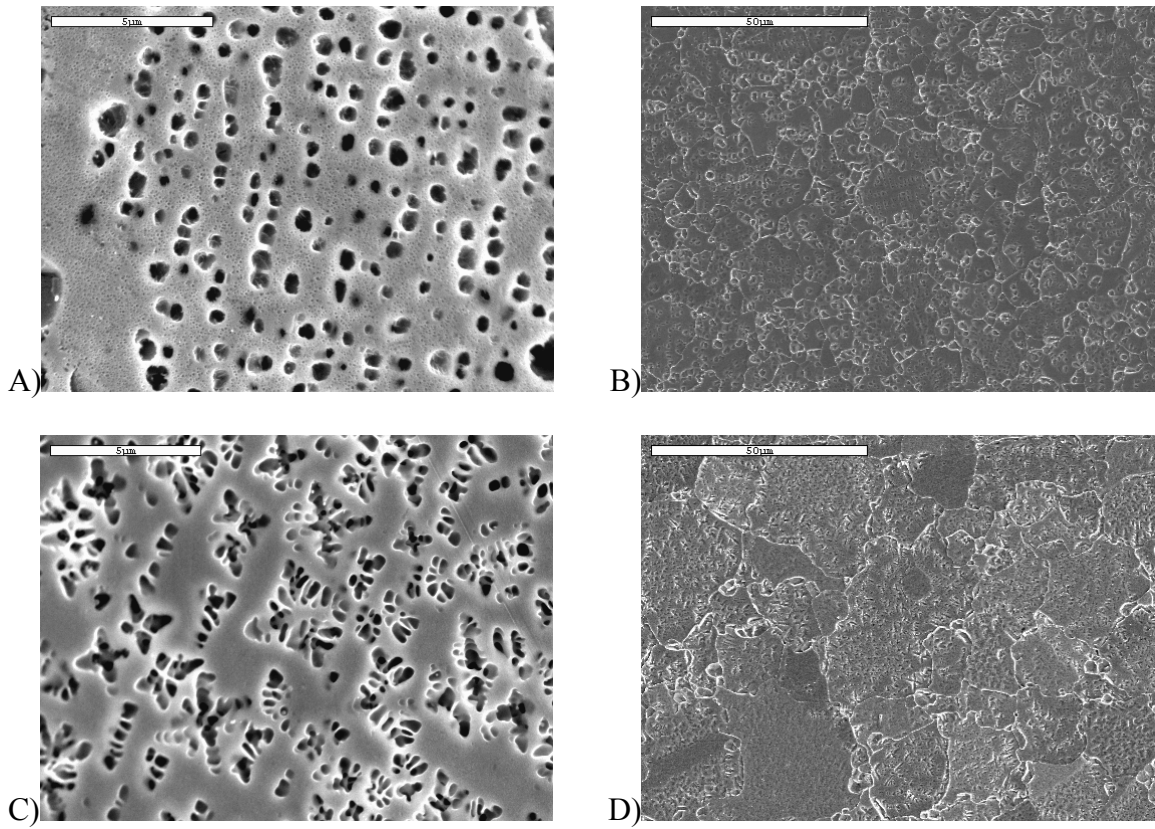


Figure 3-5: The standard and alternate heat treatment microstructures. A) Standard heat treatment at 4300X magnification. B) Standard heat treatment at 570X. C) Alternate heat treatment at 4300X. D) Alternate heat treatment at 570 X.

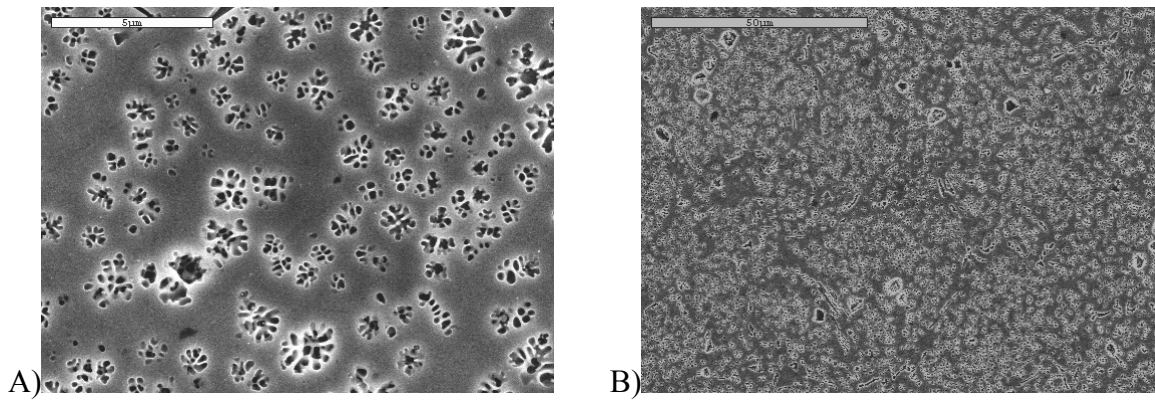


Figure 3-6: MPB 96SW865 after solution heat treating at 1175°C (2147°F). A) 4300X magnification. B) 570X magnification.

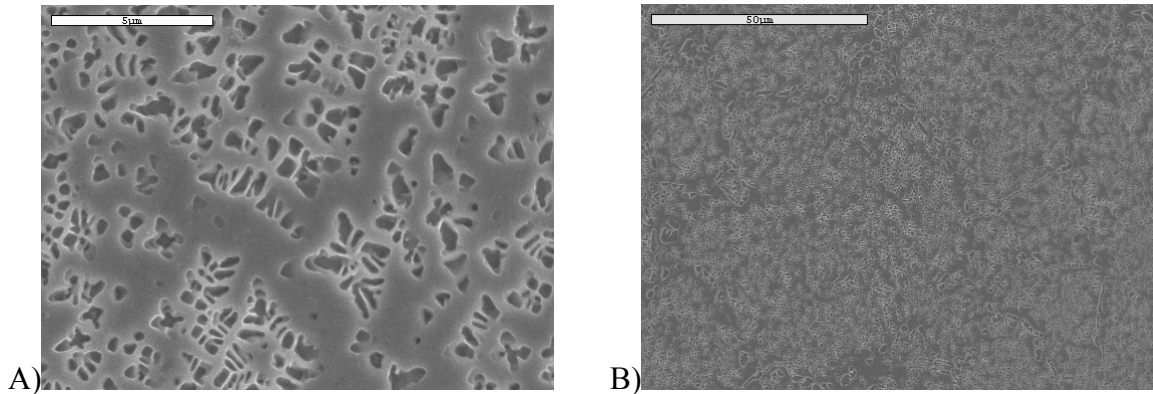


Figure 3-7: MPB 96SW865 after solution heat treating at 1165°C (2129°F). A) 4300X magnification. B) 570X magnification.

### Heat treatment

The standard, subsolvus heat treatment was carried out in two separate batches. These samples were heated to 1100°C (2012°F) at 10°C/min. They were left at this temperature for 2 h. Upon completion of the heat treatment, they were removed from the furnace and given a fan-air-cooling. The alternate, supersolvus heat treatment was carried out in three batches. The first two batches were ramped to 1175°C (2147°F) at 10°C/min. A two hour soak at this temperature was followed by a controlled cool (3°C/min) through the  $\gamma'$  solvus until the final temperature of 1020°C (1868°F) was reached. At this temperature, the test bars were removed and given a fan-air-cooling. The third batch consisted of the following MPB's: 96SW865, 97SW984, and 98SW035. Due to the differences noted between these three MPB's and the remaining samples during the heat treatment trials, the solution temperature was lowered to 1165°C (2129°F). All of the samples were then given the same aging heat treatment in a total of four batches. The first step of the age involved heating the samples to 760°C (1400°F); holding them for 8 h, then fan air cooling them back to room temperature. The final step was to heat the test bars to 650°C (1202°F) and hold them for 24 h before fan-air-cooling them to room temperature. Only one problem was encountered during these heat

treatments. A few of the creep and tensile bars developed a significant oxide scale that eliminated these bars as possible test specimens. It was determined that these particular bars had been sectioned so that they were either too close to the stainless steel HIP can or actually contained part of the can. New samples were shipped from Crucible Compaction to the University of Florida for completion of the heat treatments. These samples were tested for HIP can remnants by passing a magnet over them. Any sample that still contained part of the HIP can would be magnetic, while the ones that only contained Alloy 720LI would not be magnetic. These samples were heat treated according to the schedules listed above. When all the heat treatments were completed, the test bars were sent back to Crucible to be machined into test specimens.

### **Characterization**

After the heat treatments were complete, a full characterization of Alloy 720LI's response to the heat treatments was carried out. First, the  $\gamma'$  solvus temperature was determined as a comparison to the reported value from literature. Two methods of determining this temperature were used. The first was through differential thermal analysis (DTA) and the second was by metallographic inspection of quenched samples. Additionally, the  $\gamma$ - $\gamma'$  microstructure was fully evaluated through SEM, TEM, grain size measurements, volume fraction measurements, and hardness indents.

### **Determination of $\gamma'$ Solvus**

During the preliminary heat treatments, three of the eight master powder blends (MPBs) of Alloy 720LI had a different microstructural response to the heat treatment than the other MPBs. This difference was thought to be related to the  $\gamma'$  solvus temperatures of the different master powder blends as there was no noticeable trend with

chemistry. To verify this phenomenon and to determine the  $\gamma'$  solvus temperatures of the MPBs, samples were sent off for differential thermal analysis.

MPB # 96SW863 and MPB # 96SW865 were chosen as representative samples of the MPBs thought to have higher  $\gamma'$  solvus and lower  $\gamma'$  solvus temperatures respectively. Two samples from each MPB were sectioned and sent for DTA analysis at two independent laboratories. The purpose of using two laboratories was to ensure the accuracy of the results. The results obtained from the DTA analysis performed at the M&P Laboratories are in Table 3-1. The “maximum thermal effect” is the temperature

Table 3-1: The DTA results from M&P Laboratories

	96SW863a	96SW863b	96SW865a	96SW865b
Max Thermal Effect °C (°F)	1162 (2124)	1160 (2120)	1158 (2116)	1150 (2102)
$\gamma'$ solvus °C (°F)	1192 (2178)	1192 (2178)	1200 (2192)	1193 (2179)
Solidus °C (°F)	1279 (2334)	1279 (2334)	1279 (2334)	1280 (2336)
Liquidus °C (°F)	1352 (2466)	1349 (2460)	1348 (2458)	1349 (2460)

at which the rate of volume change in the  $\gamma'$  precipitates is at a maximum during heating [69]. This was measured at a local minimum that occurred in the DTA curve, while the  $\gamma'$  solvus temperature was determined from a local maximum immediately following the “maximum thermal effect”. The solidus was measured at the change in slope that occurred immediately before the minimum in the graph. Finally, the liquidus was measured at this minimum. The results of the samples sent to Dirats Laboratories for DTA analysis are contained in Table 3-2. The  $\gamma'$  solvus temperature was measured at a local maximum in the derivative of temperature curve. On the other hand, the solidus and liquidus were measured in the same method as M&P Laboratories. Dirats

Table 3-2: The DTA results from Dirats Laboratories

	96SW863c	96SW865c
$\gamma'$ solvus °C (°F)	1182 (2160)	1185 (2165)
Solidus °C (°F)	1251 (2284)	1235 (2255)
Liquidus °C (°F)	1334 (1169)	1333 (2431)

Laboratories did not report a value for the maximum thermal effect of the two samples; however, from the graphs the value can be estimated as approximately 1165°C for sample 96SW863c and 1160°C for sample 96SW865c. As can be seen from these two tables, M&P measured a lower temperature for the maximum thermal effect, but a higher temperature for the  $\gamma'$  solvus temperature. All of the DTA graphs can be found in Appendix A.

To more accurately determine the  $\gamma'$  solvus temperature for Alloy 720LI, the DTA data above was complimented with a metallographic study of samples quenched from various temperatures. The first set of these samples was heated to temperatures at 5°C (9°F) intervals between 1100°C (2012°F) and 1200°C (2192°F). They were allowed to soak at the temperature for 1 h and then quenched in an iced-brine solution. These samples were then polished, etched, and examined on the SEM. The important temperature range for the solutioning of  $\gamma'$  was determined to be between 1120°C (2048°F) and 1140°C (2084°F) during this study. Figure 3-8 shows micrographs for samples heated to these temperatures. At 1140°C (2084°F), all of the  $\gamma'$  was in solution. The only contrast present after etching was due to preferential attack of the grain boundaries and some small, discrete carbides. The samples heated to 1130°C (2066°F) and 1125°C (2057°F) exhibited coarse grain boundary  $\gamma'$  in addition to very small amounts of the secondary, intragranular  $\gamma'$  that had not completely gone into solution

after 1 h. Finally, the sample heated to 1120°C (2048°F) had no secondary or primary  $\gamma'$  in solution.

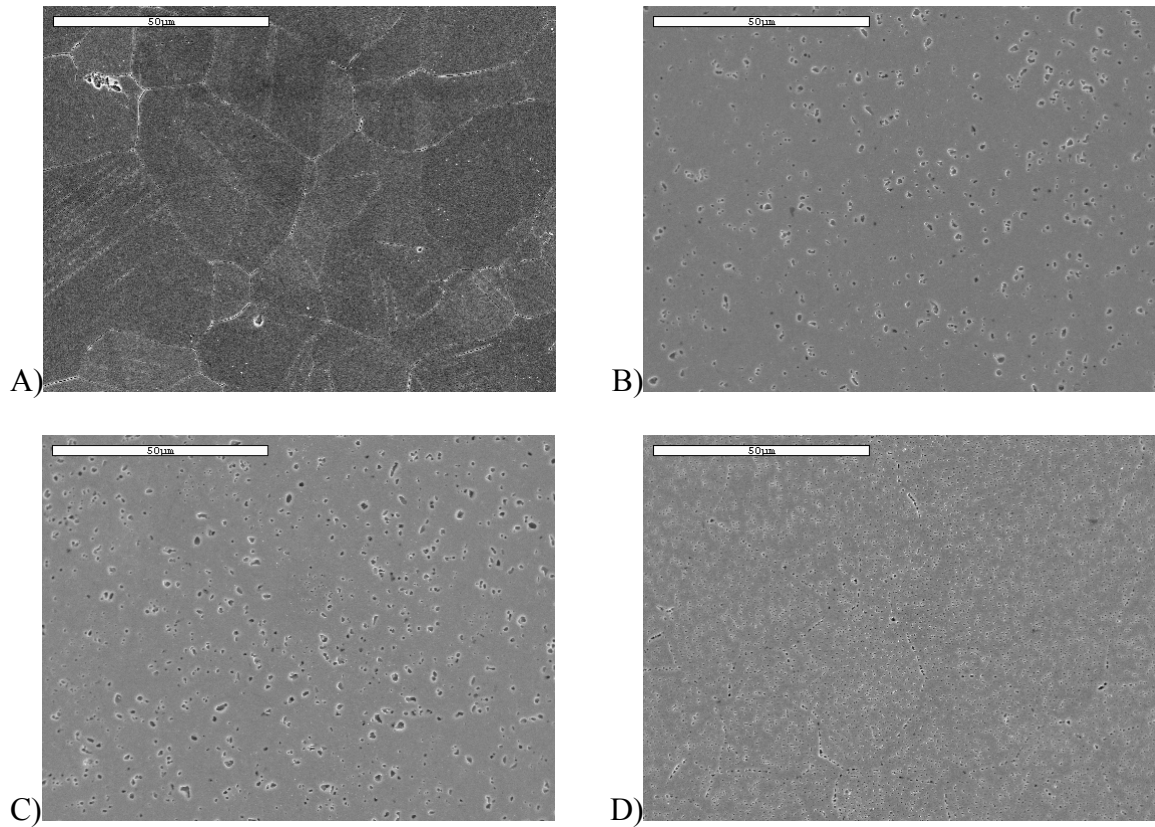


Figure 3-8: The  $\gamma'$  solvus trials quenched in iced brine after an hour at the solutioning temperature. A) 1140°C (2084°F). B) 1130°C (2066°F). C) 1125°C (2057°F). D) 1120°C (2048°F).

Additionally, a number of samples were heated to 1175°C (2147°F) and allowed to soak for 1 h to allow all second phase particles to go into solution. These samples were then control cooled in the furnace to temperatures at 5°C (41°F) intervals between 1120°C (2048°F) and 1140°C (2084°F). They were allowed to soak at this temperature for 1 h to allow all precipitation of secondary phases to occur. After 1 h, the samples were quenched in an iced-brine solution. Figure 3-9 contains micrographs of these samples. Once again, the sample quenched after soaking at 1140°C (2084°F) only had contrast due to preferential etching of the grain boundaries and discrete carbides. No  $\gamma'$

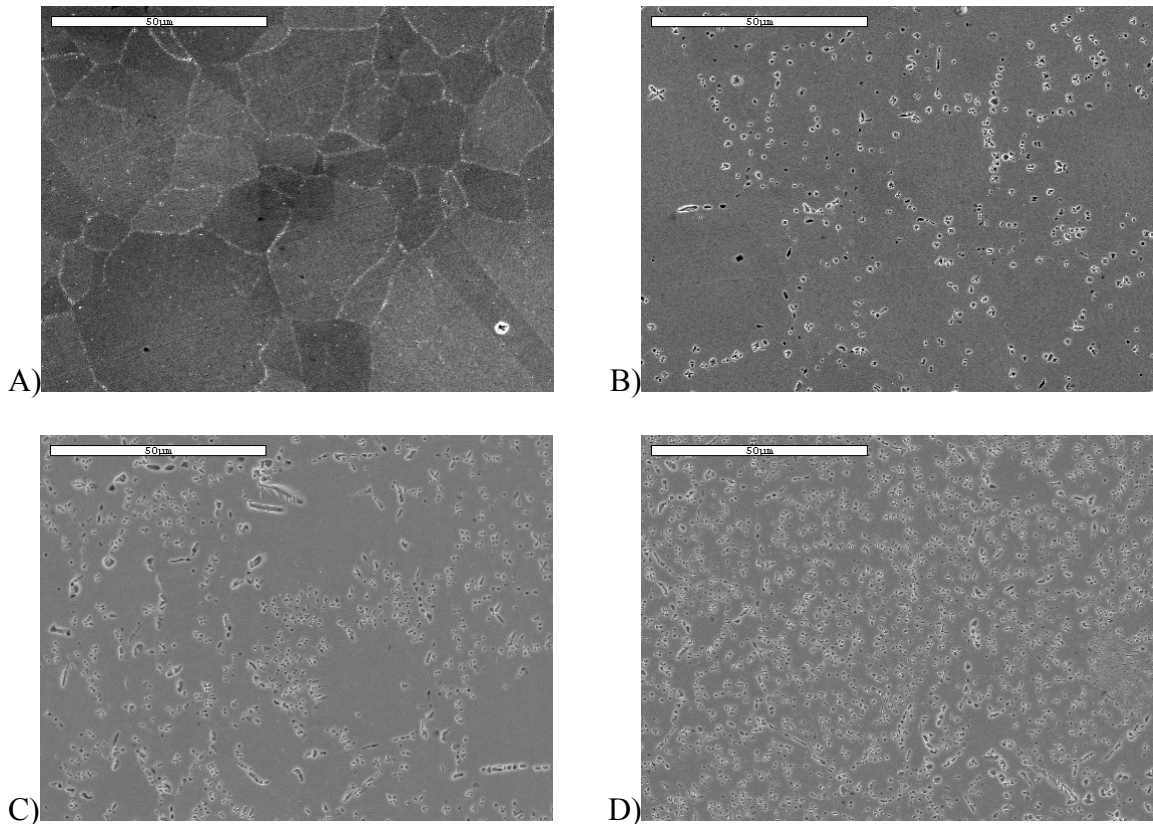


Figure 3-9: The solvus trials that were fully solutioned and then control-cooled. A) 1140°C (2084°F). B) 1130°C (2066°F). C) 1125°C (2057°F). D) 1120°C (2048°F).

had precipitated out at this temperature. After cooling to 1130°C (2066°F), the primary  $\gamma'$  had precipitated along the grain boundaries. The 1125°C (2057°F) sample had no additional precipitation. However, the sample that was cooled to 1120°C (2048°F) before quenching exhibited secondary, intragranular  $\gamma'$  in addition to the primary  $\gamma'$ .

### Microstructural characterization

Small blocks of each master powder blend were heat treated along with the sample bars to ensure that the proper microstructure was achieved for every test specimen and to fully characterize the microstructures that were produced. Representative micrographs of the two heat treatments after etching with Pratt & Whitney etchant #17 are included in Figure 3-10. As can be seen, the standard heat treatment produced smaller, more

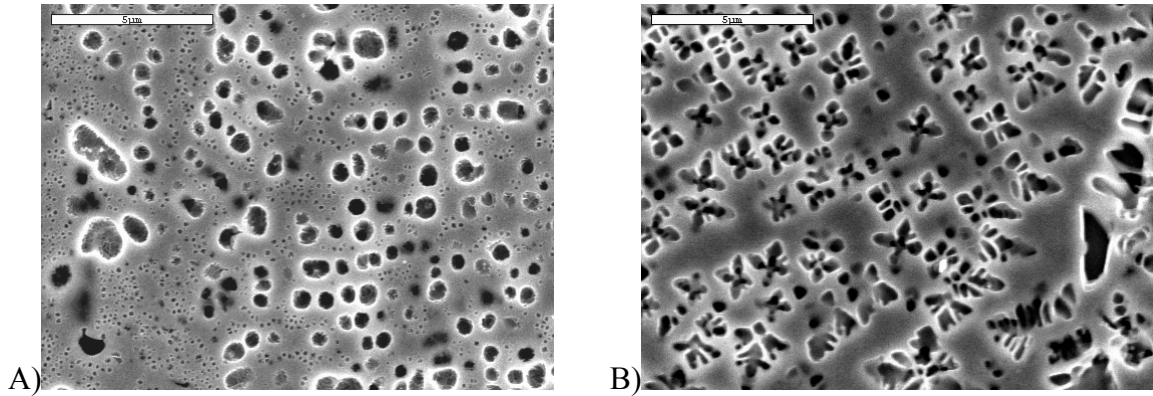


Figure 3-10: The  $\gamma/\gamma'$  microstructure in heat treated Alloy 720LI. A) The standard heat treatment. B) The alternate heat treatment.

cuboidal, secondary  $\gamma'$  precipitates compared to the larger, dendritic  $\gamma'$  produced by the alternate heat treatment. Both samples contained large primary  $\gamma'$  precipitates along the grain boundaries as seen in the far left of Figure 3-10A and the far right of Figure 3-10B. The ultrafine, tertiary  $\gamma'$  is readily evident in the standard heat treatment samples. However, a FEG SEM was needed to view these tertiary precipitates in the alternate heat treatment because of their smaller size and the better resolution capabilities of this instrument.

The  $\gamma'$  volume fraction and the average ASTM grain size were measured as detailed in Chapter 2. The  $\gamma'$  volume fraction was calculated on specimens etched with Pratt & Whitney etchant #17. This etchant did not reveal the grain boundary morphology as well as it revealed the  $\gamma/\gamma'$  microstructure. As a result, waterless Kallings solution was used to etch the grain boundaries for the grain size measurements. Figure 3-11 shows micrographs of both the standard and alternate heat treatments after etching with waterless Kallings reagent. The standard heat treatment has a smaller and more uniform grain size distribution, while the alternate heat treatment has larger and more varied grain

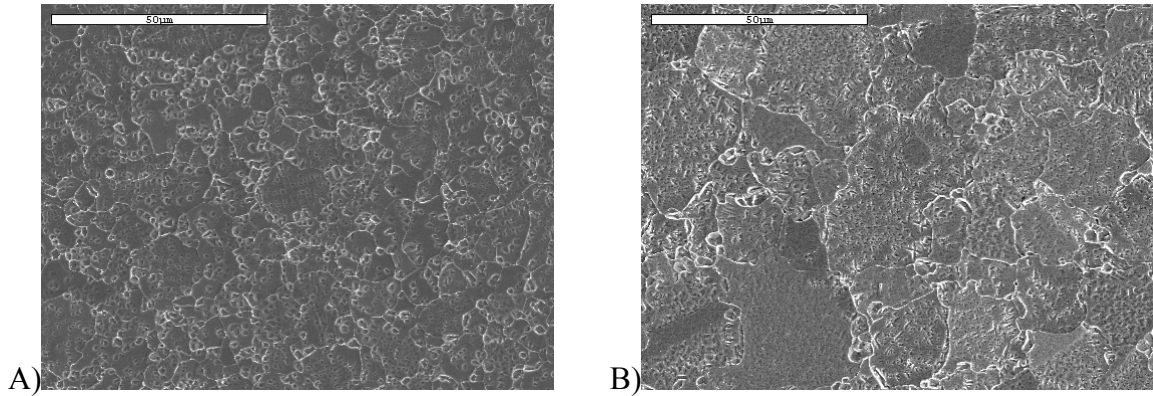


Figure 3-11: Grain boundary microstructure of heat treated Alloy 720LI. A) The standard heat treatment. B) The alternate heat treatment.

size distribution. The data and calculations for the  $\gamma'$  volume fraction measurements, mean  $\gamma'$  size, and the ASTM average grain size can be found in Appendix B. Table 3-3 shows the results of all of these calculations. While both heat treatments result in the same  $\gamma'$  volume fraction, the alternate heat treatment has a larger average ASTM grain size than the standard heat treatment. Additionally, the porosity of the as-HIP material was measured on a polished and unetched sample to be  $0.3 \pm 0.3\%$  by volume.

Table 3-3: The total  $\gamma'$  volume fraction, and ASTM grain size

Heat Treatment	$\gamma'$ volume fraction	ASTM Grain Size
Standard	50.7	11.8
Alternate	49.6	8.2

Hardness tests were conducted on heat treated samples after the solution heat treatment and after the aging heat treatment. The results of the Rockwell C hardness tests are contained in Table 3-4 below. While both heat treatments produced an increase in

Table 3-4: Results from Rockwell C hardness tests for both heat treatments

Heat Treatment	as-HIP	Solution H.T.	Aging H.T.
Standard	$37.8 \pm 0.6$	$42.5 \pm 0.3$	$45.8 \pm 0.3$
Alternate		$39.9 \pm 0.2$	$42.9 \pm 0.2$

the hardness of the alloys, the standard heat treatment has a greater hardness than the alternate heat treatment both before and after the aging heat treatment. The statistical

analysis for the hardness testing can be found in Appendix B. All of these data sets are statistically unique from each other. The increase in hardness after aging indicates that both heat treatments successfully produced the ultrafine tertiary  $\gamma'$ . The data and statistical calculations for the hardness testing are also contained in Appendix B.

## **Mechanical Testing and Fracture Analysis**

### **Low Cycle Fatigue**

Numerous problems were encountered when attempting to test samples in LCF. The first difficulty was with the push/pull rods initially used for the testing. A test was setup with the same push/pull rods that had been used during the creep and tensile testing. These were 27.3 cm (10.75 in) long and 1.91 cm (0.75 in) in diameter. The first sample was loaded, the test conditions were input into the computer, and the furnace was heated to the test temperature. However, when the test was started, the sample broke on the first cycle. After examination of the deformed sample, it was obvious that the test had been run without proper sample alignment (Figure 3-12). One of the push/pull rods and the extensometer frame were bent beyond repair. This was probably the result of the sample being off-axis during the compression cycle. It was necessary to design new push/pull rods specifically for fatigue testing that had a smaller length-to-diameter ratio to eliminate any potential bending during compression. The new design also contained a lip that would be flush against the actuator so that any potential deflection due to slack in the threads would be minimized. These new bars were cast by Special Metals (Figure 3-13a). They were then shipped to Low Stress Grind to be machined into the new push/pull rods. Figure 3-13b shows the new push/pull rods used for fatigue testing.



Figure 3-12: Low cycle fatigue sample that was misaligned and tested in compression

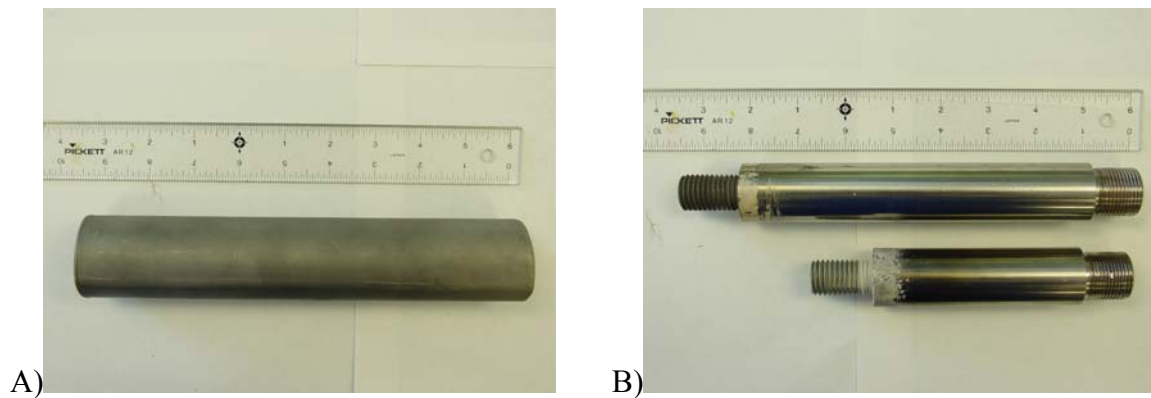


Figure 3-13: Push/pull rods. A) As-cast B) Machined into final form.

After a lengthy setback due to the production of these new push/pull rods, testing was resumed. The new push/pull rods worked better, but some additional issues still needed to be resolved. Anytime a sample was loaded, the test would begin properly, but it was obvious after a few cycles that the maximum and minimum loads were not at the expected values. Either the extensometer frame was slipping on the sample itself or the extensometer was slipping on the extensometer frame. In this setup, round knife-edge inserts attached directly to the polished specimen surface. This worked well for the

initial cycle; however, the knife-edges would slip with each cycle. To counteract this, two fatigue samples were sent to Low Stress Grind to machine a notch into the shoulder for the inserts to “hold onto” during the fatigue testing. Additionally, notches were machined onto the extensometer frame where the extensometer attaches to ensure that the extensometer itself would not slip. When the new notched specimens were received, they were loaded into the frame and tested. The system appeared to control the strain well on these tests, however they both broke at the notch, invalidating the data accumulated from these tests. Two more samples were then sent to Low Stress Grind to machine a notch just after the threaded region of the sample. Figure 3-14 shows one of these samples.

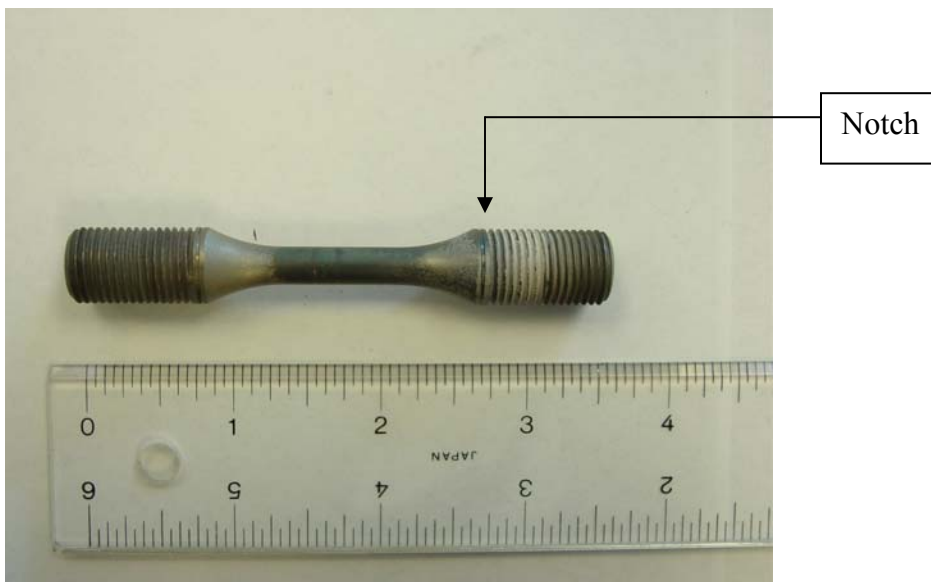


Figure 3-14: Low cycle fatigue sample with notches machined just after the threaded region and before the shoulder of the sample

Larger diameter (12.7 mm) inserts were also ordered from Satec for these new samples. This new set-up appeared to work well on these two samples. At this point, the remaining samples were shipped to Low Stress Grind to have similar notches machined onto their shoulders.

A number of tests were run to failure and some to run-out at 1,000,000 cycles. The computer appeared to be controlling strain well; however, the maximum and minimum stresses and the amount of plastic strain reported during the tests were different from what was expected. At this point, the total length of the tested samples was measured to determine the actual deformation that they had endured. These values were much lower than those reported by the fatigue software. While the notches had minimized the slippage, they still had not completely eliminated it. It was decided to test the remaining samples in high cycle fatigue (HCF) rather than waste any more fatigue specimens. The LCF fracture surfaces were examined as they could provide some valuable insight into the effect of the different heat treatments and their resulting microstructure on the crack initiation type and propagation mode.

Three samples failed for each heat treatment, all at 538°C (1000°F). The strain ranges were supposed to be either 1.0% or 1.1% for all of these tests. However, due to the complications listed above, these strain ranges were not accurate for the strain actually seen by the samples. All three standard heat treatment samples that fractured failed from processing defects. Two of the samples failed from ceramic inclusion initiation types as seen in Figure 3-15. The third standard heat treatment sample contained two different types of defects that initiated cracks. These can be seen in Figure 3-16. The first defect was in the middle of the sample. This initiation point had too much mechanical damage to determine the type of defect. The second initiation (ceramic inclusion) was located at the bottom of the sample as seen in the overview micrograph. It was inside the sample, but very near to the surface. This initiation was responsible for the eventual fast fracture and failure of this sample. It is important to note that faceted

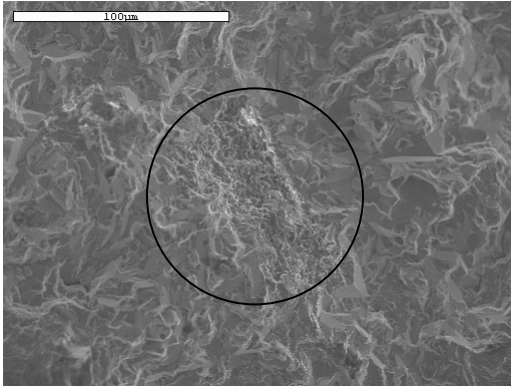


Figure 3-15: Ceramic inclusion type defect in standard heat treatment sample tested at 538°C (1000°F) and a strain range of 1.1%

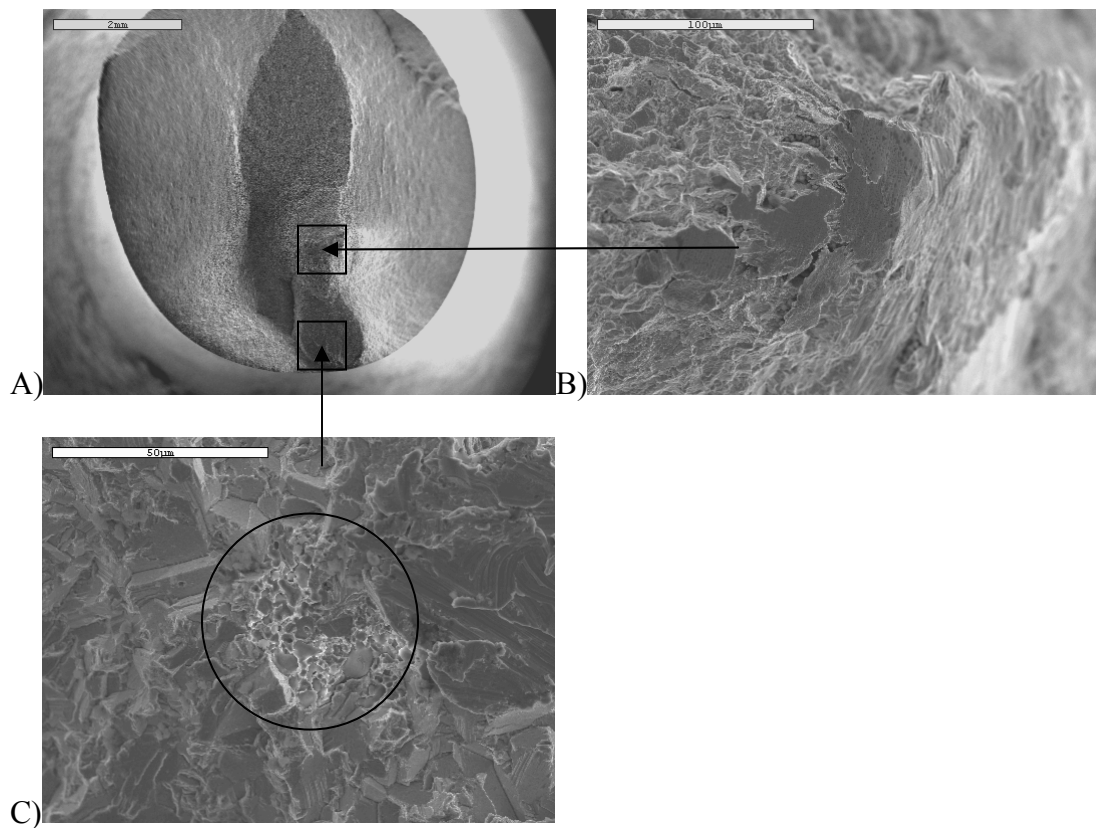


Figure 3-16: Standard heat treatment sample tested at 538°C (1000°F) and a strain range of 1.0%. A) The overview of the fracture surface. B) Initiation from unknown type of defect. C) Initiation from a ceramic agglomerate.

grains were found near the various defects for the standard heat treatment. These grains are examples of slip band cracking; however, they did not function as the crack instigator.

In contrast to the standard heat treatment samples, the alternate heat treatment LCF fracture surfaces all had faceted grains as the initiation. These cracks all initiated inside the sample, but near the surface. A representative micrograph of one of these initiation sites is in Figure 3-17. The arrows in these micrographs indicate the direction of crack propagation. The grain that served as the initiation point also has a twin boundary that

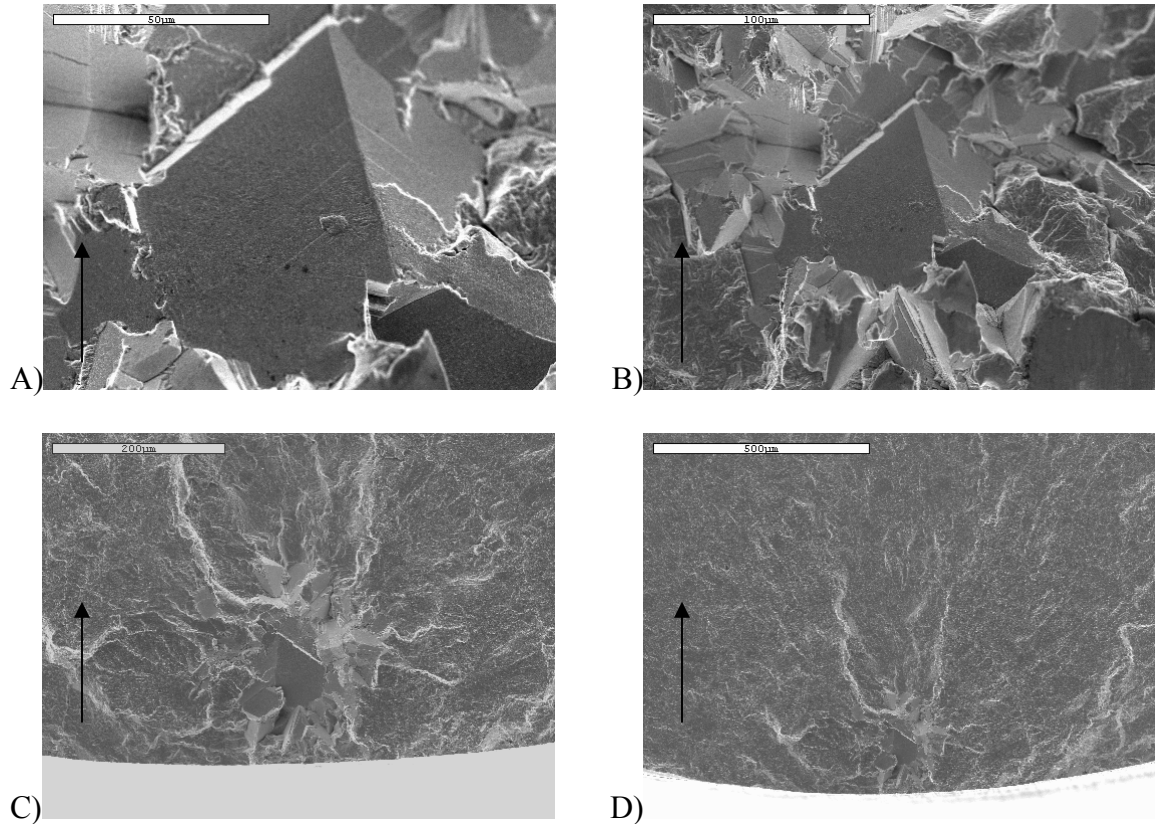


Figure 3-17: Alternate heat treatment sample tested at 538°F (1000°C) and a strain range of 1.0%. A) 570X magnification. B) 285X. C) 115X. d) 57.5X.

resulted from the deformation to the grain. The lower magnification fractographs show secondary cracks propagating radially outward from this initiation point. After initiation, the cracks propagated in a similar manner for both the standard and the alternate heat treatments. Immediately after the initiation region, there was a flat relatively featureless region of crack growth as can be seen in Figure 3-18. This region of the crack surface

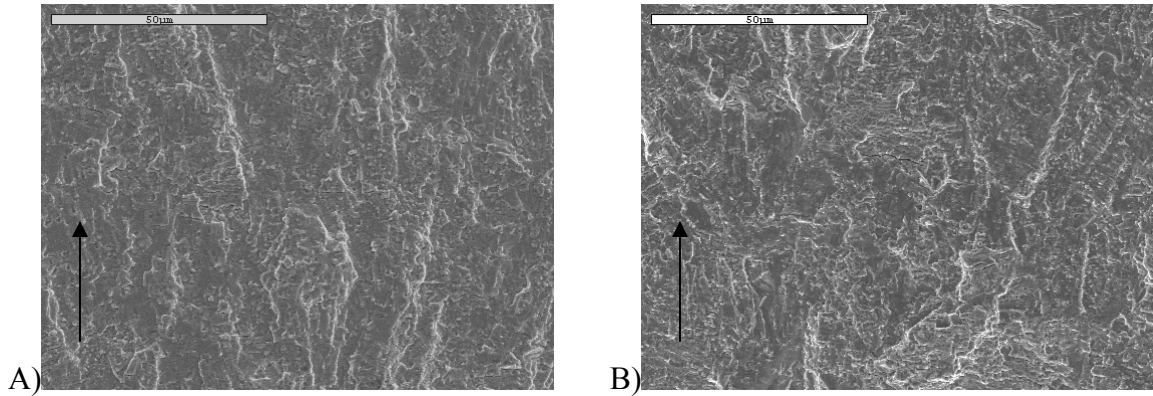


Figure 3-18: Relatively flat featureless region just after crack initiation in low cycle fatigue. A) Standard heat treatment. B) Alternate heat treatment.

extended approximately one millimeter from the initiation in all directions. It was marked by discoloration on the fracture surface due to longer exposure to the oxidizing atmosphere during testing. At the edge of this discolored region, the surface transitions from a featureless region to what can best be described as an area of undulating peaks and valleys. These features persists until either the specimen surface or shear lips. As the crack moves further from the discolored region, these “hills and valleys” become more and more pronounced. There appears to be a size difference between the features for the two heat treatments in this area. Figure 3-19 shows representative micrographs of this area of the propagation paths.

### High Cycle Fatigue

After the initial complications with the LCF testing, high cycle fatigue (HCF) tests were conducted to determine the effect of the supersolvus heat treatment on fatigue lifetime and crack initiation type compared to the standard subsolvus heat treatment. A test matrix was setup to determine the role of microstructure in the fatigue failure of the remaining samples. Tests were performed with an R ratio ( $\sigma_{\min}/\sigma_{\max}$ ) of 0.1 at 538°C (1000°F) and 649°C (1200°F) and at three different stress ranges: 993MPa (144Ksi),

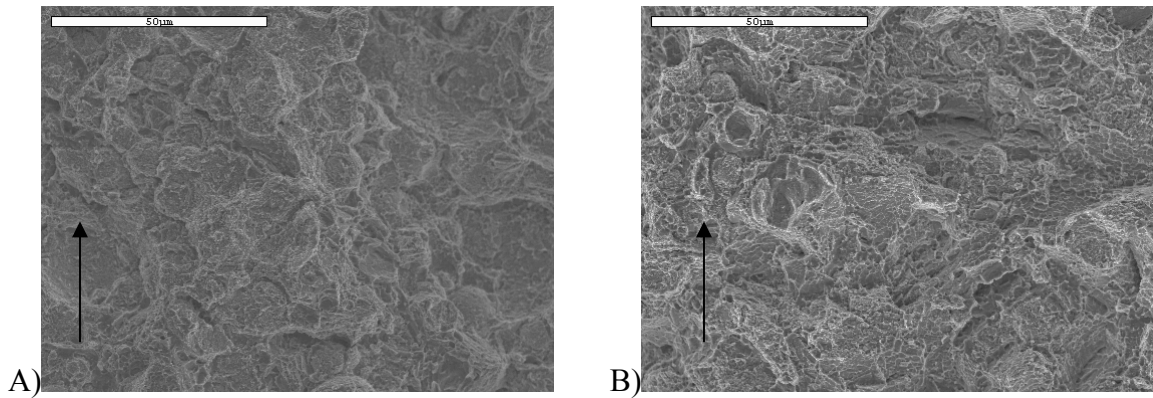


Figure 3-19: Representative micrographs of the fast fracture region of LCF samples. A) Standard heat treatment. B) Alternate heat treatment.

1034MPa (150Ksi), and 1086MPa (157.5Ksi). All tests were run at a frequency of 10 Hz. The fracture surfaces were then examined to evaluate the fracture features and to determine the crack initiation type and the mode of crack propagation.

### HCF results

The HCF testing was completed without any of the problems encountered during LCF testing. All of the tests failed before 1,000,000 cycles. There were three extra fatigue specimens (two standard heat treatment and one alternate heat treatment) remaining after all test conditions had been examined. After examining the HCF test results, these samples were tested at conditions to determine the amount of data scatter in fatigue properties and when test results indicated a longer or shorter than expected lifetime. The stress range is plotted versus the number of cycles to failure on a log scale for both heat treatments at 538°C (1000°F) in Figure 3-20. At the low and middle stress ranges of 993 MPa (144 Ksi) and 1034 MPa (150 Ksi), the standard heat treatment had superior fatigue lifetimes. However, at the highest stress range of 1086 MPa (157.5 Ksi), the alternate heat treatment had the longer fatigue lifetime. Similar results were found for the testing performed at 649°C (1200°F). (Figure 3-21) Once again, the standard heat

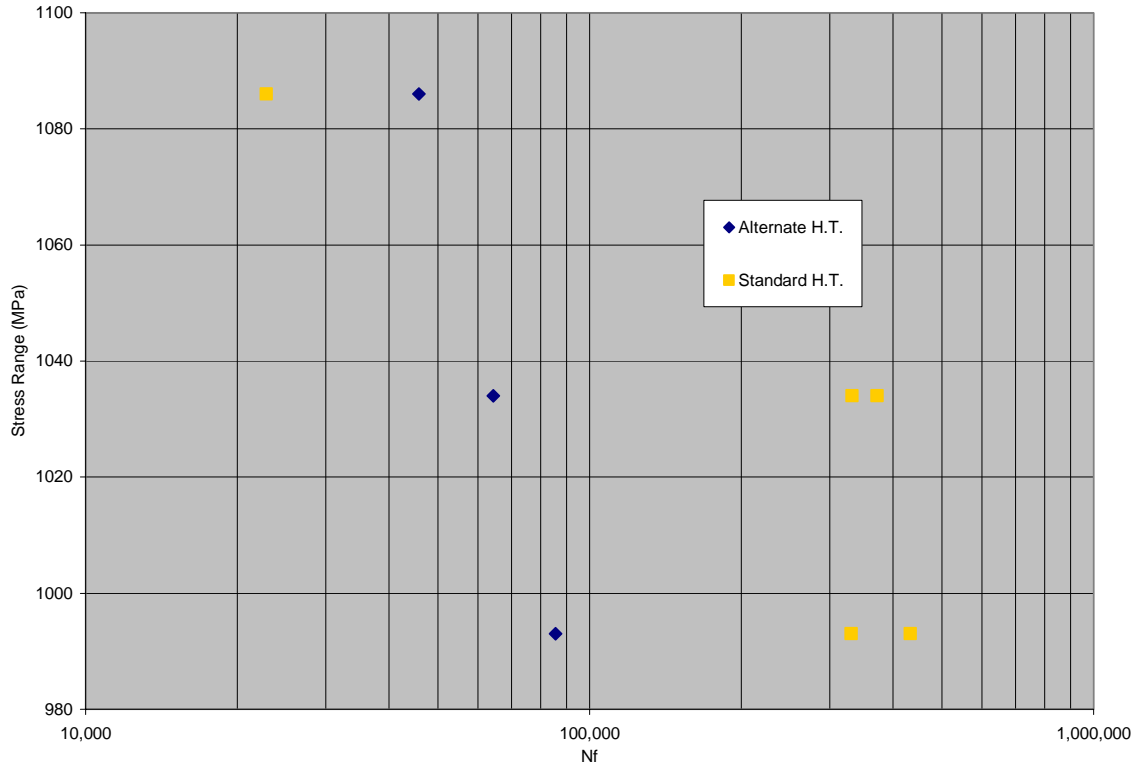


Figure 3-20: High cycle fatigue S-N curves for specimens tested at 538°C (1000°F) treatment exhibited the longer lifetimes at the low and middle stress ranges, but not at the highest stress range. This data would suggest that there is a change in crack initiation or propagation behavior at higher stresses that increases the fatigue lifetime of the alternate heat treatment compared to the standard heat treatment. Analysis of the fracture surfaces would evaluate this phenomenon.

It is also interesting to plot the S-N curves for the two different test temperatures for each heat treatment. Figure 3-22 contains a plot of the standard heat treatment at both 538°C (1000°F) and 649°C (1200°F). The lower test temperature exhibited longer fatigue lifetimes at both the high and the middle stress ranges. However, as the stress range went below about 1000 MPa, the higher test temperature had the superior lifetime.

The same type of relationship between test temperature, stress range, and cycles to failure was seen in the alternate heat treatment as well (Figure 3-23).

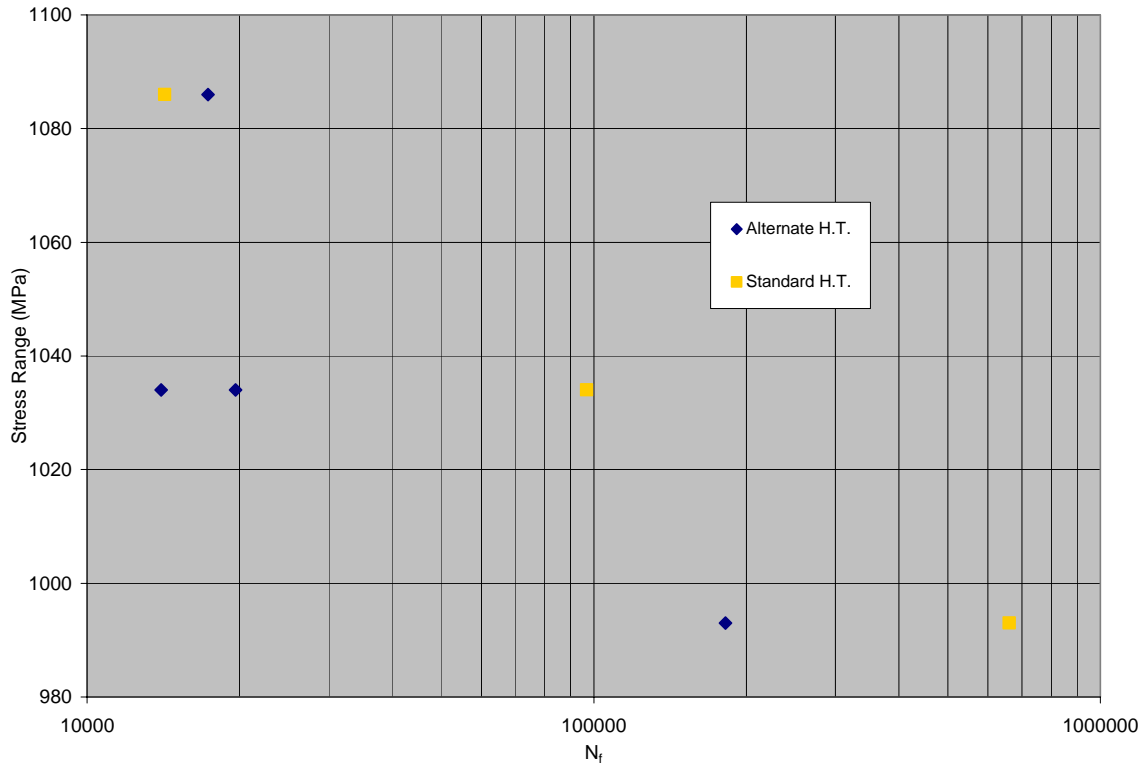


Figure 3-21: High cycle fatigue S-N curves for specimens tested at 649°C (1000°F)

### HCF fractography

After failure, the fractured surfaces were examined using both an optical microscope and a SEM. The fracture surfaces of both heat treatments looked similar when first examined visually. Optical pictures of fracture surfaces from standard and alternate heat treatments are contained in Figure 3-24. The crack initiation points on the fracture surfaces of the HCF samples could readily be determined. Circular regions of discoloration were present at the point of origin for all samples, due to being exposed to the oxidizing environment for longer times than the fast fracture area. The samples in Figure 3-24 are situated so that the crack origin is at the bottom of the picture.

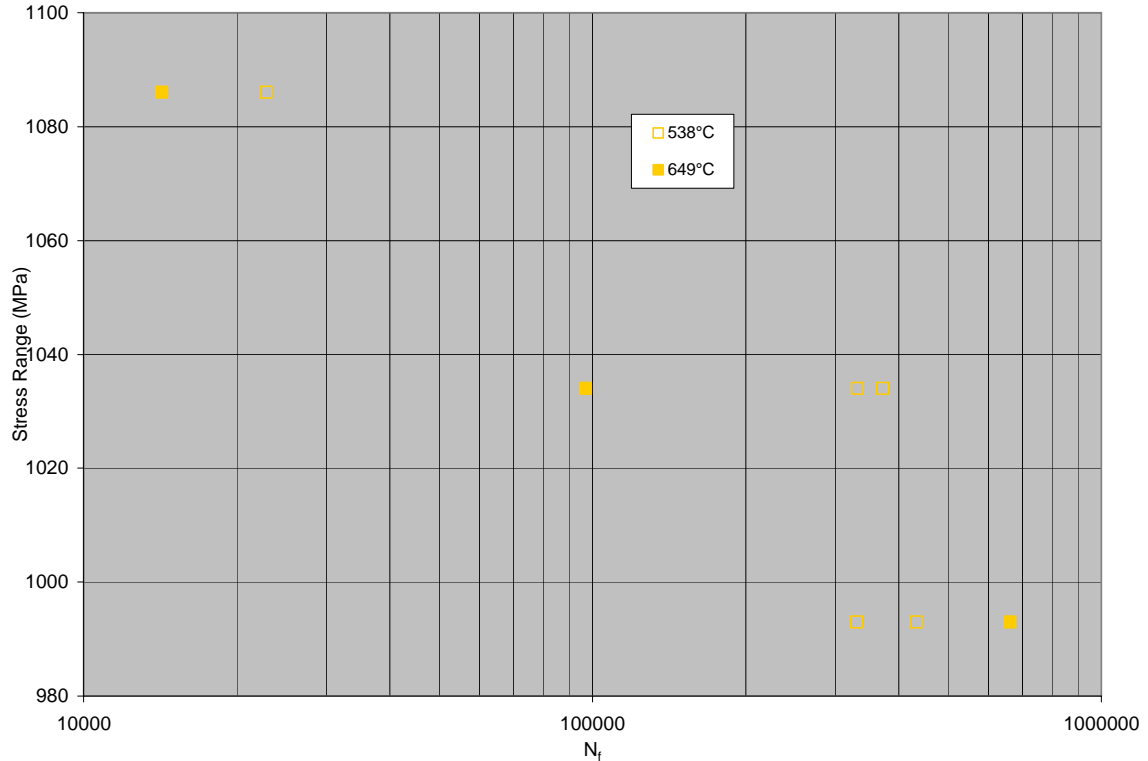


Figure 3-22: High cycle fatigue S-N curves for tests of the standard heat treatment at both 538°C (1000°F) and 649°C (1200°F)

Additionally, the region of slow crack growth was visible and ranged in shape from semi-elliptical to circular. This can be seen at the bottom of both of the optical pictures in Figure 3-24. The fatigue samples had small shear lips on the sides of the sample leading away from the initiation site.

After the fracture surfaces were examined optically, they were viewed on the SEM to determine the crack initiation points and the surface features at higher magnifications. The crack initiation points varied in appearance from sample to sample, but there were in general three different types of initiations: ceramic inclusions, primary carbides, and slip band cracking. None of the samples failed from cracks that initiated at PPB particles. Table 3-5 lists the fatigue lifetime and crack initiation type for each of the HCF specimens.

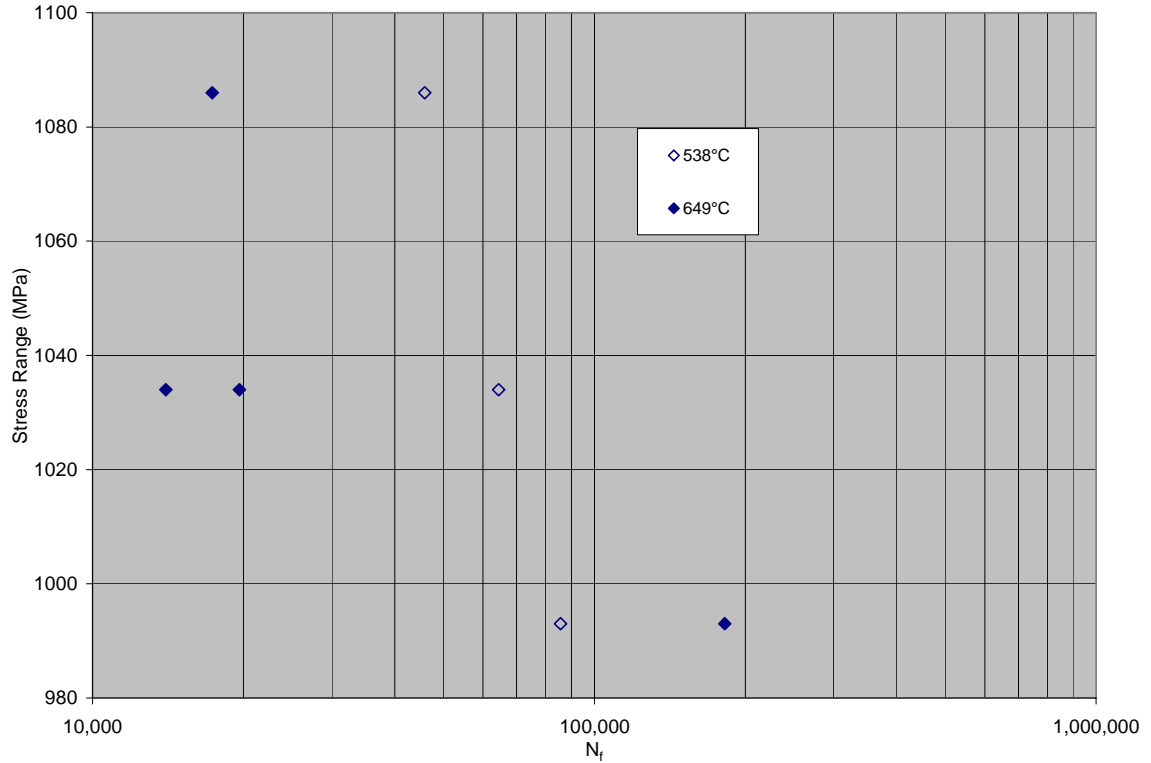


Figure 3-23: High cycle fatigue S-N curves for tests of the alternate heat treatment at 538°C (1000°F) and 649°C (1200°F)

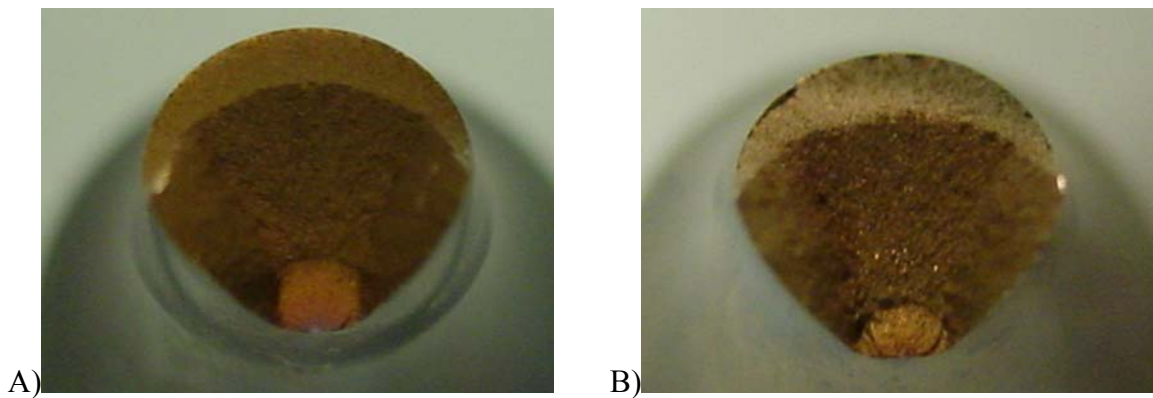


Figure 3-24: Optical micrographs of HCF fracture surfaces of samples tested at 649°C and 1086 MPa. A) Standard heat treatment. B) Alternate heat treatment.

Ceramic inclusions can be rather deleterious to the fatigue lives of Ni-base superalloys. They can be present in the form of either a large blocky inclusion or an agglomerate of small ceramic particles. Figure 3-25 shows a typical fracture initiation site at a ceramic inclusion. When viewed with backscattered electron imaging (BSE) in

Table 3-5: The HCF test results and crack initiation types

Sample	Temperature °C (°F)	$\sigma_a$ MPa (Ksi)	$N_f$	Initiation Type
Standard H.T.				
ULA5	538 (1000)	993 (144)	330,536	Ceramic( $Al_2O_3$ )
ULA15	538 (1000)	993 (144)	432,715	$Al_2O_3$
ULA11	538 (1000)	1034 (150)	331,895	$Al_2O_3$
ULA14	538 (1000)	1034 (150)	371,796	$Al_2O_3$
ULA16	538 (1000)	1086 (157.5)	22,828	$Al_2O_3$
ULA3	649 (1200)	993 (144)	661,396	$Al_2O_3$
ULA13	649 (1200)	1034 (150)	96,859	$Al_2O_3$
ULA10	649 (1200)	1086 (157.5)	14,244	TiC?
Alternate H.T.				
ULB7	538 (1000)	993 (144)	85,646	Crystallographic
ULB10	538 (1000)	1034 (150)	64,431	Crystallographic
ULB17	538 (1000)	1086 (157.5)	45,868	Unknown
ULB6	649 (1200)	993 (144)	181,975	Crystallographic
ULB13	649 (1200)	1034 (150)	13,994	$Al_2O_3$
ULB15	649 (1200)	1034 (150)	19,629	$\gamma$ grain
ULB9	649 (1200)	1086 (157.5)	17,324	$Al_2O_3$

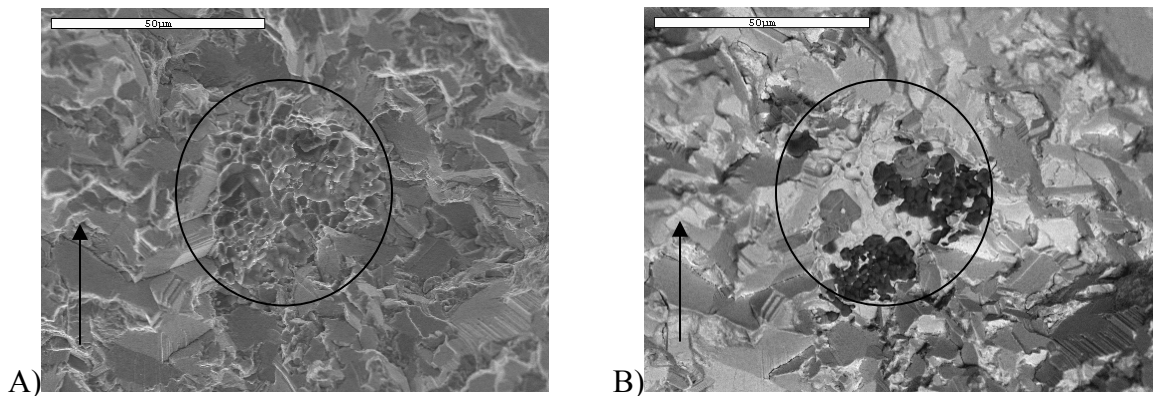


Figure 3-25: Ceramic agglomerate as initiation point in standard heat treatment sample tested at 538°C (1000°F) and a stress range of 1034 MPa (150 Ksi). A) Secondary electron imaging (SE). B) Backscattered electron imaging (BSE). EDS showed these to be  $Al_2O_3$  inclusions.

the SEM, these defects showed contrast due to atomic number difference between the particles and the matrix. This type of initiation was found mostly in the standard heat treatment at both test temperatures. Only two of the alternate heat treatment samples contained this type of initiation. These two specimens were tested at the middle and high stress ranges respectively at 649°C (1200°F). Energy dispersive spectrometry (EDS) was

performed on these agglomerates to reveal the approximate composition of these particles (Figure 3-26). The ceramic agglomerates were determined to be  $\text{Al}_2\text{O}_3$ . Some samples

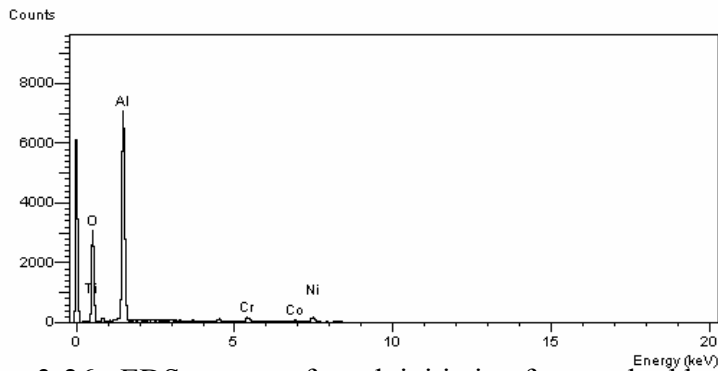


Figure 3-26: EDS spectra of crack initiation for standard heat treatment sample tested at  $538^\circ\text{C}$  and 1034 MPa

contained regions of the fracture initiation sites that were very round and were first thought to be PPB defects. However, upon closer inspection using backscattered electron imaging and EDS, it was revealed that these were also  $\text{Al}_2\text{O}_3$  inclusions. (Figure 3-27).

Once again, the phase identification was verified using BSE imaging and EDS.

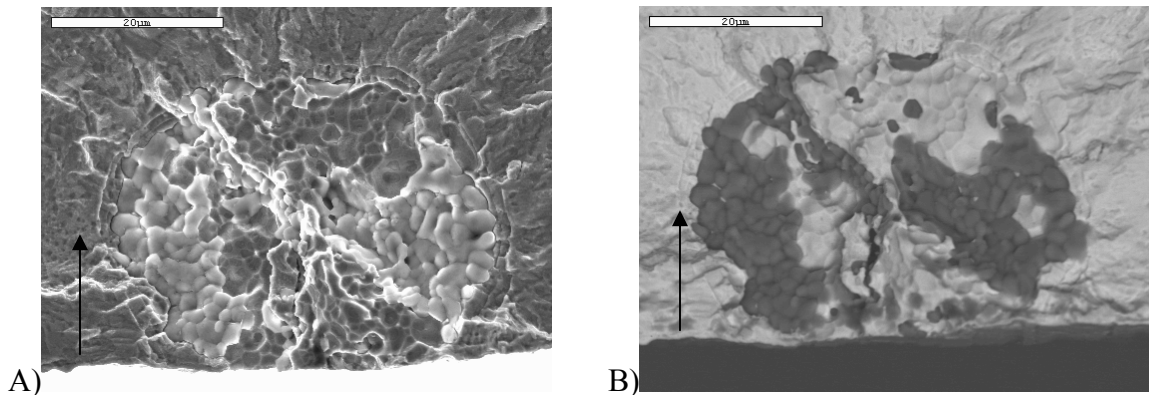


Figure 3-27: Ceramic agglomerate as initiation point for standard heat treatment sample tested at  $538^\circ\text{C}$  ( $1000^\circ\text{F}$ ) and a stress range of 1086 MPa (157.5 Ksi). A) SE imaging. B) BSE imaging. The ceramic agglomerate was identified as  $\text{Al}_2\text{O}_3$ .

The second main type of initiation site observed on the HCF fracture surfaces was associated with slip band cracking. It is characterized by faceted features that appear as brittle fracture on first analysis. Figure 3-28 shows fractographs typical of this type of failure. While slip band cracking served as the source of crack initiation in the alternate

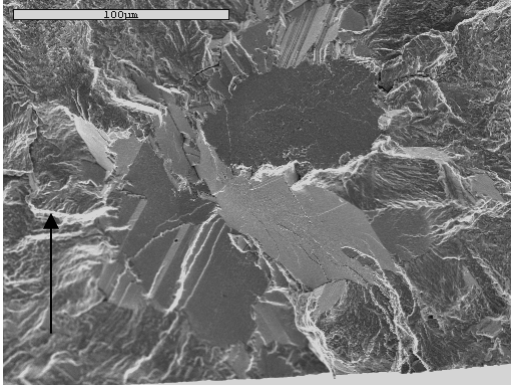


Figure 3-28: Slip band cracking as initiation point an alternate heat treatment sample tested at 538°C (1000°F) and 993 MPa (144 Ksi)

heat treatment and not in the standard heat treatment, they were present surrounding most of the standard heat treatment crack initiation points. The slip band cracking features were larger in the alternate heat treatment due to the larger grain size. Secondary cracks were evident leading radially away from these initiation sites.

The final type of initiation site encountered in this study was at a Ti-rich particle. The only sample to show this type of crack initiation was the standard heat treatment sample tested at 649°C (1200°F) and 1086 MPa (157.5 Ksi). This failure started at the specimen surface as seen in Figure 3-29. A crack was observed running through the

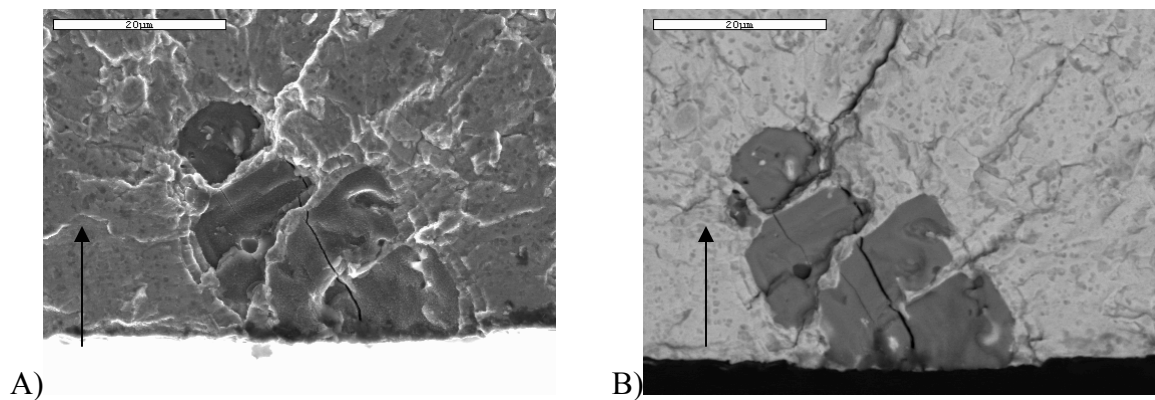


Figure 3-29: Primary carbide as the initiation type for the standard heat treatment sample tested at 649°C (1200°F) and 1086 MPa (157.5 Ksi). A) SE imaging. B) BSE imaging.

length of the particle, as well as many secondary cracks leading radially away from the origin. As can be seen, this precipitate appears darker than the matrix phase during BSE imaging, indicating a lower atomic number. EDS revealed that this particulate had large amounts of titanium. The EDS spectrum for this particle is in Figure 3-30. This particle maybe a ceramic inclusion or even a TiO particle; however, it is unclear at this point the exact nature of this particle.

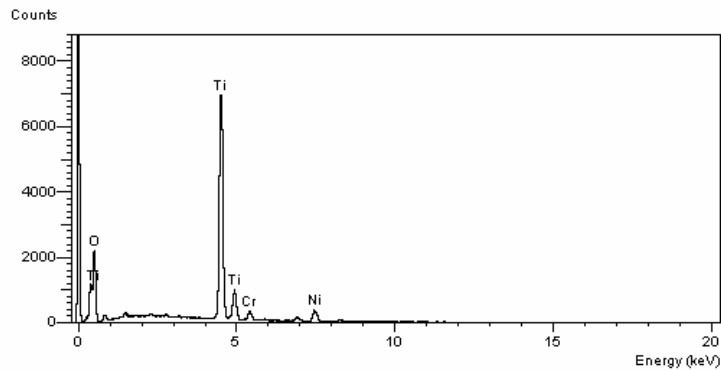


Figure 3-30: EDS spectra of Ti-rich particle as initiation point of standard heat treatment sample tested at 649°C and 1086 MPa

There were a few samples that it was not possible to determine the type of fracture initiation. Figure 3-31 shows a clear initiation feature for the alternate heat treatment sample tested at 649°C (1200°F) and 1034 MPa (150 Ksi). The BSE image did not reveal any noticeable atomic number difference nor did the EDS spectra conclusively determine what type of particle this was. In addition, the initiation type for the alternate heat treatment sample tested at 538°C (1000°F) and 1086 MPa (157.5 Ksi) could not be determined (Figure 3-32).

One final interesting note on the crack initiation points is that the samples which had internal crack initiation always contained slip band cracking in the area immediately surrounding the crack origin, whereas those that failed at the surface did not have any slip

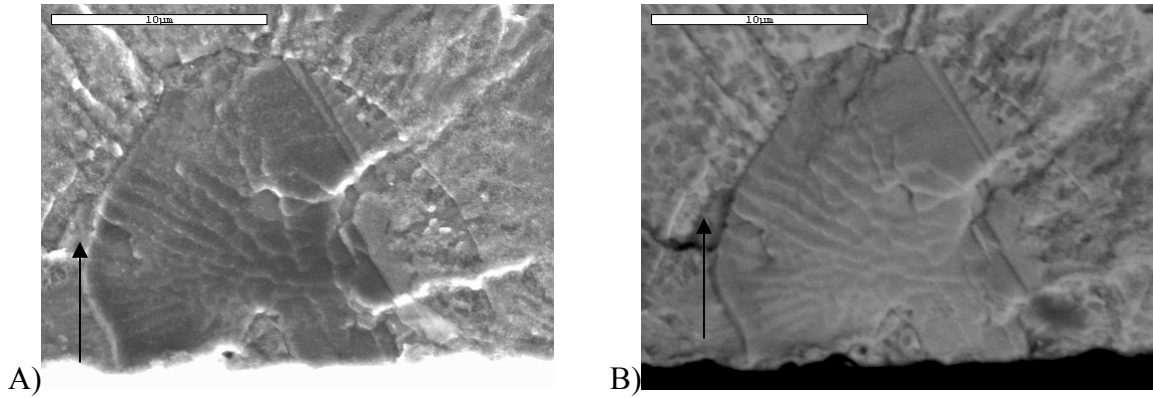


Figure 3-31: Unknown initiation type for alternate heat treatment sample tested at 649°C (1200°F) and 1034 MPa (150 Ksi). A) SE imaging. B) BSE imaging.

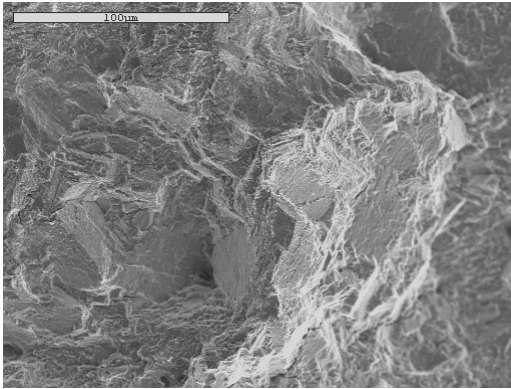


Figure 3-32: Crack origin for alternate heat treatment sample tested at 538°C (1000°F) and 1086 MPa (157.5 Ksi)

band cracking around the defect. This held true for both heat treatments and can be seen in the micrographs in Figure 3-33.

In addition to examination of the fracture initiation types, the fracture surface features along the propagation path were examined in the SEM to determine the crack propagation path. Micrographs were taken at three different locations along the fracture path. Inside the region of discoloration for each sample, the fracture surface appeared flat and relatively featureless as can be seen by representative micrographs in Figure 3-34. This portion of the fracture surface has the same appearance for all test conditions for both heat treatments. In some areas, fatigue striations were present. Unfortunately, these

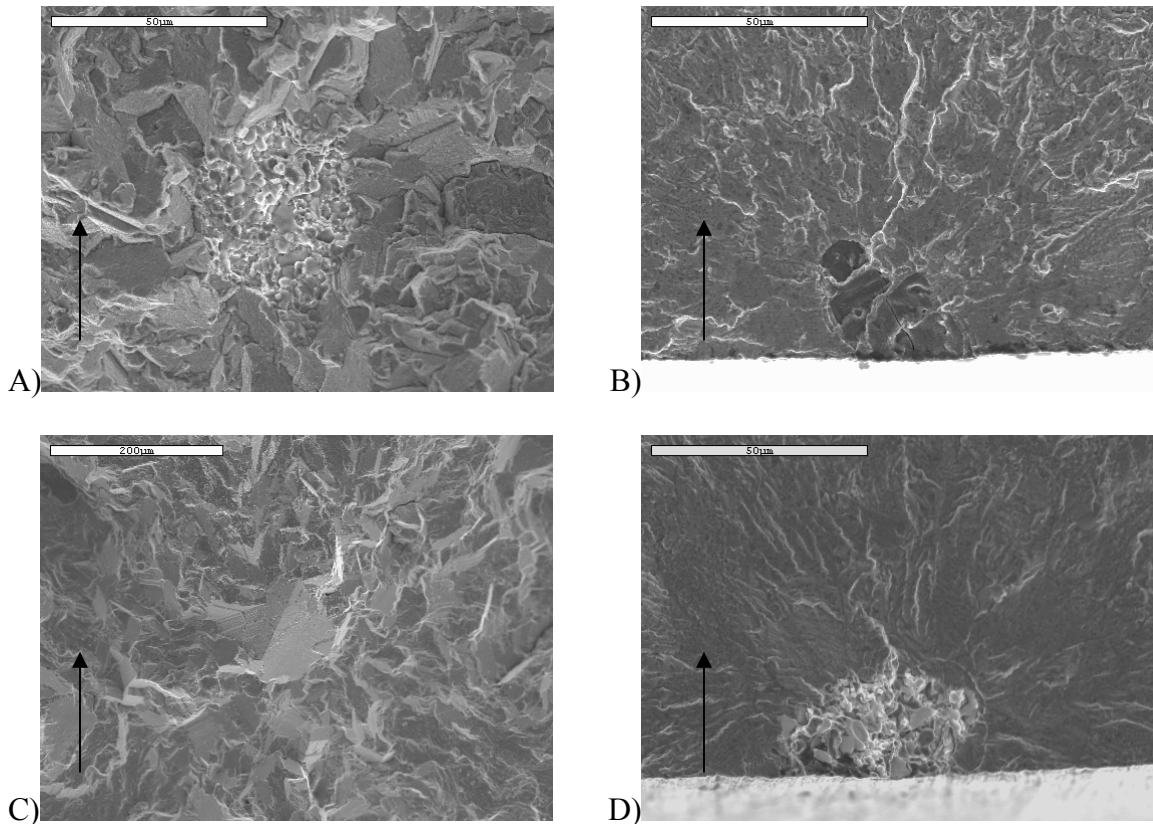


Figure 3-33: Initial crack region of fatigue samples. A) Standard heat treatment that failed internally. B) Standard heat treatment that failed at the surface. C) Alternate heat treatment that failed internally. D) Alternate heat treatment that failed at the surface.

areas are not distinct enough to measure the striation spacing and eventually approximate the fracture toughness of the two heat treatments.

The region immediately after the discolored area displayed a noticeable change in microstructure. The crack path became much more tortuous at this point. The surfaces transitioned from being flat and featureless to being undulating and more indicative of ductile fracture. Figure 3-35 is a representative fractograph from this area of the specimen surface. Both heat treatments resulted in similar features indicative of interparticle or intergranular failure. These interparticle/intergranular features were present throughout the remainder of the fracture surfaces up to the point of fast fracture.

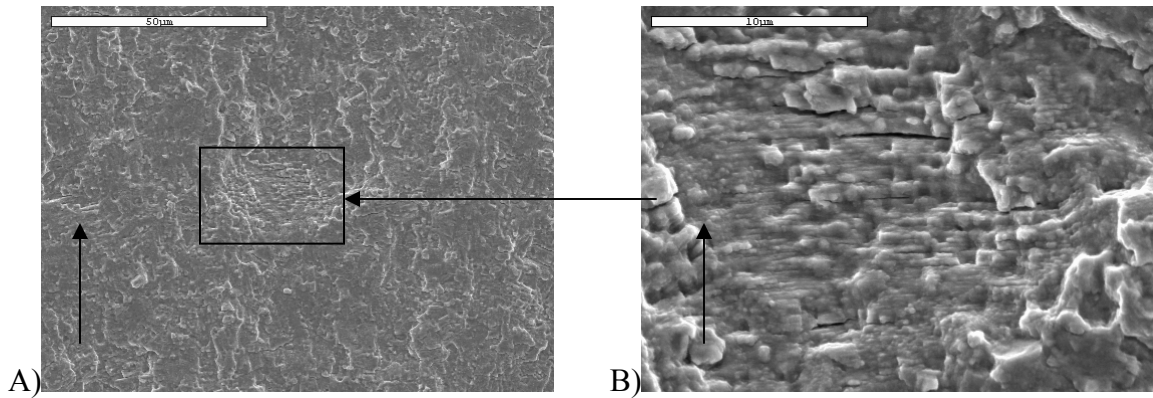


Figure 3-34: Fracture surface near initiation in standard heat treatment sample tested at 538°C (1000°F) and a stress range of 1034 MPa (150 Ksi). A) 570X. B) 2850X.

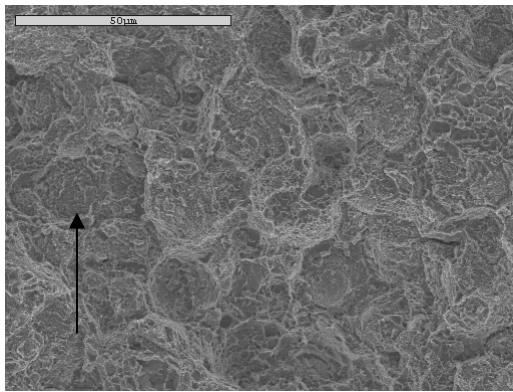


Figure 3-35: Fracture surface of standard heat treatment tested at 538°C (1000°F) and a stress range of 1086 MPa (157.5 Ksi) outside of discolored region

However, there appears to be a slight size difference for the features between the two heat treatments. The alternate heat treatment surfaces appear to have larger features that are more varied in size than the standard heat treatment surfaces. These differences can be seen in Figure 3-36. The individual test conditions, however, do not appear to have an effect on the surface features of the propagation path within each heat treatment.

In order to complete a detailed study of the fracture mechanics during the fatigue testing of the two heat treatments, the fracture surface features were measured from SEM micrographs of all of the surfaces. The initial area of crack growth (Stage I) before the

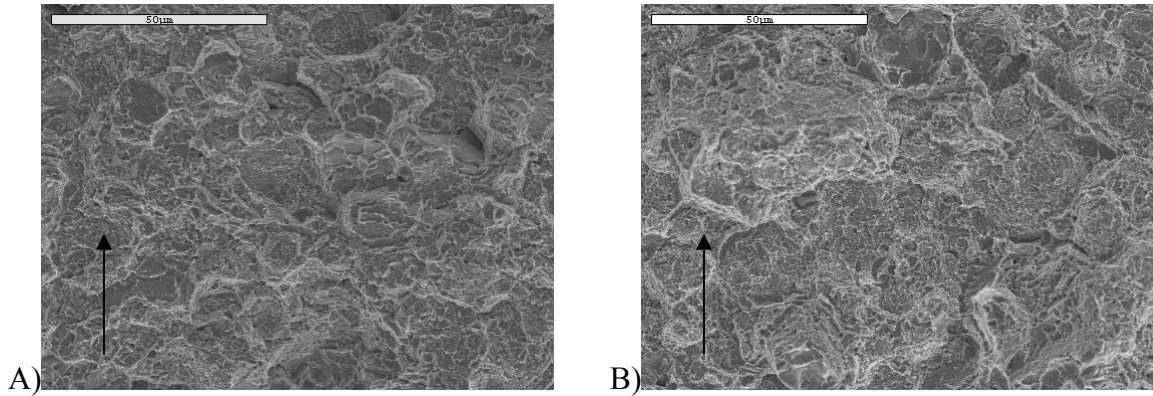


Figure 3-36: Fracture surfaces far from origin of samples tested at 538°C (1000°F) and 993 MPa (144 Ksi). A) Standard heat treatment. B) Alternate heat treatment.

transition to transgranular crack growth was measured in addition to the area of total crack growth before fast fracture. These measurements can be found in Table 3-6. In

Table 3-6: Area of crack growth regions on the HCF fracture surfaces

Sample	Temp (°C)	$\Delta\sigma$ (MPa)	$\sigma_{\max}$ (MPa)	$N_f$	$A_i$ ( $\mu\text{m}^2$ )	$A_f$ ( $\text{mm}^2$ )
Standard Heat Treatment						
ULA5	538	993	1103	330536	22000	1.3
ULA15	538	993	1103	432715	26000	1.5
ULA14	538	1034	1149	371796	14000	1.4
ULA11	538	1034	1149	331896	15000	1.4
ULA16	538	1086	1207	22829	5000	1.3
ULA3	649	993	1109	661397	22000	2.5
ULA13	649	1034	1149	96859	15000	2.2
ULA10	649	1086	1207	14245	7000	1.7
Alternate Heat Treatment						
ULB7	538	993	1103	85647	41000	1.5
ULB10	538	1034	1149	64432	16000	1.4
ULB6	649	993	1103	181979	56000	2.0
ULB15	649	1034	1149	19629	13000	1.4
ULB13	649	1034	1149	13994	16000	1.4
ULB9	649	1086	1207	17324	11000	1.4

this table,  $A_i$  refers to the area of the initial crack before transgranular crack growth, and  $A_f$  refers to the final area of slow crack growth just prior to overload and fast fracture.

These two areas are plotted versus stress range in Figures 3-37 and 3-38. The alternate

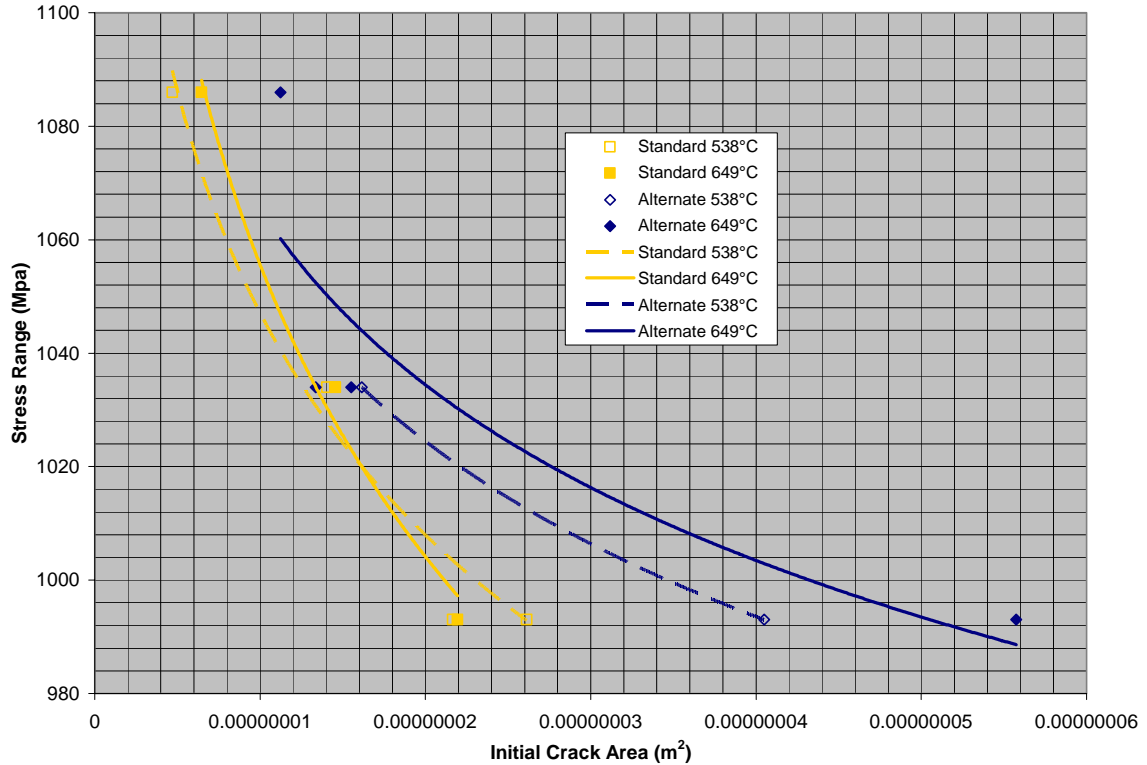


Figure 3-37: Initial crack area versus stress range for the high cycle fatigue specimens. The plot shows that for both test temperatures and all stress ranges, the alternate heat treatment has a larger area of slow crack growth before the transition to transgranular crack growth. The final crack size increases with decreasing stress range for both heat treatments at both test temperatures. If the specimen fractures at the max load of the fatigue cycle, then it would follow that all of the specimens fractured at the same critical stress intensity value ( $K_C$ ) for each test temperature. A smaller stress range would require a larger crack before the stress intensity factor reaches  $K_C$ . Additionally, the two heat treatments resulted in similar areas for the slow crack growth region at 538°C. However, at 649°C, the standard heat treatment had a significantly larger final area of slow crack growth.

After careful analysis of the fracture surfaces was complete, the fractured ends of the specimens were sectioned, mounted longitudinally, polished, and etched to reveal the

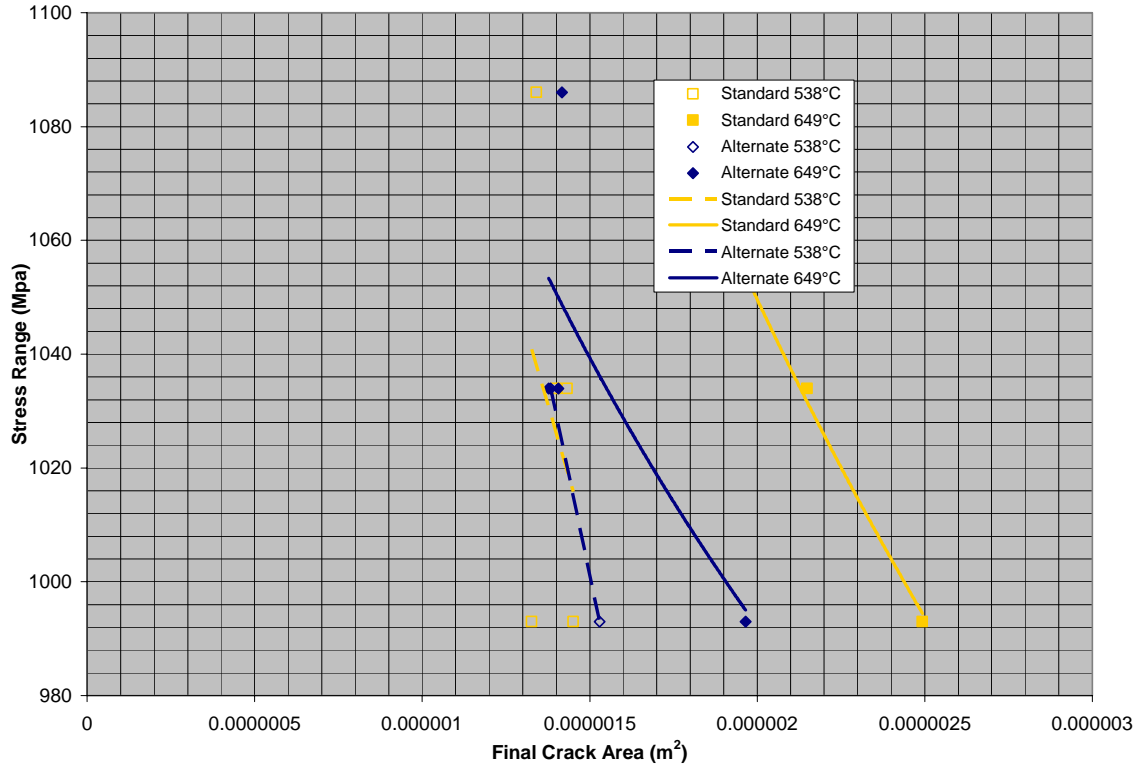


Figure 3-38: Final crack area versus stress range for the high cycle fatigue specimens path of the secondary cracks through the microstructure. The samples from both heat treatments tested at both test temperatures and a stress ranges of 993 MPa (144 Ksi) exhibited secondary cracks at the boundary between the primary and secondary  $\gamma'$  and the  $\gamma$  matrix. This can be seen in Figure 3-39. The arrows in these pictures indicate the tensile direction. The alternate heat treatment samples exhibited secondary cracks that formed in lines through the grains, while the standard heat treatment sample's cracks appeared to be more randomly placed.

At both test temperatures at the stress range of 1034 MPa (150 Ksi), samples from the two heat treatments had different secondary crack morphologies. These can be seen in Figure 3-40. The standard heat treatment samples still exhibited secondary cracks at the primary and secondary  $\gamma'$  precipitates; however, now these cracks appear to line up in

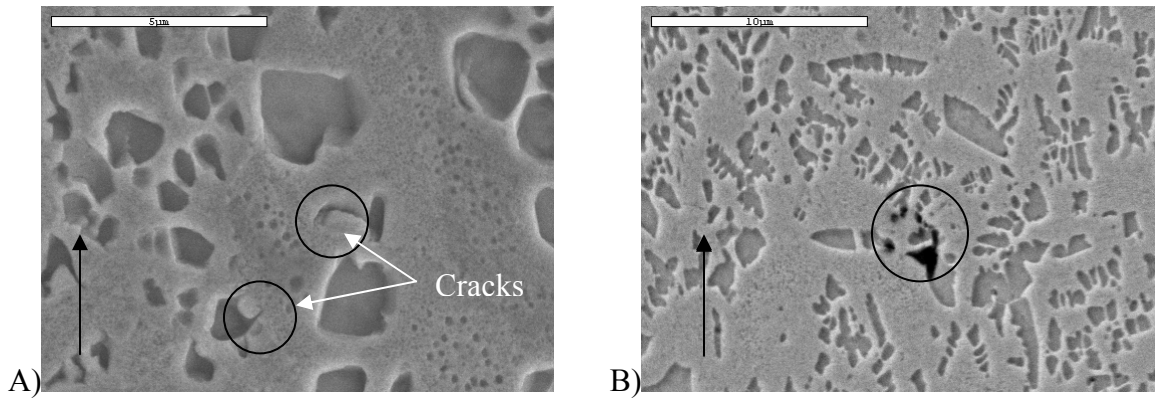


Figure 3-39: Secondary cracks at primary and secondary  $\gamma'$  precipitates in samples tested at 538°C and 993 MPa. A) Standard heat treatment. B) Alternate heat treatment. The arrows show the tensile direction.

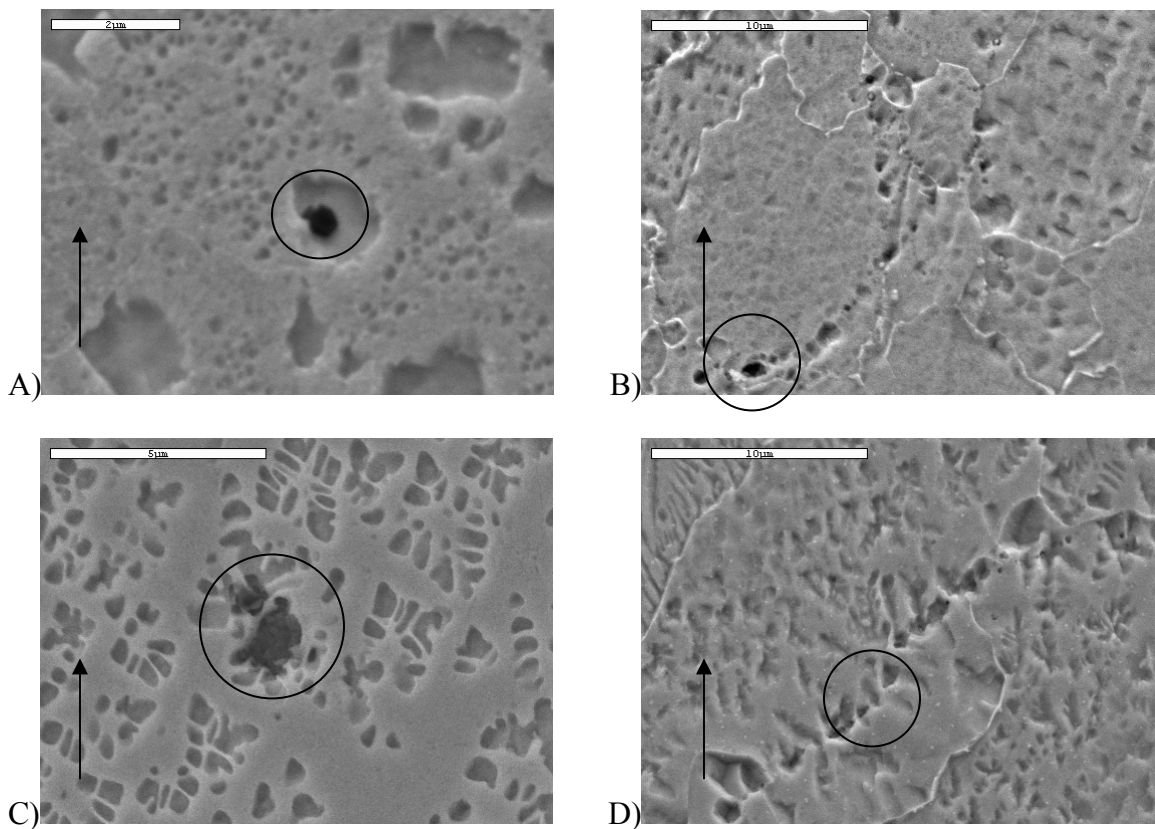


Figure 3-40: Secondary cracks in fatigue samples tested at 1034 MPa. A) Standard heat treatment at 538°C. B) Standard heat treatment at 538°C again. C) Alternate heat treatment at 538°C. D) Alternate heat treatment at 649°C.

a curved manner through the grains. In contrast, the alternate heat treatment samples exhibited the same behavior as in the low stress range. The secondary cracks occurred at

both primary and secondary  $\gamma'$  precipitates, but they did not align in rounded shapes. Instead, they appeared to form in straight lines through the grains.

Finally, at the highest strain range of 1086 MPa (157.5 Ksi) samples from both heat treatments exhibited secondary cracks at TiC and  $\text{Al}_2\text{O}_3$  particles. As with the other stress ranges, there were also cracks at the primary and secondary  $\gamma'$  precipitates. There were not many long cracks present. Some of these propagated along the grain boundaries and some formed rounded shapes within the grains. Both heat treatments exhibited both of these types of secondary cracks. All of these features can be seen below in Figure 3-41.

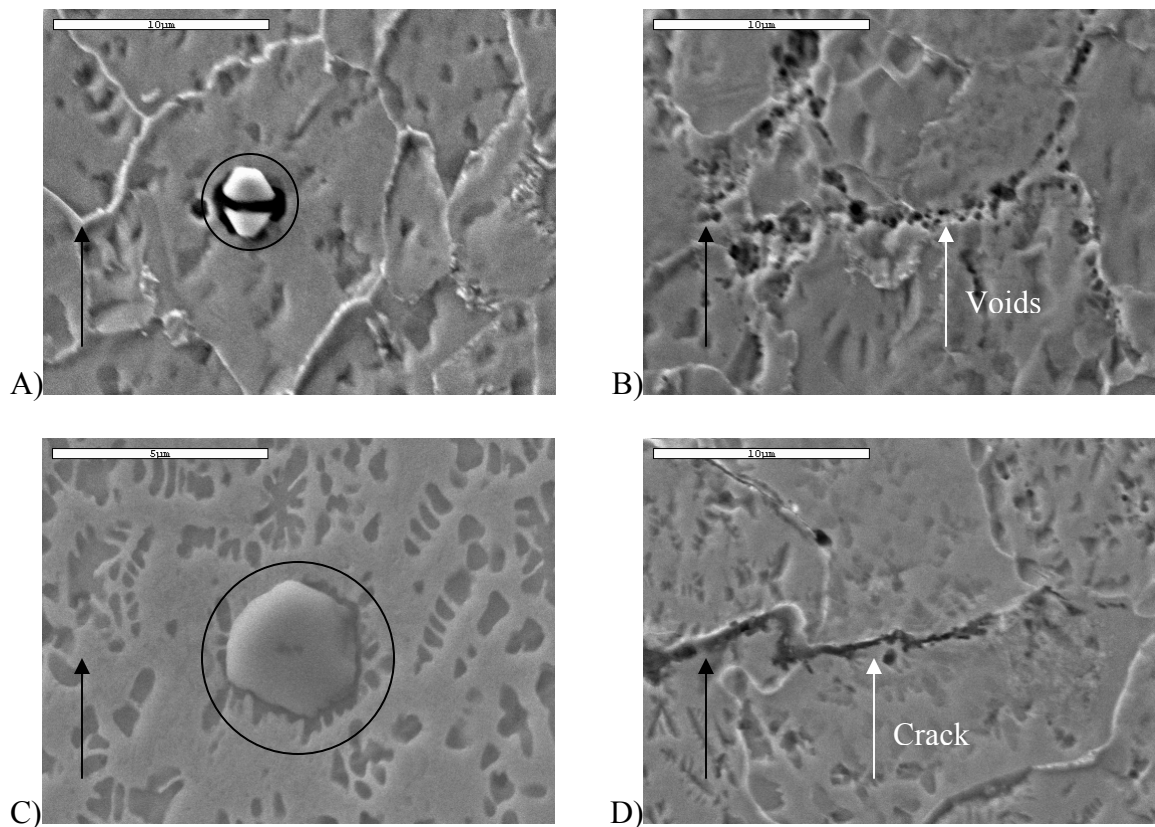


Figure 3-41: Fatigue samples tested at 538°C and 1086 MPa showing secondary cracks. A) At a TiC in standard heat treatment. B) Along grain boundaries in standard heat treatment. C) At a TiC in alternate heat treatment. D) Transgranularly in alternate heat treatment.

## Tensile Testing

The tensile testing was performed at room temperature, 538°C (1000°F), 649°C (1200°F), and 760°C (1400°F) on an Instron servo-hydraulic test frame. Alloys designed as turbine disk materials need excellent tensile strength at elevated temperatures. An improvement in one mechanical property can have an adverse impact on the other mechanical properties. Therefore, it was necessary to determine if the alternate heat treatment would not result in too large of a debit in tensile strength.

## Tensile results

Table 3-7 shows the results of the tensile testing performed in this study. The extensometer slipped on some of the samples after yielding. As a result, the data for percent strain at UTS was not available. In addition, the data for samples UCA1 and

Table 3-7: Tensile test results

Sample	Temp. (°C)	Modulus (GPa)	Yield Strength (MPa)	UTS (MPa)	Strength at failure (MPa)	Total Elongation (%)
Standard Heat Treatment						
UCA4	RT	228	1225	1710	1675	23.3
UCA23	RT	234	1241	1696	1669	21.1
UCA24	538	172	1078	1510	1464	23.3
UCA5	649	181	1087	1471	1324	23.0
UCA7	649	156	1103	1476	1351	22.4
UCA8	760	174	1018	1180	1103	11.1
UCA10	760	171	1069	1145	1076	10.7
Alternate Heat Treatment						
UCB4	RT	224	990	1524	1517	27.6
UCB21	RT	225	1066	1568	1558	25.3
UCB2	649	212	880	1367	1296	29.4
UCB5	649	185	887	1395	1317	26.0
UCB3	760	112	827	1123	1034	17.1
UCB8	760	165	780	1103	993	17.4

UCB1 that appear in the original matrix in Table 2-6 was lost due to a software error during testing. There were a few extra samples that were machined with the creep geometry. To make up for the lost tensile samples, these two extra samples were tested at

room temperature. Also, sample UCA24 was tested at 538°C. The standard heat treatment had greater yield stress, ultimate tensile strengths, and failure strengths at all conditions compared to the alternate heat treatment. However, the standard heat treatment tensile samples displayed a corresponding deficit in strain at maximum load and elongation at failure. All of the elevated temperature tensile tests for both conditions had a slight decrease in strength before failure, denoting that the samples experienced some amount of necking prior to failure. The room temperature tests had a smaller decrease in strength. The alternate heat treatment samples basically showed no evidence of necking. The standard heat treatment specimens showed very minimal amounts of necking. Figure 3-42 shows the decrease in yield strength with temperature for both heat treatments. As can be seen, the yield strength at 649°C (1200°F) is less than that at room

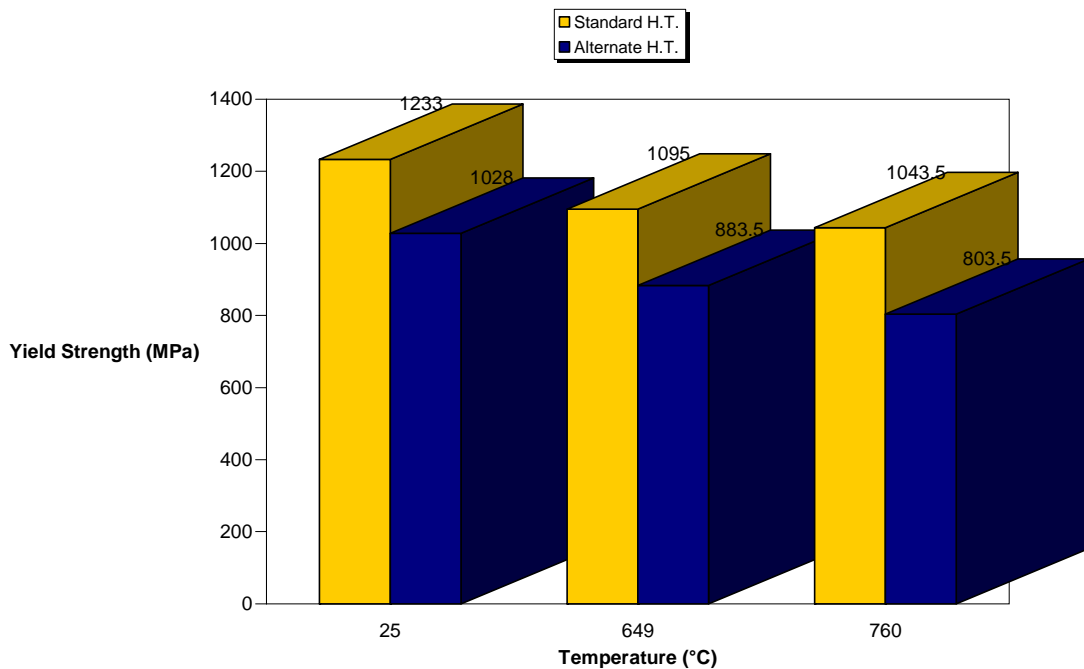


Figure 3-42: Yield strength vs. temperature for both heat treatments

temperature. As the temperature is increased to 760°C (1400°F), the yield strength decreased even further. The elongation stayed constant up to 649°C (1200°F) (Figure 3-43). However, there was a precipitous drop in elongation at 760°C (1400°F).

Representative stress-strain curves are shown for each heat treatment for a sample tested at 760°C (1400°C) in Figure 3-44 and 3-45.

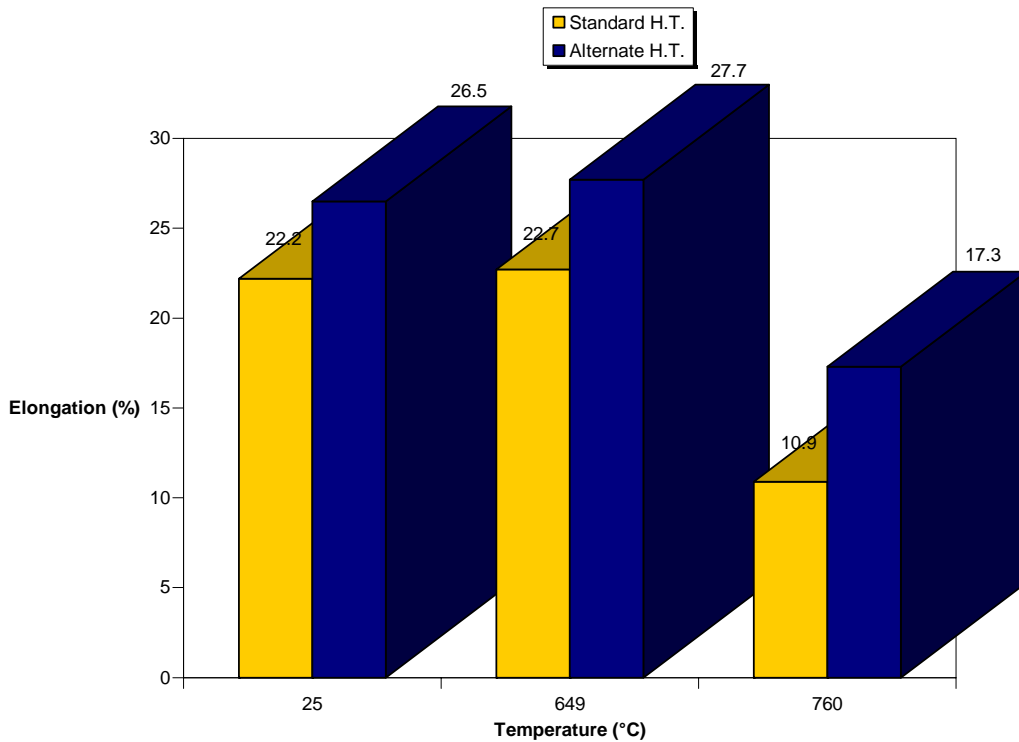


Figure 3-43: Elongation at failure vs. temperature for both heat treatments

### Tensile fractography

Fractured tensile samples from each test condition were analyzed on the SEM to determine crack initiation type, if possible, and crack propagation paths. Figure 3-46 shows the crack initiation region for one sample at each test temperature for the standard heat treatment. The samples tested at room temperature and 649°C (1200°F) both show a

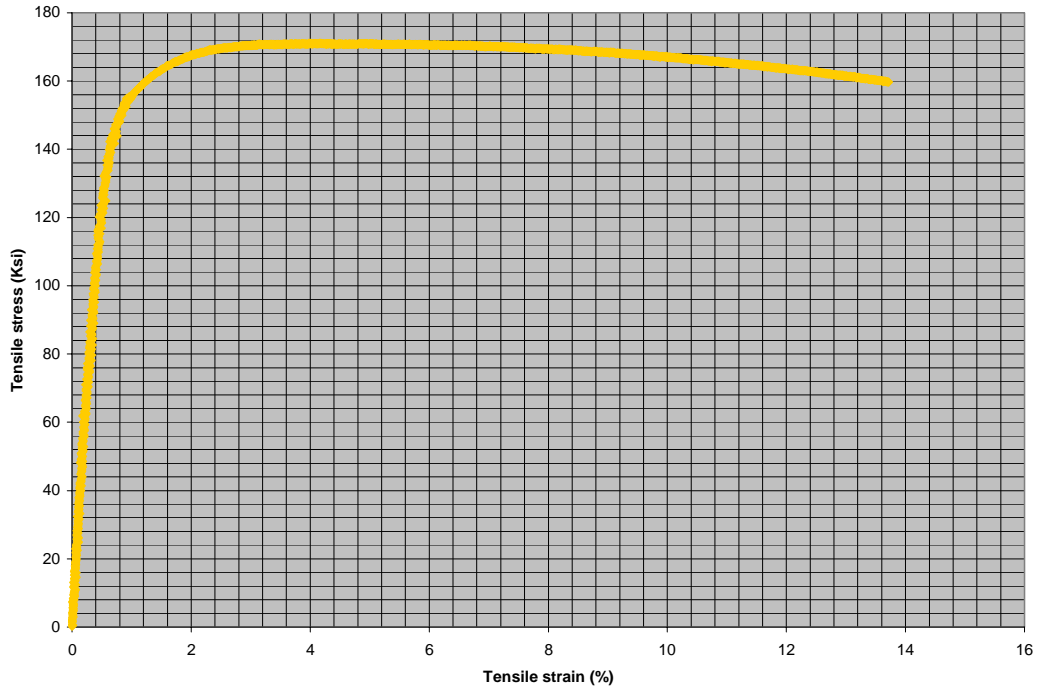


Figure 3-44: Tensile stress-strain curve for standard heat treatment sample tested at 1400°F

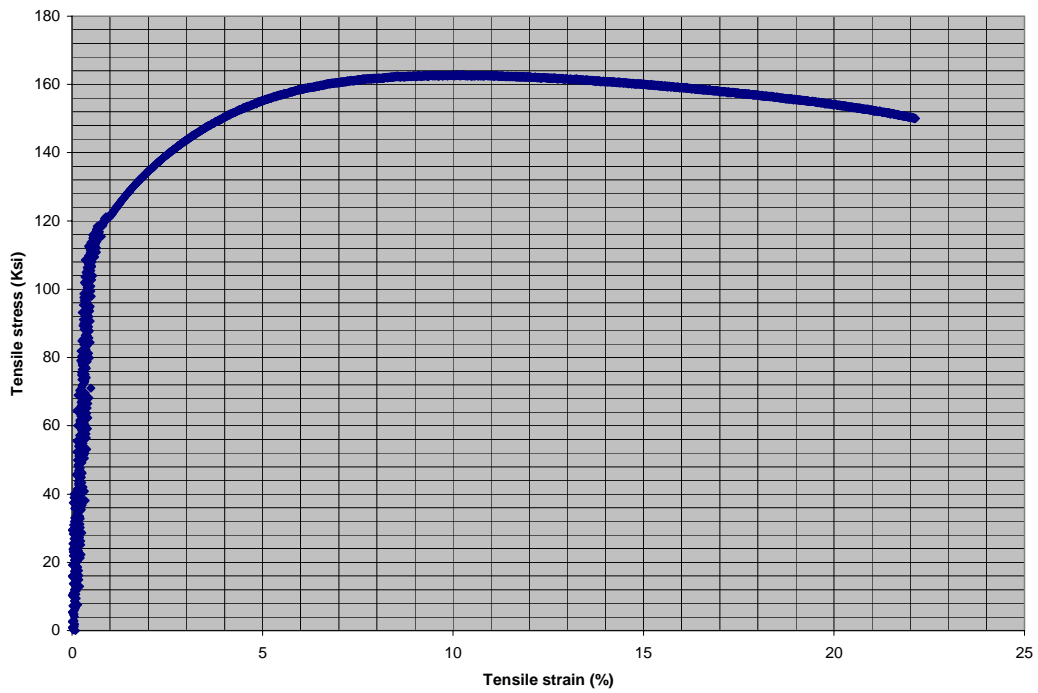


Figure 3-45: Tensile stress-strain curve for alternate heat treatment sample tested at 1400°F

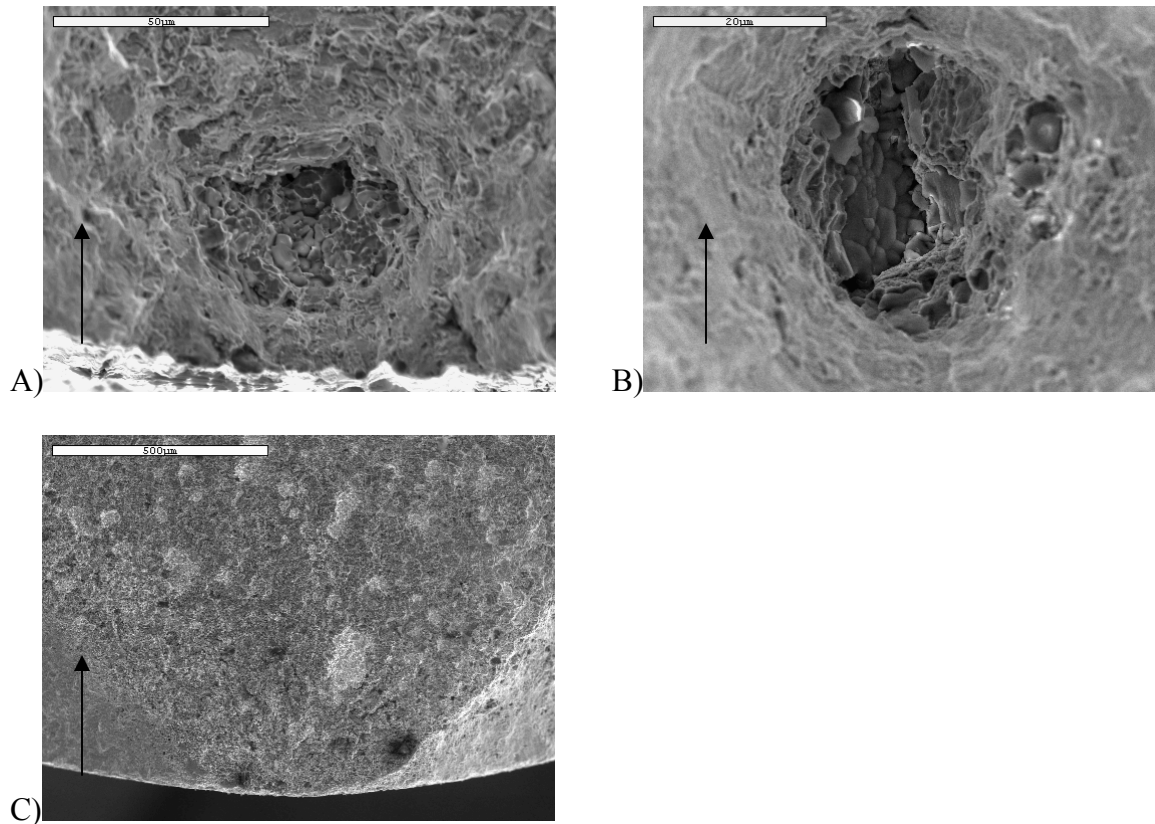


Figure 3-46: Crack initiation region in standard heat treatment tensile samples. A) Tested at room temperature. B) Tested at 649°C (1200°F). C) Tested at 760°C (1400°F).

distinct crack initiation point. EDS analysis of this initiation did not have enough signal to determine the composition of the initiation since the defect was well below the fracture surface. However, the fracture surfaces of these samples were similar to those of the HCF fracture surfaces. Therefore, it is thought that this initiation is due to an agglomerate of  $\text{Al}_2\text{O}_3$ . On the other hand, the sample tested at 760°C (1400°F) did not show a unique point of origin. Crack propagation features pointed back to a region near the surface; however, it was not possible to determine the type of crack origin on this sample.

While it was easy to locate the crack origin on the alternate heat treatment tensile samples, it was not possible to determine the type of fracture origin for any of these

samples. Micrographs of the origin area for each of the tensile test temperatures are shown in Figure 3-47. The samples tested at room temperature and 760°C (1400°F)

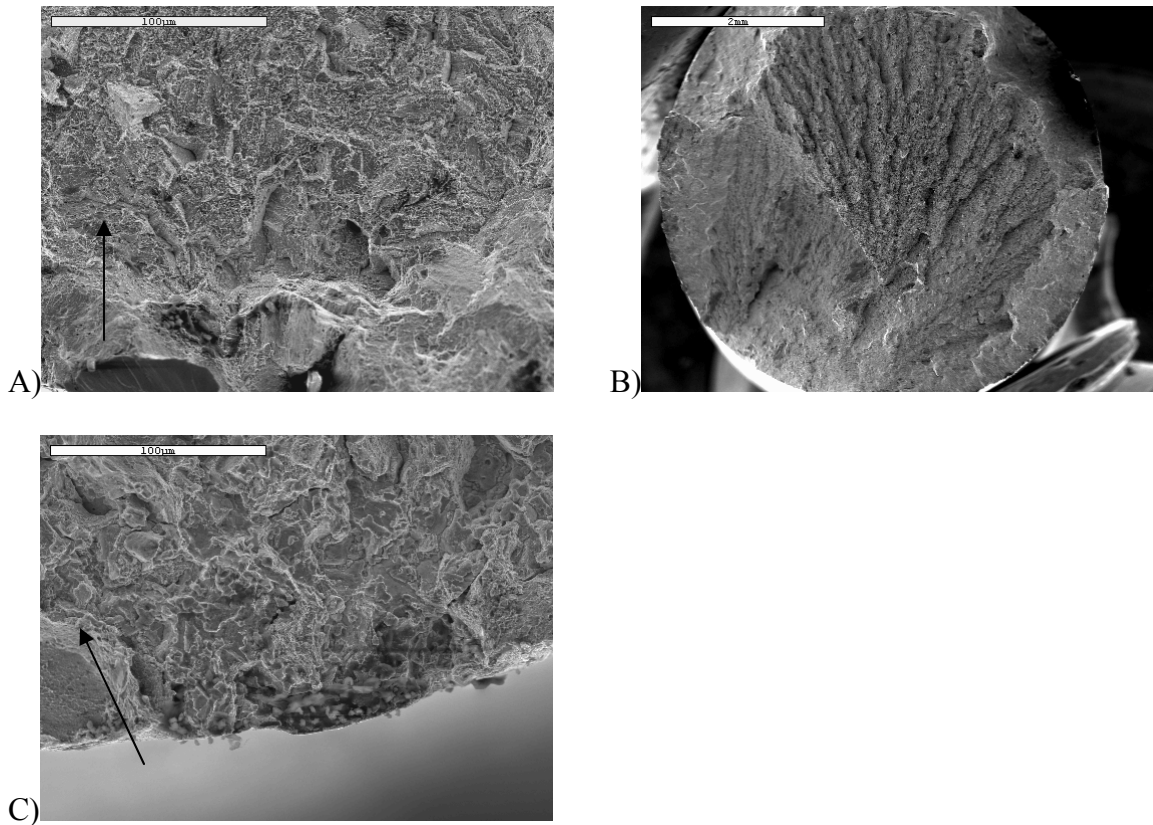


Figure 3-47: Crack initiation region in alternate heat treatment tensile samples treatment. A) Room temperature. B) 649°C (1200°F). C) 760°C (1400°F).

failed from the propagation of a crack that began near the surface. One of the samples that were tested at 649°C (1200°F) (Figure 3-47b) actually had at least two distinct origin points. The surface had a fan-shape appearance indicating that multiple cracks were propagating through the sample at failure. In Figure 3-47b, one clear initiation point can be seen in the lower left corner of the specimen, with another directly in the middle of the sample. Secondary cracks can be seen propagating radially from both of these initiation points.

### **Creep Testing**

Creep testing was carried out at several different temperature and load conditions on both the standard and the alternate heat treatments. While fatigue properties are more critical for turbine disk materials, it is still important to maintain good creep strength especially in the rim (outer edge connected to the turbine blades). However, generally an increase in tensile or fatigue properties for a material is accompanied by a corresponding decrease in creep properties. This creep test matrix was designed to insure that any improvements in tensile or fatigue properties through the alternate heat treatment would not result in a deficit in creep rupture lifetime.

### **Creep results**

The results of the creep testing performed in this study are contained in Table 3-8. For the standard heat treatment, the condition that produced the longest lifetime was at 677°C (1250°F) and 793 MPa (115 Ksi). The shortest creep rupture lifetime for this heat treatment was found at 677°C (1250°F) and 1034 MPa (150 Ksi). In contrast, the test conditions that produced the longest creep lifetimes for the alternate heat treatment were 732°C (1350°F) and 483 MPa (70 Ksi) and the shortest lifetimes were 677°C (1250°F) and 1034 MPa (150 Ksi). It is also evident that the alternate heat treatment produced a much more ductile material than the standard heat treatment, as the elongation was greater at all test conditions for the alternate heat treatment. It should also be noted that generally longer creep lifetimes corresponded to lower elongation values for both heat treatments.

The creep frames additionally recorded time to 0.1%, 0.2%, 0.5%, 1.0%, 2.0%, and 5.0% creep for each of the tests. This data was compiled to produce Larson-Miller (L-M) plots for each of these times as well as for time to creep rupture. L-M curves show

Table 3-8: The creep results

Sample	Temp. (°C)	Stress (MPa)	T <sub>f</sub> (Hours)	Elongation %
Standard Heat Treatment				
UCA12	677	1034	11.1	6.3
UCA16	677	1034	17.1	7.0
UCA9	677	793	396.8	5.9
UCA11	677	793	362.7	7.2
UCA13	704	689	143.9	8.5
UCA18	704	689	128.9	10.8
UCA20	732	483	134.5	4.9
UCA21	732	483	157.9	7.1
UCA19	760	483	25.7	3.6
UCA22	760	483	34.4	7.6
Alternate Heat Treatment				
UCB11	677	1034	5.8	13.0
UCB18	677	1034	4.8	14.7
UCB7	677	793	288.4	10.9
UCB10	677	793	233.4	16.0
UCB6	704	689	148.0	17.5
UCB12	704	689	220.9	14.0
UCB19	732	483	452.1	7.4
UCB20	732	483	559.4	9.1
UCB14	760	483	112.0	9.7
UCB23	760	483	126.2	11.0

stress on a log stress scale versus the L-M parameter, P, on a traditional scale. This parameter is calculated using the equation:

$$P = T_a * [\text{Log} (t_r + 20)]$$

where  $T_a$  is the absolute test temperature and  $t_r$  is the time to the percent creep for that particular plot. In such a plot, the higher temperature and longer lifetime tests will be at greater values of the P parameter. This provides a succinct way of comparing creep lifetimes for different microstructures of the same alloy or for different alloys altogether. Data points with larger P values represent longer lifetimes and greater temperatures. Therefore, given the same stress condition and test temperature, points that lie to the right on the plot have better creep properties than those that lie to the left of the graph.

The Larson-Miller plot for rupture is shown below in Figure 3-48. The alternate heat treatment has the best lifetime for creep at 704°C (1300°F) and 689 MPa (100 Ksi), 732°C (1350°F) and 483 MPa (70 Ksi), and 760°C (1400°F) and 483 MPa (70 Ksi) for all strain values. These are the points that lie on the far right of the graph. However, at the lower temperature and higher stress conditions the standard heat treatment outperforms the alternate heat treatment.

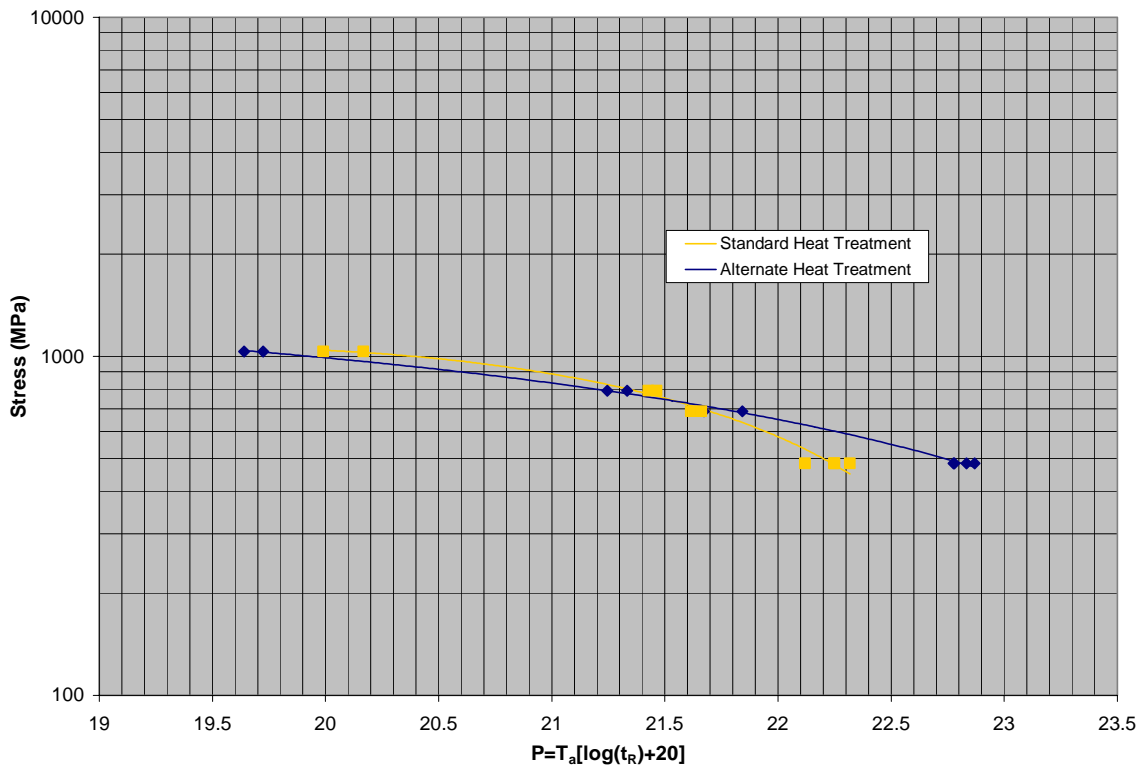


Figure 3-48: Larson-Miller plot for creep rupture in Alloy 720LI

### Creep fractography

To fully understand the effect of the two microstructures on the creep properties of this alloy, it was necessary to examine the fracture surfaces of creep samples from each test condition for each heat treatment. Therefore, the surfaces were examined on the SEM. If possible, failure origins were noted and analyzed. Additionally, the

microstructure of the propagating crack path was inspected to determine the propagation mode. In general, the creep fracture surfaces were not as straightforward as the fatigue or tensile sample surfaces. Discoloration due to oxidation was again used to locate the origin region for most of these samples; however, it was not as easy to determine the type of origin for the creep samples as it was with the fatigue samples.

Due to the difficulty in determining the fracture origin type for the creep samples, more attention was paid to the fracture surface features during propagation. There was a distinct change in the types of features present for some of the standard heat treatment specimens from near the origin to points further from the origin (Figure 3-49). Near the origin, the scale of the fracture features is on the order of 5  $\mu\text{m}$ . However, further down the fracture path, these features eventually reach a scale of about 20-30  $\mu\text{m}$  in diameter signaling a change in crack propagation path. The change in feature size is not nearly as dramatic for the alternate heat treatment samples tested at 704°C (1300°F) and 689 MPa (100 Ksi) (Figure 3-50). There still does appear to be a slight change at these conditions, but the transition is not as obvious as at the higher stress conditions. Finally, as the test

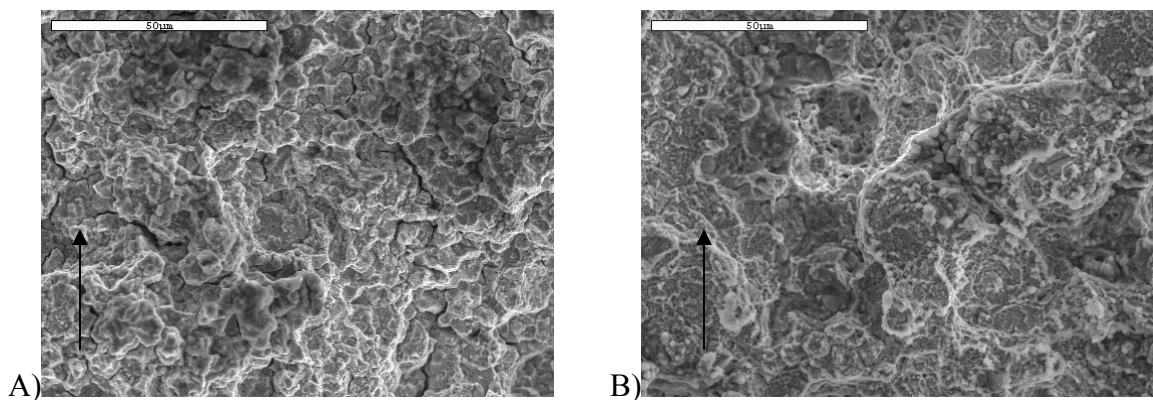


Figure 3-49: Fast fracture propagation path for standard heat treatment sample tested at 677°C (1250°F) and 1034 MPa (150 Ksi). A) Near the initiation. B) In the fast propagation region.

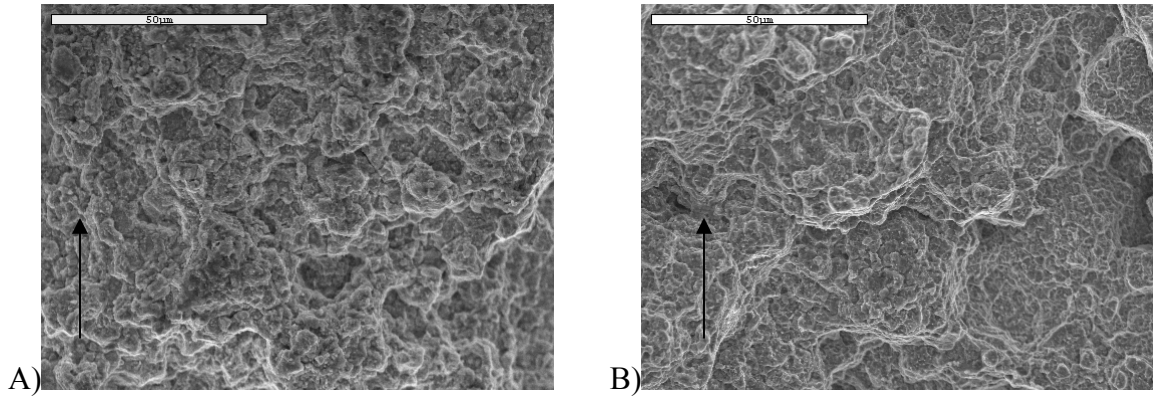


Figure 3-50: Fast fracture propagation path for alternate heat treatment at 704°C (1300°F) and 689MPa (100Ksi). A) Near the initiation. B) In the fast propagation region.

temperature rose to 760°C (1400°F) and the load was reduced to 483 MPa (70 Ksi), there was no change at all in feature size between these two regions. Figure 3-51 shows one of the samples tested at these conditions.

Once examination of the fracture surfaces was completed, the fractured ends of the specimens were sectioned approximately 1 cm (0.39 in) from the fracture. The sectioned ends were mounted longitudinally, polished, and etched to examine the path of secondary

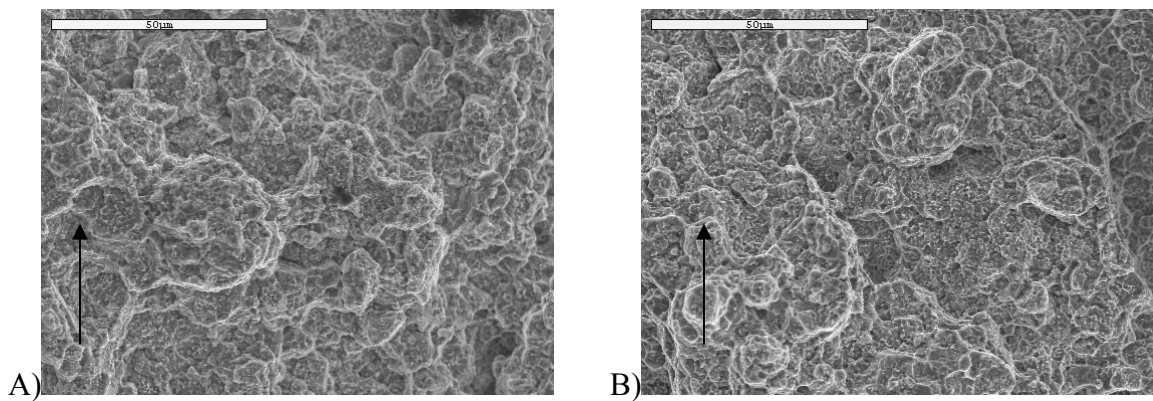


Figure 3-51: Standard heat treatment sample tested at 760°C (1400°F) and 483 MPa (70 Ksi) showing fast fracture propagation path.. A) Near the initiation B) During the fast propagation region.

cracks through the microstructure. This proved to be a useful way to view both the initiation and propagation behavior of cracks in the creep tests. The cross-sectioned

samples not only served to catalogue differences between the two heat treatments but also between test conditions within the same heat treatment. One sample was examined for each heat treatment at each test condition.

For both heat treatments, the lowest temperature, 677°C (1250°F), and the greatest stress state, 1034 MPa (150 Ksi), resulted in few secondary cracks propagating through the microstructure near the fracture surface. The standard heat treatment sample exhibited some voids that formed at grain boundary triple points (Figure 3-52). Samples from both heat treatments exhibited cracks that propagated transgranularly (Figure 3-53). Although the large crack in the standard heat treatment micrograph appears to follow the grain boundary on the left side of the picture, it clearly propagates through the grain on the right side of the micrograph. The alternate heat treatment sample contained at least one crack that propagated from the fracture surface down through the sample along the grain boundaries (Figure 3-54). This micrograph also shows the propensity for microvoids to form within the grains at this test condition.

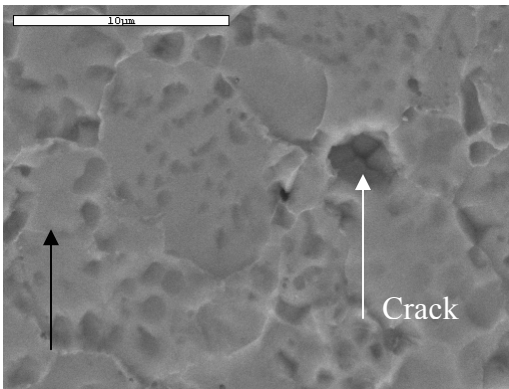


Figure 3-52: Standard heat treatment sample tested at 677°C and 1034 MPa with crack initiation at a grain boundary triple point

In contrast, all the samples tested at 704°C (1300°F) and higher exhibited many secondary cracks in the microstructure (Figure 3-55). These cracks propagate mostly

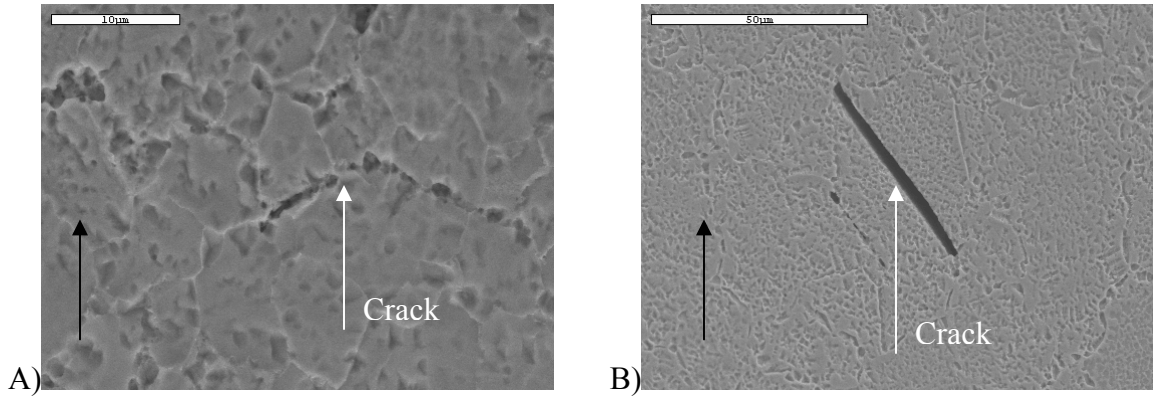


Figure 3-53: Transgranular cracking during fatigue testing in samples tested at 677°C and 1034 MPa. A) Standard heat treatment. B) Alternate heat treatment.

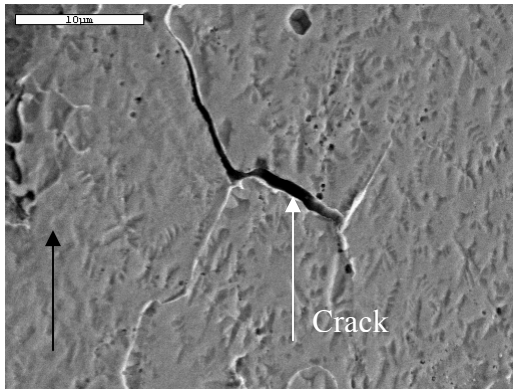


Figure 3-54: Large secondary crack in alternate heat treatment sample tested at 677°C and 1034 MPa

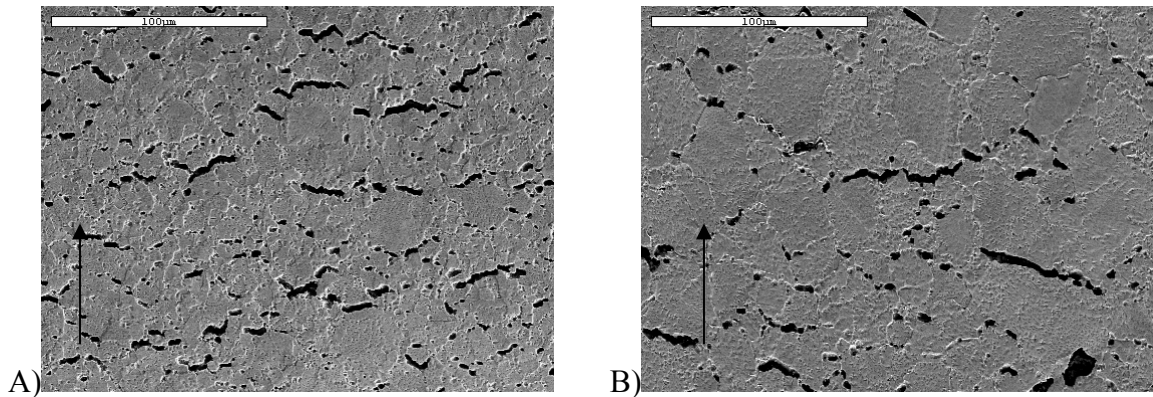


Figure 3-55: Secondary cracks in high temperature creep tests. A) Standard heat treatment sample tested at 760°C and 483 MPa. B) Alternate heat treatment sample tested at 732°C and 483 MPa.

along the grain boundaries. They appear to nucleate at primary  $\gamma'$  precipitates, with adjacent cracks linking up during testing. Figure 3-56a shows cracks initiating at primary  $\gamma'$  precipitates, while Figure 3-56b shows small voids forming along the grain boundaries. Crack initiation within the  $\gamma$  grains is not observed at these higher temperature and lower stress test conditions for either heat treatment.

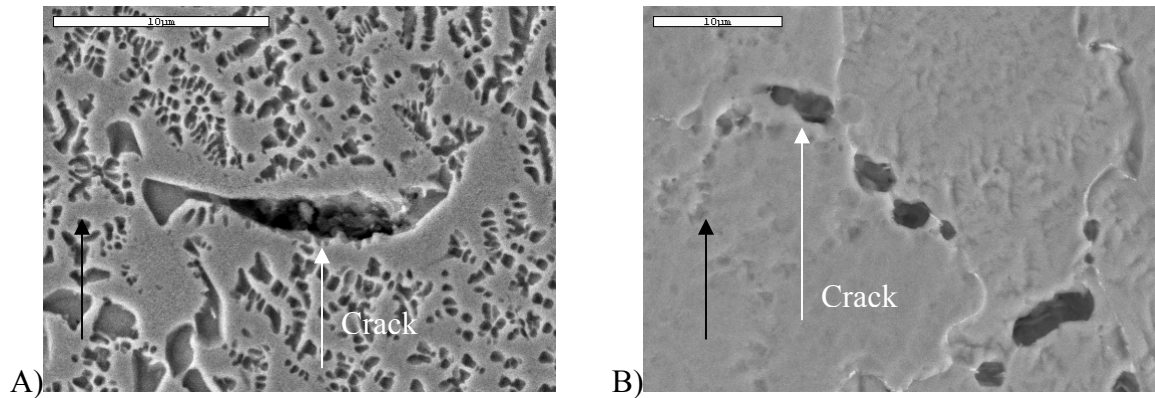


Figure 3-56: Grain boundary crack initiation in alternate heat treatment creep samples.  
 A) Tested at 704°C and 689 MPa. B) Tested at 760°C and 483 MPa.

The only test condition that exhibited different microstructural behavior for the two heat treatments was 677°C (1250°F) and 793 MPa (115 Ksi). The standard heat treatment sample exhibited many long cracks similar to the higher temperature tests, while the alternate heat treatment sample had a limited number of secondary cracks similar the highest stress condition. These differences can be seen in Figure 3-57. The cracks in the standard heat treatment sample propagate entirely along the grain boundaries, with very few void initiation sites found within the grains. In contrast, cracks in the alternate heat treatment sample showed equal preference for initiating at grain boundary triple points as well as within the grains at dendritic-shaped  $\gamma'$  precipitates. However, the grain boundary voids were much larger than those within the grains.

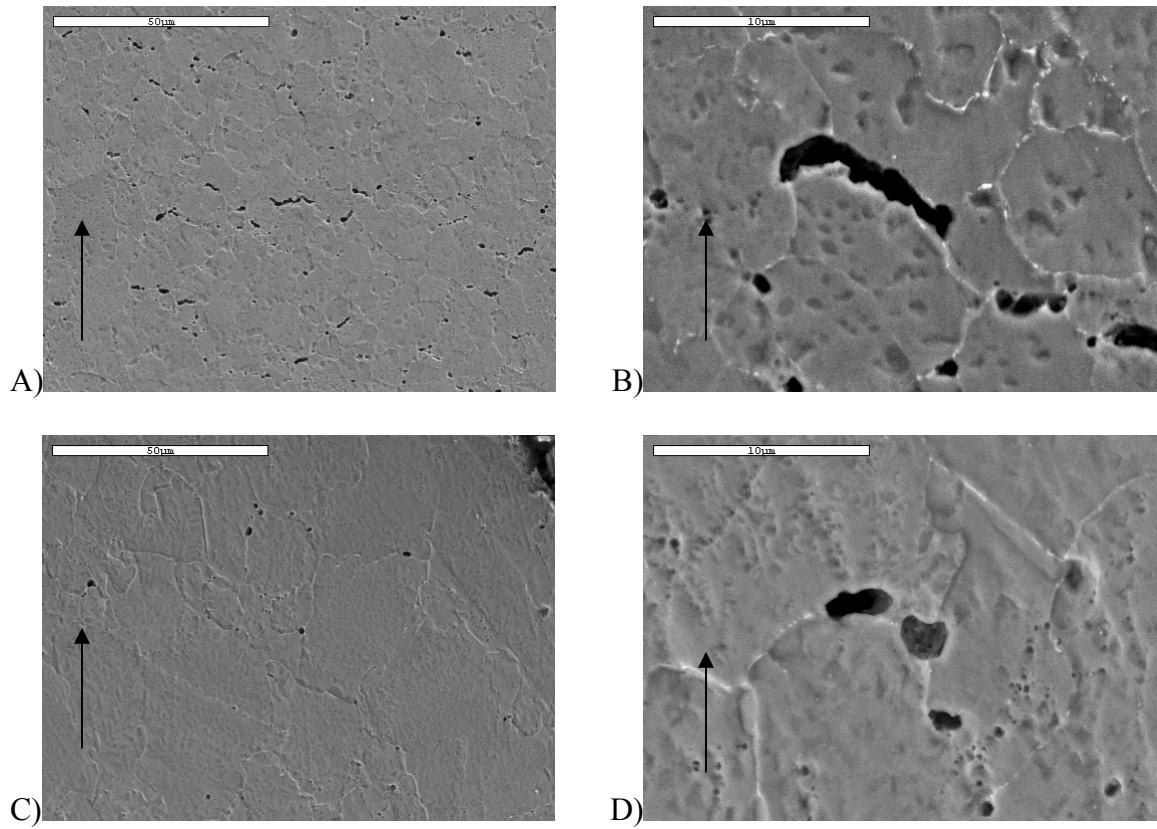


Figure 3-57: Secondary cracks in creep samples tested at 677°C (1250°F) and 793 MPa (115 Ksi). A) Standard heat treatment at 570X. B) Standard heat treatment at 2850X. C) Alternate heat treatment at 570X. D) Alternate heat treatment at 2850X.

## CHAPTER 4 DISCUSSION

### **Microstructure**

#### **Heat Treatment**

This study investigated the impact of an alternate, supersolvus solution heat treatment on the microstructure and mechanical properties of powder processed Alloy 720LI. This alternate heat treatment was compared to a standard, subsolvus heat treatment. The alternate heat treatment was designed to produce a microstructure with large, dendritic-shaped  $\gamma'$  precipitates in larger  $\gamma$  grains than in the standard heat treatment. In a study by Pratt & Whitney, a similar microstructure dramatically improved the fracture toughness and fatigue properties of a single crystal alloy. The investigation examined the role of various heat treatment parameters on the precipitation of  $\gamma'$  in this alloy.

The first parameter examined was the solution heat treatment temperature. It was necessary for the solution temperature to be above the  $\gamma'$  solvus to completely dissolve all of the  $\gamma'$  in the alloy into the  $\gamma$  matrix. However, if the solution temperature was too high, the resulting microstructure after slow cooling was more irregular in shape. Additionally, the greater heat treatment temperature would require a longer total time for the entire heat treatment. This would result in an unnecessary increase in cost to heat treat actual parts. A solution temperature of 1175°C (2147°F) was chosen for the alternate heat treatment in this study.

The cooling rate through the  $\gamma'$  solvus temperature had the single biggest impact on the resulting size and shape of the secondary  $\gamma'$  precipitates. Too fast of a cooling rate resulted in smaller, more cuboidal  $\gamma'$  precipitates. (Figure 3-1B). Conversely, when the cooling rate was too slow, the  $\gamma'$  precipitates formed large, but irregular shaped dendrites. (Figure 3-2a) An intermediate cooling rate of approximately  $3.0^{\circ}\text{C}/\text{min}$  ( $5.4^{\circ}\text{F}/\text{min}$ ) produced a regular array of dendritic-shaped  $\gamma'$  precipitates as desired.

The final temperature before fan air cooling also affected the size of the secondary  $\gamma'$  precipitates. Both final temperatures examined,  $1020^{\circ}\text{C}$  ( $1868^{\circ}\text{F}$ ) and  $1075^{\circ}\text{C}$  ( $1967^{\circ}\text{F}$ ), produced dendritic-shaped  $\gamma'$  when given the proper cooling rate. However, as can be seen in Figure 3-3, the lower temperature produced larger, more fully developed dendrites than the higher temperature. Therefore,  $1020^{\circ}\text{C}$  ( $1868^{\circ}\text{F}$ ) was chosen as the final temperature for the heat treatment.

The microstructural variations with heat treatment parameters agree with those seen in literature [70]. At fast cooling rates, more undercooling is achieved and the precipitate nucleation density is high. The resulting precipitates are constrained in their growth and cannot develop into dendrites, but remain more cuboidal. However, at lower cooling rates, the number of nucleation sites decreases. The precipitates begin as spheroids. The spheres can grow into cubes and eventually dendrites through diffusion controlled growth. In a near zero misfit alloy like Alloy 720LI, the precipitates eventually lose coherency with the  $\gamma$  matrix during the dendritic growth. The growth direction during this process is along the  $\langle 111 \rangle$  directions of the original  $\gamma'$  cubes.

While this chosen heat treatment worked well for most of the master powder blend's (MPBs) used in this study, three MPBs required a slightly lower soak temperature

in order to develop the alternate microstructure. There do not appear to be any consistent differences in chemistry from one MPB to the next that would explain this difference. Differential thermal analysis (DTA) curves were also examined to attempt to determine if there was a change in the  $\gamma'$  solvus temperature that could account for this difference. From Tables 3-1 and 3-2, there is a slight difference in  $\gamma'$  solvus and the maximum thermal effect between MPB #96SW863 to #96SW865. The former MPB has a slightly greater temperature for the maximum thermal effect, but a slightly lesser  $\gamma'$  solvus temperature than the latter MPB. The maximum thermal effect corresponds to the point where the  $\gamma'$  phase has the greatest rate of dissolution into the matrix. It appears that the soak temperature can not be too far above this temperature in order to achieve the desired microstructure through this heat treatment. This agreed with the heat treatment trials, where greater soak temperatures produced irregular shaped  $\gamma'$  precipitates. A decrease in the soak temperature by 10°C produced the alternate microstructure for the three MPBs in question.

### **Characterization**

Once the heat treatments were complete, the microstructure of both heat treatments was fully characterized. This included accurately determining the  $\gamma'$  solvus temperature and determining the volume fraction and size range of all modes of  $\gamma'$  particles found in the microstructure of both heat treatments. This data helps understand the microstructural evolution during heat treatment and the strengthening and fracture mechanisms active during mechanical testing.

### Temperature of $\gamma'$ solvus

Due to the role of the  $\gamma'$  solvus temperature in both the standard and the alternate heat treatments, it was important to accurately determine the  $\gamma'$  solvus temperature for Alloy 720LI to fully understand the microstructural evolution during heat treatment. DTA analysis was performed at two independent laboratories to determine the  $\gamma'$  solvus, the solidus, and the liquidus of Alloy 720LI. Since the DTA analysis is performed on-heating, it can lead to results that differ from the equilibrium values of these temperatures. This is due to superheating in the alloy before dissolution or melting reactions takes place. Therefore, microstructural analysis samples were examined to compliment the DTA data and to determine the solvus temperatures after quenching from a soak temperature both on-heating and on-cooling.

The DTA analysis measured the  $\gamma'$  solvus temperature to be approximately 1185-1195°C (2165-2183°F). This is well above the value typically reported in literature of 1150-1155°C (2102-2111°F). The temperature reported as the maximum thermal effect is much closer to this reported  $\gamma'$  solvus temperature. Moreover, the metallographic study of quenched samples determined that there were at least two separate  $\gamma'$  solvus temperatures. These are approximately 1130°C (2066°F) and 1120°C (2048°F), and are lesser than the reported solvus temperature. These two temperatures correspond to the solvus temperatures for the primary and the secondary  $\gamma'$  precipitates respectively. It would also follow that there is another solvus temperature for the nucleation of the fine tertiary  $\gamma'$  precipitates at an even lower temperature.

DTA data can be misleading since it is not an equilibrium method of determining various reaction temperatures and can only give a range of temperatures over which the

$\gamma'$  phase goes into solution. The  $\gamma'$  solvus temperature is determined as the temperature at which the last  $\gamma'$  phase goes into solution during heating [69]. As a result, DTA analysis will tend to overestimate the value of the solvus temperatures versus the equilibrium solvus temperature. Additionally, it is difficult to resolve two peaks on a DTA curve that occur within 10°C (18°F) of each other. The DTA data suggests that there is only one  $\gamma'$  solvus; however, the metallographic study disputed this by revealing two distinct solvus temperatures for the primary and secondary  $\gamma'$  precipitates. While DTA is a useful means to approximate reaction temperatures, it is beneficial to augment its data with a metallographic study of quenched-in microstructures for accurate determination of solvus temperatures.

### **Microstructure**

The microstructure of both the alternate and the standard heat treatments were characterized to help understand the role the microstructure plays in the mechanical properties of these two heat treatments. The calculations and statistics for the microstructural characterization are found in Appendix B. The standard heat treatment consisted of small  $\gamma$  grains (ASTM 11.8) that are approximately  $5.3 \pm 0.8 \mu\text{m}$  ( $2.1 \pm 0.3 \times 10^{-4}\text{in}$ ) in diameter and decorated with large, primary  $\gamma'$  precipitates. These particles are blocky in shape with an average size of  $1.7 \pm 0.4 \mu\text{m}$  ( $6.7 \pm 1.6 \times 10^{-5}\text{in}$ ) on edge. Within the grains, the secondary and tertiary  $\gamma'$  precipitated as regular arrays of small cubes approximately  $0.6 \pm 0.2 \mu\text{m}$  ( $2.5 \pm 0.7 \times 10^{-5}\text{in}$ ) and  $230 \pm 50 \text{ nm}$  ( $9.1 \pm 1.9 \times 10^{-6}\text{in}$ ) on edge respectively. Additionally, even smaller  $\gamma'$  precipitates were seen when using a FEG SEM. These “quaternary”  $\gamma'$  precipitates can be seen in Figure 4-1. They are approximately 40nm ( $1.6 \times 10^{-6}\text{in}$ ) on edge. The total  $\gamma'$  volume fraction was found to

be  $51 \pm 3\%$  for this heat treatment. The primary  $\gamma'$  had a volume fraction of  $17 \pm 3\%$ , while the secondary  $\gamma'$  had a volume fraction of  $9 \pm 2\%$ . There was almost as much tertiary  $\gamma'$  as there was combined primary and secondary  $\gamma'$  in this heat treatment. The tertiary  $\gamma'$  had a volume fraction of  $25 \pm 4\%$ . It was not possible to resolve the quaternary  $\gamma'$  well enough to measure an accurate volume fraction. However, it is assumed to be less than 1.0% by volume.

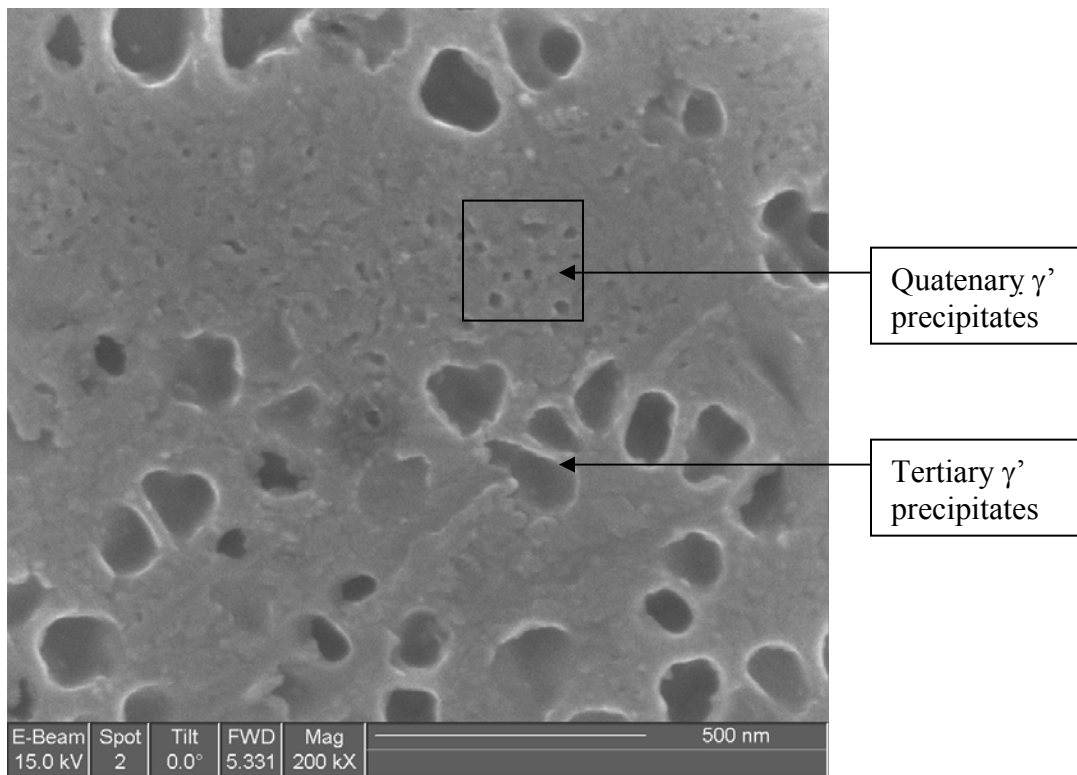


Figure 4-1: The tertiary and “quaternary”  $\gamma'$  precipitates in the standard heat treatment

In contrast, the alternate heat treatment resulted in a larger grain size (ASTM 8.2) that is approximately  $18.4 \pm 1.6 \mu\text{m}$  ( $7.2 \pm 0.6 \times 10^{-4}$  in) in diameter. The primary  $\gamma'$  precipitates pin grain boundary motion during the standard subsolvus heat treatment. However, during the soak for the alternate heat treatment, these primary  $\gamma'$  particles are completely in solution, giving the grain boundaries the freedom to grow in a manner that

minimizes the total surface area of the grains. The grain boundaries developed a serrated structure in the alternate heat treatment due to the dendritic-shaped  $\gamma'$  precipitates impinging on the grain boundaries during growth. This can be seen in Figure 4-2.

During cooling from the maximum heat treatment temperature, the primary  $\gamma'$  particles

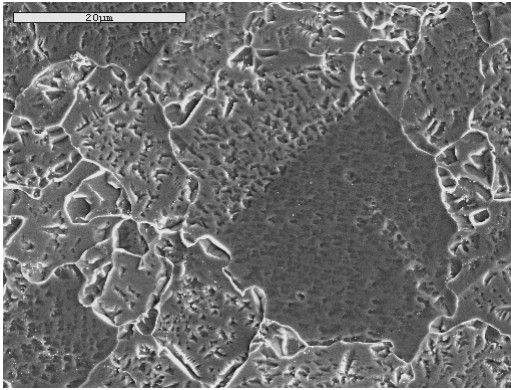


Figure 4-2: Serrated grain boundary structure present in the alternate heat treatment microstructure

precipitate along the  $\gamma$  grain boundaries. As the temperature is decreased further, the secondary  $\gamma'$  precipitates begin to nucleate intragranularly. Finally, at even lower temperatures, the fine tertiary  $\gamma'$  particles precipitate out of the  $\gamma$  matrix. In this heat treatment, the secondary  $\gamma'$  forms a regular array of dendritic-shaped  $\gamma'$  within the grains. In this heat treatment, the primary  $\gamma'$  occupy  $6 \pm 2\%$  by volume and their average size is  $1.4 \pm 0.6 \mu\text{m}$  ( $5.5 \pm 2.4 \times 10^{-5}$  in). The secondary  $\gamma'$  occupy a much larger volume in this heat treatment:  $44 \pm 4\%$ . These precipitates have a mean lineal intercept of  $1.0 \pm 0.2 \mu\text{m}$  ( $3.9 \pm 0.6 \times 10^{-5}$  in); however they can be as large as  $5 \mu\text{m}$  ( $1.97 \times 10^{-4}$  in) from tip to tip. However, this is a misleading size due to grain orientation and the  $\langle 111 \rangle$  growth direction of these precipitates. It is difficult to obtain a true radius for these particles. Due to the large size of these secondary  $\gamma'$  precipitates, not much  $\gamma'$  remains in solution after the initial solution heat treatment. As a result, the tertiary  $\gamma'$  can not grow as large

as in the standard heat treatment. Their volume fraction is assumed to be less than 1.0%. They are approximately 40 nm ( $1.6 \times 10^{-6}$  in) on edge in this heat treatment. No quaternary  $\gamma'$  was evident in this heat treatment. The total  $\gamma'$  volume fraction for this heat treatment was measured to be  $50 \pm 3$  %. Both heat treatments have the same volume fraction of  $\gamma'$ . Figure 4-3 is a histogram of the  $\gamma'$  volume fractions for the different modes of precipitate in each heat treatment.

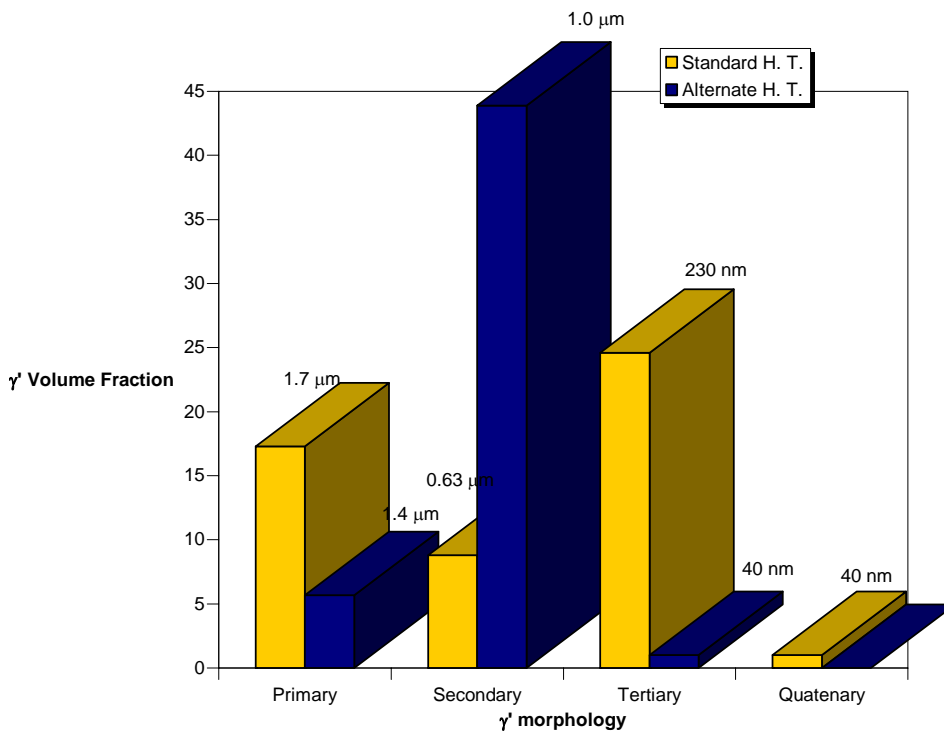


Figure 4-3: Histogram of  $\gamma'$  volume fraction for the two heat treatments

Samples of both heat treatments without the aging heat treatment, along with an as-HIPed sample, were polished and etched to study the precipitation and growth of the tertiary  $\gamma'$ . Micrographs of these three samples are displayed in Figure 4-4. The large precipitates in these micrographs are primary  $\gamma'$  in the as-HIPed micrograph and

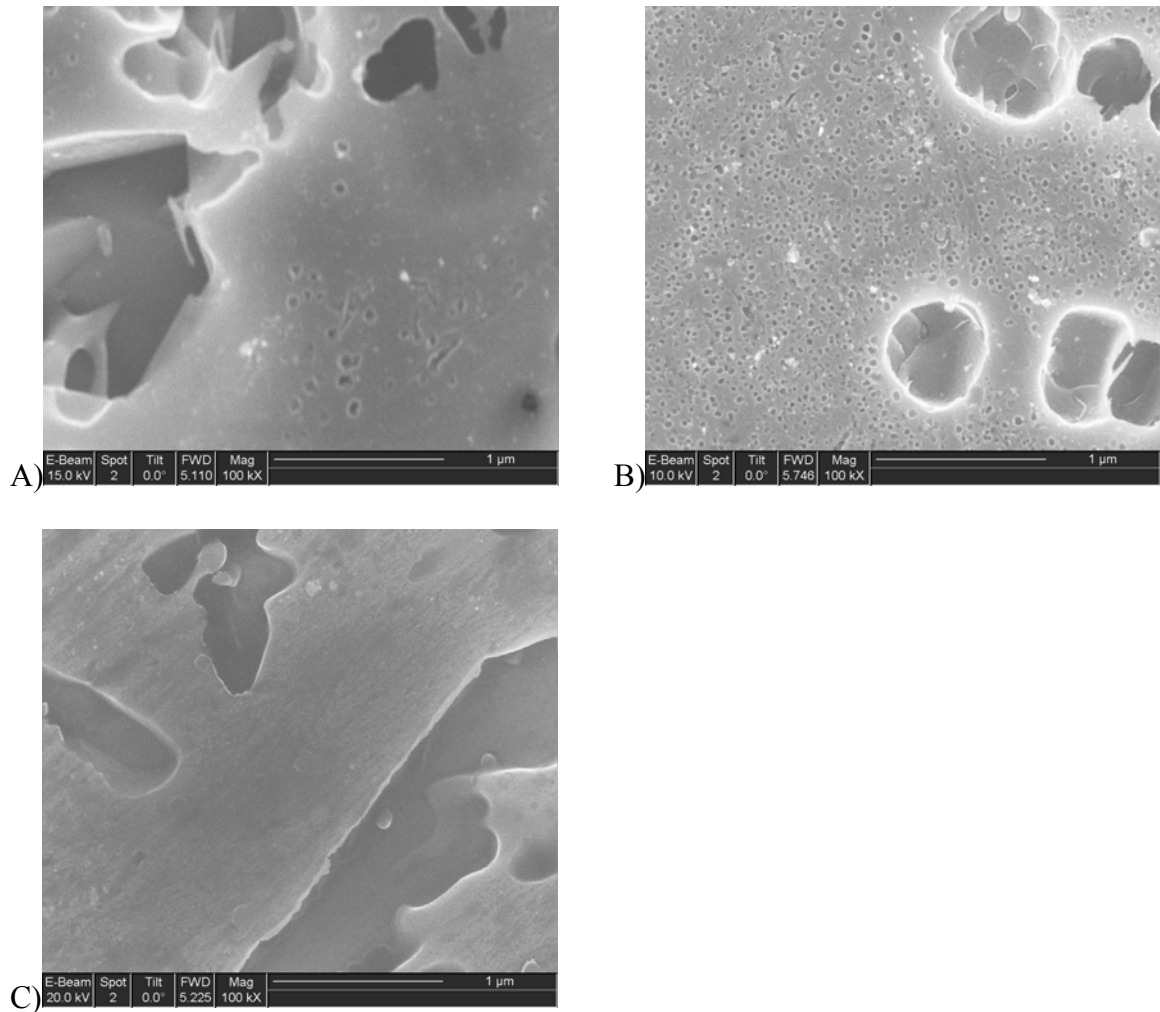


Figure 4-4: Secondary and tertiary  $\gamma'$  precipitates. A) As-HIPed microstructure. B) Standard heat treatment without aging heat treatments. C) Alternate heat treatment without aging heat treatments.

secondary  $\gamma'$  particles in the standard and alternate heat treatment micrographs. Fine tertiary  $\gamma'$  precipitates can be seen in the as-HIPed and standard heat treatment micrographs; however, this fine, tertiary  $\gamma'$  is not visible in the alternate heat treatment. The tertiary  $\gamma'$  in the as-HIP and standard heat treatment microstructures are approximately 50nm on edge. However, there is a much higher volume fraction visible after the standard heat treatment. It is possible that the tertiary  $\gamma'$  has already precipitated from solution after the alternate heat treatment but are not visible because of limitations

in polishing, etching, and microscope resolution. The other possibility is that the tertiary  $\gamma'$  precipitates may actually nucleate during subsequent aging heat treatments.

From this characterization data, the microstructural evolution during consolidation and heat treatment can be accurately described. The HIP cycle was carried out at 1129°C. According to literature, this would have been below the  $\gamma'$  solvus temperature for this alloy. From the data collected in this project though, it is thought that this is below the primary  $\gamma'$  solvus temperature, but, in fact, is above the secondary  $\gamma'$  solvus temperature. The primary  $\gamma'$ , which is only present at the grain boundaries will restrict grain boundary motion and prevent the grains from growing during consolidation; however, the secondary and tertiary  $\gamma'$  will go into solution. During cooling from the consolidation temperature,  $\gamma'$  precipitates intergranularly in at least two modes (secondary and tertiary). It also appears that at the right conditions, a fourth mode (quaternary) of  $\gamma'$  will precipitate during cooling. The result of this HIP cycle is a fine grain sized material with primary  $\gamma'$  along the grain boundaries and irregular shaped secondary and tertiary  $\gamma'$  within the grains.

The standard heat treatment is applied at a subsolvus temperature. This heat treatment is a partial solution heat treatment designed to refine the size and shape of the secondary  $\gamma'$  precipitates. It is not clear from the results collected during this study whether this heat treatment is a solution heat treatment or if it is only a high temperature aging heat treatment. It would be interesting to examine the solvus temperature of the tertiary  $\gamma'$  with a metallographic study below 1120°C. A comparison of the secondary  $\gamma'$  size difference before and after the solution heat treatment would help in determining if this heat treatment is a true solution heat treatment.

During the standard heat treatment, the secondary  $\gamma'$  transforms from slightly irregular shaped particles to more or less cuboidal shaped particles through diffusion. During this process, the size and shape of the secondary precipitates is refined until they are cubes that are  $0.63 \pm 0.17 \mu\text{m}$  ( $2.5 \pm 0.7 \times 10^{-5}$  in) on edge. In addition, the tertiary  $\gamma'$ , which previously nucleated during the HIP cycle, begins to grow in size and volume fraction through diffusion. It is only after the final aging heat treatments that the tertiary and quaternary  $\gamma'$  reach their final size and volume fractions. These final aging heat treatments only affect the fine  $\gamma'$  and not the primary or secondary  $\gamma'$  precipitates.

In contrast, the alternate heat treatment is carried out at a supersolvus temperature. The  $\gamma'$  phase that precipitates during the consolidation is completely in solution at this temperature. Without any primary  $\gamma'$  precipitates present, the grains are free to grow past their original size within the powder particles. During the slow cooling through the solvus temperature,  $\gamma'$  precipitates nucleate both along the grain boundaries as primary  $\gamma'$  and within the grains as secondary and possibly as tertiary  $\gamma'$  precipitates. It is not possible to tell when the tertiary  $\gamma'$  precipitates during the alternate heat treatment with the current data. During the slow cooling, the secondary  $\gamma'$  precipitates grow along the  $\langle 111 \rangle$  directions to form dendritic-shaped particles. Finally, the aging heat treatments possibly nucleate and increase the size and volume fraction of the tertiary  $\gamma'$  precipitates.

### **Mechanical Testing**

After heat treating, the test bars were machined into mechanical test specimens. Hardness, tensile, creep and fatigue testing were performed on samples from both heat treatments to understand the effects of the new, alternate microstructure on the

mechanical properties of Alloy 720LI. In addition, fractography was performed on fractured test specimens to understand the mechanisms of failure in both heat treatments.

### **Hardness Testing**

There was a significant difference in the Rockwell C hardness for the two heat treatments, both before and after the aging heat treatments (Table 3-4). The differences in hardness can be related directly to the microstructures of the two heat treatments. The size and larger volume fraction of the tertiary  $\gamma'$  precipitates in the standard heat treatment appear to result in a greater strength due to more effective blocking of dislocation motion. The secondary and tertiary  $\gamma'$  in the standard heat treatment are coherent and have a small mean free path. As a result, the dislocations shear these precipitates causing antiphase boundaries to develop [12]. In contrast, the alternate heat treatment has a very small volume fraction of tertiary  $\gamma'$  precipitates. In addition, the larger  $\gamma'$  precipitates are incoherent and more widely spaced. It is not clear if the dislocations are shearing these precipitates or bowing around them. It follows that the different  $\gamma'$  morphologies of the two heat treatments leads to the difference in hardness. The standard heat treatment has a moderate amount of small, finely spaced, coherent secondary  $\gamma'$  precipitates compared to the large amount of widely spaced, incoherent secondary  $\gamma'$  in the alternate heat treatment. The more finely spaced, coherent precipitates are expected to be more effective at blocking dislocation motion due to  $\gamma'$  shearing and the creation of antiphase boundaries [12]. In addition, the standard heat treatment has a large amount of fine, closely-spaced tertiary  $\gamma'$ . The alternate heat treatment, in contrast, has very little of this tertiary  $\gamma'$  precipitate. This ultrafine phase of  $\gamma'$  is thought to be very effective at blocking dislocation motion because of its small

mean lineal intercept. The higher hardness and larger volume fraction of tertiary  $\gamma'$  in the standard heat treatment suggests that this mode of  $\gamma'$  has a large impact on the hardness and, in turn, strength of the alloy. In generally, the hardness of metals is proportional to the tensile strength [11]. A second reason for these differences in hardness is the smaller grain size of the standard heat treatment. The grain boundaries block dislocation motion from one grain to the next. As a result, fine grained materials exhibit greater strength and greater hardness. Finally, both heat treatments experienced an increase in hardness after the aging heat treatment. During these aging heat treatments, only the tertiary  $\gamma'$  precipitates grow. The other modes of  $\gamma'$  precipitates remain basically unchanged in morphology and volume fraction. This increase in hardness after aging is due to the coarsening of the tertiary  $\gamma'$  precipitates.

### **Fatigue Testing**

The goal of this study was to develop an alternate heat treatment that produced a microstructure with better fatigue properties. Unfortunately, the standard heat treatment had longer high cycle fatigue (HCF) lifetimes than the alternate heat treatment at stress ranges of 1034 MPa (150 Ksi) and 993 MPa (144 Ksi) at both test temperatures. However, the alternate heat treatment outperformed the standard heat treatment at the greatest stress range of 1086 MPa (157.5 Ksi) at both 538°C (1000°F) and 649°C (1200°F). A detailed study of the fracture surfaces was performed to help identify the fracture mechanisms that led to these results.

The initial step of fatigue failure is plastic deformation before the nucleation of microcracks around a processing defect or persistent slip band [71]. A sufficient amount of deformation will cause microcracks to initiate in the matrix surrounding a defect or

cracked slip band. These microcracks propagate until they link up to form one or more large crack. The next phase of failure is fatigue crack propagation before the onset of overload and fast fracture when these cracks reach a threshold size. Fatigue failure in metals is generally broken up into three stages [72]. During Stage I, fatigue crack initiation occurs along with some crack growth. This most often occurs due to cracking of slip bands because of the repetitive reversals of deformation along these slip bands during fatigue testing. The crack follows crystallographic planes and the fracture surfaces are left with faceted features. During Stage II, the fatigue crack propagates transgranularly, leaving behind fatigue striations on a relatively featureless surface. Finally, in Stage III crack growth, the specimen undergoes overload and the crack growth is unstable until final fracture.

The initiation point for each specimen was located by SEM and identified using energy dispersive spectrometry (EDS). Every standard heat treatment specimen failed at a processing defect. The majority of these were at ceramic agglomerates introduced to the alloy possibly from the melting crucible, the pouring tundish, or the nozzle during atomization. Screening through fine mesh sieves removes many of these ceramic inclusions; however, some of them are smaller than the sieve sizes used. It is not economically feasible to sieve to a finer mesh size, so it is necessary to engineer the alloy to have some degree of tolerance to these inclusions. The smaller grains in the standard heat treatment have a smaller displacement along the slip bands during fatigue testing [17]. This slows down the formation of microcracks around the slip bands. As a result, a small grained material is not as likely to fail by slip band cracking. Instead, it is more probable that a small grained material will fail from cracks emanating from processing

defects. While the majority of the fatigue specimens failed at ceramic inclusions, one of the samples, ULA10, fractured at a Ti-rich particle left on the surface of the machined test specimen (Figure 3-29). This carbide was cracked either before or during testing and as a result initiated microcracks in the matrix surrounding it. These microcracks eventually linked up and led to failure.

The standard heat treatment samples tested at the low and middle stress ranges failed at defects that were near the surface but not actually on the surface. These defects were surrounded by a region of faceted fracture features (Figure 3-33A). This area is an example of Stage I fatigue crack growth [72]. This region eventually transitioned to a flat, featureless region after approximately  $100\ \mu\text{m}$  ( $3.94 \times 10^{-3}$  in). This flat region is indicative of Stage II transgranular fatigue crack growth [72]. In contrast, the two tests at the highest stress range actually failed at processing defects on the surface of the machined samples. These defects were only surrounded by a flat, relatively featureless region (Figure 3-33B). There were no faceted features near the failure initiation point for the highest stress range condition. In these samples, Stage I crack growth was completely bypassed and the cracks propagated entirely in a Stage II crack growth mode until fast fracture. At larger values of strain during fatigue testing, cracks will initiate at most defects in the material. The stress intensity at defects on the surface have a greater stress intensity than internal defects as can be seen in Equations 4-1 and 4-2 below. Cracks at the surface will propagate faster under these conditions because they have greater stress intensity than cracks at internal defects and because of the deleterious effects of oxidation [17]. In contrast, at small strains, cracks will only initiate at acute inclusions, and internal initiation is favored.

The alternate heat treatment test samples had a little more variability in their initiation sites (Table 3-4). Three of the seven samples exhibited initiations at persistent slip bands. Ceramic inclusions led to failure in two of the samples. The fracture initiation of the final two samples is unclear. In one specimen, ULB17, no clear initiation point was discovered after examining the fracture surface (Figure 3-32). Another sample, ULB15, clearly failed from a crack that began at a processing defect on the surface. However, after examining it with both backscattered electron imaging (BSE) and EDS, it is still not clear what type of defect is present. It seems to be a large  $\gamma$  grain containing no  $\gamma'$  precipitates. (Figure 3-31). It is not clear how such a defect might have formed and remained throughout the heat treatment. This defect has cracks that extend from its interior into the surrounding matrix.

Excluding sample ULB17 (no initiation point found), the only samples to fail internally for the alternate heat treatment were the two tested at 993MPa (144Ksi). The rest failed at surface defects. The two internal failures were at large faceted persistent slip bands (Figure 3-33C). These were surrounded immediately by a region of faceted features as with the standard heat treatment samples. This region again extended for approximately  $100\mu\text{m}$  ( $3.94 \times 10^{-3}\text{in}$ ) before entering a region of Stage II crack propagation. However, the samples that failed at surface defects were again only surrounded by a relatively featureless region with no faceted features present (Figure 3-33D).

The faceted features are examples of typical Stage I fatigue fracture by slip band cracking [72]. The dislocations move along the active slip planes, (111) in this case, until they reach the grain boundaries. After enough dislocations pile up at the grain

boundaries, microcracks begin forming around the grain. These microcracks link up and lead to the initial crack front that eventually propagates to failure. When this initial crack is formed, the grain fractures along the slip plane. This leaves a faceted feature on both halves of the fracture surface. These features resemble brittle fracture visually, but are the result of dislocation motion. As the cracks grew, the fracture surfaces exhibited a transition to typical Stage II fracture that is defined by a relatively flat region. The cracks propagate transgranularly through this region of slow crack growth. Fatigue striations are sometimes present on the specimens in this region of the surface. These striations are caused by the repetitive opening and closing of the crack tip during propagation. Eventually, the crack reaches a point where the specimen is overloaded and fast fracture begins. This is marked by the transition from the transgranular region to an area with a more tortuous surface features as seen in Figure 3-35. At this point, the crack transitions to either an intergranular or interparticle propagation mode here. It is not clear which of these two modes of failure is active for this alloy. It is possible that they are both active. The feature sizes appear to match the grain size for the heat treatments; however, the features are much more rounded than those usually seen from intergranular fracture. This could be due to cracking at the particle boundaries (Figure 4-5).

The depth and width of the initial cracks were measured for all of the fatigue samples. The area used for this initial crack measurement coincided with the onset of the Stage II transgranular fracture. It was then possible to measure the maximum stress intensity as well as a change in stress intensity for the stress ranges tested. The equations used for the fracture mechanics calculations were taken from Anderson [73]. The flaws

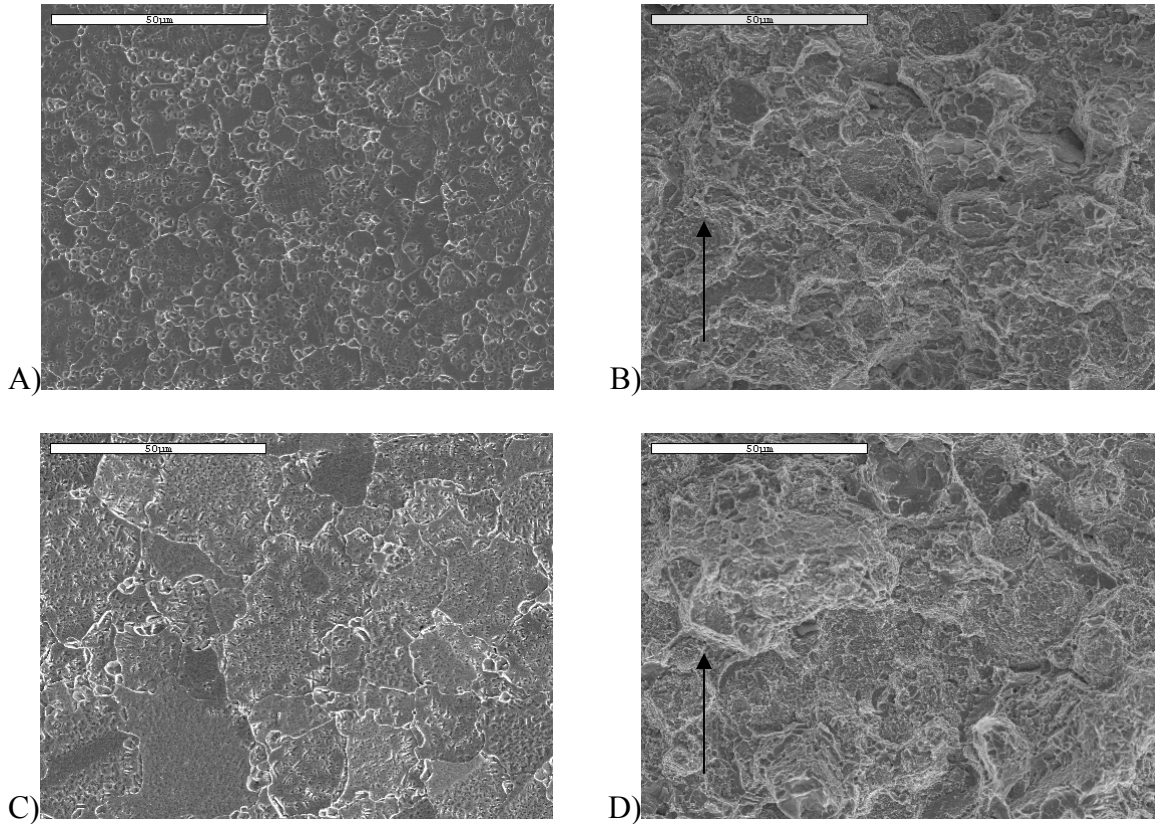


Figure 4-5: Comparison of fast fracture features during HCF fatigue and grain size. A) Standard heat treatment grain size. B) Standard heat treatment fatigue fracture surface features. C) Alternate heat treatment grain size. D) Alternate heat treatment fatigue fracture surface features.

were approximated based on the stress intensity factors for elliptical and semi-elliptical cracks. The equation for an embedded elliptical crack is

$$K_{\max} = \frac{\sigma\sqrt{\pi a}}{\Psi} \quad (4-1)$$

The equation for a surface, semi-elliptical crack is

$$K_{\max} = \frac{1.12\sigma\sqrt{\pi a}}{\Psi} \quad (4-2)$$

where  $a$  is the crack depth,  $K_{\max}$  is the stress intensity factor at the maximum stress, and  $\Psi$  is a geometrical factor based on the crack shape and size.  $\Psi$  can be estimated by the following equation:

$$\Psi = \frac{3\pi}{8} + \frac{\pi a^2}{8 c^2} \quad (4-3)$$

Once the stress intensity factor for these initial cracks was determined, the plastic zone size was estimated by the plane stress and plane strain approximations:

$$r_p = \frac{1}{2\pi} \frac{K^2}{\sigma_{ys}^2} \quad (\text{plane stress}) \quad (4-3)$$

$$r_p = \frac{1}{6\pi} \frac{K^2}{\sigma_{ys}^2} \quad (\text{plane strain}) \quad (4-4)$$

This equation was applied to both  $K_{max}$  and  $\Delta K$ . All of this data is contained in Table 4-1.

Table 4-1: Stress intensity factors and plastic zone sizes for the initial crack in HCF tests

Sample	$K_{max}$ (MPa*m <sup>0.5</sup> )	$r_p(K_{max})$ ( $\mu\text{m}$ ) plane stress	$r_p(K_{max})$ ( $\mu\text{m}$ ) plane strain	$\Delta K$ (MPa*m <sup>0.5</sup> )	$r_p(\Delta K)$ ( $\mu\text{m}$ ) plane stress	$r_p(\Delta K)$ ( $\mu\text{m}$ ) plane strain
Standard Heat Treatment						
ULA5	12	18	6	10	15	5
ULA15	12	20	7	11	16	5
ULA14	11	16	5	10	13	4
ULA11	11	16	5	10	13	4
ULA16	11	17	6	10	14	5
ULA3	12	18	6	10	15	5
ULA13	11	16	5	10	13	4
ULA10	13	21	7	11	17	6
Alternate Heat Treatment						
ULB7	15	45	15	13	36	12
ULB10	14	44	15	13	35	12
ULB6	15	44	15	13	35	12
ULB15	14	4	14	13	34	11
ULB13	14	42	14	13	34	11
ULB9	14	40	13	13	32	11

The calculations and statistics for these stress intensity factors can be found in Appendix B. The yield strength of the alternate heat treatment at 538°C was estimated to be approximately 870 MPa. This estimate was based on the yield strength of the alternate heat treatment at 649°C in conjunction with the lower yield strength in the standard heat

treatment tensile sample at 538°C. The alternate heat treatment fatigue samples transition to transgranular Stage II crack growth at a larger stress intensity and plastic zone size. It has been suggested previously that this transition occurs when the plastic zone size is approximately equal to the grain size [74]. This is the case in this study if the plane strain approximation is used. As these test bars were not designed to be either plane strain or plane stress, the actual situation will lie in between these two extreme cases. From this data, it is definitely possible that the transition to Stage II crack growth occurs when the calculated plastic zone size is approximately equal to the grain size for the two different heat treatments. However, since the crack area for the two heat treatments is approximately equal, it can not be ruled out that this transition simply occurs at a threshold crack size when the microcracks link up into one continuous crack front. One way to determine the mechanism for this transition in crack propagation mode would be to test samples at smaller stress ranges. If there is a threshold crack size needed for microcrack link-up, then the initial crack size would not change with stress range. However, if this transition is controlled by the size of the plastic zone compared to the grain size, then the initial crack size should increase with decreasing stress range. In this case, the plastic zone size and stress intensity factor for the initial crack would remain constant with changes in the stress range.

In the same manner, the crack dimensions for the final slow crack growth region were measured from SEM micrographs. The stress intensity factor and plastic zone size were also measured for both the max stress for each cycle. It is assumed that  $K_{\max}$  approaches  $\Delta K$  as the crack approaches overload. The results are listed in Table 4-2. Once again, the yield strength for the alternate heat treatment at 538°C was taken to be

Table 4-2: Stress intensity factors and plastic zone sizes for the final crack in HCF tests

Sample	$\sigma_{ys}$ (MPa)	$\sigma_{max}$ (MPa)	$K_{max}$ (MPa*m <sup>0.5</sup> )	$r_p(K_{max})$ ( $\mu$ m)
Standard Heat Treatment				
ULA5	1078	1103	37	190
ULA15	1078	1103	39	211
ULA14	1078	1149	40	218
ULA11	1078	1149	41	227
ULA16	1078	1207	42	238
ULA3	1095	1103	45	274
ULA13	1095	1149	45	272
ULA10	1095	1207	45	263
Alternate Heat Treatment.				
ULB7	~870	1103	40	334
ULB10	~870	1149	39	322
ULB6	883.5	1103	42	360
ULB15	883.5	1149	41	342
ULB13	883.5	1149	41	345
ULB9	883.5	1207	43	384

870 MPa. These values are lower than the  $K_C$  values reported in literature of up to 70 MPa(m)<sup>0.5</sup> [75]. While the value of  $K_{max}$  at the final crack size is not equivalent to the  $K_{IC}$  fracture toughness, it can be used to compare the stress intensity ( $K_C$ ) to cause overload for the two heat treatments in this study. As can be seen by this table, the  $K_C$  of the two heat treatments is approximately equal. Additionally, Alloy 720LI has a higher stress intensity factor at 649°C than at 538°C. These samples appear to fracture when  $K_{max}$  reaches a threshold value irrespective of the plastic zone size. One way to determine whether this is in fact the case would be to test da/dn samples from both heat treatments to accurately determine  $K_C$ .

Any interactions between secondary cracks and the microstructure were examined by polishing and etching transverse slices of the gauge section. For the standard heat treatment samples tested at both temperatures and a stress range of 993 MPa (144 Ksi), the secondary cracks developed at primary  $\gamma'$  precipitates and at grain boundary triple

points. There were very few secondary cracks observed in samples tested at this stress range. The samples tested at stress ranges of 1034 MPa (150 Ksi) and 1086 MPa (157.5 Ksi) exhibited more secondary cracks that appeared to nucleate along sites that formed rounded shapes through the grains. There were also some cracks that nucleated along the grain boundaries as well. Examples of both are found in Figure 4-6. The rounded appearance of these secondary cracks through the grains suggests that they are along prior particle boundaries. At the highest stress condition, there is also evidence of a secondary crack initiating at a cracked TiC particle. (Figure 3-41A).

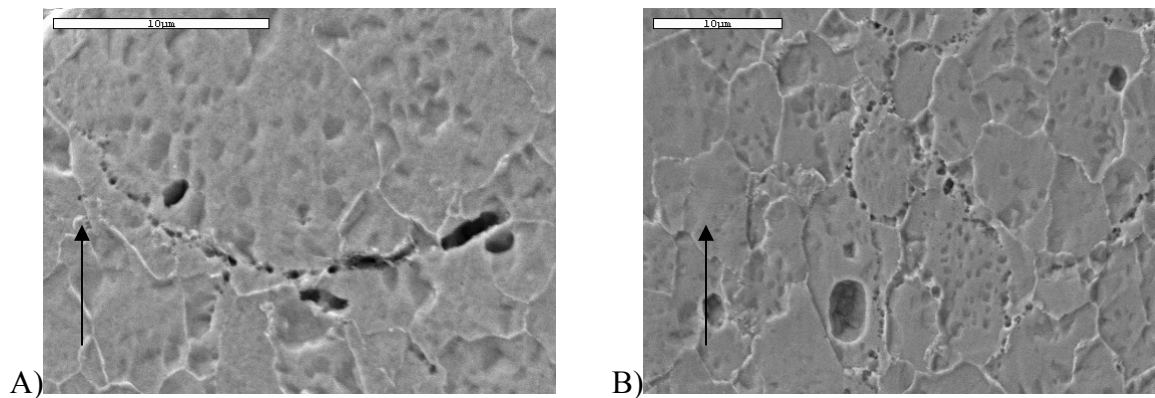


Figure 4-6: Secondary cracking in standard heat treatment fatigue samples. A) Running through the grains in sample tested at 538°C and 1034 MPa. B) Propagating intergranularly in sample tested at 538°C and 1086 MPa.

In the alternate heat treatment samples tested at both temperatures, the secondary cracks appear to have a slightly different nature than in the standard heat treatment. At stress ranges of 993 MPa (144 Ksi) and 1034 MPa (150 Ksi), the cracks initiate at both primary and secondary  $\gamma'$  precipitates. These cracks appear to occur in straight lines at an angle to the tensile direction as seen in Figure 4-7. This suggests that these cracks might be forming along the slip bands at the  $\gamma/\gamma'$  interface. The samples tested at a stress range of 1086 MPa (157.5 Ksi) had a few secondary cracks that began at TiC's and  $Al_2O_3$

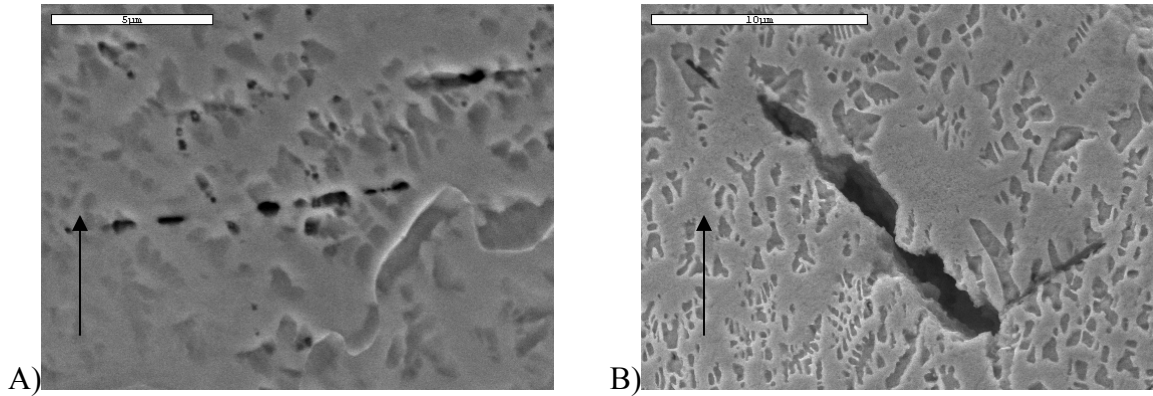


Figure 4-7: Secondary cracks propagating transgranularly in alternate heat treatment fatigue samples. A) Tested at 538°C and 993 MPa. B) Tested at 538°C and 1034 MPa.

ceramic inclusions as seen in Figure 3-41C. They also had voids initiating at the interface between the matrix and the primary and secondary  $\gamma'$  precipitates as seen in Figure 3-40c. Finally, there were some instances of large pores forming at grain boundary triple points. (Figure 4-8). These are thought to form as a result of thermally

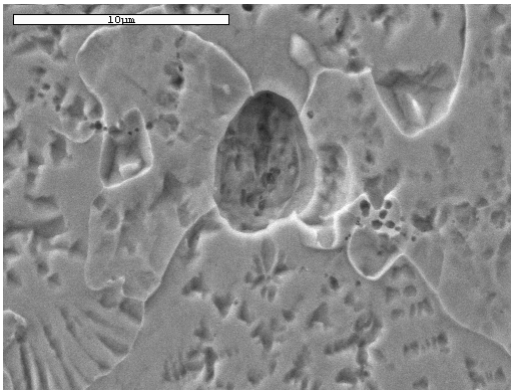


Figure 4-8: Large pore at a grain boundary triple point in alternate heat treatment sample tested at 538°C and 1086 MPa

induced porosity (TIP) due to entrapped argon gas from atomization. For the most part, there were not many large cracks at this condition. However, the ones that were present appeared to propagate transgranularly as seen below in Figure 4-9. There were no

secondary cracks that appeared to follow prior particle boundaries as in the standard heat treatment specimens.

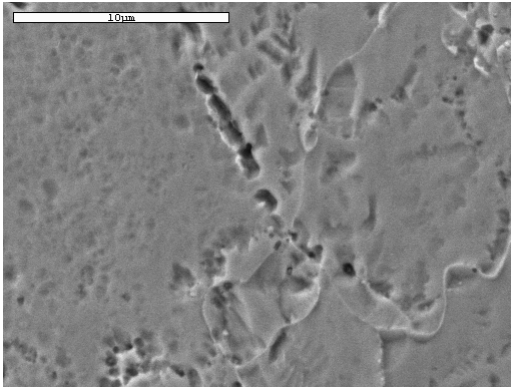


Figure 4-9: Long secondary cracks in alternate heat treatment fatigue sample tested at 538°C and 1086 MPa

While the fatigue test data shows that the standard heat treatment outperforms the alternate heat treatment at the low and middle stress ranges, but not at the high stress range; it is necessary to examine the tests on a case by case basis in order to understand the mechanisms behind these differences. At the highest stress range (1086 MPa), all samples failed from cracks that began at processing defects on the surface. These cracks propagated entirely in Stage II crack growth. For this condition, the alternate heat treatment lasted more cycles, but had a smaller crack size before fast fracture. At this high of a stress range, it is reasonable to assume that the number of cycles to initiate a continuous crack front is small compared to the total lifetime. The number of cycles for Stage II crack propagation dominated the lifetime of the fatigue specimens. With this in mind, it can be concluded that the alternate heat treatment had a slower crack growth rate. It took more cycles to propagate a shorter distance. This difference in propagation rate would be applicable to all of the fatigue tests for the Stage II crack growth region.

At the middle stress range (1034 MPa), the standard heat treatment samples failed at internal defects, while the alternate heat treatment samples failed from either surface defects or persistent slip bands at the surface. This difference in initiation location is probably partly caused by the difference in yield strengths between the two materials. The standard heat treatment had a greater yield strength than the alternate heat treatment (Table 3-7). For the standard heat treatment, the fatigue tests are run only slightly into the plastic regime. In contrast, the alternate heat treatment samples received significant plastic deformation on each cycle. The stress intensity is high enough to favor crack initiation at the surface. Microcracks at defects on the surface initiate rather quickly. They link up to form a continuous crack front in a relatively small number of cycles, and once again the number of cycles for Stage II propagation dominates the lifetime. However, it takes a significant number of cycles for internal crack initiation and Stage I propagation for the standard heat treatment. While the Stage II propagation rate may be quicker, the lifetime is dominated by crack initiation. The slower time to crack initiation explains why the standard heat treatment samples outperform the alternate heat treatment samples at the middle stress range.

At the lowest stress range (993 MPa), all of the samples failed at internal initiation sites. The standard heat treatment samples failed from cracks originating at processing defects, while the alternate heat treatment samples failed at cracks propagating from the slip bands. At this stress range, the lifetimes of the test specimens are controlled by the number of cycles to crack initiation. While the standard heat treatment produces persistent slip bands, the displacement of the slip bands at the grain boundaries is small due to the small grain size. As a result, these samples tend to fail at small processing

defects that were not eliminated during the powder screening process instead of at the slip bands. These defects are slightly larger in size than the grains. In contrast, the large grains of the alternate heat treatment produce very large displacements at the grain boundaries through slip mechanisms during the fatigue testing. These large displacements lead to a faster crack initiation than the defects found in the standard heat treatment because the initial cracks are larger. This difference in cycles to crack initiation lead to longer lifetimes for the standard heat treatment at the lowest stress range.

In general, higher ductility materials have longer fatigue lifetimes at higher strain (stress) values [17]. Conversely, higher strength materials have longer fatigue lifetimes at lower strain (stress) values. At low stress ranges, it takes a greater amount of cycles for the microcracks surrounding a processing defect or slip band to finally link up and form the initial crack. As a result, the fatigue lifetime is dominated by the number of cycles to crack initiation. The large size of the grains in the alternate heat treatment results in a faster crack initiation compared to the small processing defects at which failure initiates in the standard heat treatment because the stress intensity around the large grains is greater than that around the small grains. The smaller grain sized material (standard heat treatment) has longer fatigue lifetimes at the small stress ranges.

From this data, it is expected that at even larger stress ranges, the alternate heat treatment will outperform the standard heat treatment. However, at lower stress ranges the standard heat treatment will perform better. The microstructure does not seem to have as much of an impact on the fatigue properties as grain size does.

### **Tensile Testing**

At all test temperatures, the standard heat treatment had greater values for yield strength, ultimate tensile strength (UTS), and strength at failure than the alternate heat

treatment. However, the standard heat treatment had a corresponding deficit in ductility. While both heat treatments maintain their strength and elongation up to 649°C (1200°F), they suffer a deficit in these properties at 760°C (1400°F). This can be seen in Figure 4-10. Additionally, the macroscopic features of both heat treatments were similar for

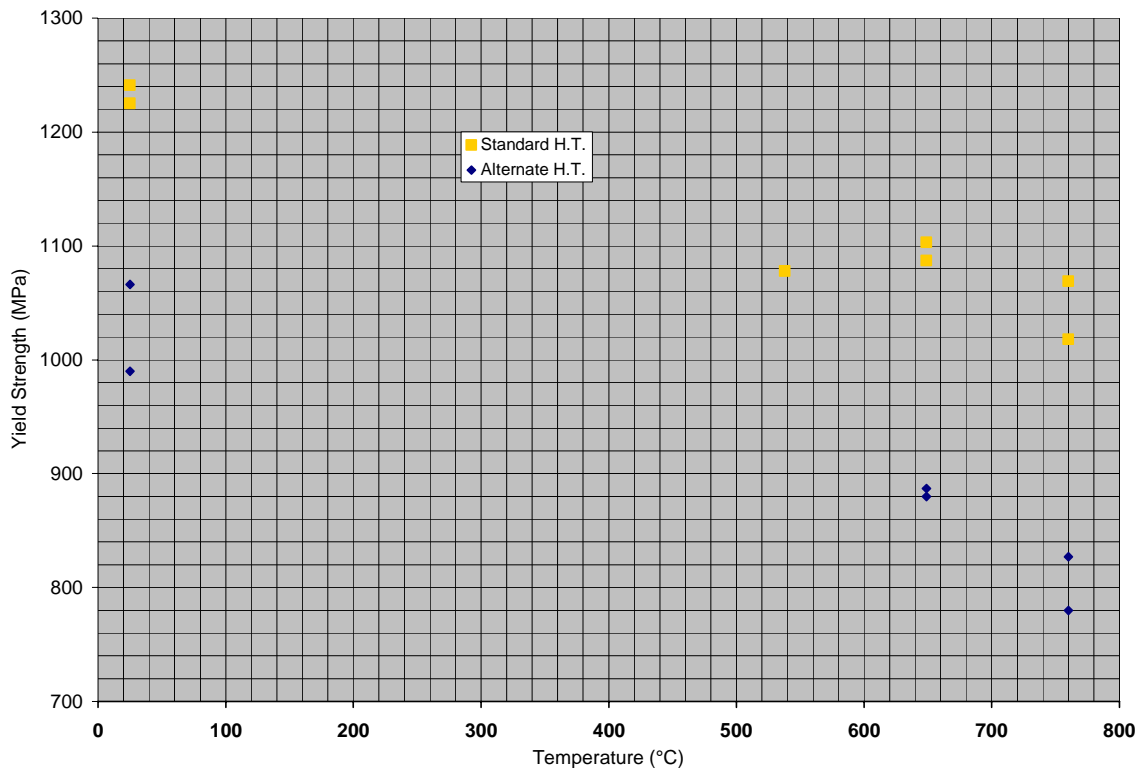


Figure 4-10: Yield strength vs. test temperature for both heat treatments

each test temperature. The room temperature tests had a flat surface with small shear lips. The tests at 649°C (1200°F) had a very distinct radial crack pattern with pronounced ridges leading away from the initiation source and small shear lips. Finally, the 760°C (1400°F) tests had surfaces with a flat arrowhead-shaped section leading away from the origin and larger shear lips on either side of the arrowhead. Optical pictures of these surface features can be found in Figure 4-11.

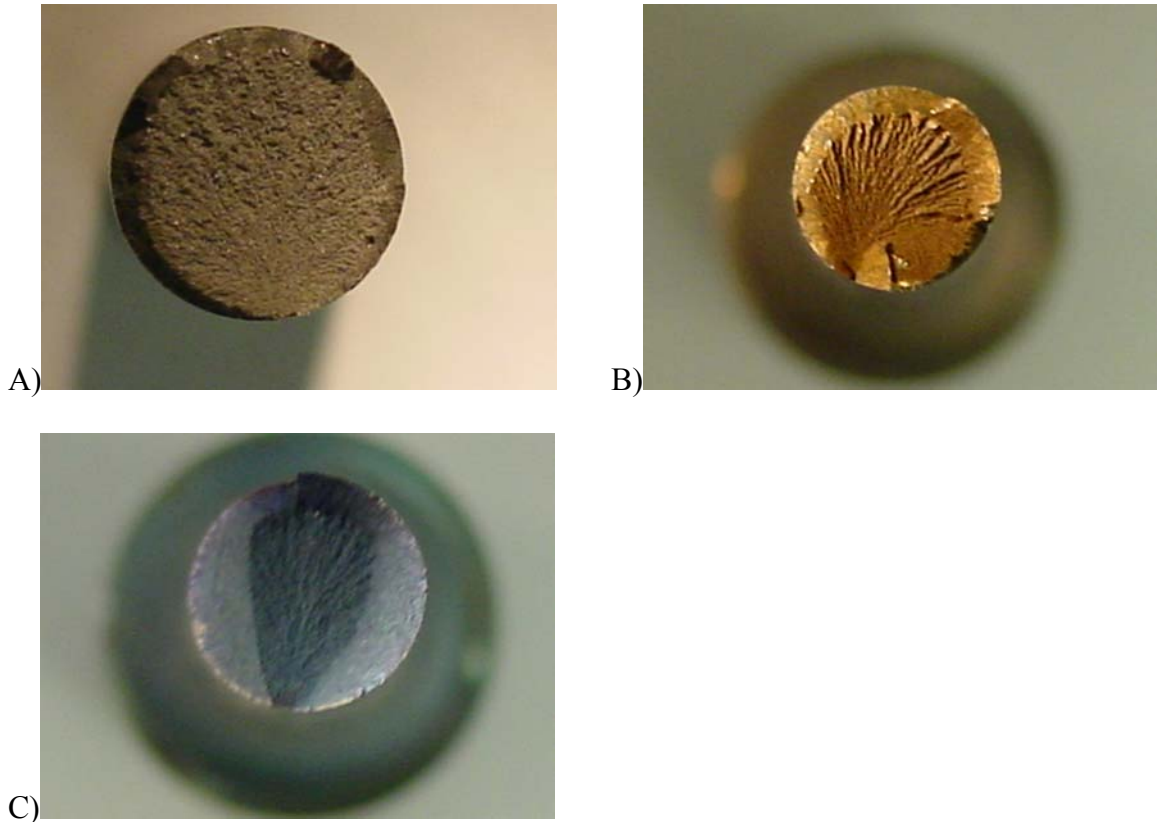


Figure 4-11: Optical pictures showing the fracture surfaces of tensile samples. A) Tested at room temperature. B) Tested at 649°C (1200°F). C) Tested at 760°C (1400°F).

The fracture surfaces of the tensile tests showed no difference in crack nucleation or propagation between the two heat treatments. Neither heat treatment had a preference for crack origin type. A few cracks began at ceramic particles ( $\text{Al}_2\text{O}_3$ ); however, the majority of the fractures began at undetermined origin types. Neither heat treatment displayed a tendency to exhibit failure initiation at ceramic inclusions. Additionally, the microstructural features along the crack path were similar for both heat treatments. A study of the fracture mechanics of the tensile samples is contained in Appendix C. Samples were polished to view secondary cracks interacting with the microstructure. However, the tensile specimens had almost no secondary cracks for either heat treatment.

It is thought that the difference observed in tensile properties between the two heat treatments is due to the  $\gamma'$  morphology and, to a lesser extent, the grain size differences between the two heat treatments. As discussed in the section on hardness testing, the  $\gamma'$  morphology and volume fraction of the standard heat treatment provide an effective hindrance to dislocation motion. Dislocations shear the secondary, tertiary, and possibly quaternary  $\gamma'$  precipitates creating antiphase boundaries within the precipitates. It is necessary for a second dislocation to shear the precipitates in order to restore the ordered structure. The large volume fraction of tertiary  $\gamma'$  in the standard heat treatment plays a crucial role in the strength of this microstructure. In addition, the standard heat treatment has a finer grain size. It has a much higher grain boundary density. These grain boundaries are also an effective barrier to dislocation motion through the test specimens. In contrast, the alternate heat treatment has a microstructure that does not provide as effective of a barrier to dislocation motion. The small amount of tertiary  $\gamma'$  does not provide much additional strengthening in the samples given this heat treatment. The dendritic-shaped secondary  $\gamma'$  precipitates are larger and have a greater mean free path between them than in the standard heat treatment. It is possible that the dislocations are able to bypass these  $\gamma'$  precipitates instead of shearing them. This bypass mechanism produces dislocation loops that provide some strengthening but not as much as the shearing mechanism produces. Finally, the larger grain size does not block dislocation motion as much as the small grains present in samples given the standard heat treatment.

Since the microstructure of the standard heat treatment has more hindrances to dislocation motion than the alternate heat treatment, it takes a greater stress to produce dislocation motion and, therefore, plastic strain during tensile loading. As a result, the

yield stress, UTS, and stress at failure are all greater in the standard heat treatment samples. Likewise, the microstructure of the alternate heat treatment specimens allows for much easier dislocation motion over longer distances. This heat treatment produces a more ductile microstructure.

### **Creep Testing**

During creep testing, the alternate heat treatment outperformed the standard heat treatment at the tests run at 704°C (1300°F) and above. However, the opposite was the case for the tests at 677°C (1250°F). This is evident from the results in Table 3-8. However, the alternate heat treatment samples experienced greater elongation at all test conditions.

The fracture surfaces of select samples, along with polished, longitudinal slices of the gauge section of these samples, were examined to determine the mechanisms involved during creep testing. It was not possible to determine the type of crack origin for any of these samples by examining the fracture surface. The origin was located using two complimentary methods: discoloration due to longer oxidation times at the origin and radial cracks leading from the origin. However, none of the origins found were of a distinct defect type. They appeared to be due to crystallographic failure rather than to processing defects.

The path of secondary cracks within the microstructure was examined by polishing into a longitudinal slice of the gauge section of the creep specimens. The tests at 704°C (1300°F) and higher had a high density of secondary cracks propagating roughly perpendicular to the tensile axis. When these specimens were treated with a grain boundary etchant (waterless Kallings reagent), it was obvious that these secondary cracks ran along the grain boundaries for both heat treatments. Moreover, higher magnification

SEM micrographs revealed that the grain boundaries served as nucleation sites for voids or cavities to form during creep testing. This can be seen in Figure 4-12. These cracks

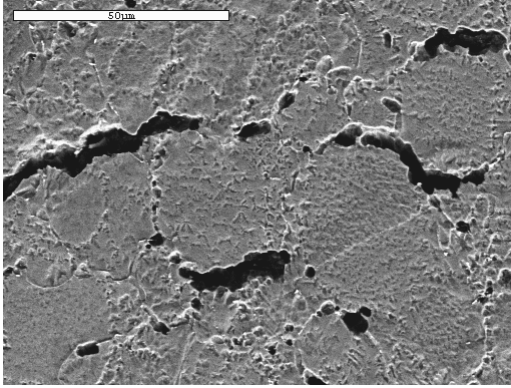


Figure 4-12: Alternate heat treatment creep sample tested at 732°C and 483 MPa showing secondary cracks initiating at and propagating along grain boundaries appear to initiate at cavitations formed between the grain boundary and the primary  $\gamma'$  precipitates as shown in Figure 3-56. These cracks are an indication that the failure mechanism at these test conditions is governed by grain boundary sliding [76]. This mechanism explains why the alternate heat treatment test specimens have longer lifetimes at these test conditions. The alternate heat treatment microstructure contains a smaller grain boundary density due to its larger grain size. Therefore, there is a much smaller area for cracks to nucleate. Additionally, the alternate heat treatment has successfully produced a serrated grain boundary structure that provides additional resistance to grain boundary sliding. As a result, this heat treatment is more resistant to grain boundary sliding than the standard heat treatment.

In contrast, the specimens tested at 677°C (1250°F) and 1034MPa (150Ksi) contained very few secondary cracks in the transverse slices. These cracks nucleated at voids created either at grain boundary triple points or between the secondary  $\gamma'$  precipitates and the  $\gamma$  matrix. There does not appear to be a preference for these cracks to

nucleate at either the grain boundaries or within the grains for this test condition. Voids nucleating at both sites can be seen in Figure 4-13. This type of cracking indicates that

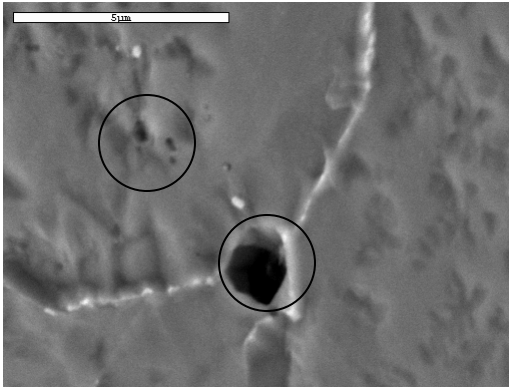


Figure 4-13: Alternate heat treatment creep sample tested at 677°C and 1034 MPa showing void nucleation at a grain boundary triple point and at the interface between secondary  $\gamma'$  precipitates and the matrix

grain boundary sliding is not the primary mechanism at work at this condition. Instead, dislocation motion is the main mechanism that leads to creep failure. As was stated before, the standard heat treatment microstructure is more effective at blocking dislocation motion. The standard heat treatment has a larger volume fraction of tertiary  $\gamma'$ , as well as small grains, that are very effective at blocking dislocation motion. In contrast, the alternate heat treatment has very little tertiary  $\gamma'$ , large grains, and large, incoherent secondary  $\gamma'$  that are not as effective at blocking dislocation motion. Hence, the microstructure in samples given the standard heat treatment is more resistant to creep at lower temperatures and higher stresses.

The only test condition where the primary mechanism for failure seems to differ is 677°C (1250°F) and 793 MPa (115 Ksi). The secondary cracks for the standard heat treatment sample nucleate both intergranularly and intragranularly. However, the cracks along the grain boundaries appear to be more frequent and longer. These are similar to the secondary cracks present in the high temperature creep tests. Grain boundary sliding

is the main mechanism leading to failure in the standard heat treatment sample. However, the alternate heat treatment sample at this test condition has relatively few secondary cracks that appear to nucleate without bias to the grain boundaries or within the grains in a similar fashion to the tests at 1034 MPa (150 Ksi). It is thought that the mechanism that led to failure for this sample is dislocation motion along the slip planes.

The fracture surface features along the crack path also provide clues as to the dominant mechanism for creep failure. The samples tested at the highest stress condition, 1034MPa (150Ksi), have small dimples near the crack initiation site; while those tested at higher temperatures have larger rounded features (Figure 3-49, 3-50, and 3-51). These larger features correspond roughly to the grain size of the material. This is an indication that the fracture mechanism near the initiation site is along the grain boundaries. This is evidence of grain boundary sliding as the primary mechanism for the samples tested at higher temperatures and dislocation motion as the mechanism for the samples at the highest stress condition. As the cracks propagate radially from the initiation site, all samples regardless of test condition eventually have larger features representative of grain size. Therefore, once the cracks reached fast fracture, they propagated along the grain boundaries.

### **Conclusions**

The following conclusions can be made based on this study on the effect of a slow cooling rate from above the  $\gamma'$  solvus temperature on the microstructure and mechanical properties of Alloy 720LI:

1. The morphology of the secondary  $\gamma'$  precipitates can be readily tailored by varying the cooling rate after a supersolvus soak.

2. At a cooling rate of approximately 3°C/min (5°F/min), the secondary  $\gamma'$  precipitates formed with a dendritic-shaped morphology. These precipitates have a mean lineal intercept of  $1.0 \pm 0.2 \mu\text{m}$  ( $3.9 \pm 0.6 \times 10^{-5}$  in), but can grow up to  $5 \mu\text{m}$  ( $1.97 \times 10^{-4}$  in) from tip to tip.
3. Tertiary  $\gamma'$  precipitates were cuboidal and approximately 40nm ( $1.6 \times 10^{-6}$  in) on edge after aging heat treatments for the alternate heat treatment material.
4. The standard (subsolvus) heat treatment resulted in cuboidal, secondary  $\gamma'$  that was approximately  $0.6 \pm 0.2 \mu\text{m}$  ( $2.5 \pm 0.7 \times 10^{-5}$  in). Aging heat treatments produced cuboidal tertiary  $\gamma'$  that was about  $230 \pm 48 \text{ nm}$  ( $9.1 \pm 1.9 \times 10^{-6}$  in) on edge and “quaternary”  $\gamma'$  that was approximately 40nm ( $1.6 \times 10^{-6}$  in) on edge.
5. The alternate heat treatment produced a larger grain size (ASTM 8.2) than the standard heat treatment (ASTM 11.8) due to solutioning of the primary  $\gamma'$  precipitates at the soak temperature. Additionally, the grains in the alternate heat treatment material formed coarse serrations during the heat treatment from the growth of the large secondary  $\gamma'$  precipitates.
6. The  $\gamma'$  volume fraction for both heat treatments was approximately 50%. For the alternate heat treatment, the primary and secondary  $\gamma'$  phase accounted for almost all of the  $\gamma'$  phase volume. However, in the standard heat treatment, the primary and secondary  $\gamma'$  phase accounted for about half  $\gamma'$  phase present and the tertiary  $\gamma'$  phase accounted for the other half.
7. The standard heat treatment had a greater hardness after both the solution and the aging heat treatments than the alternate heat treatment.
8. The standard heat treatment had longer fatigue lifetimes at the low and mid-range stress conditions, but shorter lifetimes at the greatest stress range.
9. The fatigue life was controlled by crack initiation at the low and middle stress ranges, but by crack propagation at the greatest stress range.
10. Grain size had the biggest effect on fatigue lifetimes.
11. The standard heat treatment had larger yield strengths, tensile strengths, and strengths at failure for all test temperatures. The larger amount of tertiary  $\gamma'$  plays an important role in this greater strength. Additionally, the smaller grains are a more effective barrier to dislocation motion.
12. The alternate heat treatment had more ductility at all test temperatures. This is also a result of the  $\gamma'$  morphology and the larger grains not being as effective a barrier to dislocation motion.
13. The standard heat treatment had longer creep lifetimes for both stress conditions at 677°C (1250°F). However, the alternate heat treatment had longer lifetimes for all

tests at 704°C (1300°F) and above. In general, the alternate heat treatment creep samples had greater values of total elongation at failure.

14. At the lower temperatures, dislocation motion was the primary mechanism for creep failure. The standard heat treatment had longer lifetimes.
15. At the higher temperatures, grain boundary sliding was the failure mechanism. The larger grain size and correspondingly lower grain boundary density of the alternate heat treatment was not affected by grain boundary sliding as much as the smaller grains in the standard heat treatment.

### **Future Work**

This research investigated the effect of a supersolvus heat treatment with a slow cooling rate on the microstructure and mechanical properties of a P/M Ni-base superalloy, Alloy 720LI. The supersolvus heat treatment did not perform as well in tensile and fatigue testing as hoped. However, this heat treatment was not completely refined. Further studies into the precipitation behavior of the secondary  $\gamma'$  particles in P/M Alloy 720LI would help understand the variety of  $\gamma'$  morphologies that can be achieved through variation in the heat treatment parameters. It would also be interesting to examine the tensile properties for a range of microstructures. This study suggests that most of the strengthening for the standard heat treatment is from the development of the tertiary  $\gamma'$  and not the secondary  $\gamma'$ . With a fast enough cooling rate from a supersolvus heat treatment temperature and subsequent aging at the proper temperatures, it may be possible to develop a fairly fine grained material with mostly tertiary  $\gamma'$  precipitates. Another interesting microstructure that could be developed is one similar to the alternate heat treatment in this study, but with a smaller grain size. This might be able to be accomplished if the soak time is reduced from 2 h.

The alternate heat treatment material did have a slower crack propagation rate during the fatigue testing as a result of its larger grain size. Since the alternate heat

treatment microstructure is much more ductile, it would be beneficial to compare the LCF lifetimes of the two heat treatments. It would also be important to perform HCF testing at lower and higher stress ranges as those in this study. This study was not able to establish the repeatability of the fatigue results for the alternate heat treatment. It is possible that this heat treatment's tendency to fracture at slip bands instead of processing defects means that its fatigue lifetimes are more repeatable than the standard heat treatment. Even with lower lifetimes, this repeatability would be a step towards developing the desired defect-tolerant microstructure. Fatigue crack growth testing would also help characterize the crack propagation rate and the toughness of the two heat treatments.

APPENDIX A  
DIFFERENTIAL THERMAL ANALYSIS GRAPHS

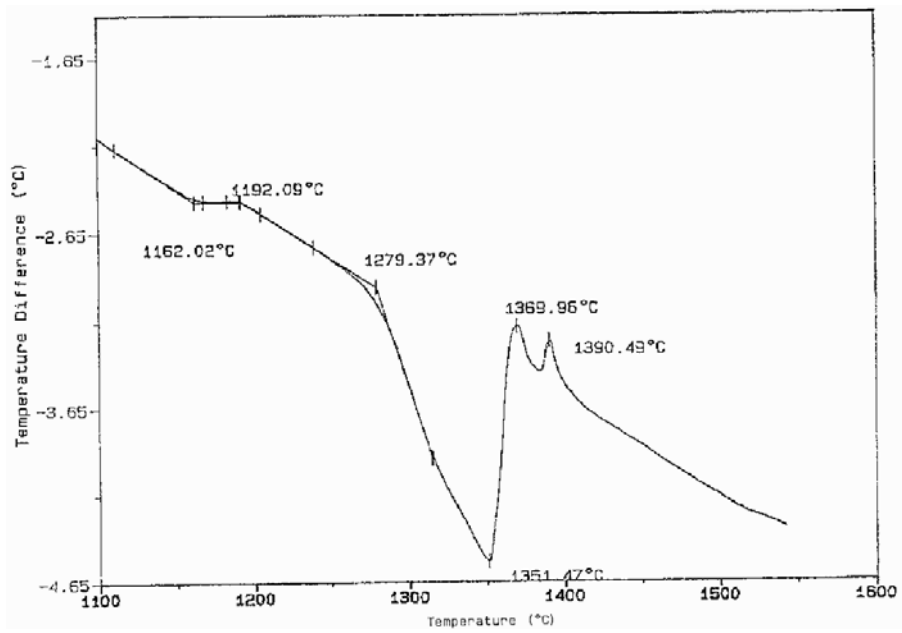


Figure A-1: The DTA Graph of sample UMBCa

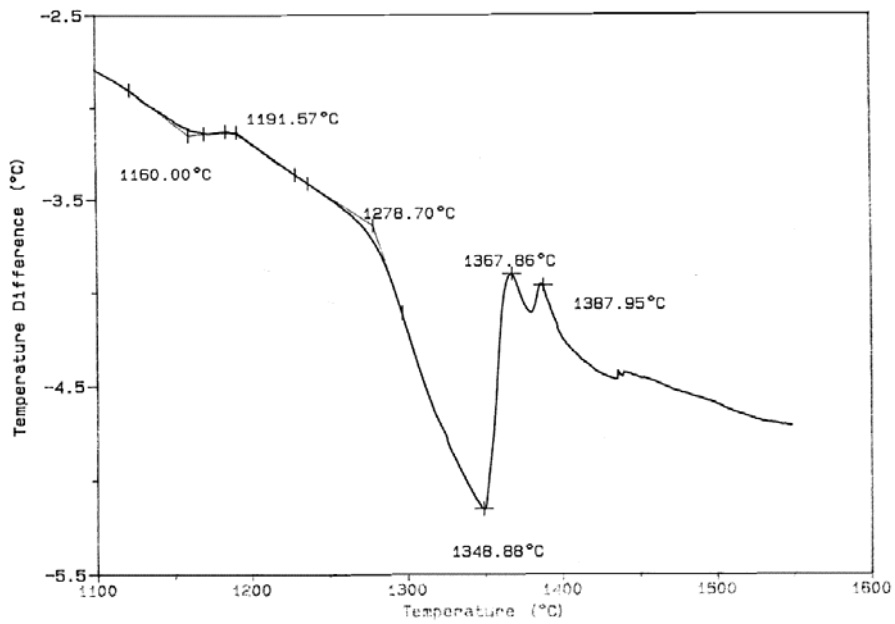


Figure A-2: The DTA graph of sample UMBCb

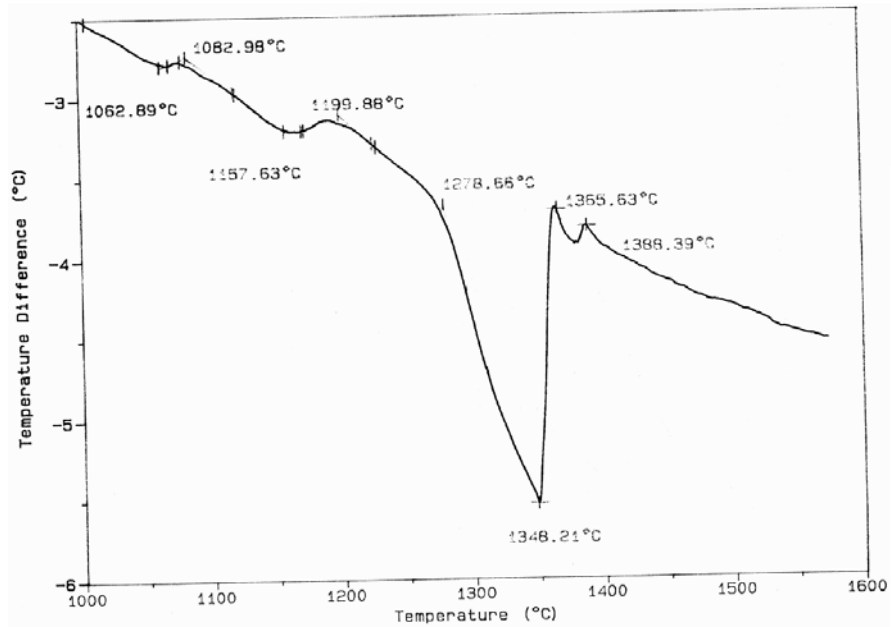


Figure A-3: The DTA graph of sample UMBEa

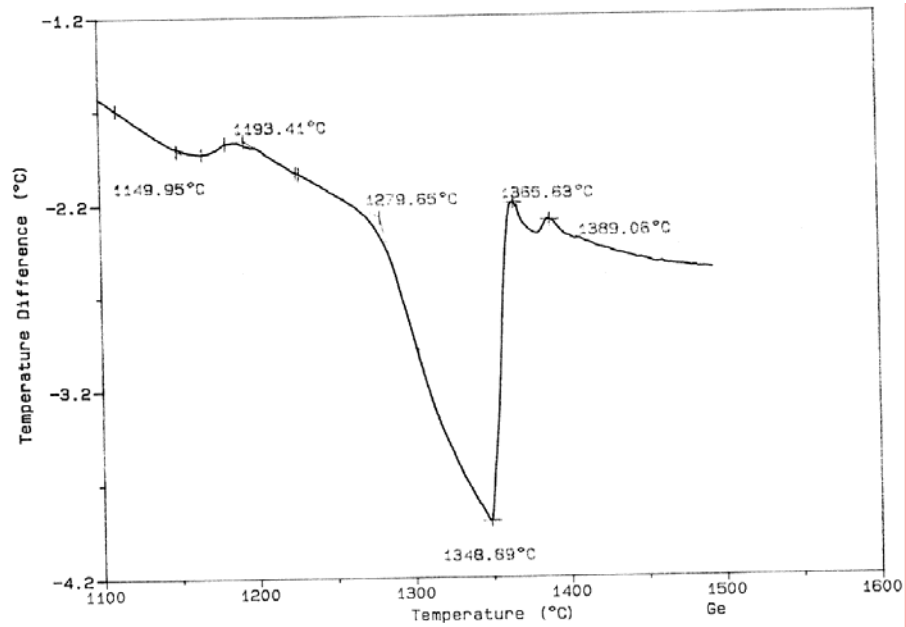


Figure A-4: The DTA graph of sample UMBEb

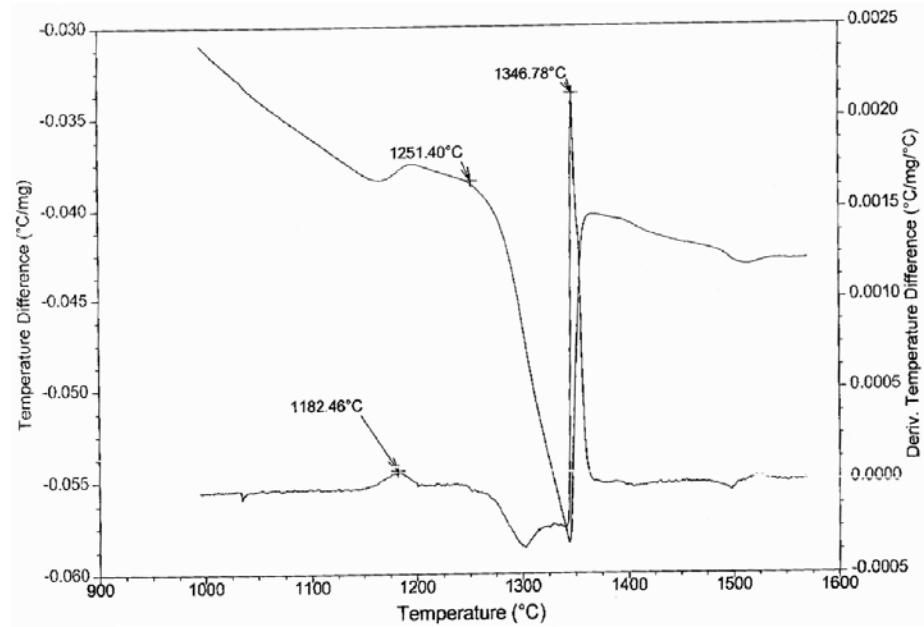


Figure A-5: The DTA graph of sample UMBCc

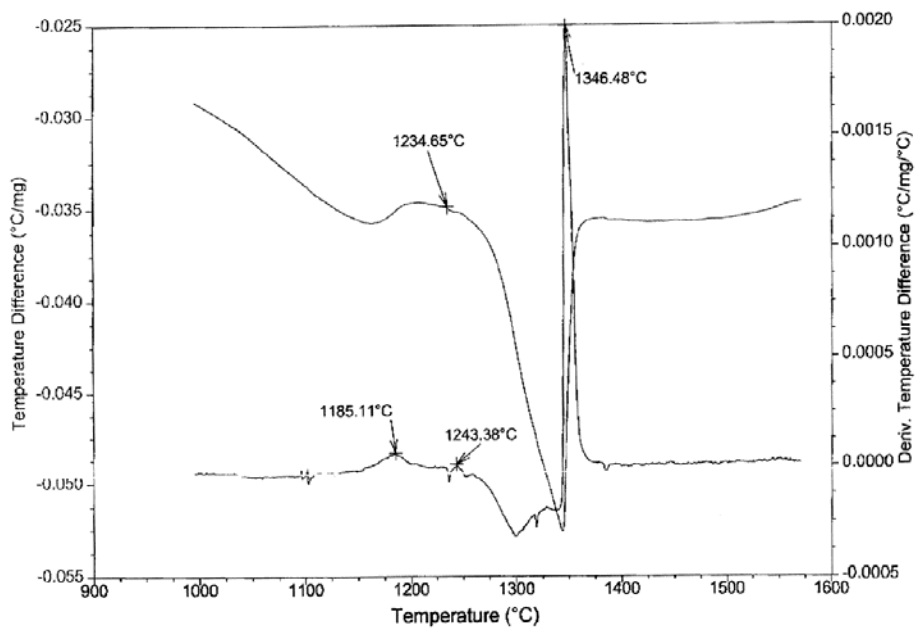


Figure A-6: The DTA graph of sample UMBEc

APPENDIX B  
STATISTICAL DATA

**Hardness Testing**

Rockwell C hardness testing was performed on an as-HIP sample as well as samples given the standard and alternate heat treatments, both before and after the aging heat treatment. In total, there were five different sets of hardness data. The individual measurements and the statistics for these measurements are given below in Table B-1.

Table B-1: The hardness testing statistical data

	As-HIP	Std. H.T. w/out Age	Std. H.T. w/ Age	Alt H.T. w/out Age	Alt H.T. w/ Age
1	37.4	42.3	45.4	40.4	42.9
2	37.2	42	46.1	39.7	43.2
3	37.1	42.8	45.4	39.7	42.7
4	38.4	42.4	45.7	39.9	43.3
5	38	42.5	46.5	39.7	42.5
6	38.5	42.4	46	39.8	42.7
7		42.5	46.1	40.3	43.3
8		43.3	45.4	40	42.8
9		42.7	45.6	40	43
10		42.3	45.4	39.8	43
Mean	37.8	42.5	45.8	39.9	42.9
Std. Dev.	0.615	0.352	0.392	0.250	0.272
t	2.571	2.262	2.262	2.262	2.262
95% CI	0.6	0.3	0.3	0.2	0.2

The standard deviation is given by the following equation:

$$s = \left[ \frac{1}{n-1} \sum_{i=1}^n [x(i) - \bar{x}]^2 \right]^{1/2} \quad (\text{B-1})$$

The 95% confidence interval is calculated by this equation:

$$95\%CI = t \times \frac{s}{\sqrt{n}} \quad (\text{B-2})$$

where the t parameter is estimated for the 95% confidence level according to the number of degrees of freedom for each data set.

In addition, t-tests were performed to determine whether these data sets are unique from one another. To accomplish this, the standard deviations of the two tests in question were weighted to determine the pooled sample estimator,  $s_p^2$ . The equation for this is as follows:

$$s_p^2 = \frac{(n_1 - 1)s_1^2 + (n_2 - 1)s_2^2}{n_1 + n_2 - 2} \quad (\text{B-3})$$

Then, the difference in the means is compared with a 95% confidence interval by Equation B-4:

$$(\bar{x}_1 - \bar{x}_2) \pm t_{\alpha/2} \sqrt{s_p^2 \left( \frac{1}{n_1} + \frac{1}{n_2} \right)} \quad (\text{B-4})$$

If this interval contains zero, then the two data sets are not distinctly statistically. The t-test values for the hardness tests are contained in Table B-2. All of these data sets were statistically distinct from each other.

Table B-2: The t-test data for the hardness testing

	$s_p^2$	t	Mean Difference	95% CI
As-HIP vs. Std.	0.215	2.145	4.75	0.51
As-HIP vs. Std. + Age	0.234	2.145	7.99	0.54
As-Hip vs. Alt.	0.175	2.145	2.16	0.46
As-HIP vs. Alt. + Age	0.183	2.145	5.17	0.47
Std. vs. Std. + Age	0.139	2.101	3.24	0.35
Std. vs. Alt.	0.093	2.101	2.59	0.29
Std. vs. Alt. + Age	0.099	2.101	0.42	0.30
Std. + Age vs. Alt.	0.108	2.101	5.83	0.31
Std. + Age vs. Alt. + Age	0.114	2.101	2.82	0.32
Alt. vs. Alt. + Age	0.068	2.101	3.01	0.25

### The Volume Fraction of the Gamma Prime Phase

The volume fraction of the  $\gamma'$  phase was calculated for each mode of precipitate present in each of the two heat treatments using ASTM Standard E562-99. Volume fractions were determined for the primary, secondary, and tertiary  $\gamma'$  in the standard heat treatment and for the primary and secondary  $\gamma'$  in the alternate heat treatment. The volume fraction of the tertiary  $\gamma'$  in the alternate heat treatment and the quaternary  $\gamma'$  in the standard heat treatment were assumed to be less than 1.0%. A circular grid of 24 points was superimposed onto each micrograph. The number of test points that fell within the respective  $\gamma'$  mode was counted and then divided by the total number of grid points. These values were then averaged for all ten fields of view. The standard deviation, the 95% confidence interval, and the percent relative accuracy were all calculated. The number of counts for each field of view (out of a total of 24 possible points), the volume fraction for each field of view ( $P_{P(i)}$ ), the average volume fraction for all of the fields of view ( $\bar{P}_p$ ), the standard deviation ( $s$ ),  $t$  parameter, and the 95% confidence interval are all listed in this table. The corresponding equations for these calculations are:

$$\bar{P}_p = \frac{1}{n} \sum_{i=1}^n P_p(i) \quad (\text{B-5})$$

$$s = \left[ \frac{1}{n-1} \sum_{i=1}^n [P_p(i) - \bar{P}_p]^2 \right]^{1/2} \quad (\text{B-6})$$

$$95\%CI = t \times \frac{s}{\sqrt{n}} \quad (\text{B-7})$$

where  $n$  is the total number of fields of view and  $t$  is the same parameter described in the hardness testing section. The calculations for each of the different modes of  $\gamma'$  are contained in Tables B-3 through B-7.

Table B-3: The primary  $\gamma'$  volume fraction data for the standard heat treatment

Point Counts	$P_p(i)$	$\bar{P}_p$	Std. Dev.	$t$	95%CI
4	16.7	17.3	3.68	2.262	2.63
5	20.8				
3	12.5				
4	16.7				
5	20.8				
5	20.8				
4	16.7				
2.5	10.4				
4	16.7				
5	20.8				

Table B-4: The secondary  $\gamma'$  volume fraction data for the standard heat treatment

Point Counts	$P_p(i)$	$\bar{P}_p$	Std. Dev.	$t$	95% CI
2	8.33	8.75	2.37	2.262	1.69
3	12.5				
3	12.5				
2	8.33				
1.5	6.25				
2	8.33				
1.5	6.25				
2.5	10.4				
1.5	6.25				
2	8.33				

Table B-5: The tertiary  $\gamma'$  volume fraction data for the standard heat treatment

Point Counts	$P_p(i)$	$\bar{P}_p$	Std. Dev.	t	95% CI
6	25.0	24.6	5.45	2.262	3.90
7	29.2				
6.5	27.1				
4	16.7				
8	33.3				
5.5	22.9				
5	20.8				
7	29.2				
6	25.0				
4	16.7				

Table B-6: The primary  $\gamma'$  volume fraction data for the alternate heat treatment

Point Counts	$P_p(i)$	$\bar{P}_p$	Std. Dev.	t	95% CI
0.0	0.00	5.73	4.73	2.093	2.21
0.0	0.00				
1.0	4.17				
1.5	6.25				
1.0	4.17				
2.0	8.33				
0.0	0.00				
1.0	4.17				
0.0	0.00				
4.0	16.7				
2.5	10.4				
1.5	6.25				
2.0	8.33				
2.0	8.33				
2.5	10.4				
0.0	0.00				
1.0	4.17				
2.0	8.33				
0.5	2.08				
3.0	12.5				

Table B-7: The secondary  $\gamma'$  volume fraction data for the alternate heat treatment

Point Counts	$P_p(i)$	$\bar{P}_p$	Std. Dev.	t	95% CI
14	58.3	43.9	9.43	2.093	4.41
11.5	47.9				
8	33.3				
9	37.5				
9.5	39.6				
14.5	60.4				
14.5	60.4				
12	50.0				
12	50.0				
8.5	35.4				
8	33.3				
11.5	47.9				
9.5	39.6				
9.5	39.6				
8.5	35.4				
13.5	56.3				
10	41.7				
9	37.5				
10	41.7				
7.5	31.3				

### Gamma Prime Size Distributions

In addition to their volume fractions, the average size of each mode of  $\gamma'$  precipitates in the two heat treatments was calculated. Once again, the tertiary  $\gamma'$  in the alternate heat treatment and the quaternary  $\gamma'$  in the standard heat treatment were not analyzed because of their small volume fraction. A line of known length was superimposed on the micrographs and the number of intercepts between the line and the  $\gamma'$  precipitates were counted. The mean ( $\langle x \rangle$ ), standard deviation, and confidence interval for the number of intercepts were calculated. The average number of counts per  $\mu\text{m}$  ( $\langle P_L \rangle$ ) was calculated by dividing  $\langle x \rangle$  by the total line length. The surface area ( $S_V$ ) of the precipitates was taken as twice this value. Finally, the mean lineal intercept was calculated according to the following equation:

$$\langle \lambda \rangle = \frac{4V_v}{S_v} \tag{B-8}$$

where  $V_v$  is the volume fraction of that mode of  $\gamma'$ . This mean lineal intercept is equivalent to the average precipitate size. The data for these calculations is in Tables B-8 through B-12.

Table B-8: The primary  $\gamma'$  size data for the standard heat treatment

Intercepts	$\langle x \rangle$	Std. Dev.	Line Length ( $\mu\text{m}$ )	$\langle P_L \rangle$ ( $1/\mu\text{m}$ )	$S_v$ ( $1/\mu\text{m}$ )	$\langle \lambda \rangle$ ( $\mu\text{m}$ )	95% CI
3	6.4	2.7	31.9	0.20	0.40	1.71	0.39
9							
4							
8							
5							
8							
5							
5							
11							

Table B-9: The secondary  $\gamma'$  size data for the standard heat treatment

Intercepts	$\langle x \rangle$	Std. Dev.	Line Length ( $\mu\text{m}$ )	$\langle P_L \rangle$ ( $1/\mu\text{m}$ )	$S_v$ ( $1/\mu\text{m}$ )	$\langle \lambda \rangle$ ( $\mu\text{m}$ )	95% CI
12	8.9	4.1	31.9	0.28	0.56	0.63	0.17
12							
15							
5							
5							
9							
12							
7							
3							

Table B-10: The tertiary  $\gamma'$  size data for the standard heat treatment

Intercepts	$\langle x \rangle$	Std. Dev.	Line Length ( $\mu\text{m}$ )	$\langle P_L \rangle$ ( $1/\mu\text{m}$ )	$S_V$ ( $1/\mu\text{m}$ )	$\langle \lambda \rangle$ ( $\mu\text{m}$ )	95% CI
6	6.8	4.0	3.19	2.12	4.25	.232	.048
2							
3							
6							
3							
7							
15							
6							
13							
3							
13							
3							
14							
5							
3							
6							
0							
10							
4							
7							
9							
9							
12							
11							
11							
8							
4							
3							
3							
4							

Table B-11: The primary  $\gamma'$  size data for the alternate heat treatment

Intercepts	$\langle x \rangle$	Std. Dev.	Line Length ( $\mu\text{m}$ )	$\langle P_L \rangle$ ( $1/\mu\text{m}$ )	$S_V$ ( $1/\mu\text{m}$ )	$\langle \lambda \rangle$ ( $\mu\text{m}$ )	95% CI
0	1.9	2.3	24.0	0.079	0.158	1.45	0.62
1							
1							
2							
2							
0							
4							
0							
0							
0							
2							
4							
0							
8							
4							
2							
2							
0							
2							
0							
2							
0							
2							
2							
7							
0							
2							
8							
0							
0							

Table B-12: The secondary  $\gamma'$  size data for the alternate heat treatment

Intercepts	$\langle x \rangle$	Std. Dev.	Line Length ( $\mu\text{m}$ )	$\langle P_L \rangle$ ( $1/\mu\text{m}$ )	$S_V$ ( $1/\mu\text{m}$ )	$\langle \lambda \rangle$ ( $\mu\text{m}$ )	95% CI
21	20.8	2.25	24.0	0.87	1.73	1.01	0.15
25							
20							
22							
20							
18							
24							
20							
19							
19							

### Grain Size

The average ASTM grain size was calculated using the Abrams Three-Circle Procedure found in ASTM standard E112. Three concentric circles with a total circumference length of 500 mm were superimposed on a micrograph. The number of intersections between a grain boundary and the circles ( $P_1$ ) were counted. Five fields of view were analyzed for each heat treatment. For each field of view, the number of grain boundary intersections per unit line ( $\langle P_L \rangle$ ) were calculated by:

$$\langle P_L \rangle = \frac{\langle x \rangle}{L/M} \quad (\text{B-9})$$

where  $L$  is the total test line length (500mm) and  $M$  is the magnification. With this value, the mean lineal intercept value for each field,  $\langle \lambda \rangle$ , by:

$$\langle \lambda \rangle = \frac{1}{P_L} \quad (\text{B-10})$$

The average grain size was then calculated by averaging the number of grain boundary intersections per unit line over the five fields of view. The grain size was calculated using the following equation:

$$G = (6.64 \log_{10} \langle P_L \rangle) - 3.3 \quad (\text{B-11})$$

After determining the average grain size, the standard deviation, the 95% confidence interval, and the percent relative accuracy were all determined in the same manner as the volume fraction described previously. The data for the grain size calculations are contained in Table B-13 and Table B-14.

Table B-13: The grain size data for the standard heat treatment

Intercepts	$\langle x \rangle$	Std. Dev.	Line Length ( $\mu\text{m}$ )	$\langle P_L \rangle$ ( $1/\mu\text{m}$ )	$\langle \lambda \rangle$ ( $\mu\text{m}$ )	95% CI	ASTM Grain Size
53	55.8	6.46	299	0.19	5.35	0.77	11.8
59							
65							
48							
54							

Table B-14: The grain size data for the alternate heat treatment

Intercepts	$\langle x \rangle$	Std. Dev.	Line Length ( $\mu\text{m}$ )	$\langle P_L \rangle$ ( $1/\mu\text{m}$ )	$\langle \lambda \rangle$ ( $\mu\text{m}$ )	95% CI	ASTM Grain Size
50	49.4	3.44	909	0.054	18.4	1.6	8.2
46							
48							
48							
55							

### Stress Intensity Factors

A statistical analysis was performed on the initial crack stress intensity factors to determine whether the data for the standard heat treatment was distinct from the data for the alternate heat treatment. As with the hardness testing data, a t-test was performed to determine this. The eight data points for  $K_{\max}$  of the standard heat treatment were compared against the six data points for  $K_{\max}$  of the alternate heat treatment. Table B-15 contains the pertinent data for this study. When the confidence interval is added or subtracted to the difference in means, the resulting range does not contain zero. The two data sets have distinctly different means.

Table B-15: The t-test data for the initial crack stress intensity factors

	$\langle K_{\max} \rangle$ ( $\text{MPa} \cdot \text{m}^{0.5}$ )	Std. Dev.	$s_p^2$	t	Mean Difference	95% CI
Standard H.T.	11.4	0.72	0.32	2.179	3.0	0.67
Alternate H.T.	14.4	0.05				

APPENDIX C  
TENSILE FRACTURE MECHANICS

As with the fatigue fracture surfaces, the crack dimensions for the flaws that eventually led to tensile failure was measured when possible. Due to difficulty in locating the crack initiation point on samples UCA24, UCB4, and UCB2, it was not possible to measure the crack depth of these samples. The crack depth measured for the rest of the samples is contained in Table C-1. It should be noted that measurements of the crack dimensions for the tensile fracture surfaces was much more difficult than with the fatigue fracture surfaces. The crack area was not as distinct as with the fatigue samples. This is in part because of the difference in fracture and crack growth between tensile testing and fatigue testing. In fatigue testing, there is a period of slow deformation and crack growth followed by fast fracture at overload. Tensile testing, on the other hand, contains large amounts of plastic deformation during a fast fracture mode at overload.

Table C-1: Area of crack in fractured tensile specimens

Sample	Temp. (°C)	YS (MPa)	UTS (MPa)	Crack Depth
Standard Heat Treatment				
UCA4	25	1225	1710	54 $\mu\text{m}$
UCA23	25	1241	1696	84 $\mu\text{m}$
UCA5	649	1087	1471	0.38 mm
UCA7	649	1103	1476	0.40 mm
UCA8	760	1018	1180	130 $\mu\text{m}$
UCA10	760	1069	1145	35 $\mu\text{m}$
Alternate Heat Treatment				
UCB21	25	1066	1568	65 $\mu\text{m}$
UCB5	649	887	1395	0.41 mm
UCB3	760	827	1123	77 $\mu\text{m}$
UCB8	760	780	1103	63 $\mu\text{m}$

From these data, an approximate stress intensity factor at failure was calculated based on the estimated flaw size and the ultimate tensile strength. Results are shown in Table C-2. While it was more difficult to measure the crack size in the fractured tensile

Table C-2: Stress intensity factor for tensile tests

Sample	Temp. (°C)	UTS (MPa)	Elongation (%)	$K_{\max}$ (MPa*m <sup>0.5</sup> )
Standard Heat Treatment				
UCA4	25	1710	23.3	18
UCA23	25	1696	21.1	19
UCA5	649	1471	23.0	40
UCA7	649	1476	22.4	37
UCA8	760	1180	11.1	8
UCA10	760	1145	10.7	17
Alternate Heat Treatment				
UCB21	25	1568	25.3	16
UCB5	649	1395	26.0	35
UCB3	760	1123	17.1	12
UCB8	760	1103	17.4	11

samples compared to the fatigue samples, the stress intensity factors calculated for the tensile samples at 649°C and the fatigue samples at 649°C are similar. Additionally, it follows that the stress intensity factor at failure would drop dramatically at 760°C as a result of the large drop in ultimate tensile strength and total elongation. However, the results of a similar analysis for the room temperature tests do not exhibit a good correlation with the expected stress intensity factor at overload. The stress intensity factor at failure in these tests should be closer to the values at 649°C, but are much lower than expected. This is probably due to the difficulty in measuring tensile fracture features on a sample that has undergone heavy plastic deformation and the very different types of deformation during tensile and fatigue testing.

## LIST OF REFERENCES

1. R. Schafrik and R. Sprague, "Saga of Gas Turbine Materials: Part I," *Advanced Materials & Processes*, **162**, No. 3, 2004, pp. 33-36.
2. C. T. Sims, "Superalloys: Genesis and Character," *Superalloys II*, eds. C. T. Sims, N. S. Stoloff, and W. C. Hagel, Wiley, New York, New York 1987, pp. 3-26.
3. Eds. J. R. Davis and Davis & Associates, "Metallurgy, Processing, and Properties of Superalloys," *Heat-Resistant Materials*, ASM-International, Materials Park, Ohio, 1997, pp. 221-254.
4. E. W. Ross and C. T. Sims, "Nickel-Base Alloys," *Superalloys II*, eds. C. T. Sims, N. S. Stoloff, and W. C. Hagel, Wiley, New York, New York, 1987, pp. 97-133.
5. H. E. Miller and W. L. Chambers, "Gas Turbine Design and Superalloys," *Superalloys II*, eds. C. T. Sims, N. S. Stoloff, and W. C. Hagel, Wiley, New York, New York, 1987, pp. 27-57.
6. R. Schafrik and R. Sprague, "Saga of Gas Turbine Materials: Part II," *Advanced Materials & Processes*, **162**, No. 4, 2004, pp. 27-30.
7. N. S. Stoloff, "Wrought and P/M Superalloys," *ASM Handbook*, **1**, ASM-International, Materials Park, Ohio, 1993.
8. R. W. Guard and J. H. Westbrook, "Alloying Behavior of Ni<sub>3</sub>Al ( $\gamma'$  phase)," *Transactions of the Metallurgical Society of AIME*, **215**, 1959, pp. 807-814.
9. R. G. Davies and N. S. Stoloff, "On the Yield Stress of Aged Ni-Al Alloys," *Transactions of the Metallurgical Society of AIME*, **233**, 1965, pp. 714-719.
10. R. W. K. Honeycombe, *The Plastic Deformation of Metals*, 2<sup>nd</sup> ed., Edward Arnold, London, England, 1984.
11. G. E. Dieter, *Mechanical Metallurgy*, 3<sup>rd</sup> ed., McGraw-Hill, Boston, Massachusetts, 1986.
12. N. S. Stoloff, "Fundamentals of Strengthening," *Superalloys II*, Eds. C. T. Sims, N. S. Stoloff, and W. C. Hagel, Wiley, New York, New York, 1987, pp. 61-96.

13. J. E. Dorn, P. Pietrokowsky, and T. E. Tietz, "The Effect of Alloying Elements on the Plastic Properties of Aluminum Alloys," *Transactions of AIME*, **188**, 1950, pp. 933-943.
14. W. R. Hibbard, Jr., "Solid Solution Hardening," *Transactions of AIME*, **212**, 1958, pp. 1-5.
15. R. M. Pelloux and N. J. Grant, "Solid Solution and Second Phase Strengthening of Nickel Alloys at High and Low Temperatures," *Transactions of the Metallurgical Society of AIME*, **218**, 1960, pp. 232-237.
16. R. L. Fleischer, "Substitutional Solution Hardening," *Acta Metallurgica*, **11**, 1963, pp. 203-209.
17. G. H. Gessinger, Powder Metallurgy of Superalloys, Butterworths, London, England, 1984.
18. V. A. Tracey, G. T. Poyner, and J. F. Watkinson, *Journal of Metals*, **13**, 1961, pp. 363-369.
19. B. Ewing, F. Rizzo, and C. zurLippe, "Powder Metallurgy Products for Advanced Gas Turbine Applications," Superalloys 1972, The Metallurgical Society of AIME, 1972, pp. BB1-BB20.
20. Eds. J. R. Davis and Davis & Associates, "Powder Metallurgy Superalloys," Heat-Resistant Materials, ASM-International, Materials Park, Ohio, 1997, pp. 272-289.
21. R. D. Eng and D. J. Evans, "High Strength HIP Consolidated Merl 76 Disks," Superalloys 1980, Eds. J. K. Tien, S. T. Wlodek, H. Morrow III, M. Gell, and G. E. Maurer, The Metallurgical Society of AIME, 1980, pp. 491-500.
22. J. H. Moll and B. McTiernan, "Powder Metallurgy Superalloys," ASM Handbook, **7**, ASM-International, Materials Park, Ohio, 1993.
23. L. N. Moskowitz, R. M. Pelloux, and N. J. Grant, "Properties of IN-100 Processed by Powder Metallurgy," Superalloys 1972, The Metallurgical Society of AIME, 1972, pp. Z1-Z25.
24. S. Reichman and D. S. Chang, "Powder Metallurgy," Superalloys II, Eds. C.T. Sims, N. S. Stoloff, and W. C. Hagel, Wiley, New York, New York, 1987, pp. 459-493.
25. R. M. German, Powder Metallurgy Science, 2<sup>nd</sup> ed., Metal Powder Industries Federation, Princeton, New Jersey, 1994.
26. G. Raisson and Y. Honnorat, "P.M. Superalloy for High Temperature Components," Superalloys 1976, Eds. B. H. Kear, D. R. Muzyka, J. K. Tien, and S. T. Wlodek, The Metallurgical Society of AIME, 1976, pp. 473-482.

27. J. H. Moll and J. J. Conway, "Characteristics and Properties of As-HIP P/M Alloy 720," Superalloys 2000, Eds. T. M. Pollock, R. D. Kissinger, R. R. Bowman, K. A. Green, M. McLean, S. L. Olson, and J. J. Schirra TMS, 2000, pp. 135-142.
28. C. A. Morris and J. W. Smythe, "Comparison of Astroloy Powder Consolidation Processes, Forging, and Testing of Astroloy Powder Billet," Superalloys 1972, The Metallurgical Society of AIME, 1972, pp. Y1-Y26.
29. J. F. Barker and E. H. VanDerMolen, "Effect of Processing Variables on Powder-Metallurgy René 95," Superalloys 1972, The Metallurgical Society of AIME, 1972, pp. AA1-AA23.
30. J. D. Buzzanell and L. W. Lherbier, "Processing Effects on the Properties of P/M René 95 Near Net Shapes," Superalloys 1980, Eds. J. K. Tien, S. T. Wlodek, H. Morrow III, M. Gell, and G. E. Maurer, The Metallurgical Society of AIME, 1980, pp. 149-158.
31. J. N. Fleck, V. K. Chandhok, and L. P. Clark, "HIP of Near-Net Turbine Disks," Superalloys 1976, Eds. B. H. Kear, D. R. Muzyka, J. K. Tien, and S. T. Wlodek, The Metallurgical Society of AIME, 1976, pp. 509-521.
32. J. J. Conway and F. J. Rizzo, "Hot Isostatic Pressing of Metal Powders," ASM Handbook, 7, ASM-International, Materials Park, Ohio, 1993.
33. E. Arzt, M. F. Ashby, and K. E. Easterling, "Practical Applications of Hot-Isostatic Pressing Diagrams: Four Case Studies," *Metallurgical Transactions A*, **14A**, 1983, pp. 211-221.
34. J. L. Bartos and P. S. Mathur, "Development of Hot Isostatically Pressed (As-HIP) Powder Metallurgy René 95 Turbine Hardware," Superalloys 1976, Eds. B. H. Kear, D. R. Muzyka, J. K. Tien, and S. T. Wlodek, The Metallurgical Society of AIME, 1976, pp. 495-508.
35. W. Betz, B. Borchert, and W. Track, "Comparative Assessment of PM Material For Turbine Disks," Superalloys 1980, Eds. J. K. Tien, S. T. Wlodek, H. Morrow III, M. Gell, and G. E. Maurer, The Metallurgical Society of AIME, 1980, pp. 643-650.
36. K. R. Bain and R. M. Pelloux, "Effect of Oxygen on Creep Crack Growth in PM/HIP Nickel-Base Superalloys," Superalloys 1984, Eds. M. Gell, C. S. Kortovich, R. H. Bricknell, W. B. Kent, and J. F. Radavich, The Metallurgical Society of AIME, 1984, pp. 387-396.
37. D. M. Carlson, "P/M AF115 Dual Property Disk Process Development," Superalloys 1980, Eds. J. K. Tien, S. T. Wlodek, H. Morrow III, M. Gell, and G. E. Maurer, The Metallurgical Society of AIME, 1980, pp. 501-511.

38. R. D. Kissinger, S. V. Nair, and J. K. Tien, "Influence of Powder Particle Size Distribution and Pressure on the Kinetics of Hot Isostatic Pressing (HIP) Consolidation of P/M Superalloy René 95," Superalloys 1984, Eds. M. Gell, C. S. Kortovich, R. H. Bricknell, W. B. Kent, and J. F. Radavich, The Metallurgical Society of AIME, 1984, pp. 285-294.
39. D. R. Chang, D. D. Krueger, and R. A. Sprague, "Superalloy Powder Processing, Properties and Turbine Disk Applications," Superalloys 1984, Eds. M. Gell, C. S. Kortovich, R. H. Bricknell, W. B. Kent, and J. F. Radavich, The Metallurgical Society of AIME, 1984, pp. 245-273.
40. C. Aubin, J. H. Davidson, and J. P. Trottier, "The Influence of Powder Particle Surface Composition on the Properties of a Nickel-Based Superalloy Produced by Hot Isostatic Pressing," Superalloys 1980, Eds. J. K. Tien, S. T. Wlodek, H. Morrow III, W. B. Kent, and J. F. Radavich, The Metallurgical Society of AIME, 1980, pp. 345-354.
41. G. E. Maurer, W. Castledine, F. A. Schweizer, S. Mancuso, "Development of HIP Consolidated P/M Superalloys for Conventional Forging to Gas Turbine Engine Components," Superalloys 1996, eds. R. D. Kissinger, D. J. Deye, D. L. Anton, A. D. Cetel, M. V. Nathal, T. M. Pollock, and D. A. Woodford, TMS, 1996, pp. 645-652.
42. M. Dahlén and H. Fischmeister, "Carbide Precipitation in Superalloys," Superalloys 1980, Eds. J. K. Tien, S. T. Wlodek, H. Morrow III, M. Gell, and G. E. Maurer, The Metallurgical Society of AIME, 1980, pp. 449-454.
43. W. H. Chang, H. M. Green, and R. A. Sprague, "Defect Analyses of P/M Superalloys," Rapid Solidification Processing Principles and Technologies III, Ed. R. Mehrabian, Bureau of Standards, 1982, pp. 500-509.
44. S. V. Nair and J. K. Tien, "Densification Mechanism Maps for Hot Isostatic Pressing (HIP) of Unequal Sized Particles," *Metallurgical Transactions A*, **18A**, 1987, pp. 97-107.
45. J. C. Borofka, R. D. Kissinger, and J. K. Tien, "HIP Modeling of Superalloy Powders," Superalloys 1988, Eds. S. Reichman, D. N. Duhl, G. Maurer, S. Antolovich, and C. Lund, TMS, 1988, pp. 111-120.
46. D. U. Furrer, "A Review of U720LI Alloy and Process Development," Materials Design Approaches and Experiences, Eds. J.-C. Zhao, M. Fahrman, and T. M. Pollock, TMS, Warrendale, Pennsylvania, 2001, pp. 281-296.
47. F. E. Sczerzenie and G. E. Maurer, "Development of Udimet 720 For High Strength Disk Applications," Superalloys 1984, Eds. J. K. Tien, S. T. Wlodek, H. Morrow III, M. Gell, and G. E. Maurer, The Metallurgical Society of AIME, 1984, pp. 573-580.

48. K. R. Bain, M. L. Gambone, J. M. Hyzak, and M. C. Thomas, "Development of Damage Tolerant Microstructures in Udimet 720," *Superalloys 1988*, Eds. S. Reichman, D. N. Duhal, G. Maurer, S. Antolovich, and C. Lund, TMS, 1988, pp. 13-22.
49. G. A. Whitlow, C. G. Beck, R. Viswanathan, and E. A. Crombie, "The Effects of a Liquid Sulfate/Chloride Environment on Superalloy Stress Rupture Properties at 1300 °F (704 °C)," *Metallurgical Transactions A*, **15A**, 1984, pp. 23-28.
50. P. W. Keefe, S. O. Mancuso, and G. E. Maurer, "Effects of Heat Treatment and Chemistry on the Long-Term Phase Stability of a High Strength Nickel-Based Superalloy," *Superalloys 1992*, Eds. S. D. Antolovich, R. W. Stusrud, R. A. MacKay, D. L. Anton, T. Khan, R. D. Kissinger, D. L. Klarstrom, TMS, 1992, pp. 487-496.
51. J. R. Mihalisin, C. G. Bieber, and R. T. Grant, "Sigma-Its Occurrence, Effect, and Control in Nickel-Base Superalloys," *Transactions of the Metallurgical Society of AIME*, **242**, 1968, pp. 2399-2414.
52. R. C. Reed, M. P. Jackson, and Y. S. Na, "Characterization and Modeling of the Precipitation of the Sigma Phase in UDIMET 720 and UDIMET 720LI," *Metallurgical and Materials Transactions A*, **30A**, 1999, pp. 521-533.
53. N. Saunders, "Phase Diagram Calculations for Ni-Based Superalloys," *Superalloys 1996*, Eds. R. D. Kissinger, D. J. Deye, D. L. Anton, A. D. Cetel, M. V. Nathal, T. M. Pollock, and D. A. Woodford, TMS, 1996, pp. 101-110.
54. D. J. Bryant and D. G. McIntosh, "The Manufacture and Evaluation of a Large Turbine Disc in Cast and Wrought Alloy 720LI," *Superalloys 1996*, Eds. R. D. Kissinger, D. J. Deye, D. L. Anton, A. D. Cetel, M. V. Nathal, T. M. Pollock, and D. A. Woodford, TMS, 1996, pp. 713-722.
55. H. Hattori, M. Takekawa, D. Furrer, and R. J. Noel, "Evaluation of P/M U720 for Gas Turbine Engine Disk Application," *Superalloys 1996*, Eds. R. D. Kissinger, D. J. Deye, D. L. Anton, A. D. Cetel, M. V. Nathal, T. M. Pollock, and D. A. Woodford, TMS, 1996, pp. 705-711.
56. M. P. Jackson and R. C. Reed, "Heat Treatment of UDIMET 720Li: The Effect of Microstructure on Properties," *Materials Science & Engineering A*, **A259**, 1999, pp. 85-97.
57. J. Mao and K. Chang, "Growth Kinetics of  $\gamma'$  Precipitates in P/M Superalloys," *Materials Design Approaches and Experiences*, Eds. J.-C. Zhao, M. Fahrman, and T. M. Pollock, TMS, Warrendale, Pennsylvania, 2001, pp. 309-319.
58. D. Furrer and H. Fecht, " $\gamma'$  Formation in Superalloy U720LI," *Scripta Materialia*, **40**, 1999, pp. 1215-1220.

59. D. Furrer and H. Fecht, "Superalloys for Turbine Disc Applications," *JOM*, **51**, 1999, pp. 14-17.
60. K. A. Green, J. A. Lemsky, and R. M. Gasior, "Development of Isothermally Forged P/M Udimet 720 for Turbine Disk Applications," *Superalloys 1996*, Eds. R. D. Kissinger, D. J. Deye, D. L. Anton, A. D. Cetel, M. V. Nathal, T. M. Pollock, and D. A. Woodford, TMS, 1996, pp. 697-703.
61. S. E. Kim, M. P. Jackson, R. C. Reed, C. Small, A. James, and N. K. Park, "Quantification of the Minor Precipitates in UDIMET™ Alloy 720(LI) Using Electrolytic Extraction and X-ray Diffraction," *Materials Science and Engineering A*, **A245**, 1998, pp. 225-232.
62. M. F. Henry, Y. S. Yoo, D. Y. Yoon, and J. Choi, "The Dendritic Growth of  $\gamma$ ' Precipitates and Grain Boundary Serration in a Model Nickel-Base Superalloy," *Metallurgical Transactions A*, **24A**, 1993, pp. 1733-1743.
63. D. Furrer and H. Fecht, "Microstructure and Mechanical Property Development in Superalloy U720LI," *Superalloys 2000*, Eds. T. M. Pollock, R. D. Kissinger, R. R. Bowman, K. A. Green, M. McLean, S. L. Olson, and J. J. Schirra, TMS, 2000, pp. 415-424.
64. H. L. Danflou, M. Marty, and A. Walder, "Formation of Serrated Grain Boundaries and Their Effect on the Mechanical Properties in a P/M Nickel Base Superalloy," *Superalloys 1992*, Eds. S. D. Antolovich, R. W. Stusrud, R. A. MacKay, D. L. Anton, T. Khan, R. D. Kissinger, and D. L. Klarstrom, TMS, 1992, pp. 63-72.
65. H. L. Danflou, M. Macia, T. H. Sanders, and T. Khan, "Mechanisms of Formation of Serrated Grain Boundaries in Nickel Base Superalloys," *Superalloys 1996*, Eds. R. D. Kissinger, D. J. Deye, D. L. Anton, A. D. Cetel, M. V. Nathal, T. M. Pollock, and D. A. Woodford, TMS, 1996, pp. 119-127.
66. ASTM Standard E 562-99, "Standard Test Method for Determining Volume Fraction by Systematic Manual Point Count," *2001 Annual Book of ASTM Standards*, **3.01**, ASTM, West Conshohocken, Pennsylvania, 2001, pp. 538-543.
67. ASTM Standard E 112-96, "Standard Test Methods for Determining Average Grain Size," *2001 Annual Book of ASTM Standards*, **3.01**, ASTM, West Conshohocken, Pennsylvania, 2001, pp. 237-259.
68. ASTM Standard E 930-99, "Standard Test Methods for Estimating the Largest Grain Observed in a Metallographic Section (ALA Grain Size)," *2001 Annual Book of ASTM Standards*, **3.01**, ASTM, West Conshohocken, Pennsylvania, 2001, pp. 712-717.
69. D. L. Sponseller, "Differential Thermal Analysis of Nickel-Base Superalloys," *Superalloys 1996*, Eds. R. D. Kissinger, D. J. Deye, D. L. Anton, A. D. Cetel, M. V. Nathal, T. M. Pollock, and D. A. Woodford, TMS, 1996, pp. 259-270.

70. R. A. Ricks, A. J. Porter, and R. C. Ecob, "The Growth of  $\gamma$ ' Precipitates in Nickel-Base Superalloys," *Acta Metallurgica*, **31**, 1983, pp. 43-53.
71. "Fatigue and Fracture Mechanics," ASM Handbook, **8**, ASM-International, Materials Park, Ohio, 2003.
72. V. Kerlins, "Modes of Fracture," ASM Handbook, **12**, ASM-International, Materials Park, Ohio, 2003.
73. T. L. Anderson, Fracture Mechanics, CRC Press, Boca Raton, Florida, 1991.
74. J. E. King, "Effects of Grain Size and Microstructure on Threshold Values and Near Threshold Crack Growth in Powder-formed Ni-base Superalloy," *Metal Science*, **16**, 1982, pp. 345-355.
75. A. Banik and K. Green, "The Mechanical Property Response of Turbine Disks Produced Using Advanced PM Processing Techniques," Superalloys 2000, Eds. T. M. Pollock, R. D. Kissinger, R. R. Bowman, K. A. Green, M. McLean, S. L. Olson, and J. J. Schirra, TMS, 1996, pp. 69-74.
76. R. W. Herzberg, Deformation and Fracture Mechanics of Engineering Materials, 5<sup>th</sup> ed., Wiley, New York, New York, 1996.

## BIOGRAPHICAL SKETCH

Darryl Slade Stolz was born in New Orleans, LA, in September of 1976. He graduated from Jesuit High School in New Orleans, LA, in May 1994. He then matriculated at the University of Notre Dame in South Bend, IN. While a student there, Slade was a member of the Men's Swimming Team, participating in the sprint freestyle and butterfly events. He graduated Cum Laude with a Bachelor of Science degree in chemical engineering, in May 1998. In August of 1998, he enrolled at the University of Florida in the Department of Materials Science and Engineering. He received a Master of Science degree in May 2002. During the summer of 2002, Slade completed an internship with Pratt & Whitney Aircraft Engines, in East Hartford, CT. He is currently scheduled to graduate with a Doctor of Philosophy degree in materials science and engineering, in August 2004.